UNIVERSITEIT VAN PRETORIA
UNIVERSITY OF PRETORIA
YUNIBESITHI YA PRETORIA

Thermoresponsive 3D scaffolds for non-invasive cell culture

by

Avashnee Shamparkesh Chetty

A thesis submitted in partial fulfilment
of the requirements for the degree

Doctor of Philosophy

in the

Department of Chemical Engineering
Faculty of Engineering, the Built Environment and Information Technology

University of Pretoria
Pretoria

November 2012

Thermoresponsive 3D scaffolds for non-invasive cell culture

by

Avashnee Shamparkesh Chetty

Maiden Surname: Sewlall

Supervisor: Prof. Walter W. Focke; University of Pretoria, Department of Chemical Engineering, Pretoria, South Africa

Co-supervisor: Prof. Viktoria Vargha; Budapest University of Technology and Economics, Budapest, Hungary

Degree for which the thesis is submitted: Ph.D. (Chemical Technology)

ABSTRACT

Conventionally, adherent cells are cultured *in vitro* using flat 2D cell culture trays. However the 2D cell culture method is tedious, unreliable and does not replicate the complexity of the 3D dynamic environment of native tissue. Nowadays 3D scaffolds can be used to culture cells. However a number of challenges still exist, including the need for destructive enzymes to release confluent cells. Poly(*N*-isopropylacrylamide) (PNIPAAm), a temperature responsive polymer, has revolutionised the cell culture fraternity by providing a non-invasive means of harvesting adherent cells, whereby confluent cells can be spontaneously released by simply cooling the cell culture medium and without requiring enzymes. While PNIPAAm monolayer cell culturing is a promising tool for engineering cell sheets, the current technology is largely limited to the use of flat 2D substrates, which lacks structural and organisational cues for cells.

The aim of this project was to develop a 3D PNIPAAm scaffold which could be used efficiently for non-invasive 3D culture of adherent cells. This project was divided into three phases: Phase 1 (preliminary phase) involved development and characterisation of cross-linked PNIPAAm hydrogels; Phase 2 involved development and characterisation of PNIPAAm grafted 3D non-woven scaffolds, while Phase 3 focused on showing proof of concept for non-invasive temperature-induced cell culture from the 3D PNIPAAm grafted scaffolds.

In Phase 1, PNIPAAm was cross-linked with N,N'-methylene-bis-acrylamide (MBA) using solution free-radical polymerisation to form P(PNIPAAm-*co*-MBA) hydrogels. A

broad cross-link density (i.e. 1.1 - 9.1 Mol% MBA) was investigated, and the effect of using mixed solvents as the co-polymerisation medium. The P(PNIPAAm-*co*-MBA) gels proved unsuitable as a robust cell culture matrix, due to poor porosity, slow swelling/deswelling and poor mechanical properties.

Subsequently, in Phase 2, polypropylene (PP), polyethylene terephthalate (PET), and nylon fibers were processed into highly porous non-woven fabric (NWF) scaffolds using a needle-punching technology. The NWF scaffolds were grafted with PNIPAAm using oxyfluorination-assisted graft polymerisation (OAGP). The OAGP method involved a 2 step process whereby the NWF was first fluorinated (direct fluorination or oxyfluorination) to introduce new functional groups on the fibre surface. The functionalised NWF scaffolds were then graft-polymerised with NIPAAm in an aqueous medium using ammonium persulphate as the initiator.

Following oxyfluorination, new functional groups were detected on the surface of the NWF scaffolds, which included C-OH; C=O; CH_2-CHF, and CHF-CHF. PP and nylon were both easily modified by oxyfluorination, while PET displayed very little changes to its surface groups. Improved wetting and swelling in water was observed for the oxyfluorinated polymers compared to pure NWF scaffolds. PP NWF showed the highest graft yield followed by nylon and then PET. PNIPAAm graft yield on the PP NWF was ~24 ± 6 µg/cm^2 on grafted pre-oxyfluorinated NWF when APS was used; which was found to be significantly higher compared to when pre-oxyfluorinated NWF was used without initiator (9 ± 6 µg/cm^2, p= 1.7x10^{-}7); or when grafting was on pure PP with APS (2 ± 0.3 µg/cm^2, p = 8.4x10^{-12}). This corresponded to an average PNIPAAm layer thickness of ~220 ± 54 nm; 92 ± 60 nm; and 19 ± 3 nm respectively. Scanning electron microscopy (SEM) revealed a rough surface morphology and confinement of the PNIPAAm graft layer to the surface of the fibers when oxyfluorinated NWF scaffolds were used, however when pure NWF scaffolds were used during grafting, homopolymerisation was observed as a loosely bound layer on the NWF surface. The OAGP method did not affect the crystalline phase of bulk PP as was determined by X-ray diffraction (XRD), however, twin-melting thermal peaks were detected from DSC for the oxyfluorinated PP and PP-*g*-PNIPAAm NWF which possibly indicated crystal defects. Contact angle studies and microcalorimetric DSC showed that the PP-*g*-PNIPAAm NWF scaffolds exhibited thermoresponsive behaviour. Using the 2,2-Diphenyl-1-1-picrylhydrazyl (DPPH) radical method and electron-spin resonance (ESR), peroxides, as well as trapped long-lived peroxy

radicals were identified on the surface of the oxyfluorinated PP NWF, which are believed to be instrumental in initiating graft polymerisation from the NWF. A free radical mechanism which is diffusion controlled was proposed for the OAGP method with initiation via peroxy radicals ($RO^{\bullet}$), as well as $SO_4^{\bullet-}$ and $OH^{\bullet}$ radicals, whereby the latter result from decomposition of APS.

In Phase 3 of this study, proof-of-concept is demonstrated for use of the PNIPAAm grafted NWF scaffolds in non-invasive culture of hepatocytes. Studies demonstrated that hepatocyte cells attached onto the 3D PNIPAAm scaffolds and remained viable in culture over long periods. The cells were released spontaneously and non-destructively as 3D multi-cellular constructs by simply cooling the cell culture medium from 37 ℃ to 20 ℃, without requiring destr uctive enzymes. The PP-*g*-PNIPAAm NWF scaffolds performed the best in 3D cell culture. Additionally the CSIR is developing a thermoresponsive 3D (T3D) cell culturing device, whereby the 3D thermoresponsive NWF scaffolds are used in the bioreactor for cell culture. Temperature-induced cell release was also verified from the 3D thermoresponsive scaffolds in the bioreactor. This technology could lead to significant advances in improving the reliability of the *in vitro* cell culture model.

Key-words: Poly-*N*-Isopropylacrylamide; graft polymerisation; 3D scaffolds; non-wovens; hydrogels; cell culture

OUTPUTS EMANATING FROM STUDY

Papers published

1. **Avashnee S. Chetty**, Viktoria Vargha, Arjun Maity, F. Sean Moolman, Claire Rossouw, Rajesh Anandjiwala, Lydia Boguslavsky, Dalu Mancama, Walter W. Focke, Development of thermoresponsive PP-*g*-PNIPAAm non-woven 3D scaffold for smart cell culture using oxyfluorination-assisted graft polymerisation, Colloids and Surfaces A: Physicochemical and Engineering Aspects, Colloids and Surfaces A: Physicochem. Eng. Aspects, 2013; 419: 37– 45.
2. Claire L. Rossouw, **Avashnee S. Chetty**, Francis S. Moolman, Lyn-Marie Birkholtz, Heinrich Hoppe, Dalu T. Mancama, Thermoresponsive non-woven scaffolds for ‘‘smart’’ 3D cell culture, Biotechnology and Bioengineering, 2012; 109(8): 2147-2158.
3. **Avashnee S. Chetty**, János Kovács, , Viktória Vargha, Ágnes Mészáros, Jenő Fekete, Attila Domján, A versatile characterisation of poly(*N*-isopropylacrylamide-*co*-N,N’-methylene-bis-acrylamide) hydrogels for composition, mechanical strength, and rheology, EXPRESS Polymer Letters, 2012; 7(1): 95–105
4. Viktoria Vargha, **Avashnee S. Chetty,** Zsolt Sulyok, Judith Mihály, Zsófia Keresztes, Andraś Tóth, Istvań Sajó, László Korecz, Rajesh Anandjiwala, Lydia Boguslavsky, Functionalisation of polypropylene non-woven nonwoven fabrics (NWF's) by oxyfluorination as a 1st step for graft polymerisation, Journal of Thermal Analytical Calorimetry, 2012; 109:1019-1032.

Conferences

Oral presentations:

1. **Avashnee S. Chetty**, Claire Rossouw, Luvo Ntsangani, Sean Moolman, Kobus van Wyk, Dalu Mancama, Rajesh Anandjiwala, Lydia Boguslavsky, Viktoria Vargha, Smart 3D cell culture using a thermoresponsive PP non-woven scaffold”, 11th ICFPAM conference- International Conference on Frontiers of Polymers and Advanced Materials: Symposium 8: Biomaterials Africa 2011, Pretoria, South Africa, May 2011, Paper 8A133C, pg 279.
2. **Avashnee S. Chetty**, Claire Rossouw, Luvo Ntsangani, Sean Moolman, Kobus van Wyk, Dalu Mancama, Rajesh Anandjiwala, Lydia Boguslavsky, Kersch Naidoo, Viktoria Vargha, Non-invasive 3D Cell Culture: Solving the demand for large quantities of functional human cells. 3rd CSIR Biennial Conference 2010. Science Real and Relevant. CSIR International Convention Centre, Pretoria, South Africa, 30 August – 01 September 2010, pg 21.

Poster presentations:

1. Thembisile Mahlangu, **Avashnee S. Chetty**, Arjun Maity, Claire Rossouw, Development of thermoresponsive non-woven 3D scaffolds for smart cell culture. 4th CSIR Biennial Conference 2012 – Real Problems - Relevant Solutions – Programme, CSIR, Pretoria South Africa, 8-9 October 2012.
2. Viktória Vargha, **Avashnee S. Chetty**, Zsolt Sulyok, Judith Mihály, Zsófia Keresztes, András Tóth, István Sajó, László Korecz, Rajesh Anandjiwala, Lydia Boguslavsky, Surface modification of polypropylene non-woven scaffolds by oxyfluorination. AMSALS 2012 International Symposium on Advanced Macromolecular Systems Across the Length Scales, Siófok, Hungary, June 3-6, P-11, pg.109.
3. János Kovács, **Avashnee S. Chetty**, Viktória Vargha, Ágnes Mészáros, Jenő Fekete, Attila Domján , András Szilágyi, Zsolt Sulyok: Characterisation of poly(*N*-isopropylacrylamide-co-N,N'-methylene-bis-acrylamide) hydrogels for composition, mechanical strength and rheology. AMSALS 2012 International symposium on advanced macromolecular systems across the length scales, Siófok, Hungary, June 3-6, P-51, pg. 149.
4. Ann Singh, Aletta Karsten, Itumeleng Mputle, **Avashnee S. Chetty**, Kersch Naidoo K, Determination of the optical properties of PNIPAAm gels used in biological applications: Progress in Biomedical Optics and Imaging - Proceedings of SPIE 7373, 2009, ISBN: 9780819476494, DOI:10.1117/12.831882
5. **Avashnee S. Chetty**, Viktoria Vargha, Fast responding PNIPAAm hydrogel (P173), TERMIS 2008 conference Sorrento, Tissue Engineering, ISSN 1937-3341, 14(4), May 2008, pg. 8.

ACKNOWLEDGEMENTS

I would like to extend my gratitude to the following people and organisation(s) for their contribution to this study:

- Prof Walter Focke for giving me the freedom to explore
- Prof Viktoria Vargha for her support, enthusiasm and guidance throughout this study
- My colleague Dr Arjun Maity for the many fruitful discussions, and assistance with the mechanisms
- Claire Rossouw – for her excellent work with the cell culture studies!
- Thembisile Mahlangu, Segametsi Songwane, Lerato Mokaleng, Luvo Ntsangani, Itumeleng Mputle, Stephanie Naidoo, and the vacation students for all their hard work on the experiments
- Dr Rajesh Anandjiwala and Lydia Boguslavsky for manufacture of the non-woven fabric scaffolds
- Pelchem Pty. Ltd. for the fluorination treatment of the scaffolds
- Dr Sean Moolman for his support and encouragement through-out my studies
- Dr Mamoeletsi Mosia for giving me the time and space to complete my thesis
- CSIR and the NRF for funding this study
- My husband Ezekiel Chetty for his patience, and understanding during the trying times of my write-up
- My parents for their love, guidance throughout my life, and for being my role-models, and making all of this possible!
- Finally I dedicate this work to my adorable daughter Nikisha Chetty

"I love you so much Niki, – you are truly a gift!"

TABLE OF CONTENTS

ABSTRACT ..... **ii**

OUTPUTS EMANATING FROM STUDY ..... **v**

ACKNOWLEDGEMENTS ..... **vii**

LIST OF FIGURES ..... **xii**

LIST OF SCHEMES ..... **xv**

LIST OF TABLES ..... **xvi**

DEFINITIONS AND ABBREVIATIONS ..... **xvii**

Chapter 1 : Introduction **1**

1.1 Background 2

1.2 Problem statement 3

1.3 Recent advances in cell culture 6

1.4 Research objectives 10

1.5 Research questions 11

1.6 Delineations and limitations 11

1.7 Brief chapter overview 11

1.8 References 12

Chapter 2 : Literature Review **15**

2.1 Introduction 16

2.2 Smart polymers 16

2.2.1 Poly(*N*-isopropylacrylamide) 17

2.3 PNIPAAm hydrogels 20

2.4 Graft polymerisation methods 23

2.4.1 Radiation-induced graft polymerisation 25

2.4.2 Graft polymerisation with chemical initiator 30

2.4.3 Surface functionalisation by fluorination 33

2.5 Advances in cell culture 35

2.5.1 3D scaffolds 36

2.5.2 PNIPAAm substrates for cell culture 41
2.5.3 Cell culturing in bioreactors 50
2.6 Conclusions 55
2.7 References 56
Chapter 3 : Instrumentation and Characterisation 68
3.1 Introduction 69
3.2 Chemical characterisation 69
3.2.1 UV-VIS 70
3.2.2 ATR-FTIR 72
3.2.3 XPS 74
3.2.4 XRD 75
3.2.5 ESR 77
3.3 SEM 78
3.4 Contact Angle 79
3.5 DSC 81
3.6 Rheometer 83
3.7 References 85
Chapter 4 : Development of P(NIPAAm-*co*-MBA) Hydrogels 87
4.1 Introduction 88
4.2 Experimental 90
4.2.1 Materials 90
4.2.2 Synthesis of P(NIPAAm-*co*-MBA) hydrogels 90
4.2.3 Characterisation of P(NIPAAm-*co*-MBA) hydrogels 92
4.3 Results & discussion 94
4.3.1 Mechanism for free radical polymerisation 94
4.3.2 Assessment of gel formulations 97
4.3.3 Determination of LCST by DSC 99
4.3.4 Morphology 101
4.3.5 Swelling and de-swelling properties 104

4.3.6 Viscoelastic properties 111
4.3.7 Water contact angle 117
4.4 Conclusions and recommendations 120
4.5 References 121
Chapter 5 : Development of PNIPAAm Grafted 3D NWF Scaffolds 124
5.1 Introduction 125
5.1.1 Choice of scaffold 126
5.1.2 Graft polymerisation method-OAGP 128
5.2 Experimental 130
5.2.1 Materials 130
5.2.2 Manufacture of NWF scaffolds 130
5.2.3 Graft polymerisation of PNIPAAm onto the NWF 130
5.2.4 Characterisation of pure and functionalised NWF 132
5.3 Results and discussion 136
5.3.1 Physical properties of pure NWF scaffolds 137
5.3.2 Analysis of NWF by ATR-FTIR 139
5.3.3 XPS analysis 160
5.3.4 SEM analysis 166
5.3.5 Water contact angle and swelling of NWF scaffolds in water 175
5.3.6 Determination of peroxides on NWF 179
5.3.7 Proposed mechanism for OAGP 185
5.3.8 XRD 188
5.3.9 DSC 190
5.4 Conclusions 194
5.5 References 195
Chapter 6 : Temperature-induced Cell Culture 200
6.1 Introduction 201
6.1.1 CSIR's cell culturing device T3D 202
6.2 Experimental 204

6.2.1 Materials 205
6.2.2 Cell –scaffold interaction 205
6.2.3 Temperature-induced cell release from PNIPAAm grafted NWF scaffolds in static culture 206
6.2.4 Cell release from PP-*g*-PNIPAAm NWF in T3D bioreactor 206
6.3 Results and discussion 208
6.3.1 Cell morphology and proliferation 208
6.3.2 Temperature-induced cell culturing from PNIPAAm grafted NWF 209
6.3.3 Temperature-induced cell release from PP-g-PNIPAAm NWF in the T3D device 213
6.4 Conclusions 215
6.5 References 216
Chapter 7 : Conclusions and Prospects 218
7.1 Conclusions of study 219
7.2 Significance of study 220
7.3 Recommendations 222

LIST OF FIGURES

Figure no.	Figure description	Page no.
Figure 1.1	Schematic showing conventional cell culture process	3
Figure 1.2	Conventional two dimensional TCPS	4
Figure 1.3	Enzymatic cell release vs. temperature-induced cell release	8
Figure 2.1	Chemical structure of PNIPAAm	17
Figure 2.2	LCST and UCST behaviour of thermoresponsive polymers	17
Figure 2.3	Photo showing phase transition of PNIPAAm solution	19
Figure 2.4	Effect of temperature on PNIPAAm hydrogel	19
Figure 2.5	Phase transition of PNIPAAm attached to a surface	20
Figure 2.6	Skin formation on PNIPAAm hydrogels after de-swelling	22
Figure 2.7	Schematic showing graft polymer on a polymer backbone	23
Figure 2.8	Schematic for “grafting from” and “grafting to” concepts	25
Figure 2.9	Schematic showing the oxyfluorination process	35
Figure 2.10	Research publications in the field of 3D cell culture	37
Figure 2.11	Images showing cells growing as spheroids in AlgiMatrix™	39
Figure 2.12	Images showing Cytodex 1, 3D Insert™ and Sponceram® disk	40
Figure 2.13	Mechanism of cell release on PNIPAAm –TCPS trays	43
Figure 2.14	Influence of graft thickness on chain mobility during cell release	45
Figure 2.15	Tissue reconstruction using cell sheets	46
Figure 2.16	Cell detachment from PNIPAAm porous membranes	48
Figure 2.17	Image of FiberCell hollow fibre system	52
Figure 2.18	The BioLevitator™ - a compact bench-top device	55
Figure 3.1	Electromagnetic spectrum	70
Figure 3.2	Schematic diagram of a typical absorption spectrometer	71
Figure 3.3	Image showing an ATR-FTIR instrument	73
Figure 3.4	Schematic showing working principle of ATR-FTIR	74
Figure 3.5	X-ray- atom interactions during XPS analysis	74
Figure 3.6	Principle of Bragg’s law for X-ray diffraction	76
Figure 3.7	Schematic showing principle of ESR	77
Figure 3.8	Schematic representation of a SEM	78
Figure 3.9	Image showing a contact angle goniometer	80
Figure 3.10	Contact angle measurement on a solid surface	80
Figure 3.11	Relationship between surface energy and contact angle	81

Figure no.	Figure description	Page no.
Figure 3.12	Illustration of principal of rheology using parallel-plate model	84
Figure 4.1	Optical image of standard R 90 P(NIPAAm-co-MBA) hydrogel	97
Figure 4.2	PNIPAAm gels prepared using mixed solvent systems	98
Figure 4.3	Typical DSC thermogram of P(NIPAAm-co-MBA) hydrogels	99
Figure 4.4	Image showing phase transition of P(NIPAAm-co-MBA) hydrogel	101
Figure 4.5	ESEM images of P(NIPAAm-co-MBA) hydrogels at 25 ℃	102
Figure 4.6	ESEM images of P(NIPAAm-co-MBA) hydrogels at 37 ℃	103
Figure 4.7	Swelling kinetics for hydrogels prepared in mixed solvents	106
Figure 4.8	Swelling kinetics at 20 ℃ for hydrogels prepared in water	108
Figure 4.9	Water retention for hydrogels synthesised in mixed solvents	109
Figure 4.10	De-swelling kinetics at 37 ℃ for P(NIP AAm-co-MBA) hydrogels	110
Figure 4.11	Storage and loss modulus for P(NIPAAm-co-MBA) hydrogels	112
Figure 4.12	Viscoelastic properties of hydrogels with varying cross-linker	113
Figure 4.13	Viscoelastic properties of hydrogels as a function of temperature	114
Figure 4.14	Viscoelastic properties of hydrogels with varying cross-linker	116
Figure 4.15	Viscoelastic properties of hydrogels from frequency sweep	118
Figure 5.1	Morphology and thermoresponsive behaviour of NWF	127
Figure 5.2	Photo showing experimental set-up for graft polymerisation	132
Figure 5.3	PP, PET, and nylon NWF developed by needle-punching	137
Figure 5.4	Chemical structures of PP, PET, nylon, and PNIPAAm	139
Figure 5.5	ATR-FTIR spectra of pure and functionalised PP NWF	140
Figure 5.6	ATR-FTIR spectra of hydrolysis of oxyfluorinated PP	143
Figure 5.7	ATR-FTIR spectra of pure and functionalised nylon NWF	144
Figure 5.8	ATR-FTIR spectra of pure and functionalised PET NWF	146
Figure 5.9	ATR-FTIR spectrum for pure PNIPAAm	149
Figure 5.10	ATR-FTIR spectra of PP-*g*-PNIPAAm (pre-functionalised)	150
Figure 5.11	Schematic showing intramolecular H bonding in PNIPAAm	151
Figure 5.12	ATR-FTIR spectra for grafting on pure and oxyfluorinated PP	152
Figure 5.13	ATR-FTIR spectra of grafted PET NWF (pre-oxyfluorinated)	153
Figure 5.14	ATR-FTIR spectra of grafted PET (no pre-oxyfluorination)	153
Figure 5.15	ATR-FTIR spectra of grafted nylon NWF (pre-oxyfluorinated	154
Figure 5.16	ATR-FTIR spectra of grafted nylon (no pre-functionalisation)	155
Figure 5.17	ATR-FTIR spectra of grafted PP NWF (without initiator)	156
Figure 5.18	Calibration graph to determine graft yield	157
Figure 5.19	Graft yield based on ATR-FTIR	160

Figure no.	Figure description	Page no.
Figure 5.20	Wide XPS spectra for pure and functionalised PP NWF	161
Figure 5.21	Narrow C1s spectra for pure and functionalised PP NWF	162
Figure 5.22	Narrow C1s for PP-*g*-PNIPAAm	165
Figure 5.23	SEM images showing PP, nylon and PET NWF scaffolds	167
Figure 5.24	SEM images of PP NWF after oxyfluorination	168
Figure 5.25	SEM images of PP-*g*-PNIPAAm (pre-oxyfluorinated)	169
Figure 5.26	SEM images of PP-*g*-PNIPAAm (no functionalisation)	170
Figure 5.27	SEM images of nylon-*g*-PNIPAAm (pre-oxyfluorinated)	171
Figure 5.28	SEM images of nylon-*g*-PNIPAAm (no functionalisation)	172
Figure 5.29	SEM images of PET-*g*-PNIPAAm (pre-oxyfluorinated)	173
Figure 5.30	SEM images of PET-*g*-PNIPAAm (no functionalisation)	174
Figure 5.31	SEM images of PP-*g*-PNIPAAm (pre-oxyfluorinated, no initiator)	175
Figure 5.32	Photo showing water drop on NWF surfaces	176
Figure 5.33	Static water contact angle of PP NWF scaffolds	176
Figure 5.34	Percent swelling for pure and oxyfluorinated PP and PET	179
Figure 5.35	Visual observation of wettability of pure and oxyfluorinated PP	179
Figure 5.36	Scheme showing electron delocalisation in DPPH	180
Figure 5.37	Colour observation after reaction of oxyfluorinated PP - DPPH	181
Figure 5.38	UV-VIS spectra of DPPH solution after treatment with PP NWF	181
Figure 5.39	Calibration graph relating absorbance and DPPH concentration	182
Figure 5.40	Comparison of peroxides on pure PP and oxyfluorinated PP	183
Figure 5.41	ESR spectra of PP oxyfluorinated NWF	184
Figure 5.42	Change in radical concentration with time at 70 °C	185
Figure 5.43	XRD diffractograms for pure, oxyfluorinated, and grafted PP	189
Figure 5.44	DSC thermograms (1st cooling) for pure and treated PP	191
Figure 5.45	DSC thermograms (2nd heating) for pure and treated PP	191
Figure 5.46	DSC thermogram of PP-*g*-PNIPAAm showing a LCST	194
Figure 6.1	Schematic of CSIR's T3D cell culture device	204
Figure 6.2	Preliminary prototype of the CSIR's T3D device	207
Figure 6.3	Fluorescence micrographs of cells on PP-*g*-PNIPAAm scaffolds	208
Figure 6.4	Thermal release of cells from grafted PP, PET and nylon	210
Figure 6.5	Thermal release of cells from PP-*g*-PNIPAAm NWF	212
Figure 6.6	Fluorescence of cells on scaffold after thermal release	213
Figure 6.7	Final prototype T3D device	215

LIST OF SCHEMES

Scheme no.	Scheme description	Page no.
Scheme 2.1	Mechanism for free-radical polymerisation	24
Scheme 2.2	Mechanism for high-energy graft polymerisation	26
Scheme 2.3	Process for plasma-induced graft polymerisation	28
Scheme 2.4	Graft polymerisation of PNIPAAm using atmospheric plasma	28
Scheme 2.5	Mechanism of photografting	29
Scheme 2.6	Typical mechanism for free radical induced graft polymerisation	30
Scheme 2.7	Graft polymerisation using persulphate and Ce ion	32
Scheme 2.8	Proposed mechanism for functionalisation with persulphate/Ce	32
Scheme 2.9	Proposed mechanism for direct fluorination of polymers	34
Scheme 4.1	Synthesis of PNIPAAm hydrogels by free radical polymerisation	91
Scheme 4.2	Mechanism for synthesis of P(NIPAAm-co-MBA)	95
Scheme 4.3	Initiation of NIPAAm and MBA monomers using APS/TEMED	96
Scheme 5.1	OAGP of PNIPAAm onto NWF scaffolds	186
Scheme 5.2	Reaction mechanism for fluorination of NWF scaffolds	186
Scheme 5.3	Mechanism for synthesis of PNIPAAm grafted NWF scaffolds	188

LIST OF TABLES

Table no.	Table description	Page no.
Table 2.1	LCST of various PNIPAAm copolymers	22
Table 2.2	Commercial 3D scaffolds used for cell culture	38
Table 2.3	Commercially available automated cell culture systems	54
Table 4.1	Feed composition of P(NIPAAm-*co*-MBA)	92
Table 4.2	Solvent: water mixtures used during PNIPAAm polymerisation	92
Table 4.3	Composition and appearance of hydrogels 1-9	98
Table 4.4	LCST of P(NIPAAm-*co*-MBA) hydrogels determined by DSC	100
Table 4.5	Swelling ratios of PNIPAAm hydrogels	105
Table 4.6	Linear viscoelastic range of P(NIPAAm-co-MBA) hydrogels	113
Table 4.7	LCST of P(NIPAAm-*co*-MBA) hydrogels from rheometry	115
Table 4.8	Static contact angle of P(NIPAAm-*co*-MBA) hydrogels	119
Table 5.1	Processing parameters and properties of NWF scaffolds	138
Table 5.2	Assignment of FTIR peaks for pure PP NWF scaffolds	142
Table 5.3	Assignment of FTIR peaks for pure PET, and nylon 6.6 NWF	145
Table 5.4	New functionality on the oxyfluorinated NWF scaffolds	148
Table 5.5	FTIR peak assignment for pure PNIPAAm homopolymer	149
Table 5.6	Absorption wavenumbers for PNIPAAm vs. PP-*g*-PNIPAAm	151
Table 5.7	Relative surface areas of currently available 3D scaffolds	159
Table 5.8	PNIPAAm yield and thickness on PP-*g*-PNIPAAm NWF	163
Table 5.9	Atomic composition of pure and functionalised PP from XPS	164
Table 5.10	Atomic ratios for F/C/O present on pure and functionalised PP	166
Table 5.11	Moles peroxides on oxyfluorinated PP using DPPH	182
Table 5.12	Crystallisation and melting data for pure and oxyfluorinated PP	192

DEFINITIONS AND ABBREVIATIONS

2D	Two dimensional
3D	Three dimensional
APS	Ammonium persulphate
ATR-FTIR	Attenuated total reflectance Fourier transform infrared
CSIR	Council for Scientific and Industrial Research
DPPH	2,2-Diphenyl-1-1-picrylhydrazyl
DMEM	Dulbecco's Modified Eagle Medium
DSC	Differential scanning calorimetry
ECM	Extracellular matrix
ESR	Electron spin resonance
FCS	Foetal calf serum
FDA	Fluorescein diacetate
LCST	Lower critical solution temperature
LVE	Linear viscoelastic
MBA	N,N'-methylenebisacrylamide
NIPAAm	*N*-isopropylacrylamide
NWF	Non-woven fabric
OAGP	Oxyfluorination-assisted graft polymerisation
PBS	Phosphate buffered saline
PE	Polyethylene
PET	Polyethyleneterephthalate
PNIPAAm	Poly(*N*-isopropylacrylamide)
PP	Polypropylene
TCPS	Tissue-culture polystyrene
TEMED	N,N,N'-N'-tetramethylenediamine
R	Cross-link density (nMol NIPAAm/nMol MBA)
SEM	Scanning electron microscopy
THF	Tetrahydrofuran
UV-VIS	Ultraviolet-visible
XRD	X-ray diffraction
XPS	X-ray photoelectron spectroscopy

CHAPTER 1

Introduction

1.1 Background

With the global expansion in the biotechnology industry there is now a growing demand for mammalian cells and their products. High-density cell cultures are typically required for a large number of applications including drug screening, cytotoxicity testing, cancer research, stem cell research, tissue engineering, genetic engineering, regenerative medicine and for the production of cell culture therapeutics. The global cell culture market was estimated at $1.02 billion in 2005 and is projected to reach $1.86 billion by 2010 (Kulkarni, 2006). This market is predominantly driven by the larger biopharmaceutical and biotechnology companies with the main contributor being manufacture of therapeutics including vaccines, hormones, blood factors, thrombolytics, interferons, monoclonal antibodies, and therapeutic enzymes; all of which require mammalian cell cultures for their production. The cell culture market is also supported by research laboratories at universities, and contract manufacturing and research organizations that utilise large numbers of cells for new research and development or routine testing and analysis.

Mammalian cells can be in the form of either primary cells or cell lines. Primary cells are obtained from normal healthy tissue (i.e. from a human or animal source) while cell lines are typically obtained from immortalised tissue or through random mutations. Primary cells are ideal since the cells are uncompromised and exist in their native physiological state. However their use is limited in research, due to difficulty in isolation, ethical issues, challenges with cell proliferation, high costs, and typically they have a limited lifespan where they stop dividing and undergo senescence (Gomes and Reis, 2004; Salgado et al., 2004). Conversely cell lines have the ability to proliferate indefinitely, and at a much faster rate than a typical primary cell. Since they are more readily available and easier to work with, cell lines are routinely used for *in vitro* cell culture.

Cell lines however are still expensive and typically a small vial of cells is purchased (e.g. from the American Tissue Culture Collection (ATCC®)) and frozen away until required. When cells are required for a specific assay, cell stocks are thawed, and the cells are subjected to a cell culture process as shown in **Figure 1.1a**. For adherent cells, typically this process involves the use of two-dimensional (2D) tissue culture polystyrene (TCPS) trays, onto which cells are seeded and attach under

appropriate growth conditions, and the cells and then allowed to proliferate and reach confluence (**Figure 1.1b**).

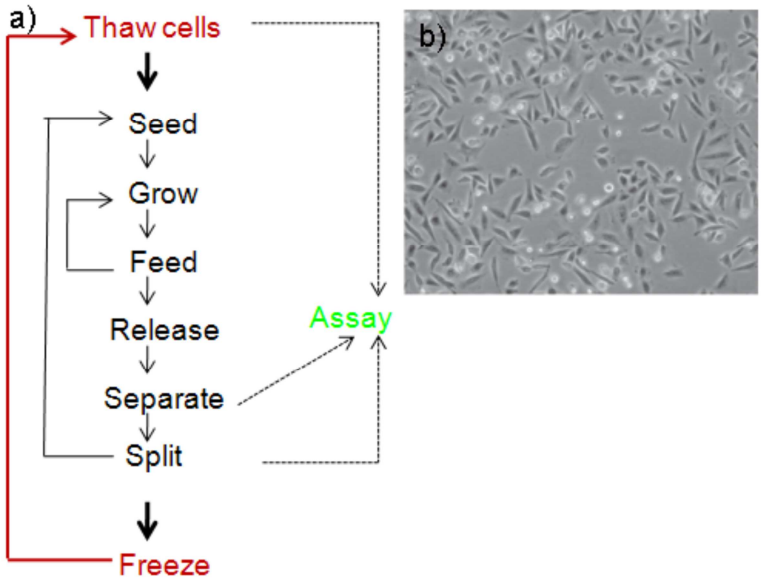

Figure 1.1: (a) Schematic showing processing steps involved in conventional cell culture process; and (b) micrograph showing ATCC® CCL-61™ cell lines growing on TCPS (ATCC®, 2012).

Confluent (or semi-confluent) cells are released from the TCPS typically using proteolytic enzymes (such as trypsin). If left to grow beyond the confluent state, cells can undergo cell death by necrosis due to space and nutrient deprivation. After cell release, cells are washed in sterile centrifuge tubes to inactivate and remove proteins such as trypsin, and other cell products. After this separation / washing step, the cell mass is now split and seeded into more 2D cell culture trays in a sub-culture process. Typically several such cycles of seeding, growth, release, washing and reseeding are required to grow sufficient numbers of cells. The cultured cells can then finally be used directly in a biological assay or frozen away for down-stream processing.

1.2 Problem statement

Although the 2D monolayer TCPS method is simple and easy to perform, this method is found to be unreliable and sometimes inaccurate, hence *in vitro* data often cannot be used to accurately predict the cellular responses of living organisms (Pampaloni

et al., 2007). Some of the main challenges with the conventional cell culture method are addressed below.

a) **Use of a 2D surface to grow cells**

The conventional TCPS trays (**Figure 1.2**) used for cell culture are flat, 2D, non-porous, and rigid, and does not represent the complex 3D cellular environment found in living tissue (Pampaloni et al., 2007).

Figure 1.2: Examples of two dimensional tissue culture polystyrene trays, flasks and plates used for cell culture of adherent cells.

Due to the unnatural constraints imposed on cells when grown in 2D, 2D cell cultures bear only limited resemblance to the complexity of the 3D dynamic environment in which cells exist naturally (Bokhari et al., 2007). Essential cellular interactions, and signalling pathways present in living tissue are absent in 2D cell cultures (Pampaloni et al., 2007). It is now well-known that cells grown in 3D display closer similarities to their *in vivo* counterparts in terms of cell migration, morphology, differentiation, phenotype, gene expression and function (Bokhari et al., 2007; Justice et al., 2009; Liu, 2008; Pampaloni et al., 2007) when compared to their 2D counterparts. A 3D scaffold is required to resemble the extracellular matrix (ECM) onto which cells naturally attach in physiological tissue. The ECM is a highly porous 3D mesh consisting of a complex mixture of proteins and sugars which is secreted by cells during normal growth. The ECM serves a number of functions, which includes providing structural support to cells; enabling diffusion of oxygen, nutrients, and removal of waste products; maintaining cell-cell interactions; and regulating signalling pathways and other important biochemical and mechanical cues (Justice et al., 2009).

b) **Harsh methods used to release confluent cells**

Confluent cells are either released using enzymes, chemicals or by mechanical scraping. The use of trypsin is by far the most popular means of releasing harvested cells. However many studies have reported disruption to the ECM and integrin receptors by trypsin use during cell release (Canavan et al., 2005). Trypsin is a proteolytic enzyme which cleaves cell adhesive proteins present in the ECM into smaller peptides and amino acids. Damage to the ECM is known to adversely influence the cell signalling pathways affecting a number of important cellular processes such as adhesion, proliferation, differentiation, migration, structure, gene expression and cell fate (Geiger et al., 2001; Guillame-Gentil et al., 2010). Furthermore trypsin is of animal origin and a potential source of contamination to cells. Over-exposure of cells to trypsin has been shown to lead to slow cell growth, unhealthy rounded morphology, and cell heterogeneity even in the same TCPS culture flask. Chelating agents (such ethylenediamine tetraacetic acid - EDTA) are also often used in conjunction with trypsin for cell release. EDTA is used to inactivate divalent cations such as Ca^{2+}, Mg^{2+}, which are known to inhibit typsin activity. However EDTA use, has alos been reported to disrupt the ion channels and important cell-to-cell junctions (Canavan et al., 2005). Ion-channels are pore-forming membrane proteins present in every cell, and changes in the ion concentration across the cell membrane affects secretion of fluids, hormones, ions. Other commonly used approaches include mechanical scraping, however this has been reported to break cell walls in particular the lipid-membrane leading to cell inflammation which induces changes to the morphological appearance of the harvested cells (Canavan et al., 2006). This implies that the current cell release methods is a major contributor to the poor repeatability, high contamination, and high variability of the conventional cell culture process (Canavan et al., 2006).

c) **Highly labour intensive and prone to contamination**

Often millions of cells are required for a specific biological assay, and the cell seeding-splitting steps must be repeated manually several times to achieve sufficient cell mass (Felder and Gildea, 2005). Typically this would involve seeding one flask, then four, then 16, then 64 etc. Due to the extra handling requirements and human operator involvement, conventional cell culture is thus prone to poor repeatability, batch to batch inconsistency, and contamination. If a specific culture is contaminated with microorganisms, typically it would be discarded and the whole process repeated.

This often results in low turn-around times and additional costs for consumables, media, etc.

d) **Static growth conditions**

Conventional cell culture is typically performed in a static environment which does not mimic the dynamic environment in living tissue. In native tissue, cells are subjected to a dynamic perfused environment which ensures a continuous supply of oxygen and fresh nutrients by blood capillaries and removal of waste products, while at the same time the fluid flow stimulates cellular behaviour. The oxygen concentration in the culture media is known to affect various cellular mechanisms, including cell cycle, cell proliferation, apoptosis, and glucose metabolism (Volkmer et al., 2008). To maintain homogenous growth rates, and cell viability, static culture requires regular manual feeding, i.e. supplementation of the media and monitoring the oxygen content which further adds an element of variability, also contributing to inconsistencies amongst operators. A dynamic fluid flow environment is also required for physical and mechanical stimulation of cells (such as in the case of bone or heart tissue) (Bancroft et al., 2002), which does not occur in a static state.

1.3 Recent advances in cell culture

It is well-known that the process in which cells are grown *in vitro* directly influence cell behaviour, growth, differentiation, gene expression and other important biological activities (Bokhari et al., 2007; Justice et al., 2009; Mueller-Klieser, 1997). Due to the limitations mentioned above, the conventional TCPS monolayer method to culture mammalian cells cannot be used to accurately predict the cellular responses of living organisms (Pampaloni et al., 2007). Hence expensive *in vivo* trials are required at an early stage of research. In the recent decades, much effort has been made towards developing more reliable cell culture scaffolds and systems.

3D scaffolds are nowadays available to culture cells. The vast majority of the commercially available 3D scaffolds are biomimetic-based and include Matrigel™, AlgiMatrix™, GEM™, Extracel™ and Cytodex™ (Justice et al., 2009). However concerns exist with regards to the production variability of some of the scaffolds, and in some cases animal components are used (Justice et al., 2009). Also the available

3D scaffolds are typically expensive, and cannot be used for routine cell-culture work. Recently bioreactors have also been developed for high-density cell proliferation, to increase oxygenation, culture media circulation, cell volumes and outputs, and include for e.g. multiple-stacked plates (e.g. AcCellerator™), spinner flasks, fluidised-bed, hollow-membrane fibre bioreactors (e.g. Cellmax) and the like. Some of these systems are also automated to alleviate contamination and the human intervention required. Although some 3D bioreactors are appearing on the market (BioLevitator™), the majority of the automated systems are still based on the use of 2D surfaces. For e.g. AcCellerator™ allows the traditional cell culture steps based on 2D trays to be automated by robots. However despite these advantages, one of the main challenges still remaining in the field is that cell release from scaffolds still largely involves the use of enzymes to degrade the cell surface proteins, or harmful chemicals to dissolve the scaffold in order to release the cells. This combined with the additional wash steps and extra handling requirements results in well-to-well variations and culture inconsistencies.

A major breakthrough in the field of cell-culture is the use of a temperature-responsive polymer i.e. poly-*N*-isopropylacrylamide, (i.e. PNIPAAm) to non-destructively release adherent cells by merely cooling the cell culture medium. PNIPAAm is a temperature-sensitive polymer that is characterised by a lower critical solution temperature (LCST) of approximately 32-33 °C (Schild, 1992). PNIPAAm switches its properties reversibly between hydrophobic (cell adhesive) and hydrophilic (non-cell adhesive) states at temperatures higher and lower than its LCST respectively. The pioneering work by Okano's group reported for the first time that cells could be released spontaneously as intact sheets from the surface of PNIPAAm coated TCPS with preserved cell-cell and cell-extracellular matrix (ECM) interactions by simply cooling the cell culture medium (Okano et al., 1995) as shown in **Figure 1.3**.

While PNIPAAm cell sheets serve as a promising tool for engineering tissue, a limitation of the current technology is that it is primarily based on the use of 2D flat substrates which lacks structural and organisational cues for cells (Isenberg et al., 2008). Existing 2D PNIPAAm substrates do not enable *in situ* cell growth in three dimensions.

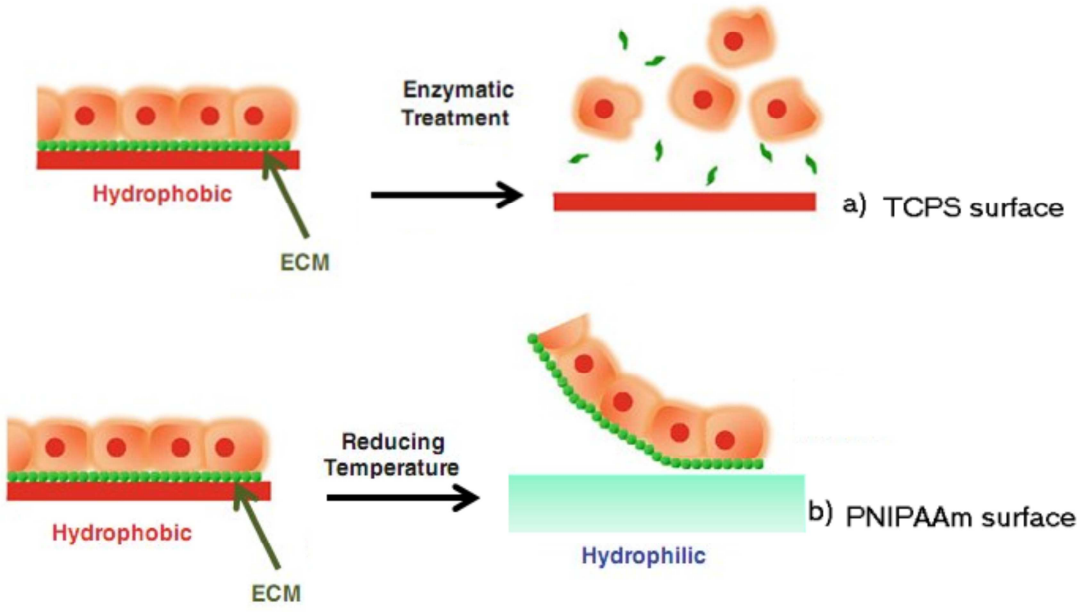

Figure 1.3: Schematic image showing cells in a monolayer whereby cell release is achieved either by a) enzymatic treatment or b) by lowering the temperature on a PNIPAAm surface. For enzymatic treatment, the deposited ECM (green) and membrane proteins are degraded and cells are released as single cells while for temperature-induced cell release, confluent cells spontaneously lift off the surface when the temperature is lowered to 20 ℃, with inta ct ECM and cell-cell junction proteins (Adapted from Kumashiro et al., 2010).

In recent years, some attempts have been made at the development of 3D PNIPAAm scaffolds based on sub-micron porous structures such as membranes (Kwon O.H., 2003; Murakami et al., 2006), hydrogels (Kwon and Matsuda, 2006; Ohya et al., 2005), micro-textured surfaces (Isenberg et al., 2008), and non-woven membranes (Okamura et al., 2008; Toshiyuki and Midori, 2006). However many of the studies focus on the culture and release of cell monolayers, and still to date little work has been done regarding applying the PNIPAAm technology to highly porous 3D scaffolds whereby cells are grown in a 3D environment and are released spontaneously as 3D cellular constructs.

Based on the literature, and discussions with various end-users (such as cell biologists, medical doctors, biochemists and molecular biologists etc.), the need for a new and efficient cell culturing system with minimal human intervention, efficiency, speed, and the ability to culture cells with minimal damage while maintaining their 3D

structure was identified. The key attributes of such a system should include the following:

- **3D porous scaffold:** A highly porous 3D scaffold should be used with large interconnected open pores to support cell-cell interactions. The porous structure should allow for oxygen and nutrient exchange, as well as cell-to-cell and cell-to-ECM interactions.
- **Non-destructive cell release:** Confluent cells should be released by a non-invasive method, without requiring harsh enzymes, chemicals, or scraping which are known to damage the cell surface. Cultured cells should retain their membrane constituents and remain in their natural state upon harvesting.
- **A bioreactor:** A bioreactor should be used to culture cells such that the cell culture medium can be perfused throughout the scaffold to enable, sufficient oxygen supply, nutrient exchange, as well as provide mechanical or physical stimulation to the growing cells.
- **High density cell culturing**: The system should allow for the cultivation of large numbers of cells (typically 1-2 orders of magnitude greater than a standard 75 cm^2 static culture flask), which would be possible with a 3D scaffold with a large surface area per volume ratio whereby a large number of cells can attach per cm^2 of scaffold.
- **Sufficient oxygenation:** To overcome diffusional constraints, oxygenation should be achieved by the use of either oxygen spargers, hollow-fibres, or oxygen carriers to support the oxygen requirements for high cell density cultures.
- **Automated operation**: The system should preferably allow for automation of the operating procedures as well as include instrumentation to automatically monitor, control and regulate the system parameters such as pH, temperature, dissolved oxygen content, agitation speed, nutrient/waste content etc. Automation would mitigate the labour-intensive process and human intervention requirement for manual cell culturing.

The Council for Scientific and Industrial Research (CSIR) in South Africa is developing a thermoresponsive 3D (T3D) cell culture device for culturing of adherent cells. The device consists of a 3D PNIPAAm scaffold of the present study, onto which cells grow and proliferate in a bioreactor and whereby cell release is non-destructive. The system will also preferably be automated to minimise contamination and human

steps. The device will enable the growth and release of 3D cellular aggregates in high-density, while enabling non-invasive temperature-induced cell harvesting without the need for destructive enzymes. A detailed description of the T3D device is given in **Chapter 6**.

1.4 Research objectives

The scope of this study is based on the design, development, and validation of a 3D thermoresponsive scaffold based on PNIPAAm for use in non-invasive temperature-induced culture of adherent cells. This project was divided into three phases: Phase 1 (preliminary study) involved development and characterisation of cross-linked PNIPAAm hydrogels using free-radical polymerisation to investigate the effect of cross-link density and mixed solvents on the physical properties of PNIPAAm hydrogels; phase 2 involved synthesis, and characterisation of highly porous 3D non-woven fabric scaffolds grafted with PNIPAAm using oxyfluorination-assisted graft polymerisation, while phase 3 focussed on showing proof of concept for use of the 3D thermoresponsive scaffolds for non-invasive cell culture.

The specific research objectives of this study were as follows:

- Phase 1 (preliminary study)
    - Synthesis of PNIPAAm hydrogels cross-linked with N,N'-methylenebisacrylamide (MBA) using free-radical polymerisation
    - Study the effect of crosslink density and solvent : water mixtures on the physical properties of the PNIPAAm hydrogels
- Phase 2 (primary focus of dissertation)
    - Development of 3D porous non-woven fabric scaffolds (based on PP, nylon and PET) grafted with PNIPAAm using oxyfluorination-assisted graft polymerisation (OAGP)
    - Physical and chemical characterisation of the PNIPAAm grafted non-woven fabric scaffolds and verification of the thermoresponsive behaviour
- Phase 3 (proof-of-concept study)
    - Cell culture of hepatocytes onto the PNIPAAm grafted NWF scaffolds at 37 ℃ and temperature-induced cell release at 20 ℃

- Cell culture of hepatocytes in the T3D cell culture device at 37 ℃ and temperature-induced cell release at 20 ℃

1.5 Research questions

The questions which this work attempts to answer are the following:

- Can the physical and mechanical properties of PNIPAAm hydrogels be improved for use in cell culture?
- How can we covalently attach PNIPAAm onto a 3D scaffold?
- Will the open porous 3D structure be maintained in the grafted scaffold?
- How does the grafting affect the properties of the non-woven material?
- Will the grafted PNIPAAm maintain its thermoresponsive properties?
- Will cells attach onto the grafted PNIPAAm surface and remain viable at 37 ℃?
- Will cells release from the grafted PNIPAAm surface at 20 °C without requiring enzymes?

1.6 Delineations and limitations

The project scope is limited to development of a new 3D scaffold for the purpose of *in vitro* cell culturing and focuses on PNIPAAm and its temperature responsive behavior and will not consider other non-destructive cell release agents. Only the following polymer scaffolds are included in this study: i.e. polypropylene (PP), polyethyleneterephthalate (PET), and nylon 6.6. Proof-of-principle studies for non-invasive cell culturing are limited to hepatocyte cell lines only.

1.7 Brief chapter overview

The chapters which are included in this dissertation will cover the following aspects:

Chapter 1: Introduction
Chapter 2: Literature review
Chapter 3: Instrumentation and characterisation techniques
Chapter 4: Development of cross-linked PNIPAAm hydrogels

Kulkarni N. 2006. Biopharma industry boosting cell culture sector in India, http://biospectrumindia.ciol.com/content/BioTrends/10601061.asp, Date accessed: 20 August 2010.

Kumashiro Y, Yamato M, Okano T. 2010. Cell attachment–detachment control on temperature-responsive thin surfaces for novel tissue engineering. Annals of Biomedical Engineering 38(6):1977–1988.

Kwon IK, Matsuda T. 2006. Photo-iniferter-based thermoresponsive block copolymers compose of poly(ethylene glycol) and poly(N-isopropylacrylamide) and chondrocyte immobilization. Biomaterials 27 986–995.

Kwon OH, Kikuchi A, Yamato M, Okano T. 2003. Accelerated cell sheet recovery by co-grafting of PEG with PIPAAm onto porous cell culture membranes. Biomaterials 24:1223–1232.

Liu Q; 3D Biotek, LLC, assignee. 13/02/2008. Three dimensional cell culture construct and apparatus for its making. United States patent US 2008/0194010 A1.

Mueller-Klieser W. 1997. Three-dimensional cell cultures: from molecular mechanisms to clinical applications. The American Physiological Society C1109-C1123.

Murakami D, Yamato M, Nishida K, Ohki T, Takagi R, Yang J, Namiki H, Okano T. 2006. The effect of micropores in the surface of temperature-responsive culture inserts on the fabrication of transplantable canine oral mucosal epithelial cell sheets. Biomaterials 27:5518–5523.

Ohya S, Kidoaki S, Matsuda T. 2005. Poly(*N*-isopropylacrylamide) (PNIPAM)-grafted gelatin hydrogel surfaces: interrelationship between microscopic structure and mechanical property of surface regions and cell adhesiveness. Biomaterials 26: 3105–3111.

Okamura A, Hagiwara T, Yamagami S, Yamaguchi M, Shinbo T, Kanamori T, Kondo S, Miwa K, Itagaki I. 2008. Effective cell separation utilizing poly(*N*-Isopropylacrylamide)-grafted polypropylene membrane containing adsorbed antibody. Journal of Bioscience and Bioengineering 105 (3):221–225.

Okano T, Yamada N, Okuhara M, Sakai H, Sakurai Y. 1995. Mechanism of cell detachment from temperature-modulated, hydrophilic-hydrophobic polymer surfaces. Biomaterials 16:297-303.

Pampaloni F, Reynaud EG, Stelzer EHK. 2007. The third dimension bridges the gap between cell culture and live tissue. Nature Reviews Molecular Cell Biololgy 8:839-845.

Salgado AJ, Coutinho OP, Reis RL. 2004. Bone tissue engineering: state of the art and future trends Macromolecular Bioscience 4:743-765.

Schild H. 1992. Poly(*N*-isopropylacrylamide): Experiment, theory, and application. Progress in Polymer Science 17:163-249.

Toshiyuki K, Midori I; 2006. Cell separation and collection apparatus and separation and collection method. United States patent PCT/JP03/16170.

Volkmer E, Drosse I, Otto S, Stangelmayer A, Stengele M, Kallukalam BC, Mutschler W, Schieker M. 2008. Hypoxia in static and dynamic 3D culture systems for tissue engineering of bone. Tissue Engineering: Part A 14(8):1331-1340.

Chapter 5: Development of PNIPAAm grafted 3D NWF scaffolds

Chapter 6: Temperature-induced cell culture

Chapter 7: Conclusions and Perspective

1.8 References

ATCC®. 2012. Animal cell culture guide: Tips and techniques for continuous cell lines, CB-0112-37-01:1-40.

Bancroft GN, Sikavitsas VI, van den Dolder J, Sheffield TL, Ambrose CG, Jansen JA, Mikos AG. 2002. Fluid flow increases mineralized matrix deposition in 3D perfusion culture of marrow stromal osteoblasts in a dose-dependent manner. Proceedings of the National Academy of Sciences 99(20):12600–12605.

Bokhari M, Carnachan RJ, Cameron NR, Przyborski SA. 2007. Novel cell culture device enabling three-dimensional cell growth and improved cell function. Biochemical and Biophysical Research Communications 354:1095–1100.

Canavan HE, Cheng X, Graham DJ, Ratner BD, Castner DG. 2006. A plasma-deposited surface for cell sheet engineering: Advantages over mechanical dissociation of cells. Plasma Processes and Polymers 3:516–523.

Canavan HE, Cheng X, Graham DJ, Ratner BD, Castner DG. 2005. Cell sheet detachment affects the extracellular matrix: A surface science study comparing thermal liftoff, enzymatic, and mechanical methods. Journal of Biomedical Materials. Research-A 75(1):1-13.

Felder RA, Gildea JJ. 2005. Automated cell culture system and process patent PCT/US2004/023222.

Geiger B, Bershadsky A, Pankov R, Yamada KM. 2001. Transmembrane extracellular matrix-cytoskelton crosstalk. Nature Reviews - Molecular Cell Biology 2:793-805.

Gomes ME, Reis RL. 2004. Tissue engineering: Key elements and some trends. Macromolecular Bioscience 4:737-742.

Guillame-Gentil O, Semenov O, Roca AS, Groth T, Zahn R, Vörös J, Zenobi-Wong M. 2010. Engineering the extracellular environment: strategies for building 2D and 3D cellular structures. Advanced Material 22:5443–5462.

Isenberg BC, Tsuda Y, Williams C, Shimizu T, Yamato M, Okano T, Wong JY. 2008. A thermoresponsive, microtextured substrate for cell sheet engineering with defined structural organization. Biomaterials 29:2565–2572.

Justice BA, Badr NA, Felder RA. 2009. 3D cell culture opens new dimensions in cell-based assays. Drug Discovery Today 14(1/2):102-107.

CHAPTER 2

Literature Review

2.1 Introduction

This chapter deals with a comprehensive literature review which covers the following key aspects: smart polymers (**Section 2.2**); PNIPAAm hydrogels (**Section 2.3**); graft polymerisation methods (**Section 2.4**); and recent advances in cell culture (**Section 2.5**).

2.2 Smart polymers

In recent years, “smart polymers” (also known as stimuli responsive polymers, intelligent polymers, or environmental-sensitive polymers) have revolutionised material science. Smart polymers display a unique ability to respond to small changes in an external stimulus by undergoing rapid, dramatic and macroscopic changes in their physio-chemical properties (Galaev and Mattiasson, 1999; Hoffman, 2000; Kumar et al., 2007). The responses are manifested by order of magnitude changes in the material with respect to shape, size, volume, solubility, water content, formation of an intricate self-assembly and/or a sol-to-gel transition (Jeong and Gutowska, 2002). What makes smart polymers so interesting is that their phase transition is reversible and can be easily manipulated (Kumar et al., 2007). The driving forces behind the phase transition varies and could for e.g. include hydrogen bonding, hydrophobic interactions or polymer-polymer interaction, neutralisation of charged groups (by a change in pH or ionic strength), molecular orientation, and/or collapse of polymer system (Galaev and Mattiasson, 1999).

A variety of triggers have been reported in literature and can be classified as follows (Hoffman, 2000; Kumar et al., 2007):

- Physical: temperature, ionic strength, solvents, electromagnetic radiation, electric field, magnetic field;
- Chemical: pH, specific ions, chemical agents; and
- Bio-chemical: enzymes, ligands, and biochemical agents

Thermoresponsive or temperature-sensitive polymers are the most widely studied class of smart polymers since temperature is the sole stimulus for their phase transition and often only modest temperatures are required for a transition to occur (Klouda and Mikos, 2008).

2.2.1 Poly(*N*-isopropylacrylamide)

Poly(*N*-isopropylacrylamide) i.e. PNIPAAm is the most popular and well-known of all the thermoresponsive polymers and is the focus of this study. The chemical structure of PNIPAAm is shown in **Figure 2.1**. PNIPAAm is amphiphilic and contains hydrophilic amide groups (-NHCO) and hydrophobic isopropyl groups (-$CH(CH_3)_2$).

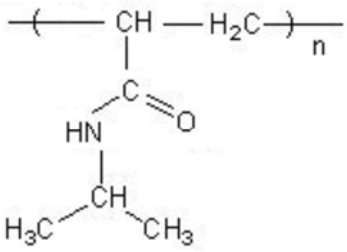

Figure 2.1: Chemical structure of PNIPAAm.

Thermoresponsive polymers can in general display two types of behaviour i.e. a lower critical solution temperature (LCST) or an upper critical solution temperature (UCST). The LCST and UCST are the respective critical temperature points below and above which the polymer and solvent are completely miscible as shown in **Figure 2.2** (Ward and Georgiou, 2011). Hence a polymer with a LCST becomes insoluble and undergoes phase separation with the solvent as the temperature exceeds its LCST. While for a polymer with a UCST, phase separation occurs when the temperature is below the UCST.

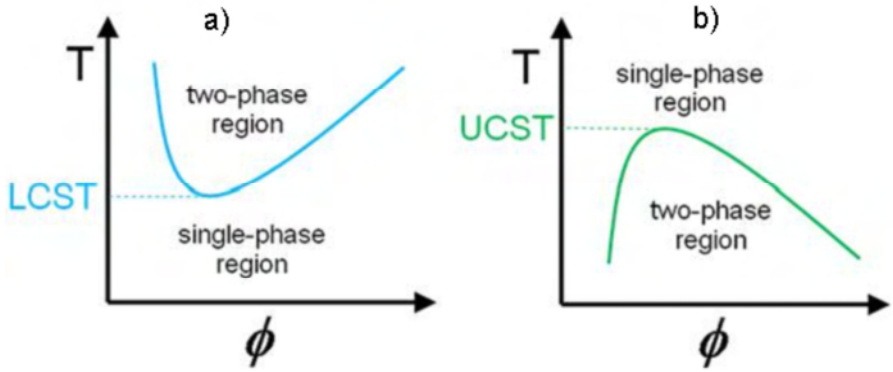

Figure 2.2: Schematic showing temperature as a function of polymer volume fraction (ϕ) for (a) LCST and (b) UCST behaviour of thermoresponsive polymers (Ward and Georgiou, 2011).

Polymers with a LCST are more widely studied. NIPAAm displays a LCST at ~32 °C which is very useful for biomedical applications since it is close to body temperature (37 °C) (Schild, 1992).

For a polymer in water, three types of interactions are possible, i.e. between polymer molecules, polymer and water molecules, and water molecules (Klouda and Mikos, 2008). For polymers with a LCST, increasing the temperature above the LCST, results in a negative Gibbs free energy (ΔG) according to the following equation:

$$\Delta G = \Delta H - T\Delta S \quad \text{(Eq 2.1)}$$

Where ΔH, and ΔS refer to the change in enthalpy, and entropy respectively.

The main driving force for the negative ΔG when the temperature exceeds the LCST, is the increase in entropy of the system due to water-water interactions when the polymer is not in solution (Klouda and Mikos, 2008; Ward and Georgiou, 2011). This favours polymer-polymer interactions while making polymer-water associations unfavourable. The phenomenon above the LCST is also known as the hydrophobic effect (Klouda and Mikos, 2008; Ward and Georgiou, 2011). However when the temperature is reduced to below the LCST, the exothermic ΔH enthalpic effects dominates due to hydrogen bonding between the hydrophilic groups in the polymer and water molecules which is the initial driving force for dissolution, swelling or expansion of the polymer chains (Schild, 1992). Likewise UCST is also an enthalpic driven effect (Ward and Georgiou, 2011).

PNIPAAm can exist in three categories based on its physical form and each displays a typical response at the LCST. This includes PNIPAAm in solution; PNIPAAm hydrogels; or PNIPAAm layers on a solid surface (Hoffman, 2000; Jeong and Gutowska, 2002; Kumar et al., 2007). For the different categories, the following changes are expected at the LCST:

- **PNIPAAm in solution** – These polymers display linear mobile chains in solution which are extended in the coil configuration below the LCST. Upon heating above the LCST, the linear polymer undergoes a reversible conformational change from disordered random coils to a compact globular form. This is often associated with a change in turbidity of the solution and precipitation or gelation as shown in **Figure 2.3.**

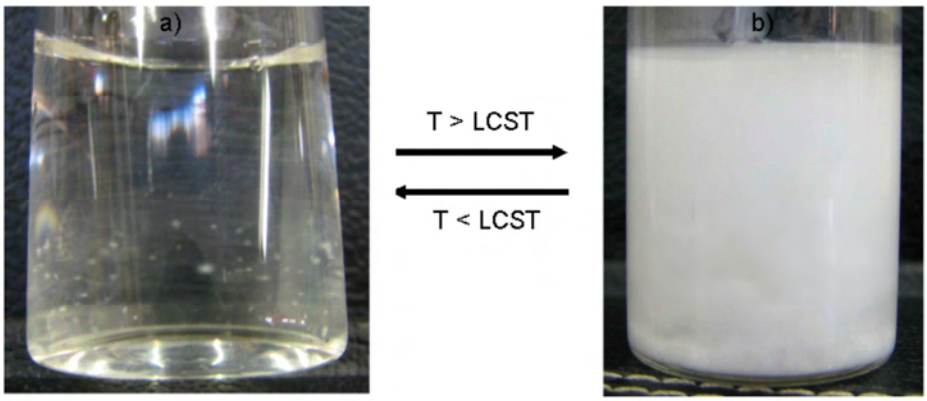

Figure 2.3: Photo showing phase transition of PNIPAAm solution (a) at 23 ℃ (T < LCST) and (b) at 40 ℃ (T > LCST).

- **PNIPAAm hydrogels** - Thermoresponsive hydrogels are generally highly swollen cross-linked polymer networks below the LCST, while the cross-linked polymer chains abruptly collapse and the polymer phase separates above the LCST. This manifests in shrinking of the hydrogel, and expulsion of water as shown in **Figure 2.4**., and the formation of a white precipitate.

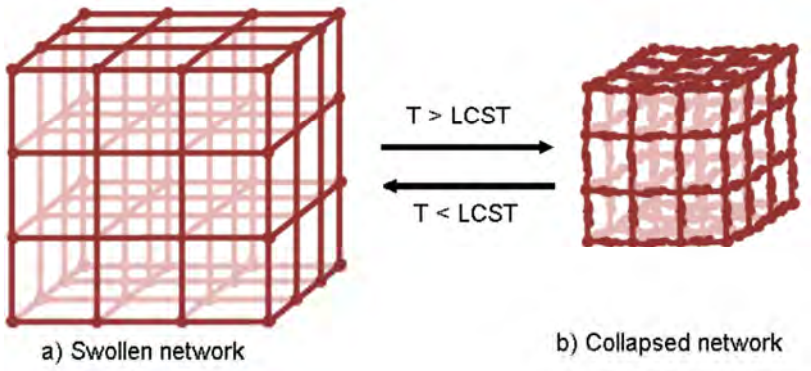

Figure 2.4: Schematic showing effect of temperature on a cross-linked PNIPAAm hydrogel which changes from the (a) swollen network to (b) collapsed network when the temperature is raised above the LCST (Ward and Georgiou, 2011).

- **PNIPAAm layer on a solid surface** - This refers to a solid surface modified by a PNIPAAm layer either by physical adsorption of a smart polymer onto the surface, or by covalent bonding i.e. grafting. Below the LCST, the PNIPAAm chains extend away from the solid surface, while above the LCST the polymer chains collapse on the surface as a result of the change in hydrophilicity/hydrophobicity at the solid-liquid interface (**Figure 2.5**).

Figure 2.5: Image showing the phase transition of PNIPAAm attached to a surface at temperatures below and above the LCST (Cooperstein and Canavan, 2010).

A lot of research has been reported with respect to PNIPAAm hydrogels and PNIPAAm grafted surfaces and these will be dealt with in **Sections 2.3 and 2.4** respectively.

2.3 PNIPAAm hydrogels

A hydrogel is a cross-linked polymer network capable of absorbing and retaining large quantities of water in its porous structure (Hennink and van Nostrum, 2002). The water holding capacity of the hydrogels arise mainly due to the presence of hydrophilic groups, i.e. amides (CONH), carboxyl (-COOH) and hydroxyl (-OH), in the polymer chains capable of forming hydrogen bonds with water molecules (Pal et al., 2009). The amount of water in a hydrogel can vary from 10% to as much as thousand times the weight of the xerogel (Pal et al., 2009). A xerogel is defined as the dried polymer network. One of the key elements of hydrogels is that it contain cross-links in its structure which enables penetration of water into the polymer network enabling the material to swell without dissolution (Milichovsky, 2010). The cross-linked structure provides hydrogels with a 3D structure.

Hydrogels can be classified as either permanent or physical hydrogels depending on the crosslinking. The former involves covalent bonds between the polymeric chains e.g. via the use of a chemical crosslinker, while the latter involves physical interactions (such as hydrogen bonding, ionic interaction, and/or interpenetrating networks) (Pal et al., 2009).

Hydrogels are particularly attractive for biological applications due to their soft consistency, and high water content which is similar to native tissue (Geever et al., 2007). Additionally hydrogels generally display good biocompatibility due to their

hydrophilic surface which typically display a low interfacial free energy in body fluids, and is non-adhesive to proteins and cells (Hennink and van Nostrum, 2002).

The most common reported synthesis methods for PNIPAAm hydrogels include chemical crosslinking by the use of free-radical polymerisation (Grinberg et al., 2000; Ortega et al., 2007; Pekcan and Kara, 2003; Zhang et al., 2005; Zhang et al., 2003a; Zhang et al., 2003b; Zhang et al., 2002b), photopolymerisation (Geever et al., 2006; Geever et al., 2007), plasma-radiation, and gamma-irradiation (Kishi et al., 1997; Ortega et al., 2007). Recently controlled polymerisation techniques such as atom transfer radical polymerisation (ATRP) and radical addition fragmentation transfer polymerisation (RAFT) have been used to synthesis PNIPAAm hydrogels (Liu et al., 2006).

Extensive work has been conducted with respect to modifying the LCST of PNIPAAm hydrogels by copolymerising NIPAAm with either hydrophilic or hydrophobic monomers as shown in **Table 2.1**. It is well-known that copolymerisation of *N*-isopropylacrylamide (NIPAAm) with hydrophilic monomers increases the LCST, due to stronger water-polymer interactions, while the use of hydrophobic co-monomers decrease the LCST due to increase in polymer-polymer interactions. NIPAAm has been polymerised with a number of other monomers including acrylamide; poly(ethylene glycol) methacrylate; poly (1-vinyl-2-pyrrolidone) amongst others (Geever et al., 2007). Attempts have also been made to render PNIPAAm hydrogels with dual stimuli response.

Despite the favourable properties of PNIPAAm, these smart polymeric hydrogels display two major limitations, i.e. poor mechanical properties and slow response time to temperature changes (Zhang et al., 2008). The slow response rate to temperature is believed to be due to the formation of a dense skin layer which forms as a result of the strong hydrophobic interactions existing among the isopropyl groups in the PNIPAAm chains which retards the outward diffusion of water molecules during the hydrogel-collapse process at temperatures above the LCST (**Figure 2.6**). Additionally, the swelling rate of the hydrogel at temperatures below LCST is even slower (Zhang et al., 2008).

Table 2.1: LCST of various PNIPAAm copolymers (Liu et al., 2009).

Abbreviation	**Co-monomer**	**LCST / ℃**
P(NIPAAm-co-PAc)	4-Pentenoic acid	19.2–36.5
P(NIPAm-co-MAAm)	Methacrylamide	32.4–43.2
P(NIPAAm-co-PAA)	Propylacrylic acid	Insoluble to soluble
P(NIPAm-co-VPBA)	Vinylphenylboronic acid	20–40
P(NIPAm-co-AAm)	Acrylamide	34.7–100
P(NIPAm-co-NIPMAm)	N-Isopropylmethacrylamide	34–45.6
P(NIPAm-co-HEMAm)	2-Hydroxyethylmethacrylamide	21.4–30.3
P(NIPAm-co-VL)	Vinyl laurate	<16
P(NIPAm-co-VP)	N-Vinyl-2-pyrrolidone	32.2–39.6
P(NIPAm-co-NHMA)	N-Hydroxylmethylacrylamide	32–80
P(NIPAm-co-NVA)	N-Vinylacetamide	30–60
P(NIPAm-co-MVA)	N-Methyl-N-vinylacetamide	33.2–39.1
P(NIPAm-co-ACMP)	4-Acryloylmorpholine	31.1–35.3
P(NIPAm-co-DMAm)	N,N-Dimethylacrylamide	32–72
P(NIPAm-co-(Ac-AAs))	N-Acryloyl amino-alkylacides	23–36
P(NIPAm-co-HIPAm)	2-Hydroxyisopropylacrylamide	32–80
P(NIPAm-co-MAH)	2-Methacryloamidohistidine	31–35
P(NIPAm-co-PEGMA)	Poly(ethylene glycol) methacrylate	34–39.5
P(NIPAm-co-BCAA)	Benzo-15-crown-5-acrylamide	22–32
P(NIPAm-co-DMA-co-BMA)	2-(Diethylamino)ethyl methacrylate butylmethacrylate	20.3–28.4

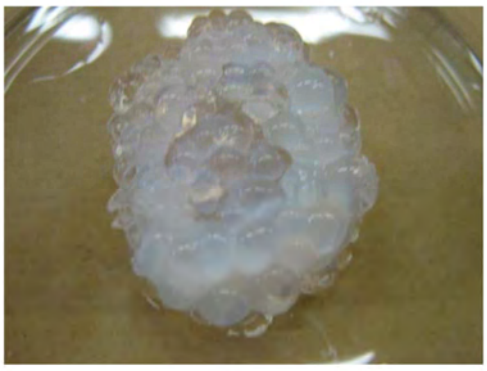

Figure 2.6: Image showing dense skin formation on bulk PNIPAAm hydrogels after de-swelling at 60 ℃ for one hour (Geever et al., 2007).

Due to these limitations the use of PNIPAAm hydrogels has been limited in some applications such as cell culture, molecular on-off switches, artificial organs, drug encapsulation, and actuators (Zhang et al., 2008). Improving the response rate of PNIPAAm hydrogels has been a major research focus for many groups (Woodward et al., 2003; Xue et al., 2002; Zhang et al., 2002a; Zhang et al., 2005; Zhang et al., 2003a).

To improve the properties of PNIPAAm hydrogels, various strategies have been employed which include cross-linking; synthesis of a heterogeneous hydrogel structure (e.g. using mixed solvents); the use of porogens (e.g. polyethylene glycol); the use of hydrophilic co-polymers; and cold polymerisation (to create a porous structure) amongst others (Zhang et al., 2008). In this study we investigate the effect of crosslinking and co-polymerisation using mixed solvent systems, on the physical properties of PNIPAAm hydrogels (**Chapter 4**).

2.4 Graft polymerisation methods

A number of strategies have been reported regarding grafting of PNIPAAm onto polymer substrates. Grafting or graft polymerisation refers to the chemical attachment of a monomer or growing macroradical via a covalent bond onto a solid polymer backbone as shown in **Figure 2.7**.

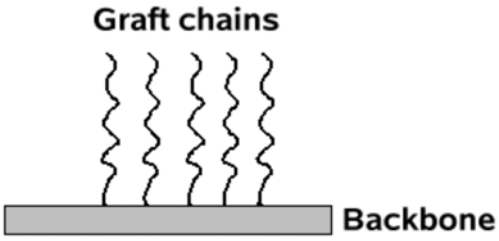

Figure 2.7: Schematic representation of a graft polymer on a polymer backbone.

Grafting involves the generation of free radicals, and the breaking and creation of covalent bonds. Graft polymerisation is often preferred over physical adsorption since covalent attachment of PNIPAAm graft chains onto a backbone polymer assures their long-term stability as opposed to a physically attached graft layer where leaching of the adsorbed layer after continued use may occur, which may pose a problem if the scaffold will be re-used. Graft polymerisation offers the advantage of

enabling materials to be developed with tailored surface properties while maintaining their bulk properties.

Typically graft polymerisation can occur via two mechanisms i.e. either free-radical or ionic (Desai and Singh, 2004). Free-radical polymerisation is commonly used to polymerise monomers into polymers, ands this method of polymerisation typically proceeds via three sequential steps i.e. initiation, propagation and termination (**Scheme 2.1**). Initiation involves the use of an initiator species which can be a chemical initiator, or a high-energy source, capable of forming free radicals on the monomer. After the initiation reaction, chain propagation occurs which involves addition of monomer units to the initiated monomer species, until the growing monomer radicals terminate. Termination can occur by combination, disproportionation or by chain transfer reactions.

Initiation:

$I \xrightarrow{\Delta} I\cdot$

$I\cdot + M \rightarrow R_1\cdot$

Propogation:

$nM + R_1\cdot \rightarrow R_{x+1}\cdot$

Termination:

$R_{x+1}\cdot + R_{x+1}\cdot \rightarrow (R)_x$

Scheme 2.1: Mechanism showing typical steps involved in polymerisation, where I, M, and R refers to the initiator, monomer, and propagating radical respectively and n and x refer to number of units of monomer and propagating radical respectively.

In the case of graft polymerisation, the graft polymer as well as the homopolymer can form in solution, and both processes compete for monomer. For formation of the graft polymer, grafting can occur either “from” the polymer backbone or “to” the polymer backbone as classified below (**Figure 2.8**):

- **Grafting from**: Initiation occurs on the polymer backbone at an active site which forms a free-radical on the polymer backbone. The polymer radical is then transferred onto the monomer thereby propagating the growing monomer radical from the backbone polymer (Huang and Sundberg, 1995).

- **Grafting to**: The monomer is propagated into a growing monomer radical or polymer chain with reactive end groups which can then covalently coupled onto the polymer backbone at a reactive site (Kato et al., 2003).

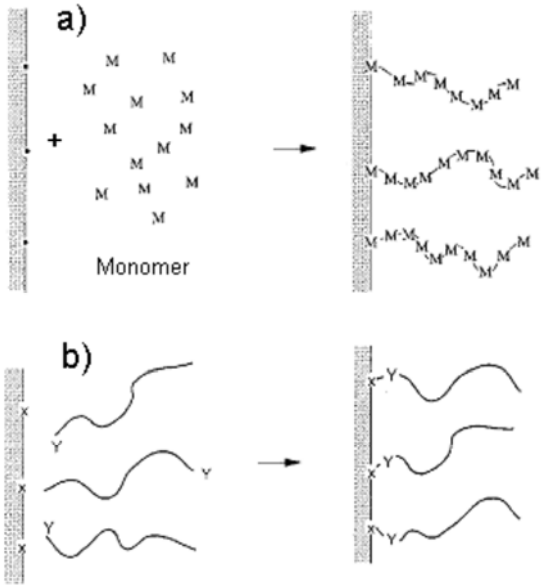

Figure 2.8: Schematic illustrating the (a) “grafting from” and (b)“grafting to concepts (Uyama et al., 1998).

Formation of a free radical on the polymer backbone typically occurs either by hydrogen abstraction, breaking of weak covalent bonds (such as O-O), or breaking of unsaturated bonds, which creates a graft site on the polymer backbone. Free-radical induced grafting techniques which have been applied for attachment of PNIPAAm onto surfaces include plasma (Cheng et al., 2005; Kim et al., 2002; Liang et al., 2000; Wang and McCord, 2007), photochemical (Curti et al., 2005; Liang et al., 1999), electron-beam (Akiyama et al., 2004; Bucio et al., 2005; Okano et al., 1995), gamma radiation (Bucio et al., 2006; Contreras-Garcıa et al., 2008; Mele'ndez-Ortiz et al., 2009; Ramirez-Fuentes et al., 2007), and chemical (Curti et al., 2002; Gupta and Khandekar, 2003). In recent years living radical polymerisation has also been employed to develop PNIPAAm graft chains with controlled chain lengths and molecular weights (Desai et al., 2003; Wan et al., 2009).

2.4.1 Radiation-induced graft polymerisation

Radiation-induced graft polymerisation techniques can be classified as high-energy radiation or ionisation radiation (electron beam, X-rays and γ-rays), mid-energy

(ultraviolet-visible/photoradiation and plasma radiation) and low energy radiation (infrared, microwave and ultrasonic radiation) (Desai and Singh, 2004). Radiation of polymers with high energy can cause cleavage of bonds since the energies are often larger than that of covalent bonds and hence free radicals can form directly on the polymer backbone (Bhattacharya and Misra, 2004). Grafting can proceed in three ways, i.e. (a) pre-irradiation (b) peroxidation and (c) mutual irradiation technique (Bhattacharya and Misra, 2004) as shown in **Scheme 2.2**.

Pre-irradiation:

$$P \xrightarrow{\Delta} P^{\cdot} + M \rightarrow PM^{\cdot}$$

Peroxidation:

$$P + O_2 \xrightarrow{\Delta} P - O - O - H \text{ (or } P - O - O - P) \xrightarrow{\Delta} P - O^{\cdot} + OH^{\cdot} \text{ (or } 2\,P - O^{\cdot})$$

$$P - O^{\cdot} + M \rightarrow P - O - M^{\cdot}$$

Mutual irradiation:

$$P + M \xrightarrow{\Delta} P^{\cdot} + M^{\cdot} \rightarrow P - M$$

Scheme 2.2: Mechanism for high-energy graft polymerisation induced by radiation (Bhattacharya and Misra, 2004).

The pre-irradiation method involves irradiation of the polymer backbone to form free radicals which is then reacted with the monomer to induce graft polymerisation (Bhattacharya and Misra, 2004). In the peroxidation method, which sometimes is also referred to as pre-irradiation by some authors, the polymer is irradiated in the presence of air or oxygen to form hydroperoxide or peroxide groups which can be activated by heat to induce graft polymerisation in the presence of the monomer (Bucio et al., 2006; Contreras-Garcıa et al., 2008; Ramirez-Fuentes et al., 2007), while in the mutual method both monomer and polymer are radiated simultaneously. The advantage of the pre-irradiation and per-oxidation methods is that since the monomer is not irradiated, grafting is typically free from homopolymerisation. The commonly used radiation-induced graft polymerisation methods, which have been used for development of PNIPAAm grafted polymeric scaffolds, are based on gamma-radiation, electron-beam, plasma radiation, and photo-irradiation, amongst others.

2.4.1.1 Gamma radiation and electron-beam radiation

Gamma and electron-beam radiation are commonly used industrial radiation processes which are based on high-energy electrons (0.1–10 MeV) and cobalt-60 (Co_{60}) (~1.25 MeV) respectively (Desai and Singh, 2004). During the process, electrons are displaced from atoms and molecules producing ions. The advantage of the high-energy radiation techniques is that a chemical initiator is not required, and graft polymerisation can be carried out without any toxic chemicals. Gamma radiation is also known to have a higher depth of penetration (Clough, 2001). A number of studies have been conducted regarding grafting of PNIPAAm onto polymer backbones using gamma-induced radiation (Bucio et al., 2006; Contreras-Garcıa et al., 2008; Meléndez-Ortiz et al., 2009; Ramirez-Fuentes et al., 2007). Okano *et al* first prepared PNIPAAm grafted tissue culture trays by coating the tissue culture tray with a NIPAAm-solvent solution, and then irradiated the surface with electron beam radiation, and recently PNIPAAm grafted cell culture trays called RepCell which are prepared by electron beam irradiation is commercially available (Hutmacher, 2005; Okano et al., 1995).

A concern with the high energy radiation techniques however is unwanted side reactions. Some of these include crosslinking, chain scission, post-irradiation degradation, discolouration, and long-term instability of the radiated products (Clough, 2001). Post-irradiation of PP has been well studied and high energy irradiation is known to lead to oxidative degradation of PP (Geuskens and Nedelkos, 1993; Mowery et al., 2007). Also gamma radiation requires a specialised facility that may not be easily accessible, and it uses a Co_{60} source which is a radioactive isotope, and hence is not environmentally friendly (Clough, 2001).

2.4.1.2 Plasma-induced graft polymerisation

Plasma modification uses a plasma source i.e. a gas in its ionised state, with an energy of 10-20 eV (Gupta and Anjum, 2003). The accelerated electrons from the plasma have sufficient energy to induce cleavage of the chemical bonds in the polymer surface and to form new functional groups, and free radicals, which subsequently initiate graft polymerization (Bhattacharya and Misra, 2004). Gases such as oxygen, helium, argon, carbon dioxide, and ammonia have been used as plasma sources. Depending on the gas used, different reactive groups can be

expected (**Scheme 2.3**). The reactive gases such as oxygen, ammonia, and carbon dioxide are used to create functional groups on the polymer surface such as peroxides, amino and carboxylic groups respectively while the inert gases create free radicals on the polymer surfaces, which are transformed into polar groups in the presence of air (Gupta and Anjum, 2003).

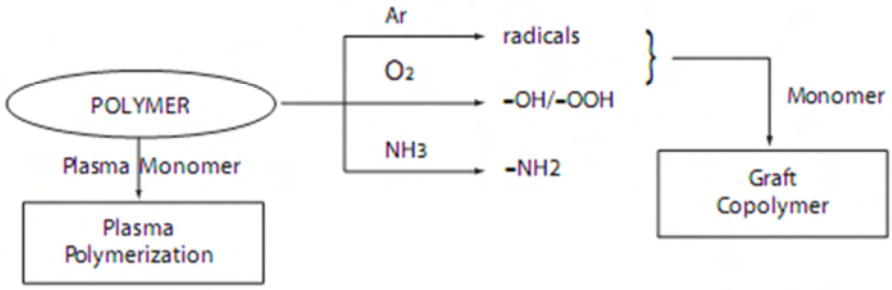

Scheme 2.3: Schematic showing process for plasma-induced graft polymerisation (Gupta and Anjum, 2003).

Atmospheric plasma has been previously used to graft PNIPAAm onto nylon and polystyrene surfaces by the peroxidation method whereby after plasma irradiation, the substrates were incubated in NIPAAm solution and heated to 60 ºC (Wang and McCord, 2007). The proposed method of grafting is shown schematically in **Scheme 2.4**, and involves the formation of peroxide functional groups on the polymer surface which are very reactive to graft polymerisation.

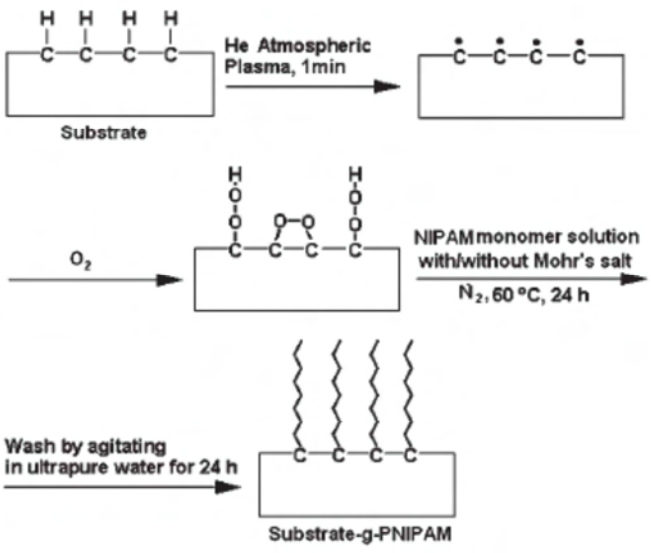

Scheme 2.4: Schematic of graft polymerisation of PNIPAAm onto nylon or polystyrene surfaces using atmospheric plasma (Wang and McCord, 2007).

Plasma modification however is conventionally line-of-sight and modification is typically not extended to the bulk of the matrix. Vacuum plasma may penetrate a few microns into the surface and depending on the scaffold porosity it may be possible to extend the modification, however conventionally this technique is limited to surface modification only.

2.4.1.3 Photo-irradiation

Photo-irradiation or photo-grafting involves irradiating a polymer surface with a UV-light source (e.g. using a mercury lamp). The energies delivered are in the wavelength range of 200-400 nm and much lower than high-energy radiation, but the energies are still comparable to covalent bond energies hence enabling bond rupture and the formation of free radicals on the polymer backbone (Desai and Singh, 2004). Typically a photo-initiator also known as a chromophore is used (such as organic peroxides and organic ketones such as benzophenone). The mechanism for photo-grafting is given in **Scheme 2.5**.

Initiation:

$$I \xrightarrow{\Delta} {}^1I^* \rightarrow {}^3I^*$$

$$PH + {}^3I^* \rightarrow {}^3IH^* + P^{\cdot}$$

$$MH + {}^3I^* \rightarrow {}^3IH^* + M^{\cdot}$$

$$P^{\cdot} + M \rightarrow PM^{\cdot}$$

Propagation:

$$PM^{\cdot} + nMH \rightarrow P(MH)_nM^{\cdot}$$ (grafting)

$$M^{\cdot} + nMH \rightarrow M(MH)_nM^{\cdot}$$ (homopolymerisation)

Termination:

$$P(MH)_nM^{\cdot} + M^{\cdot}(MH)_nP \rightarrow P(MH)_xP$$ (grafted polymer)

$$(MH)_nM^{\cdot} + M^{\cdot}(MH)_n \rightarrow (MH)_y$$ (homopolymer)

Scheme 2.5: Mechanism of photo-grafting where I, PH, MH refer to the initiator, polymer, and monomer respectively (Desai and Singh, 2004).

The initiator (I) acts by absorbing the UV light during irradiation, whereby the molecule goes from the ground state to the first excited singlet state ($^1I^*$), and then relaxes to the excited triplet state ($^3I^*$) (Desai and Singh, 2004). The extra energy is dissipated in various pathways of which energy transfer to the polymer and monomer

can occur; which can induce grafting and homopolymerisation. Grafting can proceed via hydrogen abstraction from the polymer backbone, creating a free radical on the polymer backbone ($P^{\cdot}$) which acts as an active site for graft polymerisation (Desai and Singh, 2004). The initiator also abstracts a proton from the monomer creating a monomer radical ($M^{\cdot}$) which can undergo graft polymerisation and homopolymerisation (Desai and Singh, 2004). Gueskens *et al.* grafted polyacrylamide and PNIPAAm onto PE using photochemical grafting with anthraquinone-2-sulfonate as the photo-initiator (Geuskens et al., 2000). Photo-grafting however is limited to line of sight, and formation of large amounts of homopolymer can occur.

2.4.2 Graft polymerisation with chemical initiator

In this method a chemical initiator is used to form free radicals. Typically grafting proceeds as shown below in **Scheme 2.6** where I is the initiator, $I^{\cdot}$ is the primary radical, P–H is the polyolefin backbone, and M is the monomer (Bhattacharya and Misra, 2004). Initiation proceeds as follows (1) dissociation of the initiator to form initiator radical species($I^{\cdot}$), (2) addition of a single monomer molecule to the initiating radical ($IM^{\cdot}$) and (3) formation of a free radical on the polymer backbone ($P^{\cdot}$) Propagation and finally termination occur to produce the graft copolymer.

Initiation:

$$\mathrm{I_2} \rightarrow 2\mathrm{I}^{\cdot}$$

$$\mathrm{I}^{\cdot} + \mathrm{M} \rightarrow \mathrm{IM}^{\cdot} + \mathrm{M} \rightarrow \mathrm{IMM}^{\cdot}$$

$$\mathrm{I}^{\cdot} + \mathrm{P-H} \rightarrow \mathrm{P}^{\cdot} + \mathrm{IH}$$

$$\mathrm{IMM}^{\cdot} + \mathrm{P-H} \rightarrow \mathrm{P}^{\cdot} + \mathrm{IMMH}$$

Propagation:

$$\mathrm{P}^{\cdot} + \mathrm{M} \rightarrow \mathrm{PM}^{\cdot} \xrightarrow{\mathrm{nM}} \mathrm{P(M)_nM}^{\cdot}$$

Termination:

$$\mathrm{P(M)_nM}^{\cdot} + \mathrm{IMM}^{\cdot} \rightarrow \mathrm{P(M)_{n+3}-I}$$

$$\mathrm{P(M)_nM}^{\cdot} + \mathrm{I}^{\cdot} \rightarrow \mathrm{P(M)_{n+1}-I}$$

Scheme 2.6: Typical mechanism for free radical induced graft polymerisation (Bhattacharya and Misra, 2004).

A number of chemical initiators can be used to initiate the grafting process and commonly include redox initiators or thermal initiators. Redox initiator systems

contain a reducing and oxidising pair whereby electrons are transferred from one reagent to the next, while thermal initiators have thermally labile bonds which can be activated by heating. Some of the chemical initiators which have been used for graft polymerisation for NIPAAm include peroxysulphates; ceric ammonium nitrate; benzoyl peroxide; and other organic peroxides, which are activated in solution by heating to elevated temperatures (Gupta and Sahoo, 2001; Huang and Sundberg, 1995). Peroxysulphates are one of the most widely studied initiator system for NIPAAm polymerisation. Peroxysulphates such as ammonium persulphate (APS), sodium persulphate, and potassium persulphate can be activated by various means, either thermally, or it can be reduced by Fe^{2+} or diamines to sulphate free radicals. APS and tetramethylethylenediamine i.e. TEMED are a commonly reported redox system for polymerisation and graft polymerisation of NIPAAm at room temperature. TEMED is the reducing agent thereby acting as a catalyst or promoter and the rate of radical formation from APS is enhanced (Xinqiu et al., 1989).

The primary radical produced from persulphates is $SO_4^{-\bullet}$. According to Riggs the thermal decomposition of APS yields both sulphate and hydroxyl radicals ($OH^{\bullet}$) (Riggs and Rodriguez, 1967). There are different views regarding the reactivity of $SO_4^{-\bullet}$. Some authors report that $SO_4^{-\bullet}$ can react directly with the polymer backbone to produce the polymer radical by H abstraction, while others report that the produced $OH^{\bullet}$ is responsible for forming free radicals on the polymer (Bhattacharya and Misra, 2004). Still others report on a two stage graft polymerisation method using APS, whereby the polymer backbone (P-H) is firstly hydroxylated (P-OH) by thermal decomposition of APS (70-100 ℃) and the hydroxylat ed backbone is then initiated with a transition metal such as ceric ion (Ce) to form the polymer radical ($P\text{-}O^{\bullet}$) (Bamford and Al-Lamlee, 1994).

A simple schematic of the functionalisation process is shown in **Scheme 2.7.** Due to its convenience, mild conditions, and aqueous medium, many studies have focused on the two stage method using APS/Ce (Amornsakchai and Doaddara, 2008; Curti et al., 2002; Curti et al., 2005; Zhao and Geuskens, 1999). The proposed mechanism of the 2 step process is given in **Scheme 2.8**.

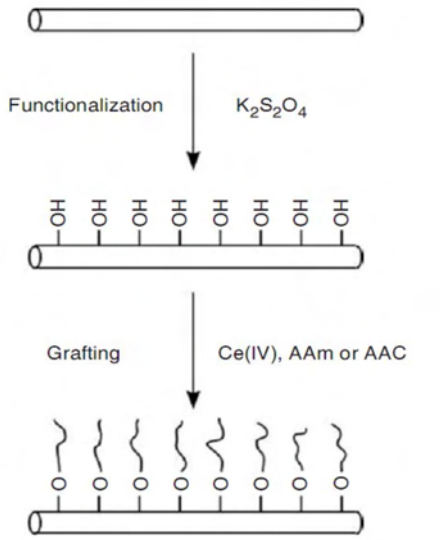

Scheme 2.7: Schematic of graft polymerisation of acrylamide and acrylic acid onto a polyethylene backbone using persulphate and Ce (Amornsakchai and Doaddara, 2008).

$$S_2O_8^{2-} \rightarrow 2SO_4^{-\cdot}$$
$$2SO_4^{-\cdot} + H_2O \rightarrow HSO_4^- + OH^{\cdot}$$
$$OH^{\cdot} + P-H \rightarrow H_2O + P^{\cdot}$$
$$OH^{\cdot} + P^{\cdot} \rightarrow P-OH$$
$$2OH^{\cdot} \rightarrow H_2O_2$$
$$P-OH + Ce^{IV} \rightarrow P-O^{\cdot} + H^+ + Ce^{III}$$

Scheme 2.8: Proposed mechanism for polymer functionalisation using persulphate & Ce ion (Zhao and Geuskens, 1999).

Free-radical induced grafting by chemical initiation offers the advantage of being a simple method, which is easy to perform and which does not involve the use of high energies, and expensive equipment, however chemical initiators are required. Due to its simplicity and ease of use, free-radical induced grafting by chemical initiation was used in this study for development of the 3D PNIPAAm grafted NWF scaffolds. Furthermore fluorination was investigated for functionalisation of the NWF prior to graft polymerisation (**Chapter 5**).

2.4.3 Surface functionalisation by fluorination

It is known that the surface functionality of a polymer backbone influences free radical formation, as well as wettability and swelling of the polymer backbone in the graft medium. Swelling of the polymer is important to ensure mobility of the free radicals from the monomer to graft sites on the polymer backbone (Bhattacharya and Misra, 2004). Many studies have focused on improving functionality of polymer backbones using various surface functionalisation techniques. Methods which have been used include UV treatment, plasma treatment, gamma irradiation, ozone treatment, use of etching agents, chemical treatment, flame treatment, corona discharge, and fluorination (Curti et al., 2002; Curti et al., 2005; Zhao and Geuskens, 1999). This review focuses on fluorination as a surface functionalisation technique as it is cost-effective and less invasive than most of the other radiation techniques.

Fluorination, i.e. treatment of a polymer with elemental fluorine (F_2) is an attractive surface functionalisation method. Fluorination involves bombarding the polymer surface with a F_2 gas mixture (containing oxygen) in the dry state under mild conditions. Fluorination can be used to modify polymer articles of any shape (Kharitonov, 2000). Additionally F_2 gas can penetrate polymer surfaces to large depth whereby the thickness of modification is within 0.01-10 µm (Kharitonov, 2000). The depth of modification is a diffusion-controlled process, and the rate of formation of the fluorinated layer is controlled by the diffusion of molecular F_2 gas through the fluorinated layer to the untreated polymer. This depends on the polymer nature, F_2 partial pressure, F_2 gas mixture, reaction time and temperature (Kharitonov et al., 2005). A further advantage of fluorination, is that due to the exothermic nature of the reaction, the reaction proceeds at room temperature in a low vacuum, with no heat, initiators, or catalysts required (Kharitonov et al., 2005).

Fluorination can be classified into two categories i.e. ordinary direct fluorination and oxyfluorination (Jeong et al., 2011). The former uses a mixture of F_2 (1-20 vol. %) and an inert gas (such as nitrogen, argon or helium), whereas the latter employs a mixture of fluorine and O_2. It is known that commercial F_2 gas contains trace amounts of O_2, and hence some authors have indicated that fluorination always accompanies oxyfluorination, while other authors have shown no oxygen containing groups in fluorinated samples (du Toit and Sanderson, 1999). Direct fluorination is typically used to improve the barrier properties of polymers by lowering the surface free energy, while oxyfluorination is commonly used to improve the adhesion properties of

polymers by increasing the polarity, surface energy, and wettability of polymers (Kharitonov and Kharitonova, 2009). Many studies have reported modification of polymer surfaces by fluorination and in recent years direct fluorination is being widely utilised for industrial applications such as barrier properties of automotive fuel tanks, and storage vessels for toxic solvents (Kharitonov, 2000; Kharitonov, 2008; Kharitonov et al., 2005).

During fluorination, F_2 reacts exothermically with the surface of a hydrocarbon by a free radical mechanism as shown in **Scheme 2.9** (du Toit and Sanderson, 1999). Due to its high electronegativity, F_2 abstracts protons from a polymer (P-H) to form polymer free radicals ($P^{\bullet}$), fluorine free radicals ($F^{\bullet}$), as well as hydrogen fluoride. The process has also become very safe and reliable nowadays whereby excess F_2 is neutralised and hydrogen fluoride is converted into the solid phase by e.g. using sodium fluoride pellets (Kharitonov and Kharitonova, 2009).

$$P-H + F_2 \rightarrow P\cdot + HF + F\cdot$$
$$P\cdot + F_2 \rightarrow P-F + F\cdot$$

Scheme 2.9: Proposed mechanism for direct fluorination of polymers.

According to Kharitonov, direct fluorination of polymers results in disruption of -C-H and -C-OH groups and saturation of double bonds which is followed by formation of fluorinated groups such as -C-F, $-CF_2$, and/or $-CF_3$ because of the higher bond energy of C-F bonds, compared to C-H or C-OH bonds (Kharitonov, 2008). During oxyfluorination, molecular O_2 reacts spontaneously with the fluorocarbon radicals generated by F_2 and oxygen and fluorine containing functional groups are formed (Kharitonov, 2000). A schematic representation of the process is given in **Figure 2.9**. Many authors have reported that acid fluoride (-COF) is hydrolysed to the highly polar carboxylic acid (-COOH) group (du Toit and Sanderson, 1999; Kharitonov et al., 2005; Lee et al., 2003). The formation of reactive peroxide (-O-O) groups and long-lived trapped peroxy radicals on oxyfluorinated polymer surfaces is also well- known (du Toit and Sanderson, 1999; Jeong et al., 2011; Kharitonov, 2000; Kharitonov et al., 2004). Tressaud *et al* demonstrated middle (–$CH(OO^{\bullet})$– or –$CF(OO)^{\bullet}$-) and “end” peroxy groups (–$CH_2OO^{\bullet}$ or –$CHFOO^{\bullet}$ or –$CF_2OO^{\bullet}$) on oxyfluorinated low-density polyethylene (LDPE). It has been reported that the amount of peroxy radicals exceeds the amount of fluororadicals (Tressaud et al., 2007).

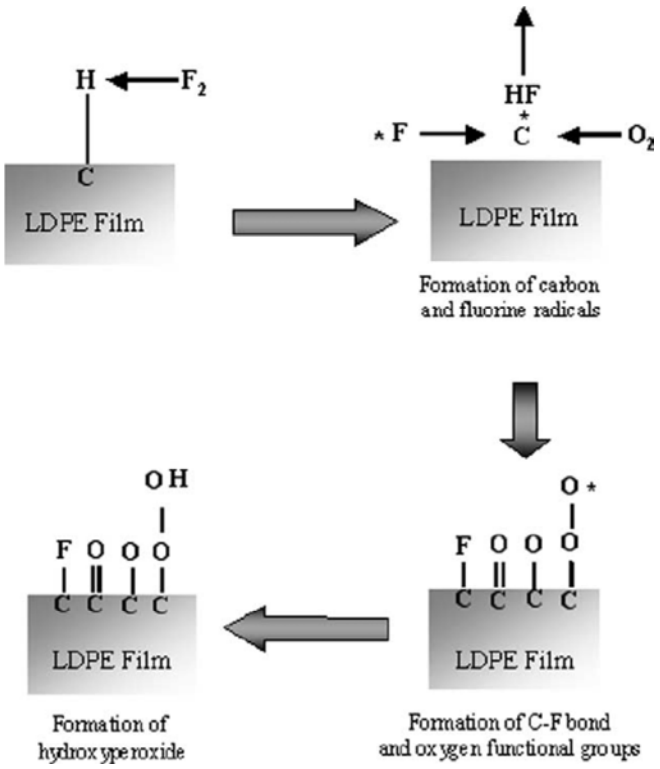

Figure 2.9: Schematic showing the oxyfluorination process (Park et al., 2005).

Despite the formation of peroxy groups on oxyfluorinated polymer, surprisingly the use of oxyfluorination as a pre-treatment prior to polymer grafting has been very limited. Recently Jeong *et al* reported for the first time graft polymerisation of methacrylic acid and styrene onto oxyfluorinated low-density polyethylene films by thermal activation of the peroxy groups and without the use of any external initiators (Jeong et al., 2011). Jeong coined the term “oxyfluorination-assisted graft polymerisation” (OAGP) technique to describe this facile two-step process. In this study PP, PET, and nylon NWF were grafted with PNIPAAm using the OAGP method. We investigate both oxyfluorination and direct fluorination as surface functionalisation methods prior to graft polymerisation.

2.5 Advances in cell culture

There is consensus in the literature that the environment in which cells are cultured *ex vivo* plays a critical role in the cells performance. Aspects such as proliferation, differentiation, metabolic activity, function and phenotype are directly influenced by the growth conditions which cells are subjected to. The ultimate goal for *in vitro* cell

culture is to maintain the cells in their native state such that the cell behaviour and function is similar to the living tissue from which they were derived.

While the monolayer cell culture process is well-established and is currently the gold standard, it leaves a lot to be desired in terms of bridging the *in vitro* to *in vivo* gap. More and more researchers and larger pharmaceutical companies are now looking for alternative approaches to improve the *in vivo* predictive power of their cell cultures. As the fields of tissue engineering, regenerative medicine, drug screening and cell and genetic engineering are advancing, there is now a growing demand for an *in vivo*-like cell culture model which can be used to more accurately predict the cellular responses of living organisms (Pampaloni et al., 2007).

In recent decades advances have been made to the conventional cell culturing process, and these include the use of 3D scaffolds (see **Section 2.5.1**); PNIPAAm substrates (**Section 2.5.2**); and bioreactors (see **Section 2.5.3**).

2.5.1 3D scaffolds

Comparative studies between 2D and 3D cultures reveal that cells grown in 3D cultures display more relevant *in vivo-like* behaviour with respect to adhesion, cell morphology and extracellular matrix composition and function (Cukierman et al., 2001). Additionally vast differences have been observed in 3D cultures with respect to migration; differentiation; gene expression; metabolic activity; general cell function, molecular mechanisms, and drug metabolism compared to monolayer 2D cultures (Bokhari et al., 2007; Guillame-Gentil et al., 2010; Justice et al., 2009; Lee et al., 2008).

This decade has seen an exponential growth in the number of peer-reviewed articles published in the literature pertaining to 3D cell culture as shown in **Figure 2.10**. The field is currently undergoing a paradigm shift where researchers, academia as well as larger pharmaceutical companies, are now looking to 3D scaffolds to improve the predictive potential of their *in vitro* cell cultures. Due to the interest amongst researchers there is now a peer-reviewed website (www.3Dcellculture.com) solely dedicated to serve as a comprehensive list of published literature in the field of 3D cell culture.

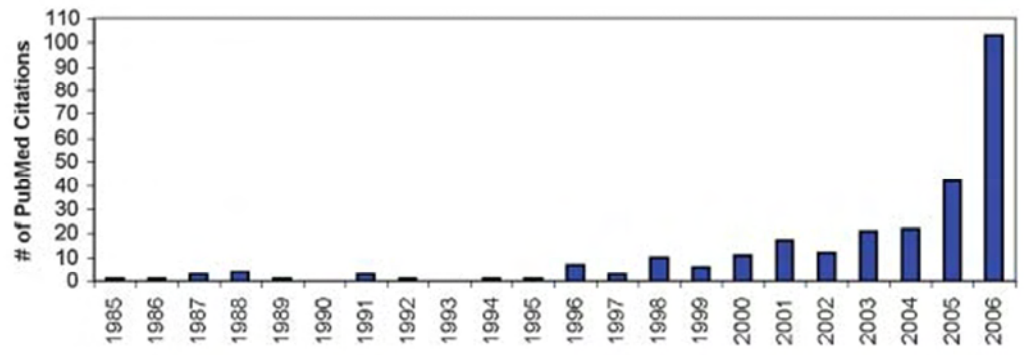

Figure 2.10: Growth in the number of research publication in the field of 3D cell culture from Pub Med citations from 1985 to 2006 (Prestwich, 2007).

Areas of application where 3D cultures and in particular physiologically relevant cell characteristics are of importance includes tumour biology for the development of cancer drugs; stem cell differentiation; proteonomics; genomics; engineering of human tissues and organs, and hepatotoxicology models for drug screening (Prestwich, 2008). It is known that hepatocytes rapidly de-differentiate in monolayer cultures while hepatospecific functions are maintained for longer periods in 3D cultures representing a more physiologically relevant model for drug evaluation (Prestwich, 2008).

Over the past several years a number of 3D scaffolds with various morphologies have been developed and these include microcarrier beads, hydrogels, sponges, nanofibers, and porous filter inserts. Some of the commercially available 3D scaffolds appear in **Table 2.2.** The vast majority of commercially available 3D scaffolds which are in common use for cell propagation and harvesting are based on biomimetic matrices such as ECM proteins or polysaccharides and include scaffolds such as Matrigel™; Extracel™; and AlgiMatrix™. The ECM-based scaffolds offer the advantage of possessing specific native proteins and growth factors which would enable integrin-ligand binding with cells thereby regulating the cell signalling pathways as well as providing 3D support for the cells (Tibbitt and Anseth, 2009). Furthermore, with the ECM based hydrogels and sponges, cells are easily encapsulated within the network to encourage 3D cell growth (Prestwich, 2007; Tibbitt and Anseth, 2009).

Table 2.2: Some of the commercial 3D scaffolds for cell growth and harvesting based on natural and synthetic materials (GE Healthcare, 2012; Justice et al., 2009; Prestwich, 2007).

Scaffold trade-name	**Supplier**	**Form**	**Composition**
Matrigel™	BD Biosciences	Hydrogel	Type IV collagen, laminin and heparin sulphate proteoglycan
AlgiMatrix™	Invitrogen	Sponge	Alginate
Extracel™	Glosan Biosciences	Covalently cross-linked hydrogel	Hyaluronan, and gelatine cross-linked with polyethylene glycol diacrylate
Cytodex™	GE Healthcare Biosciences	Microcarrier	Cross-linked dextran
GEM™	Global Cell Solutions	Microcarrier	Alginate core with a protein coat
BD Biocoat™	BD Biosciences	Coated coverslips and trays	Culture surfaces coated with ECM proteins and attachment factors
BD PureCoat™	BD Biosciences	Coated coverslips and trays	Culture surfaces coated with synthetic polymers such as Poly-L-Lysine
Fibra-Cel®	New Brunswick Scientific	Non-woven fibre mesh	Polyester mesh and polypropylene support
Biomerix 3D scaffold™	Synthecon	Foam	Polycarbonate-polyurethane urea
Millicell®	Millipore	Filter insert	Membranes based either on polytetrafluoroethylene; cellulose esters; polycarbonate and polyethylene terephthalate
Transwell®	Corning	Filter insert	Collagen treated polytetrafluoroethylene

The current industry standard with more than 80% of the 3D cell culture market share is Matrigel™ (Prestwich, 2008). Matrigel™ is a reconstituted basement membrane collected from the Engelbreth–Holm–Swarm (EHS) tumour grown in mice and is uniquely suited for the culture of epithelial cells (Justice et al., 2009). Matrigel™ cell culturing involves reconstitution of purified basement membrane components in a specified ratio by gelation which is complete in 20 minutes (Tibbitt and Anseth, 2009). Matrigel™ has been shown to support natural cell growth, differentiation, angiogenesis, cell morphology and 3D cell behaviour (Kleinman et al., 1986; Prestwich, 2008). Extracel™ is a 3D cell culture product containing hyaluronic acid and gelatin which is prepared by seeding the gel with cells and then it is covalently cross-linked *in situ* under ambient conditions within 5-30 minutes (Prestwich, 2007). The crosslinking improves the stability of the matrix and improved batch to batch consistency has been shown (Prestwich, 2007; Prestwich, 2008). AlgiMatrix™ (**Figure 2.11**) is alternatively a ready-to-use alginate-based sponge, of an animal-free origin, and is fast becoming the scaffold of choice for primary and stem-cell spheroid culture but production variability is still an issue (Justice et al., 2009). AlgiMatrix™ is commonly used for 3D spheroidal culture as shown in **Figure 2.11**.

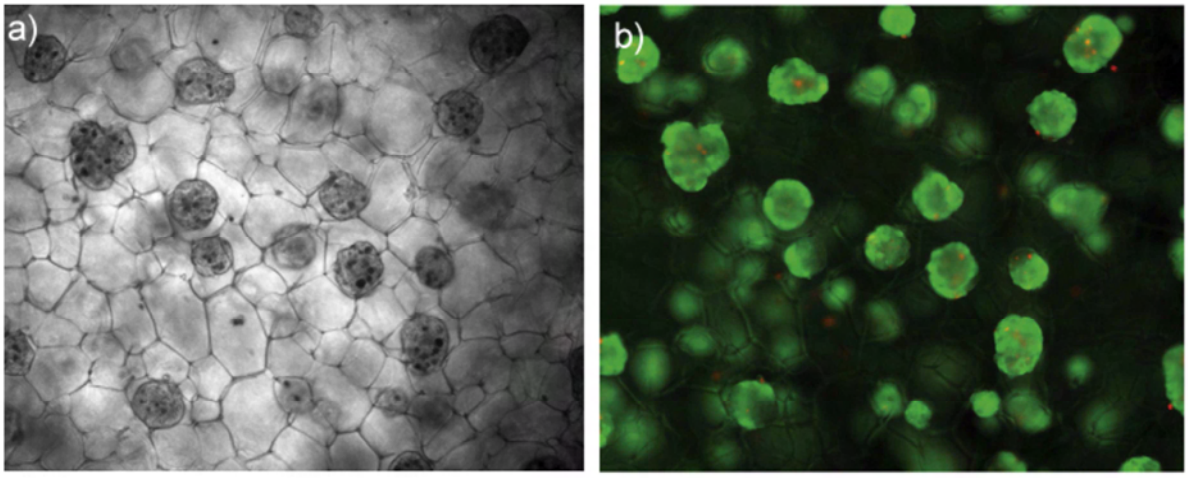

Figure 2.11: Images showing a) phase contrast microscopy; and (b) fluorescence microscopy showing human hepatocytes growing as spheroids when cultured in AlgiMatrix™ (live cells stained in green and dead cell appear red (Justice et al., 2009).

Microcarriers are promising alternatives to hydrogels for 3D cell culture in that it is more easily scalable by dispensing larger volumes per well and it is also cheaper (Justice et al., 2009). Microcarriers are small spheres, typically < 500 µm in diameter,

offering large surface area to volume ratios due to their unique curvature design thereby enabling high yield cell cultures. Microcarrier cultures can also undergo bead to bead migration, and scale-up is also possible without harvesting cells. In recent years**,** Cytodex™ and GEM™ micocarriers have been developed which are very attractive for high-density cell culture and can be used in 2D TCPS trays, or in bioreactors (**Figure 2.12)**. Cytodex™ is a cross-linked dextran microsphere (~150 µm in diameter) which is transparent and displays a very large surface area (e.g. ~4400 cm^2/g of dry weight for Cytodex 1) (GE Healthcare, 2009). Cytodex™ beads have also been developed with a thin layer of collagen (Cytodex 3) on the surface to enhance cell attachment. GEM™ i.e. Global Eukaryotic Microcarrier is a magnetic microcarrier with a gelatin coated alginate core for attachment to a wide variety of cells (Justice et al., 2009). The magnetic core allows for easy separation of the microcarriers during washing steps. An advantage of Cytodex is that various methods can be used to release adherent cell. This includes the use of dextranase which totally digests the microcarrier beads or collagenase to degrade the surface layer in Cytodex 3 (GE Healthcare, 2009).

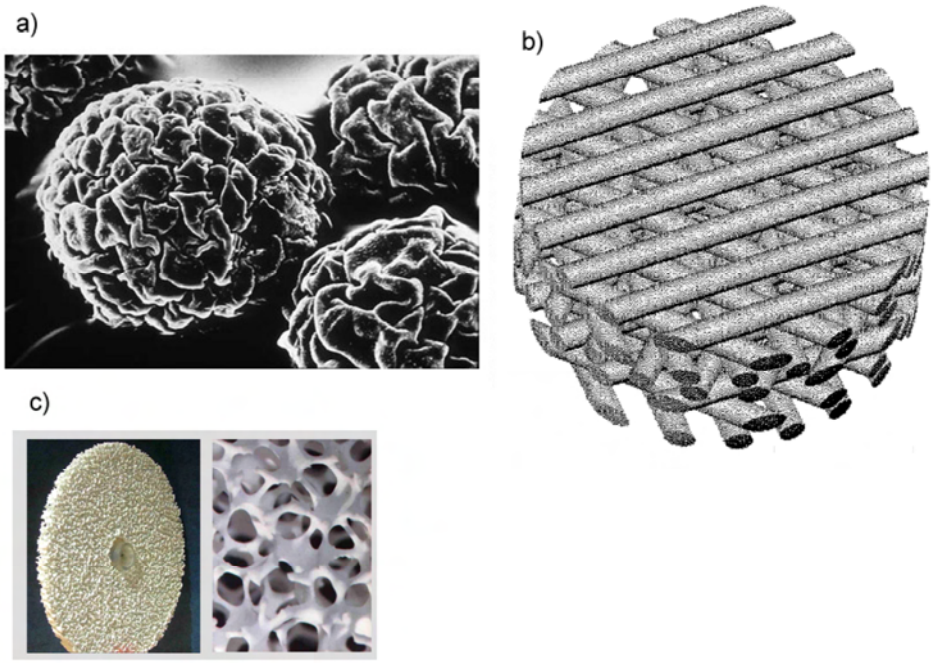

Figure 2.12: Images showing (a) pig kidney cells growing on Cytodex 1 (GE Healthcare, 2009), (b) 3D Insert™ (3D Biotek) based on polystyrene fibre construct (Lui, 2008); and (c) highly porous Sponceram® disk (ZellWerk, 2012).

Other porous 3D scaffolds include synthetic materials such as 3D insert™ which are polystyrene and polycaprolactone fibre scaffolds, and Sponceram® disks which are highly porous hydroxyapatite disks with macro and micropores and a surface area of 14 m^2/g (**Figure 2.12**).

Despite the growing popularity of the ECM based 3D scaffolds there still remain a number of challenges regarding its use in routine 3D culture. Some of these are listed below: (Justice et al., 2009; Prestwich, 2007):

- Poor reproducibility between batches of biomimetic scaffolds
- Lack of consistency between 3D cultures
- High pathogenic content and immunogenicity (Matrigel™ scaffolds)
- Some hydrogel scaffolds require preparation in-house to construct which is inconvenient and unreliable
- Limited ability to scale-up a single 3D format
- Post culturing processing and cell extraction difficult to handle
- High costs (Matrigel™ coated plates - $100/plate)
- ECM based scaffolds have limited stability and specific storage requirements
- Need for higher throughput
- Better methods needed for characterising cells in 3D scaffolds
- Cell release methods (enzymes, or chemicals) can be destructive to cells

Based on these considerations, there is a growing need for new and improved 3D cell culture scaffolds.

2.5.2 PNIPAAm substrates for cell culture

Pioneering work in the early 1990's by Okano's group revealed for the first time a novel method to spontaneously attach and release cells in a manner which is harmless to the cells (Okano et al., 1995). Okano's research demonstrated that cells grown on PNIPAAm surfaces could be harvested non-invasively as an intact layer cell sheet containing deposited ECM (refer to **Figure 1.3** shown previously). Cell attachment and spontaneous cell release is possible on PNIPAAm surfaces, since it has been shown that cells can adhere and grow more easily on a PNIPAAm layer in its hydrophobic state, while cells release when the PNIPAAm layer becomes hydrated and hydrophilic (Yamada et al., 1990). With PNIPAAm cell culturing,

released cells remain intact with the only disruption being to the cell membrane i.e.between adhesive proteins on the basal side of the cultured cells and the polymer surface, while with the conventional enzymatic cell release methods, the cells extracellular membrane (ECM), cell-to-cell gap junctions, and membrane proteins such as ion channels and growth factor receptors are damaged (Canavan et al., 2005). Temperatures between 4-20 ℃ have been inves tigated for temperature induced cell release from PNIPAAm surfaces. The optimum temperature for cell release may differ for different cell types, but typically cell release at ~20 ℃ has been shown to be efficient (Matsuda et al., 2007; Okano et al., 1995; Yamato et al., 1999).

It is now well-accepted that PNIPAAm coated TCPS trays represents a viable scaffold for non-invasive cell culture. According to Hutmacher *et al* there was a 800% increase in the number of scientific articles published on PNIPAAm in 2004 compared to 1990 (data from Medline and Sciencedirect only) with the vast majority dealing with cell culture applications (Hutmacher, 2005). Recently as a spin-off of Okano's research, PNIPAAm coated trays, called Repcell have recently been launched into the market by a company called CellSeed (Hutmacher, 2005).

The exact mechanism of temperature- induced cell release from PNIPAAm surfaces is still not fully understood since there are a number of factors which directly or indirectly influence the cell behaviour on these surfaces. These include the temperature of the cell culture medium; hydration/dehydration of PNIPAAm chains; protein adsorption/release from the surface; the PNIPAAm layer thickness and density of PNIPAAm chains; mechanical properties of the outer surface of PNIPAAm to influence cell spreading/contraction; and cellular metabolic activities requiring ATP consumption which influences the cell shape and cytoskeleton reorganisation (Cooperstein and Canavan, 2010 ; Kumashiro et al., 2010; Matsuda et al., 2007). The most well accepted mechanism for PNIPAAm-induced cell detachment is a two stage process as shown in **Figure 2.13** involving (1) passive detachment, and (2) active detachment (Cooperstein and Canavan, 2010).

"Passive detachment" involves liberation of cell adhesion molecules such as ECM proteins from the culture surface due to the hydration of the PNIPAAm. Cell attachment onto hydrophobic surfaces has been said to be mediated in part by the tight binding of ECM proteins (such as actin, and fibronectin) onto the surface. Rapid hydration of the PNIPAAm layer prevents anchorage of the ECM deposited on the culture surface, since physicochemical interactions (such as hydrophobic, columbic,

and van der Waals forces) between the cells and the surface are weakened (Yamato et al., 1999).

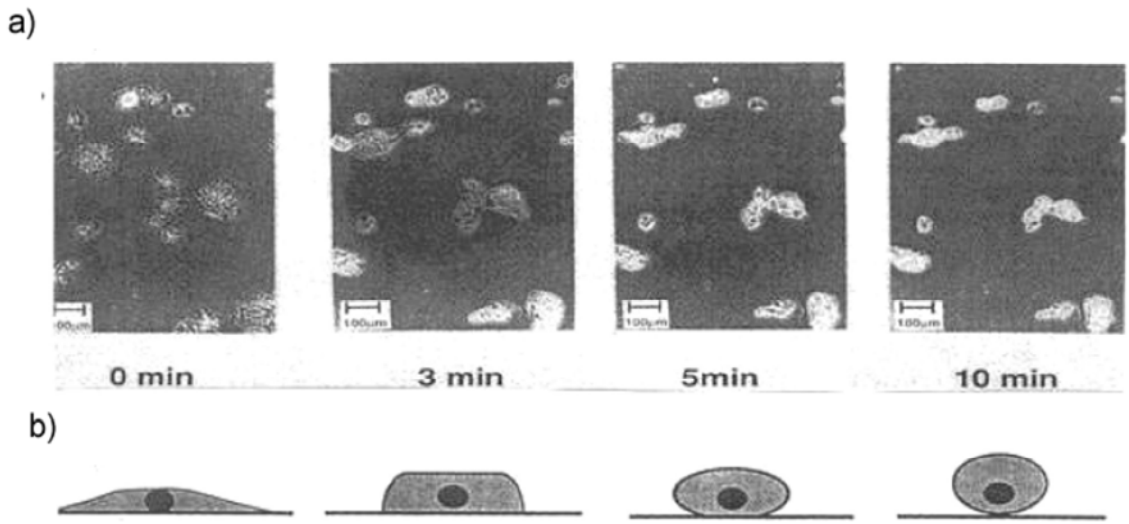

Figure 2.13: (a) Phase-contrast images of hepatocytes on PNIPAAm –TCPS trays during temperature-induced cell release at 0-10 minutes; and (b) a schematic representation of the mechanism of cell sheet detachment showing changes in cell contraction induced by an active cytoskeletal rearrangement (Scale-bar = 100 µm) (Cooperstein and Canavan, 2010).

The second step is “active detachment” which is a cell metabolic process involving contractile forces which results in a change in cell shape from flattened and spread on cell adhesive surfaces to rounded and contracted on cell repellent surfaces (Kumashiro et al., 2010; Kushida et al., 1999; Yamato et al., 1999). The active cellular metabolic process involves intracellular signal transduction and reorganization of the cytoskeleton. During adhesion, pulling forces are generated by the cytoskeletal dynamics, which is in equilibrium with the centripetal traction forces mediated by stress fibres in the ECM on the culture surfaces. When the latter is lost due to hydration, the remaining tensile forces developed by the cytoskeleton cause cell rounding and complete detachment from the substrates (Yamato et al., 1999).

Immunoassay studies have shown that following low-temperature cell lift-off from PNIPAAm grafted surfaces, ECM proteins such as fibronectin, laminin, and collagen are detached from the tray surface together with the cell sheet, and functional cell-cell junctions are preserved in the cell sheets (Chen et al., 2005; Kushida et al., 1999). Cells grown on PNIPAAm surfaces also maintain highly differentiated functions compared to cells recovered by enzymes (Yamato et al., 2007).

It has been shown that the PNIPAAm graft density and thickness on TCPS also plays a critical role when developing reliable temperature-responsive surfaces. It is known that graft thickness affects the chain mobility of the PNIPAAm layer, which indirectly influences cell attachment and release. It has been reported that for reversible cell attachment and release, the chain mobility of PNIPAAm must be restricted to a certain extent. Studies conducted by Akiyama *et al* have demonstrated that endothelial cells only attached onto PNIPAAm trays of graft thickness 15.5 nm ± 7.2 nm (1.4 ± 0.1 µg/cm^2), whereas no cells attached on surfaces when the graft layer was higher (29.3 nm ± 8.4 nm, and 5 µm) (Akiyama et al., 2004). This study reports an optimum PNIPAAm graft thickness of ~15-20 nm (Akiyama et al., 2004), however this is in disagreement with other reported works (Kumashiro et al., 2010; Mizutani et al., 2008). Mizutani *et al* used a controlled polymerisation technique to produce PNIPAAm layers with well-defined PNIPAAm thicknesses ranging from 1.8 nm to 64.7 nm (Mizutani et al., 2008). This study revealed that cell adhesion increased as the PNIPAAm layer thickness decreased, and was still possible on very thin PNIPAAm layers. Cells detached as a complete monolayer at 20 ℃ (for 1 hour) where the PNIPAAm thickness was 10.9 nm which is thinner than the conventional PNIPAAm coatings developed by Okano. This discrepancy has been attributed to differences in the coating microstructure amongst the studies, as well as a lack of understanding of the interfacial interactions with cells (Cole et al., 2009).

According to Matsuda *et al*, depending on the PNIPAAm thickness, different chain mobilities are possible at the outermost PNIPAAm surface which influences cell attachment and release as shown in **Figure 2.14** (Matsuda et al., 2007). It has been postulated that ultrathin PNIPAAm coatings display an aggregated surface layer and are unable to overcome the strong hydrophobic interactions at the PNIPAAm – TCPS interface resulting in insufficient hydration at T < LCST and cells are unable to efficiently detach (Akiyama et al., 2004; Matsuda et al., 2007). Conversely very thick coatings display a relaxed surface layer and enhanced chain mobility and hydration of the PNIPAAm chains, whereby cells cannot effectively attach at T > LCST. For reversible cell attachment and release, it has been reported that a restricted surface layer is required, such that the hydration and dehydration states are not excessive such that a quick interchange between both states is possible.

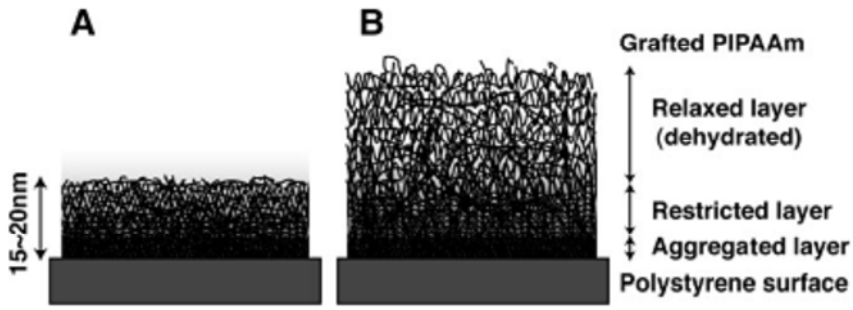

Figure 2.14: Image showing influence of graft thickness on chain mobility whereby graft thicknesses of 15-20 nm was found to be optimum for reversible cell attachment and release due to the presence of a restricted surface layer (Matsuda et al., 2007).

2.5.2.1 Cell sheet engineering

One of the major innovations in PNIPAAm cell culture has been in the area of cell sheet engineering for regenerative medicine. Cell sheet engineering refers to layering of individual cell sheets to create functional 2D or 3D tissues (Yang et al., 2005) (**Figure 2.15**). Numerous review articles have been published in the recent decade on this subject (Cole et al., 2009; Cooperstein and Canavan, 2010 ; da Silva et al., 2007; Kumashiro et al., 2010; Matsuda et al., 2007; Yamato et al., 2007; Yamato and Okano, 2004; Yang et al., 2005). Some of the advances in this field include multiple layering of heterotypic cell sheets e.g. hepatocyte cell sheets and endothelial cell sheets to create larger liver constructs (Harimoto et al., 2003). Patterned PNIPAAm surfaces with copolymers and non-cell-adhesive domains have also been developed to enable in situ co-cultures of heterotypic cells and recovery of co-cultured cell sheets for applications in regenerative medicine (Yamato et al., 2007). PNIPAAm cell sheet engineering has now been successfully applied to a variety of cell types including endothelial cells, corneal epithelial cells, chondrocytes, fibroblasts, keratinocytes, smooth muscle cells, hepatocytes, cardiomyocytes and various other stem cells (Moran et al., 2007; Murakami et al., 2006a; Nishida et al., 2004; Ohashi et al., 2007; Shimizu et al., 2002).

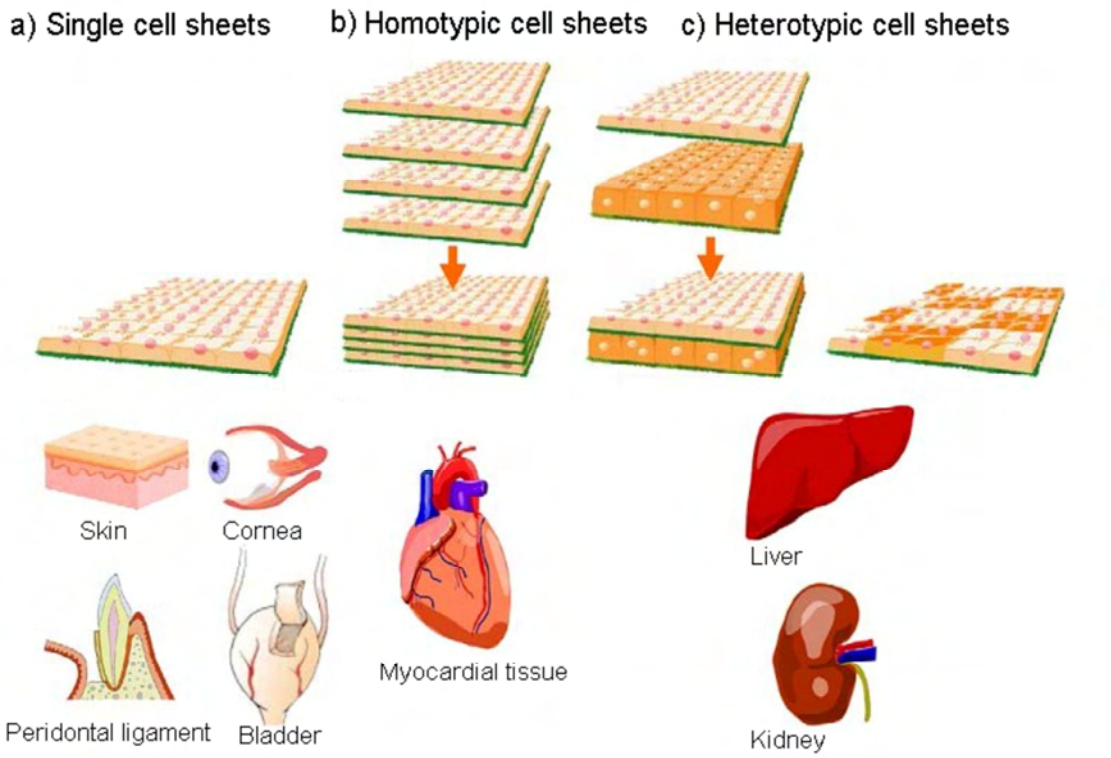

Figure 2.15: Image illustrating the concept of tissue reconstruction using cell sheet engineering whereby (a) single cell sheets (b) homotypic layering of cell sheets; (C) heterotypic cell sheet layering, and co-cultures from patterned surfaces can create lower and higher-order structures such as skin, cornea, myocardial tissue, kidney and liver (Yang et al., 2005).

Cell sheet engineering displays a number of advantages over direct cell injection or tissue engineering using biodegradable scaffolds (Yang et al., 2005). These include:

- The need for mild temperatures for spontaneous cell detachment
- No need for enzymes or harsh release methods
- Cells are released as an intact cell sheet together with the ECM proteins and cell-cell connections which are required for functional tissue
- Detached sheets can be used directly as an implant material in a host without requiring sutures, or without containing any foreign material which could induce an inflammatory response
- Possible to construct cell dense structures such as heart or liver
- Possible to develop large cell constructs without limitations of passive oxygen diffusion and loss in viability in the core of the construct

One of the challenges of this technology is cell sheet contraction upon release. Supporting membranes based on poly(ethylene terephthalate) and poly(vinylidenedifluoride) have been used to manipulate cell sheets without contraction (Matsuda et al., 2007). A recent paper reports the use of a PNIPAAm surface that was treated with oxygen plasma treatment to produce cell sheets on thin insoluble PNIPAAm layers with improved stability and storage (Shimizu et al., 2010).

While PNIPAAm cell sheets serve as a promising tool for engineering tissue, a limitation of the current technology is that it is primarily based on the use of flat 2D substrates which lacks structural and organisational cues for cells (Isenberg et al., 2008). Where layered or patterned co-culture cell sheets are used the process requires multiple steps and does not address the need for a structural matrix to enable cell growth in three dimensions.

2.5.2.1 3D PNIPAAm scaffolds for 3D cell culture

In recent years some studies have been reported with respect to development of porous PNIPAAm scaffolds, however for the majority of the scaffolds, the focus is still on the growth and release of 2D cell monolayers, whereby the pores are submicron and serve mainly for ease of hydration, oxygenation and nutrient supply to cells. Some of the recent studies are discussed below:

a) Porous PNIPAAm membranes and textured trays

Cell detachment from conventional PNIPAAm grafted TCPS trays is known to be slow since hydration is the rate limiting step as it occurs from the periphery of the PNIPAAm layer to the centre. Kwon *et al* developed a porous PNIPAAm membrane for cell culture whereby PNIPAAm was grafted onto PET membranes (with pore size of 0.45 µm, pore density = 1.6×10^6 /cm^2 and surface area = 4.2 cm^2) using electron beam irradiation (Kwon et al., 2000). The PET-*g*-PNIPAAm porous membranes displayed enhanced cell detachment of primary bovine aortic endothelial cells, whereby only 30 min was required to detach monolayer 2D cell sheets from the porous membrane as compared to 75 minutes for cell sheet detachment from PNIPAAm-*g*-TCPS trays. Enhanced cell detachment was attributed to improved hydration of the PNIPAAm layer from both the periphery as well basal side of the membranes as shown in **Figure 2.16**. Further acceleration of cell detachment was

possible by grafting polyethylene glycol (PEG)-PNIPAAm copolymer onto the porous PET membranes (Kwon et al., 2003). PEG was used to increase the hydrophilicity of PNIPAAm to increase the wetting and diffusion of water molecules, and the swelling/de-swelling characteristics of PNIPAAm. The use of 0.5 wt % PEG in the PNIPAAm-*co*-PEG copolymer, which was then grafted onto the PET porous membranes, decreased the cell detachment time to 19 minutes i.e. almost half the time which was required for the previously reported PNIPAAm-*g*-PET porous membranes (without PEG).

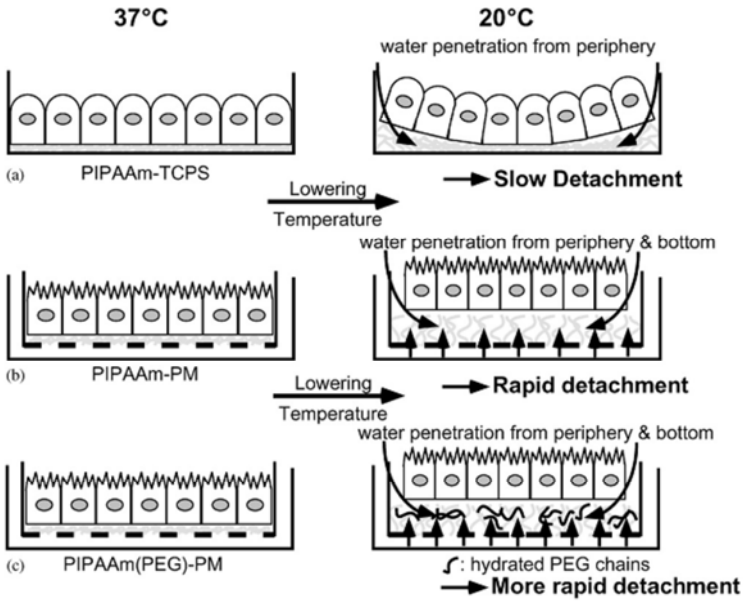

Figure 2.16: Illustration of cell detachment from (a) PNIPAAm-*g*-TCPS trays, (b) porous PNIPAAm grafted membranes, and (c) porous PNIPAAm-*co*-PEG grafted membranes whereby hydration occurs from the periphery and the basal side of the porous membranes via the pores, and the use of PEG further enhances the hydration process (Kwon et al., 2003).

Murakami *et al* used the porous PNIPAAm grafted PET membranes to investigate the expression of a differentiated phenotype when culturing primary canine oral mucosal epithelial cells without the use of xenogeneic factors (Murakami et al., 2006b). This study showed that when epithelial cells were grown on porous PNIPAAm grafted inserts, keratin expression, and stratified epithelial layers were possible and similar to when the xenogeneic factors were used, which was not possible on the rigid PNIPAAm coated trays. This was attributed to the porous structure of the inserts which enabled apical and basal supply of nutrients to the cells.

Okamura *et al* grafted PNIPAAm onto polypropylene (PP) membranes containing antibodies using plasma-induced polymerisation for selective cell separation of a specific cell type (Okamura et al., 2008; Okamura et al., 2005; Toshiyuki and Midori, 2006). Monoclonal antibodies were adsorbed onto the PP-*g*-PNIPAAm membranes at 37 ℃ due to hydrophobic interactions, and enabled binding of targeted cells due to the antigen-antibody complex, while at 4 ℃, cell release of the targeted cells was possible due to the hydration of the PNIPAAm chains (Okamura et al., 2008). Nonwoven PP membranes (average pore radius, 10 µm) were used in this study, and this study did not focus on cell expansion and propagation in 3D.

To provide cells with a defined structural organisation, Isenberg *et al* developed micro textured TCPS trays, which were grafted with PNIPAAm. The patterns on the TCPS trays, consisted of alternating grooves and ridges (50 µm wide, 5 µm deep). Vascular smooth muscle cells cultured on the PNIPAAm grafted micro textured trays, produced intact monolayer cell sheets consisting of cells that exhibited strong alignment in the direction of the micro pattern (Isenberg et al., 2008). An optimum range of PNIPAAm grafting density for the micro patterned TCPS with this method was found to be 45–50% that is slightly lower than what is typically used to graft TCPS culture dishes (53–55%) (Isenberg et al., 2008). Cells still grew in monolayers.

As mentioned previously most of the studies discussed above focus on the culture and release of 2D cell monolayers even when 3D PNIPAAm scaffolds have been used. Recently Duarte *et al* presented the first report on the development of a 3D thermoresponsive scaffold for 3D cell expansion and proliferation (Duarte et al., 2011). The scaffold used in this study is a poly(D,L-lactic acid) foam containing PNIPAAm with mean pores of 138 µm. However the release of 3D cellular structures and high-density cells was not reported.

b) Hydrogels

It has been reported that bulk linear PNIPAAm and conventional cross-linked PNIPAAm hydrogels do not support cell attachment at 37 ℃ (Akiyama et al., 2004; Haraguchi et al., 2006). The lack of thermoresponsiveness of bulk PNIPAAm surfaces can be attributed to the increased hydrophilicity, and hydration of thick PNIPAAm layers and high chain mobility which prevents cell adhesion even at 37 ℃ (Akiyama et al., 2004). Many studies have been conducted to copolymerise NIPAAm with other monomers to form 3D PNIPAAm hydrogels for use in cell culture, but with

only limited success to date. Matsuda's group developed various thermoresponsive PNIPAAm hydrogels copolymerised or grafted with gelatin (Ohya et al., 2005; Ohya et al., 2001b), hyaluronic acid (HA) (Ohya et al., 2001a), and PEG (Kwon and Matsuda, 2006) to more closely replicate the ECM. For the PNIPAAm-*g*-gelatin hydrogels it was found that adhesiveness of human umbilical vein endothelial cells increased with an increase in the PNIPAAm: gelatine ratio, while the PNIPAAm-*g*-HA hydrogels were non-cell adhesive. It was found that cell adhesiveness was influenced by the stiffness of the hydrogel and its ability to withstand the cell traction forces during spreading.

Haraguchi *et al* describes the development of PNIPAAm-clay nanocomposites with improved mechanical properties. Various cell types were tested i.e. hepatoma cells, dermal fibroblasts and umbilical vein endothelial cells and in each case cells adhered and proliferated on the PNIPAAm-clay nanocomposite hydrogels regardless of the thickness of the gel, while little adhesion and no proliferation were observed on pure PNIPAAm hydrogels (Haraguchi et al., 2006). Complete cell sheet detachment was also achieved. The authors attributed improved cell attachment and proliferation on polymer/clay hydrogels to enhanced protein absorption due to surface ionic charges contributed by the exfoliated clay, and the balance of hydrophobicity (due to PNIPAAm chains) and hydrophilicity (due to hydrophilic clay) (Haraguchi et al., 2006).

2.5.3 Cell culturing in bioreactors

It is clear that in order to develop a reliable *in vitro* cell culture system, cells must exist in a dynamic flux environment similar to the dynamic state of living tissue. In recent years there has been increasing interest in the use of bioreactors for high density and more physiologically relevant cell cultures. A bioreactor is typically a closed contained vessel in which cells are cultured on a scaffold whereby the flow of the cell culture medium containing the relevant growth factors and nutrients is controlled and the cells are oxygenated. Bioreactors can also enable control and monitoring of various parameters such as pH, conductivity, CO_2/O_2 levels, glucose consumption etc.

Bioreactors have been specifically developed to overcome the mass-transport diffusional limitations in static 2D cultures and to enable high-density cell cultures. It

is known that one of the main limitations with 3D cell cultures is the higher oxygen requirements for cell dense constructs. This particularly becomes a constraint for large scale mammalian culture such as in the case of tissue engineering and production of cell culture products. Oxygen has a poor diffusion capacity and solubility in static aqueous solution at physiological temperatures. It has been established that i*n vitro* static systems, oxygen and nutrient supply to cells is limited to a distance of 100-200 µm by passive diffusion from the fluid-scaffold interface (Volkmer et al., 2008). Studies have indicated that with cell constructs greater than ~200 µm grown in a static system, cells only survive at the periphery while the cells in the centre suffer from hypoxia (i.e. lack of oxygen supply), causing necrosis (i.e. cell death) at the centre of the constructs (Volkmer et al., 2008). This is often the limiting factor in scaling up 3D cell cultures. Perfusion bioreactors that perfuse culture medium directly through the pores of the scaffold have been found to be very efficient in reducing diffusional limitations by enhancing media transport at the construct periphery as well as within the internal pores, minimizing mass-transport limitations (Wendt et al., 2009). Bioreactors also enable enhanced oxygenation to cells by the use of external spargers or directly through the use of hollow fibres.

Bioreactors also very importantly enable fluid-driven stimulation of cells. Dynamic conditioning of cells is of particular importance in the case of cartilage, bone, cardiac tissue etc. where bioreactors have been used to apply mechanical stimulation such as stress-shielding and differential pressure to enhance the *in vitro* engineering of tissue (Wendt et al., 2009).

A number of bioreactors are in common use for cell culturing of anchorage-dependent cells, and these include stirred tank bioreactors, fluidised-bed, fixed-bed, ceramic matrix bioreactors, membrane bioreactors, spinner-flasks and hollow-fibre membrane bioreactors (Frost & Sullivan,1999). The scaffolds used in these bioreactors are variable and often include microcarrier beads, microporous spheres, ceramic particles, membranes, and/or hollow fibres. Microcarrier cell culture in stirred tanked bioreactors is the most commonly used culture method for large scale culture of anchorage-dependent cells (Frost & Sullivan,1999; Chu and Robinson, 2001; Hu and Aunins, 1997).

The most common use of bioreactors in cell culture is in the production of cell products such as proteins and monoclonal antibodies, and not necessarily for harvesting and releasing high density cells. In recent years the use of hollow-fibre

bioreactors are growing in demand for cell culture and are becoming increasingly popular for the production of monoclonal antibodies (Ye et al., 2006). Hollow-fibre bioreactors consist of networks or large bundles of hollow fibres with very small diameters (e.g. 200 µm in the case of FibreCell Hollow fibre Systems), embedded in a cylindrical housing. The hollow-fibre bioreactor contains inlet and outlet ports at the ends of the cartridge to enable flow of liquid through the inner cavity of the fibres (inner lumen), while ports present on the top of the housing allows access to the area outside the fibres i.e. the extracapillary space (Cadwell, 2004; Ye et al., 2006) as shown in **Figure 2.17**.

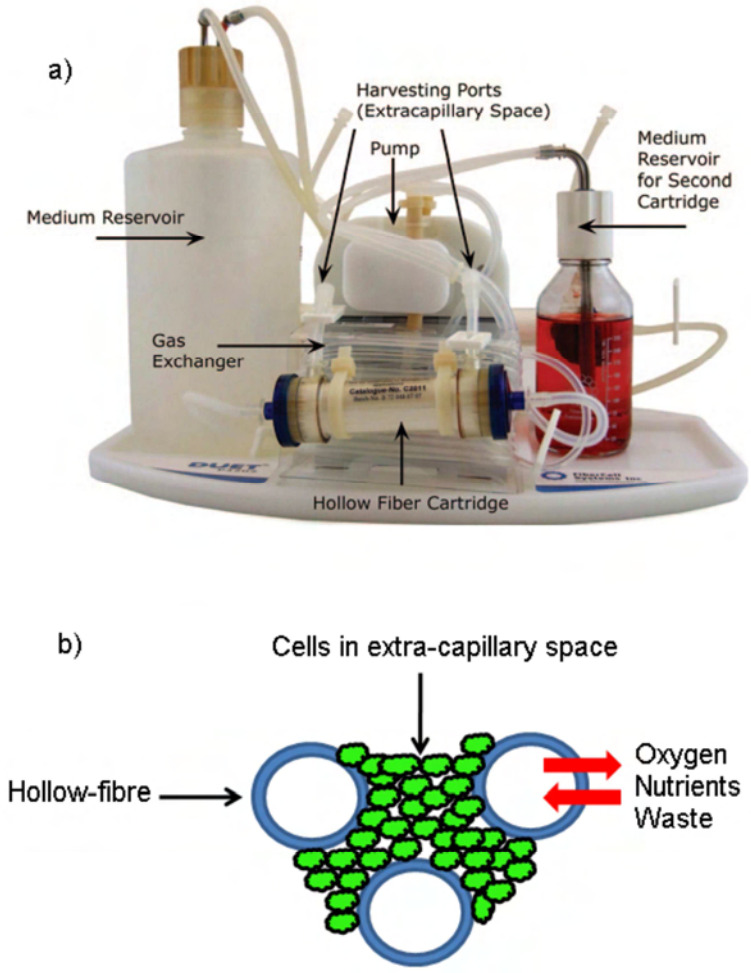

Figure 2.17: (a) Image of FiberCell hollow fibre system (FiberCell Systems Inc, 2012) and (b) schematic drawing of a hollow-fibre membrane bioreactor used in cell culturing.

Generally the cells are grown in the extracapillary space where they can attach onto the fibres and grow in clusters, while the culture medium and/or oxygen is circulated through the inner lumen of the hollow fibres. The nutrients and oxygen diffuse through the membranes to the cells, while the metabolic waste diffuse away from the

cells into the inner lumen according to hydrostatic pressure difference and concentration gradients. This creates a nutrient circulation system similar to the capillary system in native tissue (Frost & Sullivan,1999; Ye et al., 2006). A large number of commercially available bioreactors are based on hollow-fiber systems and include Primer HF; MiniMax; Maximizer; Excellerator; CellMax®; and FibreCell Systems.

Bioreactors offer several advantages when compared to static culture and include the following (Cadwell, 2004; Wendt et al., 2009):

- High-density cell cultures can be achieved and cells can grow in densities similar to that found *in vivo* i.e. > 10^8 cells/ml as compared to standard cell culture (with spinner flasks) where only 10^6 cells/ml are possible
- Dynamic cell seeding is possible to reduce the inhomogeneity of static cell seeding
- High level of supply of oxygen and nutrient to cells reducing diffusional limitations
- Cells are physically stimulated by the shear forces which can induce signal pathways which is not possible in static growth conditions
- Control, monitoring and regulation of key environmental parameters such as temperature, pH, gas composition, humidity etc.) are possible
- Continuous or semi-continuous replenishment of spent media is possible with feedback mechanisms ensuring that the homeostatic of cells is maintained and not disrupted as is the case with manual media changes.
- Systems are automated and semi-automated to reduce the human intervention required which lowers contamination and improves the reliability and reproducibility of cell culture

Automated cell culturing systems typically involve culturing cells under controlled environmental conditions, while providing the capability of monitoring cell growth and maintaining media conditions (i.e. media pH, dissolved oxygen content, nutrient and waste concentration, cell concentration and cell viability). A number of automated systems have appeared on the market with different levels of automation, and capabilities (**Table 2.3**). Systems such as Cellmate™, and AcCellerator™ involve the use of robotics to automate the traditional processes performed within manual cell

culture, i.e. cell seeding on culture trays/flasks, media changes, bottle gassing, cell sheet rinsing, trypsination and/or cell scraping (Kempner and Felder, 2002).

Table 2.3: Examples of commercially available automated cell culture systems.

Supplier	**Products**	**Application**
Cytogration	Cytogration System	Automated system with 2D Multi-well plates
Automation partnership (TAP)	Cellmate™ SelectT	2D roller-bottles and T-flasks T-flasks & microtiter plates
RTS Life Science International	AcCellerator™	Automated system stack-based culture of 2D T-flasks
CRS Biodiversity	-	Membrane well plates or microtitre plates
Hamilton	CellHost	BioLevitator™ bioreactor with GEM™ microcarriers (3D)

Consequently the same results are achieved but with improved consistency, substantially lower contamination rates, minimum human intervention, lower labour and process costs, higher yield, higher efficiency and improved turn-around times. Scale-up is also easier on these automated robotic cell culture type systems in that no regulatory approval required since the process is the same as with manual cell culture (Kempner and Felder, 2002). Automated systems are now common place especially in pharmaceutical companies where high-volume cell culturing is required on a routine basis. In recent years, the innovative BioLeviator ™ has been developed which is a small bench-top device for high density disposable microcarrier cell culture as shown in **Figure 2.18**.

Although the current bioreactors and automated cell culture systems offer major advantages to the traditional manual cell culture system, not all key issues facing anchorage-dependent cell culturing are currently being addressed (i.e. use of 3D scaffold and non-invasive cell release). Additionally very few systems offer ease of operation (i.e. seeding of cells in the bioreactor, perfusion of the cell culture and maintenance of the cell culture through monitoring and medium exchange, and harvesting of the cell culture to be analysed) and monitoring and control of the

experimental parameters. Also the traditional automated systems have been large bulky devices.

Figure 2.18: The BioLevitator™ - a compact bench-top device with controls (Justice et al., 2009).

2.6 Conclusions

PNIPAAm is the most well-known and studied thermoresponsive smart polymer. PNIPAAm is mainly being explored for use in cell culture due to its mild phase transition conditions. PNIPAAm enables spontaneous cell release from its surface by merely cooling the media and without requiring any destructive methods. PNIPAAm hydrogels display challenges with respect to slow response time and poor mechanical properties. Studies have also shown that bulk PNIPAAm hydrogels is not effective as cell culture scaffolds due to the dense skin layer. However PNIPAAm grafted TCPS trays has proven to be an attractive technology for monolayer cell culturing. Various techniques are available for graft polymerisation of PNIPAAm onto polymer surfaces with chemical initiation being the simplest and most cost-effective option. A polymer surface must also preferably be functionalised with reactive groups to enhance grafting. Fluorination is an attractive functionalisation method since it is a dry technology, it is less invasive than other radiation methods, and it can form reactive polar groups on a polymer surface at room temperature.

With respect to cell culture, it is well-known that 3D culture is far superior when compared to 2D monolayer culture. Many 3D scaffolds are available for 3D cell

culture, however many of the scaffolds still rely on destructive means to release the confluent cells. To date only limited studies have focussed on the development of a 3D porous PNIPAAm scaffold whereby such a scaffold could be used routinely as a 3D cell culture insert for the release of 3D cell clusters and in a bioreactor for high-density 3D cell cultures. Although some attempts have been made at developing 3D PNIPAAm scaffolds such as porous membranes, hydrogels and micro textured surfaces, studies have focused primarily on the release of monolayers. Also bench-top bioreactors are being developed specifically for high-density 3D cell culture; however there still remains a gap with respect to enabling 3D cell culture together with non-destructive and non-invasive cell release of 3D cellular constructs. Wendt *et al* proposed in his review article on bioreactors that PNIPAAm could be used in a bioreactor for temperature-induced cell release, thereby eliminating the need for trypsin and the associated time-consuming processing steps, however to date no such system has been developed (Wendt et al., 2009).

2.7 References

Akiyama Y, Kikuchi A, Yamato M, Okano T. 2004. Ultrathin poly(*N*-isopropylacrylamide) grafted layer on polystyrene surfaces for cell adhesion/detachment control. Langmuir 20:5506-5511.

Amornsakchai T, Doaddara O. 2008. Grafting of acrylamide and acrylic acid onto polyethylene fiber for improved adhesion to epoxy resin. Journal of Reinforced Plastics and Composites 27(7): 671-682.

Bamford CH, Al-Lamlee KG. 1994. Studies in polymer surface functionalisation and grafting for biomedical and other applications. Polymer 35(13):2844-2852.

Bancroft GN, Sikavitsas VI, van den Dolder J, Sheffield TL, Ambrose CG, Jansen JA, Mikos AG. 2002. Fluid flow increases mineralized matrix deposition in 3D perfusion culture of marrow stromal osteoblasts in a dose-dependent manner. Proceedings of the National Academy of Sciences 99(20):12600–12605.

BD Biosciences. BD Microplates. Product brochure: Available online: www. bdbiosciences. com/microplates, Date accessed 10 November 2011

Bhattacharya A, Misra BN. 2004. Grafting: A versatile means to modify polymers - Techniques, factors and applications. Progress in Polymer Science 29:767-814.

Bokhari M, Carnachan RJ, Cameron NR, and Przyborski SA. 2007. Novel cell culture device enabling three-dimensional cell growth and improved cell function. Biochemical and Biophysical Research Communications 354:1095–1100.

Bucio E, Arenas E, Burillo G. 2006. Radiation grafting of *N*-Isopropylacrylamide onto polypropylene films by preirradiation method. Molecular Crystals and Liquid Crystals 447:203/[521]-213/[531].

Bucio E, Burillo G, Adem E, Coqueret X. 2005. Temperature sensitive behaviour of Poly(N-isopropylacrylamide) grafted onto electron beam-irradiated poly(propylene). Macromolecular Materials and Engineering 290: 745-752.

Cadwell JJS. 2004. New developments in hollow fibre cell culture. American Biotechnology Laboratory. Available on-line: http:// www.fibercellsystems. com/documents/ABL-Cadwell.pdf, Date accessed: 10 June 2012.

Canavan HE, Cheng X, Graham DJ, Ratner BD, Castner DG. 2005. Cell sheet detachment affects the extracellular matrix: A surface science study comparing thermal liftoff, enzymatic, and mechanical methods. Journal of Biomedical Materials Research-A. 75(1):1-13.

Chen KS, Ku YA, Lee CH, Lin HR, Lin FH, Chin TM. 2005. Immobilization of chitosan gel with cross-linking reagent on PNIPAAm gel/PP nonwoven composites surface. Materials Science and Engineering C 25:472–478.

Cheng X, Canavan HE, Stein MJ, Hull JR, Kweskin SJ, Wagner MS, Somorjai GA, Castner DG, Ratner BD. 2005. Surface chemical and mechanical properties of plasma-polymerized *N*-Isopropylacrylamide. Langmuir 21:7833-7841.

Chu L, Robinson DK. 2001. Industrial choices for protein production by large-scale cell culture. Current Opinion on Biotechnology 12:180–187.

Clough RL. 2001. High-energy radiation and polymers: A review of commercial processes and emerging applications. Nuclear Instruments and Methods in Physics Research B 185:8-33.

Cole MA, Voelcker NH, Thissen H, Griesser HJ. 2009. Stimuli-responsive interfaces and systems for the control of protein–surface and cell–surface interactions. Biomaterials 30:1827–1850.

Contreras-Garcıa A, Burillo G, Aliev R, Bucio E. 2008. Radiation grafting of *N,N*-dimethylacrylamide and *N*-isopropylacrylamide onto polypropylene films by two-step method. Radiation Physics and Chemistry 77 936–940.

Cooperstein MA, Canavan HE. 2010 Biological cell detachment from Poly(*N*-isopropylacrylamide) and its applications. Langmuir 26(11):7695–7707.

Cukierman E, Pankov R, Stevens DR, and Yamada KM. 2001. Taking cell-matrix adhesions to the third dimension. Science 294:1708-1712.

Curti PS, De Moura MR, Radovanovic E, Rubira AF, Muniz EC. 2002. Surface modification of polystyrene and poly(ethylene terephthlate) by grafting poly(*N*-isopropylacrylamide). Journal of Material Science: Materials in Medicine 13:1175-1180.

Curti PS, de Moura MR, Veiga W, Radovanovic E, Rubira AF, Muniz EC. 2005. Characterization of PNIPAAm photografted on PET and PS surfaces. Applied Surface Science 245:223–233.

da Silva RMP, Mano JF, Reis RL. 2007. Smart thermoresponsive coatings and surfaces for tissue engineering: switching cell-material boundaries. TRENDS in Biotechnology 25(12):577-583.

Desai SM, Singh RP. 2004. Surface modification of polyethylene. Advances in Polymer Science 169:231–293.

Desai SM, Solanky SS, Mandale AB, Rathore K, Singh RP. 2003. Controlled grafting of *N*-isoproply acrylamide brushes onto self-standing isotactic polypropylene thin films: surface initiated atom transfer radical polymerization. Polymer 44:7645–7649.

du Toit FJ, Sanderson RD. 1999. Surface fluorination of polypropylene 1. Characterisation of surface properties. Journal of Fluorine Chemistry 98:107-114.

Duarte ARC, Mano JF, Reis RL. 2011. Thermosensitive polymeric matrices for three-dimensional cell culture strategies. Acta Biomaterialia 7: 526-529.

Fiber Cell Systems Inc. Hollow fibre bioreactors and related products http://www.fibercellsystems.com/documents/brochure.pdf. Date accessed: 10 June 2012.

Frost & Sullivan.1999. European cell culture systems markets. #3489-43.

Galaev IY, Mattiasson B. 1999. 'Smart' polymers and what they could do in biotechnology and medicine. Trends in Biotechnology 17:335-339.

GE Healthcare. 2009. Cytodex™ surface microcarriers. Data file 18-1060-61 AF. Available online: http:// www.gelifesciences.co.jp /catalog/ pdf/1 8106061_cytodex.pdf, Date accessed: 10 August 2012.

Geever LM, Devine DM, Nugent MJD, Kennedy JE, Lyons JG, Hanley A, Higginbotham CL. 2006. Lower critical solution temperature control and swelling behaviour of physically crosslinked thermosensitive copolymers based on *N*-isopropylacrylamide. European Polymer Journal 42:2540–2548.

Geever LM, Mínguez CM, Devine DM, Nugent MJD, Kennedy JE, Lyons JG, Hanley A, Devery S, Tomkins PT, Higginbotham CL. 2007. The synthesis, swelling

behaviour and rheological properties of chemically crosslinked thermosensitive copolymers based on *N*-isopropylacrylamide. Journal of Material Science 42:4136–4148

Geiger B, Bershadsky A, Pankov R, and Yamada KM. 2001. Transmembrane extracellular matrix-cytoskelton crosstalk Nature Reviews - Molecular Cell Biology 2:793-805.

Geuskens G, Etoc A, Michele PD. 2000. Surface modification of polymers VII. Photochemical grafting of acrylamide and *N*-isopropylacrylamide onto polyethylene initiated by anthraquinone-2-sulfonate adsorbed at the surface of the polymer. European Polymer Journal 36:265-271.

Geuskens G, Nedelkos G. 1993. The post-irradiation oxidation of poly(propylene), radical decay and oxygen absorption. Makromolekulare Chemie 194:3349-3355.

Grinberg VY, Dubovik AS, Kuznetsov DV, Grinberg NV, Grosberg AY, Tanaka T. 2000. Studies of the thermal volume transition of poly(*N*-isopropylacrylamide) hydrogels by high-sensitivity differential scanning microcalorimetry. 2. thermodynamic functions. Macromolecules 33:8685-8692.

Guillame-Gentil O, Semenov O, Roca AS, Groth T, Zahn R, Vörös J, Zenobi-Wong M. 2010. Engineering the extracellular environment: strategies for building 2D and 3D cellular structures. Advanced Materials 22:5443–5462.

Gupta B, Anjum N. 2003. Plasma and radiation-induced graft modification of polymers for biomedical applications. Advances in Polymer Science 162:35-61.

Gupta KC, Khandekar K. 2003. Temperature-responsive cellulose by ceric(IV) ion-initiated graft copolymerization of *N*-Isopropylacrylamide. Biomacromolecules 4:758-765.

Gupta KC, Sahoo S. 2001. Graft copolymerization of acrylonitrile and ethyl methacrylate comonomers on cellulose using ceric ions. Biomacromolecules 2:239-247.

Haddadi-Asl V, Burford RP, Garnett JL. 1994. Radiation graft modification of ethylene-propylene rubber I. Effect of monomer and substrate structure. Radiation Physics and Chemistry 44(4):385-393.

Haraguchi K, Takehisa T, Ebato M. 2006. Control of cell cultivation and cell sheet detachment on the surface of polymer/clay nanocomposite hydrogels. Biomacromolecules 7:3267-3275.

Harimoto M, Yamato M, Kikuchi A, Okano T. 2003. Cell sheet engineering: Intelligent polymer patterned surfaces for tissue engineered liver. Macromolecular Symposia 195:231-235.

Hennink WE, van Nostrum CF. 2002. Novel crosslinking methods to design hydrogels. Advanced Drug Delivery Reviews 54:13–36.

Hoffman AS. 2000. Bioconjugates of intelligent polymers and recognition proteins for use in diagnostics and affinity separations. Clinical Chemistry 46(9):1478–1486.

Hu W-S, Aunins JG. 1997. Large-scale mammalian cell culture. Current Opinion in Biotechnology 8:148-153.

Huang N, Sundberg DC. 1995. Fundamental studies of grafting reactions in free radical copolymerisation. III. Grafting of styrene, acrylate, and methacrylate monomers onto cis-polybutadiene using benzoyl peroxide initiator in solution polymerisation. Journal of Polymer Science Part A:Polymer Chemistry 33:2571-2586.

Hutmacher DW. 2005. A Commentary on ‘‘Thermo-responsive polymeric surfaces; control of attachment and detachment of cultured cells’’. Macromolecular Rapid Communications 26:505–513.

Isenberg BC, Tsuda Y, Williams C, Shimizu T, Yamato M, Okano T, and Wong JY. 2008. A thermoresponsive, microtextured substrate for cell sheet engineering with defined structural organization. Biomaterials 29:2565–2572.

Jeong B, Gutowska A. 2002. Lessons from nature: stimuli responsive polymers and their biomedical applications. TRENDS in Biotechnology 20(7):305-311.

Jeong E, Bae TS, Yun SM, Woo SW, Lee YS. 2011. Surface characteristics of low-density polyethylene films modified by oxyfluorination-assisted graft polymerization. Colloids and Surfaces A: Physicochemical and Engineering Aspects 373:36-41.

Justice BA, Badr NA, Felder RA. 2009. 3D cell culture opens new dimensions in cell-based assays. Drug Discovery Today 14(1/2):102-107.

Kato K, Uchida E, Kang E, Uyama Y, Ikada Y. 2003. Polymer surface with graft chains. Progress in Polymer Science 28:209–259.

Kempner ME, Felder RA. 2002. A review of cell culture automation. Journal of Laboratory Automation 7(2):56-62.

Kharitonov AP. 2000. Practical applications of the direct fluorination of polymers. Journal of Fluorine Chemistry 103:123-127.

Kharitonov AP. 2008. Direct fluorination of polymers – From fundamental research to industrial application. Progress in Organic Coatings. 61:192-204.

Kharitonov AP, Kharitonova LN. 2009. Surface modification of polymers by direct fluorination: A convenient approach to improve commercial properties of polymeric articles. Pure and Applied Chemistry 81(3):451-471.

Kharitonov AP, Moskvin YL, Syrtsova DA, Starov VM, Teplyakov VV. 2004. Direct fluorination of the polyimide matrimid® 5218: The formation kinetics and physicochemical properties of the fluorinated layers. Journal of Applied Polymer Science 92:6–17.

Kharitonov AP, Taege R, Ferrier G, Teplyakov VV, Syrtsova DA, Koops GH. 2005. Direct fluorination—Useful tool to enhance commercial properties of polymer articles. Journal of Fluorine Chemistry 126 251–263.

Kim SY, Kanamori T, Shinbo T. 2002. Preparation of thermal-responsive poly(propylene) membranes grafted with *N*-Isopropylacrylamide by plasma-induced polymerization and their water permeation. Journal of Applied Polymer Science 84:1168–1177.

Kishi R, Hirasa O, Ichijo H. 1997. Fast responsive poly(*N*-isopropylacrylamide) hydrogels prepared by γ-ray irradiation. Polymer Gels and Networks 5:145-151.

Kleinman HK, McGarvey ML, Hassell HR, Star VL, Cannon FB, Laurie GW, Martin GR. 1986. Basement Membrane Complexes with Biological Activity Biochemistry 25(3):312-318.

Klouda L, Mikos AG. 2008. Thermoresponsive hydrogels in biomedical applications. European Journal of Pharmaceutics and Biopharmaceutics 68:34-45.

Kumar A, Srivastava A, Galaev IY, Mattiasson B. 2007. Smart polymers: Physical forms and bioengineering applications. Progress in polymer Science:1205-1237.

Kumashiro Y, Yamato M, Okano T. 2010. Cell attachment–detachment control on temperature-responsive thin surfaces for novel tissue engineering. Annals of Biomedical Engineering 38(6):1977–1988.

Kushida A, Yamato M, Konno C, Kikuchi A, Sakurai Y, and Okano T. 1999. Decrease in culture temperature releases monolayer endothelial cell sheets together with deposited fibronectin matrix from temperature-responsive culture surfaces. Journal of Biomedical Materials Research 45(4):355–362.

Kwon IK, Matsuda T. 2006. Photo-iniferter-based thermoresponsive block copolymers compose of poly(ethylene glycol) and poly(*N*-isopropylacrylamide) and chondrocyte immobilization. Biomaterials 27 986–995.

Kwon OH, Kikuchi A, Yamato M, Okano T. 2003. Accelerated cell sheet recovery by co-grafting of PEG with PIPAAm onto porous cell culture membranes. Biomaterials 24:1223–1232.

Kwon OH, Kikuchi A, Yamato M, Sakura iY, Okano T. 2000. Rapid cell sheet detachment from poly(*N*-isopropylacrylamide)-grafted porous cell culture membranes. Journal of Biomedical Materials Research 50:82-89.

Lee BK, Lee YS, Chong YB, Choi JB, Rho JR. 2003. Hydrophilic modification of polypropylene film by oxyfluorination. Journal of Industrial and Engineering Chemistry 9(4):426-432.

Lee J, Cuddihy MJ, Kotov NA. 2008. Three-dimensional cell culture matrices: State of the art. Tissue engineering: Part B 2008 14(1).

Liang L, Feng X, Peurrung L, Viswanathan V. 1999. Temperature-sensitive membranes prepared by UV photopolymerization of *N*-isopropylacrylamide on a surface of porous hydrophilic polypropylene membranes. Journal of Membrane Science 162:235-246.

Liang L, Shi M, Viswanathan VV, Peurrung LM, Young JS. 2000. Temperature-sensitive polypropylene membranes prepared by plasma polymerization. Journal of Membrane Science 177:97–108.

Liu Q; 3D Biotek, LLC, assignee. 13/02/2008. Three dimensional cell culture construct and apparatus for its making. United States patent US 2008/0194010 A1.

Liu Q, Zhang P, Qing A, Lan Y, Lu M. 2006. Poly(*N*-isopropylacrylamide) hydrogels with improved shrinking kinetics by RAFT polymerization. Polymer 47: 2330–2336.

Liu R, Fraylich M, Saunders BR. 2009. Thermoresponsive copolymers: from fundamental studies to applications. Colloid Polymer Science 287:627–643.

Matsuda N, Shimizu T, Yamato M, Okano T. 2007. Tissue engineering based on cell sheet technology. Advanced Materials 19: 3089-3099.

Mele'ndez-Ortiz HI, Bucio E, Burillo G. 2009. Radiation-grafting of 4-vinylpyridine and *N*-isopropylacrylamide onto polypropylene to give novel pH and thermo-sensitive films. Radiation Physics and Chemistry 78:1-7.

Milichovsky M. 2010. Water—A key substance to comprehension of stimuli-responsive hydrated reticular systems. Journal of Biomaterials and Nanobiotechnology 1:17-30.

Mizutani A, Kikuchi A, Yamato M, Kanazawa H, Okano T. 2008. Preparation of thermoresponsive polymer brush surfaces and their interaction with cells. Biomaterials 29:2073-2081.

Moolman FS, Naidoo K, Van Wyk AJ; 2009. Non-invasive automated cell proliferation apparatus patent WO 2009/031127 A2.

Moran MT, Carroll WM, Gorelov A, Rochev Y. 2007. Intact endothelial cell sheet harvesting from thermoresponsive surfaces coated with cell adhesion promoters. Journal of Royal Society Interface 4:1151–1157.

Mowery DM, Assink RA, Derzon DK, Klamo SB, Bernstein R, Clough RL. 2007. Radiation oxidation of polypropylene: A solid-state ^{13}C NMR study using selective isotopic labeling. Radiation Physics and Chemistry 76:864-878.

Murakami D, Yamato M, Nishida K, Ohki T, Takagi R, Yang J, Namiki H, Okano T. 2006a. The effect of micropores in the surface of temperature-responsive culture inserts on the fabrication of transplantable canine oral mucosal epithelial cell sheets. Biomaterials 27:5518–5523.

Murakami D, Yamato M, Nishida K, Ohki T, Takagi R, Yang J, Namiki H, Okano T. 2006b. The effect of micropores in the surface of temperature responsive culture inserts on the fabrication of transplantable canine oral mucosa epithelial cell sheets. Biomaterials 27:5518–5523.

Nishida K, Yamato M, Hayashida Y, Watanabe K, Maeda N, Watanabe H, Yamamoto K, Nagai S, Kikuchi A, Tano Y and others. 2004. Functional bioengineered corneal epithelial sheet grafts from corneal stem cells expanded ex-vivo on a temperature-responsive cell culture surface. Transplantation 77(3):379–385.

Ohashi K, Yokoyama T, Yamato M, Kuge H, Kanehiro H, Tsutsumi M, Amanuma T, Iwata H, Yang J, Okano T and others. 2007. Engineering functional two- and three-dimensional liver systems in vivo using hepatic tissue sheets. Nature Medicine 13(7):880–885.

Ohya S, Kidoaki S, Matsuda T. 2005. Poly(*N*-isopropylacrylamide) (PNIPAM)-grafted gelatin hydrogel surfaces: interrelationship between microscopic structure and mechanical property of surface regions and cell adhesiveness. Biomaterials 26 3105–3111.

Ohya S, Nakayama Y, Matsuda T. 2001a. Thermoresponsive artificial extracellular matrix for tissue engineering: hyaluronic acid bioconjugated with poly(N-isopropylacrylamide) grafts. Biomacromolecules 2:856 863.

Ohya S, Nakayama Y, Matsuda T. 2001b. Material design for an artificial extracellular matrix: cell entrapment in poly(*N*-isopropylacrylamide) (PNIPAM)-grafted gelatin hydrogel. Journal of Artificial Organs 4:308-314

Okamura A, Hagiwara T, Yamagami S, Yamaguchi M, Shinbo T, Kanamori T, Kondo S, Miwa K, Itagaki I. 2008. Effective cell separation utilizing poly(*N*-

Isopropylacrylamide)-grafted polypropylene membrane containing adsorbed antibody. Journal of Bioscience and Bioengineering 105 (3):221–225.

Okamura A, Itayagoshi M, Hagiwara T, Yamaguchi M, Kanamori T, Shinbo T, Wang P-C. 2005. Poly(*N*-isopropylacrylamide)-graft-polypropylene membranes containing adsorbed antibody for cell separation. Biomaterials 26:1287–1292.

Okano T, Yamada N, Okuhara M, Sakai H, Sakurai Y. 1995. Mechanism of cell detachment from temperature-modulated, hydrophilic-hydrophobic polymer surfaces. Biomaterials 16:297-303.

Ortega A, Bucio E, Burillo G. 2007. Radiation polymerization and crosslinking of (N-isopropylacrylamide) in solution and in solid state. Polymer Bulletin 58:565–573.

Pal K, Banthia AK, Majumdar DK. 2009. Polymeric Hydrogels: Characterization and Biomedical Applications –A mini review. Designed Monomers and Polymers 12:197-220.

Pampaloni F, Reynaud EG, Stelzer EHK. 2007. The third dimension bridges the gap between cell culture and live tissue. Nature Reviews Molecular Cell Biology 8:839-845.

Park SJ, Song SY, Shin JS, J.M. R. 2005 Effect of surface oxyfluorination on the dyeability of polyethylene film. Journal of Colloid and Interface Science 283:190–195.

Pekcan O, Kara S. 2003. The effect of preparation temperature on phase transitions of *N*-isopropylacrylamide gels. Phase Transitions 76(6):601-609.

Prestwich GD. 2007. Simplifying the extracellular matrix for 3-D cell culture and tissue engineering: A pragmatic approach. Journal of Cellular Biochemistry 101:1370–1383.

Prestwich GD. 2008. Evaluating drug efficacy and toxicology in three dimensions: Using synthetic extracellular matrices in drug discovery. Accounts of Chemical Research 41(1):139-148.

Ramirez-Fuentes YS, Bucio E, Burillo G. 2007. Radiation-induced grafting of *N*-isopropylacrylamide and acrylic acid onto polypropylene films by two step method. Nuclear Instruments and Methods in Physics Research B 265:183–186.

Riggs IP, Rodriguez F. 1967. Persulfate-initiated polymerisation of acrylamide. Journal of Polymer Science Part A-1: Polymer Chemistry 5:3151-3165.

Schild H. 1992. Poly(*N*-isopropylacrylamide): Experiment, theory, and application. Progress in Polymer Science 17:163-249.

Shimizu K, Fujita H, Nagamori E. 2010. Oxygen plasma-treated thermoresponsive polymer surfaces for cell sheet engineering. Biotechnology and Bioengineering 106(2):303-310.

Shimizu T, Yamato M, Isoi Y, Akutsu T, Setomaru T, Abe K, Kikuchi A, Umezu M, Okano T. 2002. Fabrication of pulsatile cardiac tissue grafts using a novel 3-dimensional cell sheet manipulation technique and temperature-responsive cell culture surfaces. Circulation Research 90:40-48.

Tibbitt MW, Anseth KS. 2009. Hydrogels as extracellular matrix mimics for 3D cell culture. Biotechnology and Bioengineering 103(4):665-663.

Toshiyuki K, and Midori I; 2006. Cell separation and collection apparatus and separation and collection method. United States patent PCT/JP03/16170.

Tressaud A, Durand E, Labrugére C, Kharitonov AP, Kharitonova LN. 2007. Modification of surface properties of carbon-based and polymeric materials through fluorination routes: from fundamental research to industrial applications. Journal of Fluorine Chemistry 128:378–391.

Uyama Y, Kato K, Ikada Y. 1998. Surface modification of polymers by grafting. Advances in Polymer Science 137:1-39.

Volkmer E, Drosse I, Otto S, Stangelmayer A, Stengele M, Kallukalam BC, Mutschler W, Schieker M. 2008. Hypoxia in static and dynamic 3D culture systems for tissue engineering of bone. Tissue Engineering: Part A 14(8):1331-1340.

Wan L-S, Yang Y-F, Tian J, Hu M-X, Xu Z-K. 2009. Construction of comb-like poly(*N*-isopropylacrylamide) layers on microporous polypropylene membrane by surface-initiated atom transfer radical polymerization. Journal of Membrane Science 327:174–181.

Wang X, McCord MG. 2007. Grafting of poly(*N*-isopropylacrylamide) onto nylon and polystyrene surfaces by atmospheric plasma treatment followed with free radical graft copolymerization. Journal of Applied Polymer Science 104:3614-3621.

Ward MA, Georgiou TK. 2011. Thermoresponsive polymers for biomedical applications. Polymers 3:1215-1242.

Wendt D, Riboldi SA, Cioffi M, Martin I. 2009. Potential and bottlenecks of bioreactors in 3D cell culture and tissue manufacturing. Advanced Materials 21:3352–3367.

Woodward NC, Chowdhry BZ, Snowden MJ, Leharne SA, Griffiths PC, Winnington AL. 2003. Calorimetric investigation of the influence of cross-linker concentration on the volume phase transition of Poly(*N*-isopropylacrylamide) colloidal microgels. Langmuir 19:3202-3211.

Xinqiu G, Kunyuan Q, Xinde F. 1989. Studies of the initiation mechanism of vinyl polymerisation with the system persulphate/N-alkyl substituted ethylenediamine derivatives. Chinese Journal of Polymer Science 7(2):165-173.

Xue W, Hamley IW, Huglin MB. 2002. Rapid swelling and deswelling of thermoreversible hydrophobically modified poly(*N*-isopropylacrylamide) hydrogels prepared by freezing polymerisation. Polymer 43:5181-5186.

Yamada N, Okano T, Sakai H, Karikusa F, Sawasaki Y, Sakurai Y. 1990. Thermo-responsive polymeric surfaces, control of attachment and detachment of cultured cells. Makromolekulare Chemie, Rapid Communications 11:571–576.

Yamato M, Akiyama Y, Kobayashi J, Yang J, Kikuchi A, Okano T. 2007. Temperature-responsive cell culture surfaces for regenerative medicine with cell sheet engineering. Progress in Polymer Science 32:1123–1133

Yamato M, Okano T. 2004. Cell sheet engineering. Materials Today 42-47.

Yamato M, Okuhara M, Karikusa F, Kikuchi A, Sakurai Y, Okano T. 1999. Signal transduction and cytoskeletal reorganization are required for cell detachment from cell culture surfaces grafted with a temperature-responsive polymer. Journal of Biomedical Materials Research 44(1):44-52.

Yang J, Yamato M, Kohno C, Nishimoto A, Sekine H, Fukai F, Okano T. 2005. Cell sheet engineering: Recreating tissues without biodegradable scaffolds. Biomaterials 26:6415–6422.

Ye H, Das DB, Triffitt JT, Cui Z. 2006. Modelling nutrient transport in hollow fibre membrane bioreactors for growing three-dimensional bone tissue. Journal of Membrane Science 272:169-178.

Zhang X, Zhuo R, Yang Y. 2002a. Using mixed solvent to synthesize temperature sensitive poly(*N*-isopropylacrylamide) gel with rapid dynamics properties. Biomaterials 23:1313-1318.

Zhang XZ, Chu CC, Zhuo RX. 2005. Using hydrophobic additive as pore-forming agent to prepare macroporous PNIPAAm hydrogels. Journal of Polymer Science: Part A: Polymer Chemistry 43:5490–5497.

Zhang XZ, Wang FJ, Chu CC. 2003a. Thermoresponsive hydrogel with rapid response dynamics. Journal of Materials science: Materials in medicine 14:451-455.

Zhang XZ, Wu DQ, Chu CC. 2003b. Effect of the crosslinking level on the properties of temperature-sensitive poly(*N*-isopropylacrylamide) hydrogels. Journal of Polymer Science: Part B: Polymer Physics 41:582–593

Zhang XZ, Xu XD, Cheng SX, Zhuo RX. 2008. Strategies to improve the response rate of thermosensitive PNIPAAm hydrogels. Soft Matter 4:385–391.

Zhang XZ, Yang YY, Chung TS. 2002b. Effect of mixed solvents on characteristics of Poly(*N*-isopropylacrylamide) gel. Langmuir 18:2538-2542.

ZellWerk. 2012. Z®RP Technology - Competence in cell culture and tissue engineering Rev 103. Zellwerk GmbH. Available online: http://www.zellwerk.biz/image_en.pdf, Date accessed 15 April 2012.

Zhao J, Geuskens G. 1999. Surface modification of polymers VI. Thermal and radiochemical grafting of acrylamide on polyethylene and polystyrene. European Polymer Journal 35:2115-2123.

CHAPTER 3

Instrumentation & Characterisation

3.1 Introduction

This chapter deals with the principles of the main analytical techniques used in this study which includes:

- Ultraviolet-visible (UV-VIS) spectroscopy
- Attenuated total reflectance Fourier Transform Infrared spectroscopy (ATR-FTIR)
- X-ray photoelectron (XPS) spectroscopy
- X-ray diffraction (XRD) analysis
- Electron spin resonance (ESR) spectroscopy
- Scanning electron microscopy (SEM)
- Contact angle measurements
- Differential scanning calorimetry (DSC)
- Dynamic mechanical testing

The parameters and experimental conditions used for each instrument will be described in the relevant sections (refer to **Chapters 4-5**).

3.2 Chemical characterisation

In this study spectroscopic analyses were used to study the chemical properties of the PNIPAAm scaffolds. Spectroscopy refers to the study of matter and its interaction with electromagnetic radiation. The electromagnetic spectrum is the range of all possible electromagnetic radiation which is comprised of gamma rays, X-rays; ultraviolet; visible; infra-red; microwave; and radio waves (**Figure 3.1**). The electromagnetic spectrum of a molecule or object will display the characteristic radiation either absorbed or emitted by that particular molecule. Electromagnetic waves are typically expressed by three physical properties i.e. frequency, wavelength or photon energy as expressed in **Equation 3.1**.

$$E = h\nu\,,\ \text{where}\ \nu = c/\lambda \qquad \text{(Eq 3.1)}$$

Where E is the photon energy, h is planks constant, ν is the frequency, c is the speed of light in a vacuum, and λ is the wavelength of light.

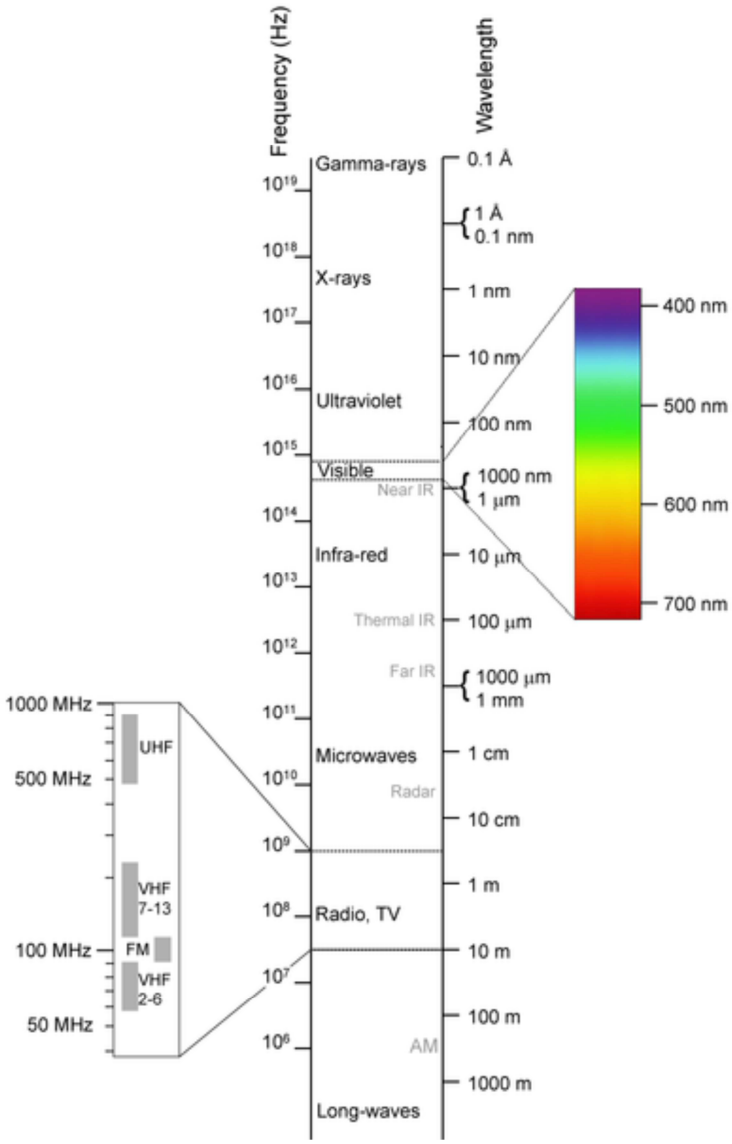

Figure 3.1: Electromagnetic spectrum (Wikipedia, 2012a).

The wavenumber (cm^{-1}) is inversely proportional to wavelength. Gamma rays occur at shortest wavelength and display the highest energy. In this study, infra-red, ultraviolet-visible, X-rays, and microwaves have been used to study the chemical structure of the PNIPAAm scaffolds.

3.2.1 UV-VIS

Ultraviolet-visible (UV-VIS) spectroscopy measures the absorption of materials in the UV-VIS region (180-800 nm). Every molecule possesses a unique series of closely spaced energy levels, the lowest of which is known as the ground state. When a photon of radiation passes near a molecule with energy equal to the energy difference between the ground state and a higher electronic state, the energy of the

photon is absorbed by the molecule as shown in **Equation 3.2**. This results in an energy transfer from the ground state to the higher excited energy state as follows;

$$M + h\nu \longrightarrow M^{*} \qquad \text{(Eq. 3.2)}$$

Whereby a species M is converted to its excited state M^{*} by the absorption of a photon hν. These transitions are responsible for the UV-visible spectra observed for molecules. This process of absorption occurs in a brief period (10^{-6} – 10^{-9} seconds) and is specific to a characteristic molecule (Skoog et al., 1996).

The basic spectrophotometer consists of five main components. These include an energy source, a monochromator, a sample cell (and reference cell), a detector and a readout device (**Figure 3.2**). Radiation from the source first passes to the monochromator, which consists of gratings or prisms that permits isolation of a specific wavelength region. The monochromatic beam is then split into two, one passing through the absorbing sample, while the other passes through a reference cell. The reference cell contains the blank, which is essentially the solvent that has no analyte element. The difference between the two signals is determined electronically and displayed on a screen by the readout device.

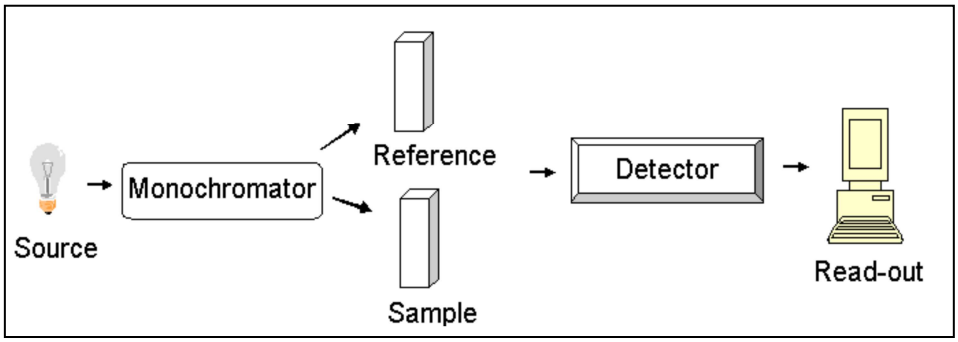

Figure 3.2: Schematic diagram of a typical absorption spectrometer.

Absorption of the analyte can be related to the concentration by the Beer-Lamberts law given by **Equation 3.3** (Skoog et al., 1996):

$$A = \varepsilon bc \qquad \text{(Eq. 3.3)}$$

Where A is absorbance, ε is the absorptivity, b is the path-length through the medium; and c is the concentration. Electrons which are easily excited by UV-VIS radiation involve those that are localised around atoms such as oxygen; sulphur; nitrogen; and halogens (Skoog et al., 1996). Some of the functional groups which typically absorb in the UV-VIS region include aromatic rings, double and triple bonds (C=C, C=O, COOH; N=N), and saturated organic compounds containing heteroatoms (incl. alcohols, ethers, halogenated compounds etc.).

3.2.2 ATR-FTIR

Fourier transform infrared (FTIR) spectroscopy is used to measure the vibration of a molecule which is a unique physical property of a molecule (Coates, 2000). IR occurs between the visible and microwave radiation. IR waves spans from the near-IR (13 000-4000 cm^{-1}); mid-IR (4000-400 cm^{-1}) and far-IR (400-10 cm^{-1}). The mid-IR region is typically used for FTIR spectroscopy. Since molecules have bonds that are continuously moving, bond vibrations can occur on adsorption of IR which include stretching (symmetric or asymmetric), and bending. In this study attenuated total reflectance Fourier transform infrared (ATR-FTIR) spectroscopy was used, which is based on internal reflectance enabling surface analysis of samples.

IR spectra is a fingerprint for identification of molecules since specific structural features in a molecule produce reproducible and characteristic adsorption spectra (Coates, 2000). The fundamental requirement for infrared activity, is that there must be a net change in dipole moment during the vibration (Coates, 2000). Hence highly polar groups (e.g. O-H, N-H) produce strong peaks in the IR region. The vibrational frequency of a molecule is given by Hookes law by **Equation 3.4**:

$$\nu = \frac{1}{2\pi c}\sqrt{k/\mu} \qquad \text{(Eq. 3.4)}$$

Where ν is the fundamental vibration frequency; k is the force constant, μ is the reduced mass which is given as $\mu = m_1 * m_2/(m_1+m_2)$,where m_1 and m_2 are the component masses for the chemical bond under consideration (Coates, 2000). Hence it stands to reason that the higher the bond strength between two atoms the higher the frequency of absorption (i.e. absorption occurs at higher wavenumbers), while the larger the masses of the atoms contained in the bond, the smaller is the wavenumber of absorption. However other factors also contribute to the vibrational

frequencies of bonds such as attraction and repulsion of the electron cloud, the bond length etc., which is not accounted for above. The adsorption intensity is dependent on the electronegativity difference between the atoms in the bond, and the number of specific bonds present.

In the FTIR technique, a polychromatic light source is used (containing light of various wavelengths) which is collimated and directed to a beam-splitter. About 50% of the light is reflected towards the fixed mirror and 50% is transmitted towards the moving mirror, after which the beams recombine to create an interferogram, and 50% of the original light then passes into the sample compartment. ATR-FTIR (**Figure 3.3**) operates by using an ATR crystal onto which the sample is placed, and the technique measures the changes that occur in a totally internally reflected infrared beam when the beam comes into contact with a sample.

Figure 3.3: Image showing an ATR-FTIR instrument.

In the ATR-FTIR technique, a beam of IR light passes through the crystal such that the light reflects of the internal surface of the crystal which is in contact with the sample (**Figure 3.4**). This creates an evanescent wave which then extends into the sample surface. The penetration depth into the sample is typically between 0.5-2 µm and hence surface analysis is possible. An ATR crystal displays a high refractive index and typically includes germanium, zinc selenide, silicon, and diamond. The ATR-FTIR offers an advantage in that solid and liquid samples can be analysed directly without any preparation. The sample absorbs all the different wavelengths characteristic to its spectrum, and the emitted light is then directed to the detector

which measures variation in energy with time at the different wavelengths. A mathematical model called a Fourier Transform is used to convert the raw data into intensity vs. wavelength.

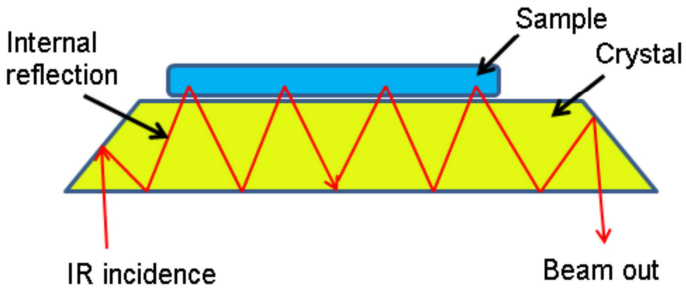

Figure 3.4: Schematic showing working principle of ATR-FTIR.

3.2.3 XPS

X-ray photoelectron spectroscopy (XPS) is used to determine the elemental composition of solid surfaces. During XPS analysis, a sample is placed in an ultrahigh vacuum, and the surface is irradiated with an X-ray source producing photons of a specific energy. Either Al Ka (1486.6 eV) or Mg Ka (1253.6 eV) x-ray sources are used (Torres, 2006). The X-ray photons penetrate the sample to a micrometer depth, hitting the core-1s electrons of the atoms which then emit a core electron leaving an electron vacancy (**Figure 3.5**). A cylindrical mirror analyzer is used to measure the kinetic energy of the emitted electrons.

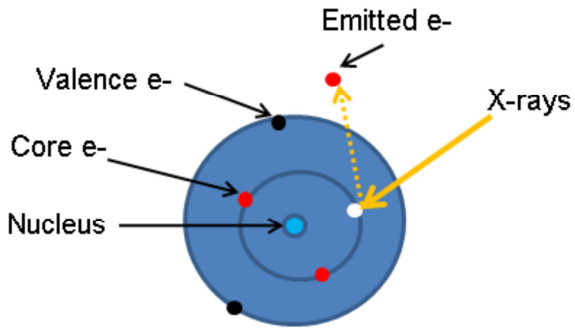

Figure 3.5: Schematic showing interaction between X-rays and an atom during XPS analysis.

The binding energy is determined as given in **Equation 3.5**.

$$KE = hv - BE - \emptyset \quad \text{(Eq 3.5)}$$

Where KE and BE is the kinetic and binding energies respectively, hν is the photon energy from the X-ray source; and ∅ is the spectrometer work function which is found by calibration.

The binding energies of the emitted electrons are plotted and the elements are identified from their binding energy peak positions. Photoelectrons are emitted from a depth of a few nanometers enabling surface analysis of materials. XPS of most elements can be measured with the exception of H_{1s} and He_{1s} where their diatomic mass is too small to enable release of core shell electrons.

3.2.4 XRD

X-ray diffraction (XRD) is a technique used to determine the chemical and crystallographic properties of solids. Solid matter is generally classified as either amorphous or crystalline (or semi-crystalline). In an amorphous material atoms are arranged randomly, while in a crystalline material atoms display a well ordered regular 3D structure.

During X-ray diffraction, electrons from a cathode are accelerated under high voltages (45-50 kV) and strike a metal anode surface which generates X-rays. Copper metal is commonly used as the anode material, and was also used in this study. When the generated X-rays impinge on the solid sample, the X-rays are scattered by the electrons contained in the atoms of the crystal lattice. The scattered X-rays produce secondary spherical waves known as elastic scattering which undergo destructive interference. However if the atoms are arranged symmetrically, the secondary waves add constructively in a few specific directions determined by Braggs law (**Figure 3.6**).

According to Braggs law, the X-rays scattered from adjacent planes will combine constructively only when the angle θ between the plane and the X-ray results in a path-length difference (2 d sinθ) that is equal to an integer multiple of the X-ray wavelength as shown in **Equation 3.6** (Wikipedia, 2012d).

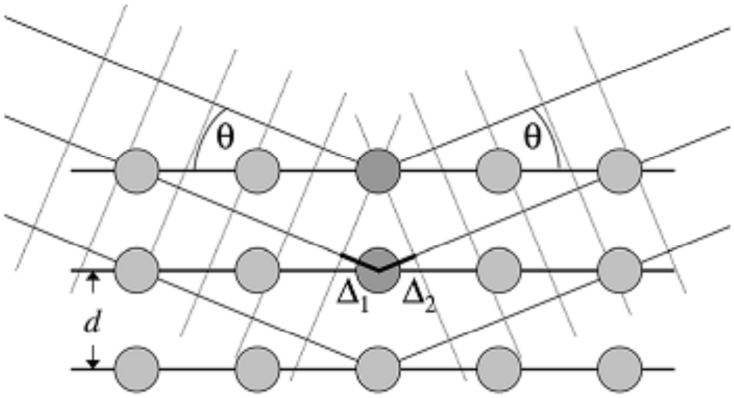

Figure 3.6: Principle of Braggs law for X-ray diffraction (Birkholz, 2006).

This causes the incoming beam to be deflected which produces a diffraction pattern.

$$n\lambda = 2d\sin\theta \qquad \text{(Eq 3.6)}$$

Where d is the spacing between diffracting planes, θ is the incident angle, n is any integer, and λ is the wavelength of the beam (Wikipedia, 2012d). X-rays are used to produce a diffraction pattern since the monochromatic wavelength is typically of the same magnitude (0.1-10 nm) as the d-spacing in the crystal lattice (Wikipedia, 2012d).

The diffraction pattern is due to the specific d-spacing in the crystalline solid, and since the d-spacing pattern is unique for every crystalline solid, the diffraction pattern produces a finger-print for the specific solid. Due to the regular periodic structures in crystalline solids, strong signals are observed whose intensity increases with an increase in the crystal plane electrons (Wikipedia, 2012d). Amorphous structures on the other hand have reduced signal intensities due to the random orientation. Less crystalline structures are detected by a broadening in the peak bands.

When the sample is placed at a short distance from the detector the diffraction maxima appear at $\theta > 5°$ and the XRD technique is referred to as wide angle X-ray scattering (WAXS). Alternatively for small-angle X-ray scattering (SAXS), the distance between the sample and the detector is larger and thus diffraction maxima occur at smaller angles with θ close to zero (Wikipedia, 2012e).

3.2.5 ESR

Electron spin resonance (ESR) which is also known as electron paramagnetic resonance is a technique used to study the interaction of an external magnetic field with an unpaired electron in a species (Bovet, 2009). ESR is an important tool which is commonly used for investigating free radicals formed in solid materials.

ESR is based on the fact that electrons are charged particles which display a spin. When an unpaired electron is placed in a magnetic field, the spin state of the electron is lifted, creating two spin states i.e. m_s = +1/2) or m_s = -1/2, whereby the latter represents the lower energy field which is aligned with the magnetic field (**Figure.3.7**).

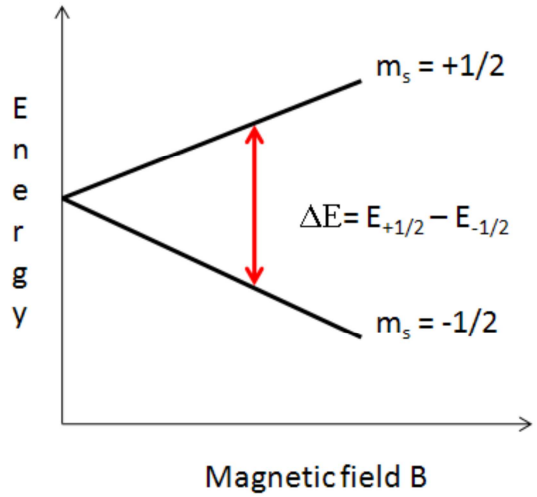

Figure 3.7: Schematic of a single electron spin during the presence of an external magnetic field.

However when electromagnetic radiation in the microwave range is applied spin transitions can occur between the two spin states (Bovet, 2009). The energy difference between the two states (ΔE) is given by **Equation 3.7** (Bovet, 2009):

$$\Delta E = E_{+} - E_{-} = g\beta B = h\nu \qquad \text{(Eq 3.7)}$$

Where β is the Bohr magneton (9.274 x 10^{-24} J T^{-1}), B is the strength of the magnetic field in Tesla, g is known as the g-factor, h is Planck's constant (6.626 x 10^{-34} J s^{-1}),

and ν is the frequency of radiation. The g-factor refers to the intrinsic magnetic moment of the electron, and the g-factor for a free electron is 2.0023 (Bovet, 2009).

When microwave radiation is applied at a frequency corresponding to ΔE, resonance occurs i.e. absorption of the electromagnetic radiation occurs, which is the principle of ESR (Simovič, 2004). ESR spectra are generally presented as the first derivative of the absorption spectra for ease of interpretation (Bovet, 2009).

3.3 SEM

Scanning electron microscopy (SEM) enables observation and characterisation of materials in 3D on a micrometer to nanometer scale. The resolution of a SEM ranges from 1-20 nm, enabling very small features to be detected which are not possible by a light microscope or the naked eye. SEM uses electrons to form a virtual image of a sample rather than a real image which is the case with an optical microscope.

The main component of a SEM is the electron gun which is located at the top of the electron column, a sample chamber which is operated under vacuum, a detector, and a viewing system (**Figure 3.8**) (Philips Electron Optics, 1996).

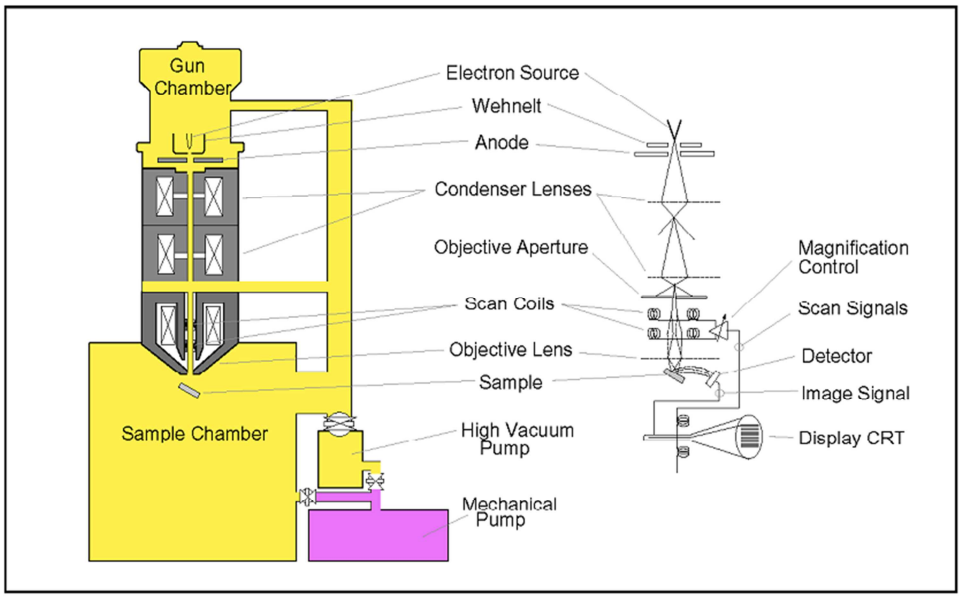

Figure 3.8 : Schematic representation of a SEM (Philips Electron Optics, 1996).

The basic principal of operation includes the following: an electron beam is generated by the electron gun which is accelerated in the electron column at high voltages, and

focused onto the sample surface. The beam is deflected in a scanning pattern over the sample, and interaction between the electron beam with atoms at or near the sample surface generates a variety of signals including: secondary electrons, back-scattered electrons, characteristic X-rays, etc. (Philips Electron Optics, 1996). Various detectors are available for detection of the different signals. Secondary electrons are of very low energy (<50 eV), and escape from the outermost surface of a sample, thereby offering the best imaging resolution (Philips Electron Optics, 1996). X-rays may also be detected in a SEM equipped with energy-dispersive X-ray spectroscopy which enables both qualitative and quantitative data to be obtained regarding the surface elemental composition (Wikipedia, 2012b).

For SEM analysis, samples must be electrically conducting to prevent the accumulation of electric charge at the surface. Metals are therefore easily imaged using SEM without requiring special preparation. However non-conducting materials (such as most polymers) tend to charge when scanned by the electron beams making imaging difficult. Non-conducting material are normally coated with an ultrathin layer of an electrically conducting material (such as gold, palladium, tungsten or graphite,) by sputter-coating prior to imaging.

While the conventional SEM offer many advantages over optical microscopy some of the constraints include the use of a high vacuum, conductive coating on material which can hide small surface features, as well as the need for drying samples prior to imaging. Biological samples are normally fixated in glutaraldehyde prior to imaging.

An advancement to the conventional SEM is the Environmental SEM (ESEM) which allows wet samples to be imaged under low vacuum by the use of a secondary-electron detector(Wikipedia, 2012b). ESEM is particularly attractive for biological and non-metallic samples, since no sample preparation is required.

3.4 Contact Angle

The contact angle of a liquid on a solid surface is a very useful property to quantify wetting, hydrophilicity, and to determine the interfacial free energy of a material. Contact angle is conventionally measured using a contact angle goniometer (**Figure 3.9**), and it is determined as the angle at which the liquid/vapour interface meets the solid surface.

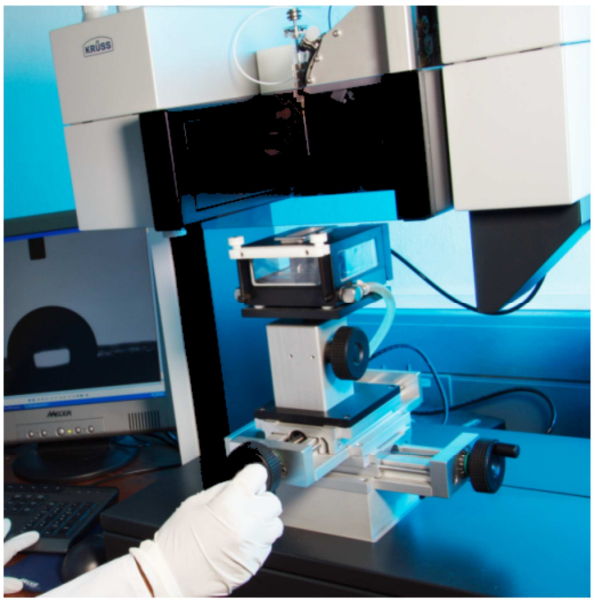

Figure 3.9: Image showing a contact angle goniometer.

The shape of a liquid/vapour interface can be determined by the Young-Laplace equation given by **Equation 3.8** (Goss, 2010):

$$\mathrm{Cos}\theta = \frac{\sigma_{SV} - \sigma_{SL}}{\sigma_{LV}} \qquad \text{(Eq. 3.8)}$$

Where $\sigma_{SV,}$ $\sigma_{SL,}$ and σ_{LV} are the interfacial surface tensions between solid and vapour, solid and liquid and liquid and vapour respectively (**Figure 3.10**).

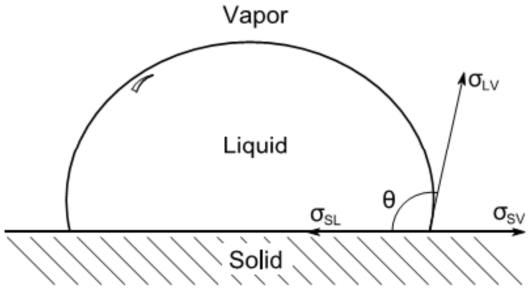

Figure 3.10: Contact angle measurement on a solid surface (Goss, 2010).

If the contact angle is small, a drop will spread on the surface indicating good wetting. If water is used a small contact angle indicates a hydrophilic surface. Conversely, a large water contact angle indicates that the drop remains intact and

beads up, which is typical of a hydrophobic surface. The relationship between contact angle and surface tension/energy is illustrated in **Figure 3.11**.

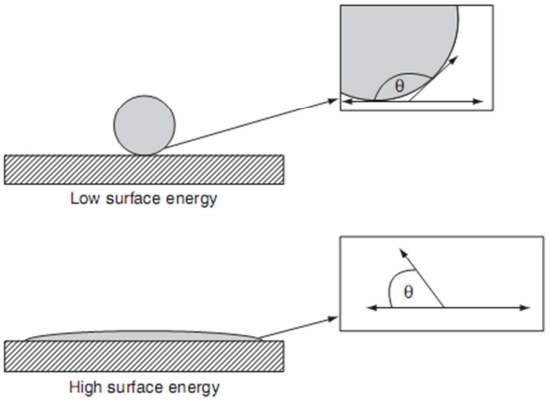

Figure 3.11: Schematic showing relationship between surface energy and contact angle (Goss, 2010).

When the contact angle is low, the surface tension or surface energy of the solid is typically higher than that of the liquid and in order to reduce the interfacial free energy the drop spreads and covers the surface (Hansen, 2000). Conversely for a high contact angle, the surface energy of the solid is typically lower than the liquid, and the drop will remain intact on the surface.

Some of the commonly used methods to determine contact angle include static sessile drop method; dynamic sessile drop method, and dynamic Wilhelmy plate method. In this study the static sessile drop method was used and the contact angle was measured using a contact angle goniometer, and a high-resolution camera was used to capture the image and the contact angle was determined using the DSA 100 software which is based on specific mathematical models.

3.5 DSC

Differential scanning calorimetry (DSC) is a technique used to measure the change in enthalpy (ΔH) or heat flux when a substance undergoes either a physical or a chemical change (Ehrenstein et al., 2004). Enthalpy refers to the amount of heat that is either absorbed or released. Thermal transitions such as melting, evaporation or glass transition are endothermic processes that increase ΔH, while crystallisation,

progressive curing and decomposition are examples of exothermic reactions which are known to decrease ΔH (Ehrenstein et al., 2004).

ΔH is a function of the specific heat capacity (C_p) of a material and change in temperature (dT) as given by **Equation 3.9**.

$$\Delta H = \int C_p . dT \qquad \text{(Eq 3.9)}$$

C_p refers to the amount of energy required to increase the temperature of 1 g of a substance by 1 ℃ at constant pressure (Ehrenstein et al., 2004). Since C_p cannot be easily determined, ΔH is measured by measuring the displacement of heat flux from the baseline. Heat flux $(\dot{Q})$ is the quantity of heat transferred per unit time and mass (m) and is given by Equation 3.10 (Ehrenstein et al., 2004).

$$\frac{\dot{Q}}{m} = v . C_p \qquad \text{(Eq. 3.10)}$$

Where $(\dot{Q})$, m, and v, is the heat flux; mass of the sample; and heating rate respectively.

The principle is based on measuring the difference in heat flow required to keep the sample at the same temperature as the reference (blank pan). During a melting process, the sample absorbs heat (endothermic) as it undergoes melting; hence more heat is required to flow to the sample than the reference to increase their temperature at the same rate. Alternatively during cooling less heat is required, as the material crystallises (exothermic). By measuring this difference in heat flow, the amount of heat absorbed (during heating/melting), or released (during cooling/crystallisation) by the sample can be determined. Both sample and reference (empty pan) are maintained at the same temperature throughout the cycle. The first 10-20 ℃ of the heating cycle compensates for the difference in the sample and reference pans, and transitions in this area are not representative of the sample. Shifts in the melting peak maximum can occur due to the weight of the sample or heating rate, therefore the onset of melting is typically reported.

From the melting and crystallisation peaks, ΔH is calculated as the area under the peak from the peak onset to end-set temperature. The area under the melting peak is

referred to as the heat of fusion ΔH_f which is used to determine the crystallinity of the material.

Two DSC methods are available for measuring heat flux, i.e. Heat flux DSC and power-compensation DSC. For the former, the reference and sample pans are heated together in the same furnace, while for the latter two furnaces are used. In this study a heat flux DSC Q2000 was used. The DSC Q2000 contains the Tzero™ technology, which contains a 3rd thermocouple in the heat flux plate to more accurately account for temperature gradients (Ehrenstein et al., 2004). Tzero™ improves the linearity of the baseline, hence providing more accurate evaluation compared to conventional heat flux DSC's.

3.6 Rheometer

A rheometer is an instrument which is used to measure the rheological properties of a material. Rheology refers to the flow of matter, primarily in the liquid state, but it can also be used to characterise 'soft solids' (e.g. gels, pastes) and/or solids which respond with plastic flow (Wikipedia; 2012c).

In this study a dynamic rheometer was used to characterise the viscoelastic behaviour of materials. An ideally elastic material can be described by Hookes law whereby strain is directly proportional to the applied shear stress and complete recovery of the strain occurs once the applied stress is removed (e.g. rubber) (RheoTec, 2012). Conversely for an ideal viscous material, the constant shear stress leads to a strain which increases linearly over time. If the stress is removed the strain at a particular time will be maintained. However a viscoelastic material displays both elastic and viscous strain whereby partial recovery of the elastic strain is observed while the viscous strain is maintained (RheoTec, 2012). Cross-linked hydrogels display viscoelastic properties.

A parallel-plate model can be used to illustrate the principal of rheology (**Figure 3.12**). The material is placed between the plates whereby the bottom plate is fixed while the top plate is moved with a shear stress and strain.

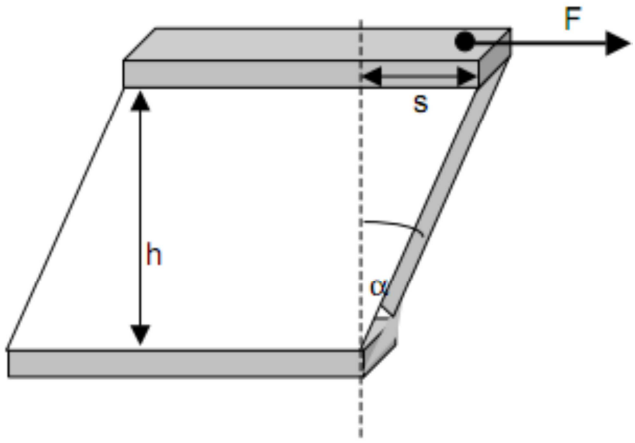

Figure 3.12: Illustration of principal of rheology using parallel-plate model (RheoTec, 2012).

The shear stress (τ) and strain (γ) is described by **Equations 3.11-3.12**.

$$\tau = \frac{F}{A} \quad \text{(Eq 3.11)}$$

$$\gamma = \frac{s}{h} = \tan\alpha \quad \text{(Eq 3.12)}$$

Where F is the applied force, A is the surface area of the plates, s is the distance of displacement, and h is the height between the plates. The complex viscosity of the material (η*) can be determined from τ and shear rate (ẏ) as follows:

$$\eta^* = \frac{\tau}{\dot{y}} \quad \text{(Eq 3.13)}$$

In an ideally elastic material the shear modulus (G) which describes the stiffness or strength of the material is determined as follows:

$$G = \frac{\tau}{\gamma} \quad \text{(Eq 3.14)}$$

However in a viscoelastic material the dynamic complex modulus (G*) is composed of the storage modulus (G′) and loss modulus (G″) as follows: (Anseth et al., 1996):

$$G^* = G' + iG'' \quad \text{(Eq 3.15)}$$

Where G′ is the real (also elastic or storage) modulus and iG″ refers to the imaginary (also viscous or loss) modulus (Anseth et al., 1996). G′ refers to the quantity of energy reversibly stored in the material which is recoverable while G″ refers to the quantity of energy given off or lost. Finally the ratio of G″: G′ describes the damping or dissipation factor (tan δ) (Anseth et al., 1996) (**Equation 3.16**).

$$\text{Tan } \delta = \frac{G''}{G'} \qquad \text{(Eq 3.16)}$$

Tan δ measures the ratio of the energy dissipated as heat to the maximum energy stored in the material during one cycle of oscillation (Anseth et al., 1996).

3.7 References

Anseth KS, Bowman CN, Brannon-Peppas, L. 1996. Review mechanical properties of hydrogels and their experimental determination. Biomaterials 17: 1647-1657.

Birkholz M. 2006. Principles of X-ray diffraction. Thin film analysis by X-ray scattering ISBN: 3-527-31052-5, WILEY-VCH Verlag GmbH & Co. KGaA, Weinheim,

Bovet C, Barron AR. 2009. EPR Spectroscopy: An Overview, http://cnx.org/content/m22370/latest/, Date accessed: 16 August 2012.

Coates J. 2000. Interpretation of infrared spectra, a practical approach. Meyers RA, editor. Chichester: JohnWiley & Sons Ltd. 10815–10837

Ehrenstein GW, Riedel G, Trawiel P. 2004. Thermal analysis of plastics - theory and practice: Hanser Gardner Publications, Inc. 1-26.

Goss B. 2010. Practical guide to adhesive bonding of small engineering plastic and rubber parts: iSmithers Rapra Publishing. 194.

Hansen CM. 2000. Hansen Solubility Parameters : A users handbook: CRC Press LLC. 208.

Philips Electron Optics. 1996. Environmental scanning electron microscope : An introduction to ESEM. Eindhover: Robert Johnson Associates.

RheoTec. Introduction to rheology. Messtechnik GmbH, Ottendorf-Okrilla 2.1E:1-48. http://www.dongjins.com/service/file/Introduction%20to%20rheology, date accessed: 20 August 2012.

Skoog DA, West DM, Holler FJ. 1996. Fundamentals of analytical chemistry: Saunders College Publishing.

Simovič D. 2004. Introduction to the technique of Electron Spin Resonance (ESR) Spectroscopy, Physics Laboratory Course, Available on-line: www. phys. ethz. ch /phys /students /bachelor /vp/VP-Expliste/ESR.pdf, Date accessed: 02 August 2012.

Torres DE. 2006. X-Ray Photoelectron Spectroscopy (XPS), http: //nanohub.org /resources /2109.

Wikipedia. 2012a. Electromagnetic spectrum; http://en.wikipedia.org/wiki/File:Electromagnetic-Spectrum.png. Date accessed 02 August 2012.

Wikipedia. 2012b. Scanning electron microscope; http://en.wikipedia.org/wiki/Scanning_electron_microscope. Date accessed 02 August 2012

Wikipedia. 2012c. Rheology; http://en.wikipedia.org/wiki/Rheology. Date accessed 03 August 2012

Wikipedia. 2012d. X-ray crystallography; http://en.wikipedia.org/wiki/Xray_ crystallography. Date accessed 21 August 2012.

Wikipedia. 2012e. X-ray scattering techniques; http://en.wikipedia.org/wiki/X ray_diffraction. Date accessed 21 August 2012.

CHAPTER 4

Development of P(NIPAAm-*co*-MBA) Hydrogels

Part of work published in EXPRESS Polymer Letters

4.1 Introduction

Poly-*N*-isopropylacrylamide (PNIPAAm) is one of the most extensively studied thermoresponsive polymer in the literature due to its remarkable volumetric phase transition properties. PNIPAAm rapidly and reversibly switches between the hydrophobic and hydrophilic states at temperatures above and below the lower critical solution temperature (LCST) (~32 °C) respectively. The main driving force for the LCST of PNIPAAm is said to be entropy of the system due to water-water interactions above the LCST. PNIPAAm is particularly attractive for biological applications, since the polymer is water-soluble, it is biocompatible, and the phase transition can be easily triggered between ambient temperature and body temperature. This unique behaviour has attracted widespread attention and many applications of PNIPAAm are being investigated which include thermo-responsive membranes, reversible immobilization of bio macromolecules, *in vitro* cell culture, separation of molecules from aqueous mixtures, and drug delivery.

Despite the favourable properties of PNIPAAm these smart polymeric hydrogels display two major limitations, i.e. poor mechanical properties and slow response time to temperature changes (Zhang et al., 2008). The slow response rate of monolithic PNIPAAm hydrogels to temperature is believed to be due to the formation of a dense skin layer which forms as a result of the strong hydrophobic interactions existing among the isopropyl groups in the PNIPAAm molecule, which retards the outward diffusion of water molecules above the LCST. Additionally, the swelling rate of the hydrogel at the temperatures below LCST is even slower (Zhang et al., 2008). Bulk PNIPAAm hydrogels may not be applicable for a range of practical applications where more robust response are required such as in cell-culture, drug delivery, and on-off switches.

The focus of many studies in recent years has therefore been on improving the mechanical properties and response rate of PNIPAAm hydrogels. Some of the strategies which are being investigated include cross-linking; synthesis of a heterogeneous hydrogel structure using mixed solvents; the use of porogens (e.g. polyethylene glycol); the use of hydrophilic co-polymers to increase hydrogen bonding; and cold polymerisation (to create a porous structure) amongst others (Zhang et al., 2008).

Chemical cross-linking is one of the simplest and most versatile tools for controlling the mechanical properties and response rate of hydrogels (Geever et al., 2007). It is well-known that chemical cross-linking can be used to increase the mechanical stability of hydrogels (Geever et al., 2007). However excessive cross-linking may compromise the swelling properties and open interconnected structures of hydrogels (Caykara et al., 2006a). Hence an optimum level of cross-linking is desired to achieve good mechanical properties and a fast response while also maintaining the LCST of the hydrogel.

The most common method for synthesising PNIPAAm hydrogels is by copolymerising NIPAAm with N,N'-methylenebisacrylamide (MBA) to produce P(NIPAAm-*co*-N,N'-methylenebisacrylamide) (P(NIPAAm-*co*-MBA)). MBA serves as the cross-linker, and ammonium persulphate (APS) and N,N,N',N'-tetramethylethylenediamine (TEMED) are commonly used the redox initiator pair.

In this study the cross-link density (R) of the hydrogels is expressed as a molar ratio of monomer to cross-linker as follows:

$$\mathrm{R} = \frac{\mathrm{nMoles\ monomer}}{\mathrm{nMoles\ crosslinker}} \qquad \text{(Eq 4.1)}$$

In the literature, various cross-link densities have been reported for P(NIPAAm-*co*-MBA) hydrogels. However cross-link densities investigated have typically being rather low ranging between R 500-50 (i.e. < 2 Mol% MBA) (Caykara et al., 2006b; DeRosa et al., 2007; Liang et al., 2000; Zhang et al., 2002b). It is known that for a number of applications PNIPAAm hydrogels with improved stability and mechanical strength are required.

Also the viscoelastic behaviour of PNIPAAm hydrogels has not been widely reported. Mechanical properties of PNIPAAm and other hydrogels have typically being investigated under stress-strain or tension/compression studies (Muniz and Geuskens, 2001; Takigawa et al., 1997). Rheology however has not been widely investigated for PNIPAAm hydrogels. Rheology provides information about the strength, relaxation and viscoelastic properties of gels, while providing a very accurate determination of the LCST.

In this study P(NIPAAm-*co*-MBA) hydrogels were synthesised for assessment of its physical and mechanical properties. The cross-link density of the hydrogels was varied from R 90-10 (1.1-9.1 MBA Mol%) and the use of mixed solvent : water systems were investigated as the co-polymerisation medium. The LCST, swelling, de-swelling behaviour, morphology, contact angle and viscoelastic properties of the P(NIPAAm-*co*-MBA) hydrogels are reported.

4.2 Experimental

4.2.1 Materials

N-isopropylacrylamide (NIPAAm, 97% purity), N,N'-methylenebisacrylamide (MBA, 99% purity) and ammonium persulphate (APS >98%, ACS reagent) were obtained from Sigma Aldrich and used as received. N,N,N',N'-tetramethylethylenediamine (TEMED) was obtained from Merck. High purity analytical grade tetrahydrofuran and acetone were used. Water was purified by the use of reverse osmosis UV ultra-purification water system.

4.2.2 Synthesis of P(NIPAAm-*co*-MBA) hydrogels

4.2.2.1 Preparation of standard P(NIPAAm-*co*-MBA) hydrogels

P(NIPAAm-*co*-MBA) hydrogels were synthesised by *in situ* free radical polymerisation of NIPAAm using MBA as the cross-linker agent, and APS and TEMED as the redox initiators as shown in **Scheme 4.1** (Zhang et al., 2003). A 10% (w/v) aqueous stock solution of NIPAAm was prepared by dissolving 10 g of NIPAAm in 100 ml of water in a volumetric flask with magnetic stirring. A 10 wt% APS solution was freshly prepared by dissolving 1 g of APS in 10 ml of deionised water. For the standard formulation (R 90), 1.5 wt% MBA in the monomer feed, and 2 wt% each APS and TEMED, was used based on the NIPAAm mass.

Briefly 10 ml of the 10 wt% NIPAAm solution was pipetted into a glass reaction vessel. 0.015 g of MBA was added to the mixture and stirred until dissolved. Thereafter 25.8 µl of TEMED was added and stirred until homogenised. The vessel was then inserted in an ice-bath at 5 ℃ and the so lution was left to pre-cool for 5 minutes. The APS solution was also placed in the ice-bath to cool. Thereafter 200 µl of a pre-cooled 10% (w/v) APS solution was added to the NIPAAm solution to initiate

polymerisation. Polymerisation was conducted at 5 ºC for 30 minutes and thereafter the solution was left to polymerise at ambient temperature of 23 ℃ for 24 hours.

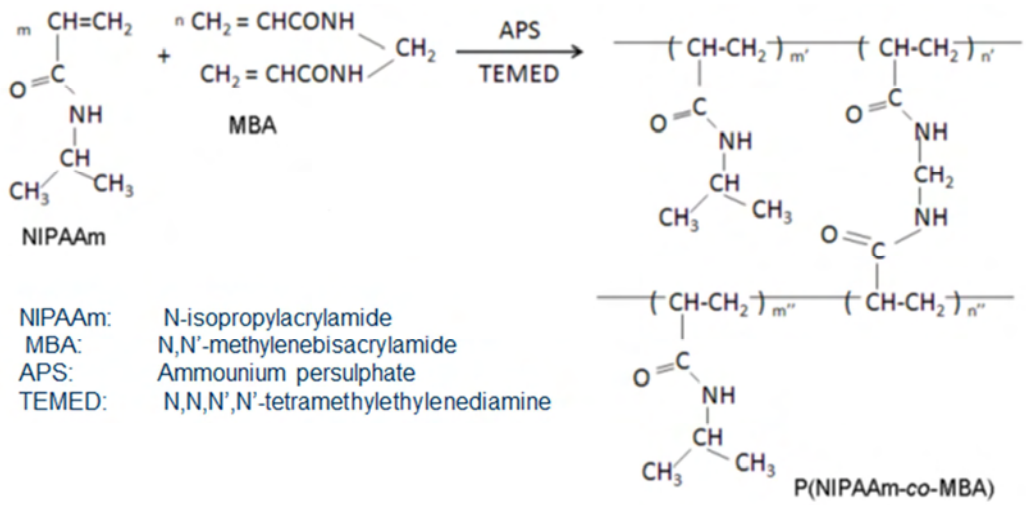

Scheme 4.1: Synthesis scheme of PNIPAAm hydrogels by free radical polymerisation using MBA as the cross-linker and APS and TEMED as the redox initiators (where m = m' + m'' and refers to the NIPAAm units, while n= n' +n'' and refers to the MBA units) (Zhang et al., 2003).

After polymerisation, the hydrogels were leached in cold deionised water for several days to remove any unreacted monomers. Residual contaminants in the water washes were monitored from 190-250 nm using a UV-VIS spectrophotometer.

4.2.2.2 Varying cross-link density

P(NIPAAm-*co*-MBA) hydrogels were prepared as detailed above, except the cross-link density was varied between R 90-10. R was determined as the molar ratio of NIPAAm to MBA. The feed composition of the P(NIPAAm-*co*-MBA) hydrogels is given in **Table 4.1**.

4.2.2.3 Use of mixed solvents

To increase porosity and improve the swelling rate of the P(NIPAAm-*co*-MBA) gels, mixed solvent systems were used as the co-polymerisation medium. The hydrogels were prepared as described in **Section 4.2.2.1** but instead of using water, acetone:water and tetrahydrofuran (THF) : water mixtures were used (Zhang et al., 2002a; Zhang et al., 2002b) (**Table 4.2**).

Table 4.1: Feed composition of cross-linked P(NIPAAm-*co*-MBA) hydrogels.

Gel No.	R	NIPAAm Mol %	MBA Mol %	MBA wt % in the monomer feed
1*	90	98.9	1.1	1.5
2	70	98.6	1.4	1.9
3	50	98.0	2.0	2.7
4	30	96.8	3.2	4.3
5	10	90.9	9.1	12.0

(*Gel 1 represents the standard formulation)

Table 4.2: Solvent:water mixtures used during co-polymerisation with R 90.

Gel No.	Solvent	Solvent : water Vol%
6	Acetone	30:70
7	Acetone	50:50
8	THF	30:70
9	THF	50:50

4.2.3 Characterisation of P(NIPAAm-*co*-MBA) hydrogels

4.2.3.1 Differential scanning calorimetry

A Perkin Elmer Differential Scanning Calorimeter (DSC 7) was used to determine the LCST of the PNIPAAm hydrogels. The cross-linked gels were swollen in water to equilibrium prior to analysis. The temperature range analysed was 5 to 60 ℃ using a scan rate of 5 ℃/min, with a nitrogen purge rate of 40 ml/min. The LCST was taken at the onset to the peak maximum.

4.2.3.2 Swelling

After polymerisation, hydrogels were carefully cut into 1.5 cm disks. The equilibrium gravimetric swelling ratios of the hydrogels were determined by equilibrating the gel pieces in deionised water at room temperature (20 ºC) for 24 hours. The swelling ratios (SR) of the P(NIPAAm-*co*-MBA) gels were calculated as follows:

$$\text{Swelling ratio} = \frac{W_w - W_d}{W_d} \quad \text{(Eq. 4.2)}$$

where Ww is the wet weight of the gel and Wd is the weight of the xerogel (dried gel). When measuring the wet weight of the gels, gel pieces were gently placed between two filter papers to remove the excess surface water, and the wet gels were weighed. Deswelling kinetics of the gels was performed gravimetrically by placing fully swollen gels in the oven at 37 ºC. Gels were weighed at following time intervals i.e. 0, 10, 20, 30, 45, 60, and 90 minutes. The percent water retention was determined as follows:

$$\%\ \text{water uptake or}\ \%\ \text{water retention} = \frac{W_w - W_d}{W_s - W_d} * 100 \quad \text{(Eq. 4.3)}$$

Where W_s is the weight of the fully swollen gel.

4.2.3.3 Environmental scanning electron microscopy (ESEM)

ESEM analysis was conducted by Prof Burton at the Centre for Electron Microscopy at the University of Kwazulu Natal in Pietermaritzburg. Analysis involved incubating polymerised gels in water at ambient temperature until fully equilibrated. Samples were then imaged using an environmental scanning electron microscope without any sample preparation. When samples were viewed at 25 ℃, a CP+ aperture holder under low vacuum mode with LFD at 1 torr. At 37 ℃, best images were obtained under wet mode - using a peltier cooling stage with a GSED and a pressure of 4 torr, and relative humidity ~ 8%.

4.2.3.4 Analysis of viscoelastic properties

For determination of the viscoelastic properties of the hydrogels, an Anton Paar UDS 200 rheometer was used with a plate-plate arrangement. The analysis was performed at the Department of Physical Chemistry and Material Science at the Budapest University of Technology and Economics. Shear strain was applied between two parallel plates which were 0.5 mm apart. The dry gel samples were applied to the plate, deionised water was added, and equilibrium swelling was attained. Excess water was wiped with a tissue paper and after the sample thickness was adjusted, excess water was again added to the plate to avoid the loss of water from the sample during the measurements. The average of three samples was taken for each measurement. To determine the linear viscoelastic region a strain of 0.01 –

100% at 10 s^{-1} angular frequency (ω) was applied at 25 ℃. Temperature and frequency sweeps were conducted to obtain the storage modulus (G′), loss modulus (G″), and damping factor (tan δ) of the P(NIPAAm-*co*-MBA) hydrogels. Temperature sweeps were carried out at 25-60 ℃ at 3 ℃/min hea ting rate at 10 s^{-1} ω and 1% strain, while the frequency sweeps were conducted at 25 ℃ and 60 ℃ with ω of 1-100 s^{-1} at 1% strain.

4.2.3.5 Water contact angle

The water contact angle of the PNIPAAm gels (gels 1-5) were measured with a Krüss DSA100 tensiometer. Contact angle measurements were taken at 20 °C, and at 40 °C at 5 second intervals over a 65 second period. Gels were equilibrated in the sample chamber for 30 minutes at the respective temperature prior to analysis. Equilibrated gels were cut into 1x1 cm dimensions, gently wiped with tissue paper to remove excess surface water, and were placed on a stage in a temperature – controlled chamber. A real-time image of the gels was obtained with the Krüss Drop Shape analysis software using the sessile drop type. At each temperature point five analyses were performed.

4.3 Results & discussion

In this study the physical properties of P(NIPAAm-*co*-MBA) hydrogels were investigated by varying the cross-link density of the hydrogels, and by evaluating the use of solvent mixtures as the co-polymerisation medium. The following results will be discussed i.e. mechanism of free radical polymerisation (**Section 4.3.1**); assessment of gel formulations (**Section 4.3.2**); LCST by DSC (**Section 4.3.3**); morphology (**Section 4.3.4**); swelling and de-swelling properties (**Section 4.3.5**), viscoelastic properties (**Section 4.3.6**); and water contact angle (**Section 4.3.7**).

4.3.1 Mechanism for free radical polymerisation

Free radical polymerisation of PNIPAAm hydrogels proceeds via addition polymerisation across the double bond of the vinyl group of the NIPAAm monomer. MBA was used as the cross-linking agent, and APS and TEMED was the redox initiator pair where APS acts as the oxidiser and TEMED is the reducing agent. The

reaction mechanism for the formation of P(NIPAAm-*co*-MBA) is given in **Scheme 4.2.** APS decomposes in the presence of TEMED to produce two free radical species i.e. sulphate ($SO_4^{-\bullet}$) radical ions and hydroxyl ($OH^{\bullet}$) radicals, both of which are capable of initiating polymerisation (Riggs and Rodriguez, 1967). Initiation involves reaction of $SO_4^{-\bullet}$ and $OH^{\bullet}$ free radicals with the NIPAAm monomer (M) and MBA monomer (B) thereby creating the NIPAAm radical ($M^{\bullet}$) and MBA radical ($B^{\bullet}$) respectively.

$$Initiation:$$

$$S_2O_8^{2-} \xrightarrow{TEMED} 2SO_4^{-\bullet}$$

$$SO_4^{-\bullet} + H_2O \longrightarrow HSO_4^{-} + {}^{\bullet}OH$$

$$SO_4^{-\bullet} + M \longrightarrow M^{\bullet}$$

$$SO_4^{-\bullet} + B \longrightarrow B^{\bullet}$$

$${}^{\bullet}OH + M \longrightarrow M^{\bullet}$$

$${}^{\bullet}OH + B \longrightarrow B^{\bullet}$$

$$\mathrm{Pr}opagation:$$

$$M^{\bullet} + nM \xrightarrow{k11} M_{n+1}^{\bullet}$$

$$B_n^{\bullet} + mB \xrightarrow{K21} B_{m+1}^{\bullet}$$

$$Ter\,\mathrm{min}\,ation:$$

$$M_{n+1}^{\bullet} + M_{n+1}^{\bullet} \longrightarrow PNIPAAm$$

$$M_{n+1}^{\bullet} + B_{m+1}^{\bullet} \longrightarrow P(NIPAAm-co-MBA)$$

$$B_{m+1}^{\bullet} + B_{m+1}^{\bullet} \longrightarrow PMBA$$

Scheme 4.2: Mechanism for the synthesis of P(NIPAAm-*co*-MBA) using free-radical polymerisation.

MBA is a very effective cross-linker since it contains two unsaturated bonds in its structure as shown in **Scheme 4.3** which are susceptible to free radical addition.
Chain propagation then pursues whereby the NIPAAm radical attacks another NIPAAm monomer to form a growing NIPAAm macroradical ($M_{n+1}\bullet$). Similarly the MBA radical attacks further MBA monomers to create the MBA macroradical ($B_{n+1}\bullet$). This involves a head-to-tail arrangement (i.e. C2 of NIPAAm radical attaches to C1 of NIPAAm monomer, and C2 or C8 of the MBA radical adds to either C1 or C9 of the MBA monomer). Finally termination occurs when two monomer macroradicals interact to form the stable polymer.

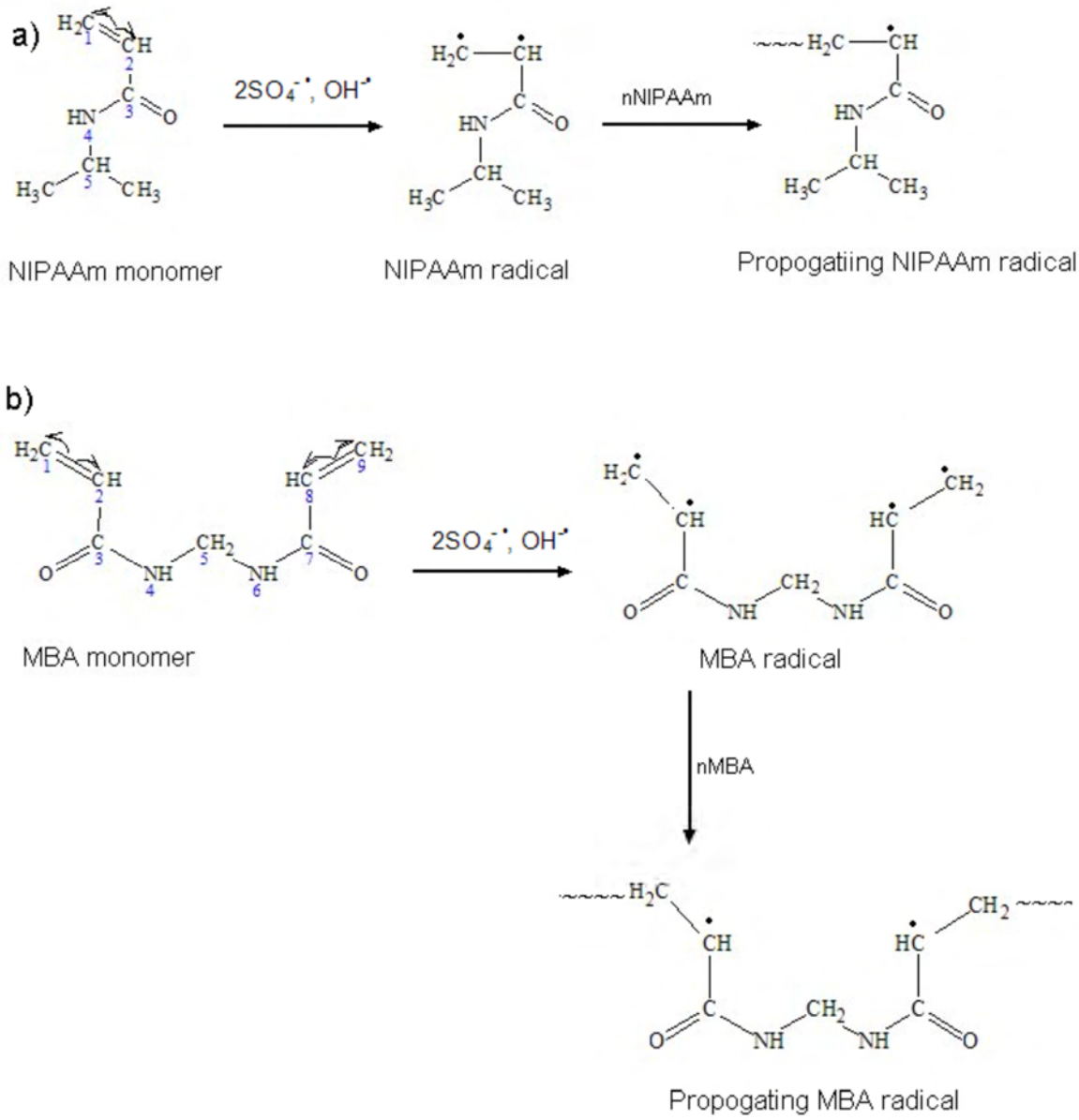

Scheme 4.3: Initiation of a) NIPAAm and b) MBA monomers using APS/TEMED.

In addition to P(NIPAAm-*co*-MBA), PNIPAAm and Poly-N,N'-methylenebisacrylamide (PMBA) can also form as shown in **Scheme 4.2**. The PNIPAAm and PMBA homopolymers were removed by washing the hydrogel in water. The composition of the forming copolymer changes in every picosecond which is known as composition drift. The composition of the final polymer can be determined by the rate constants of the respective reactions, however this was not considered in this study since it was not the subject of this investigation.

4.3.2 Assessment of gel formulations

When water was used as the co-polymerisation medium, P(NIPAAm-*co*-MBA) hydrogels with R 90-30 appeared clear and transparent (**Figure 4.1).** However when the cross-linker content was increased to 9.1 Mol% MBA (R 10), the gel underwent syneresis and appeared opaque following polymerisation.

.

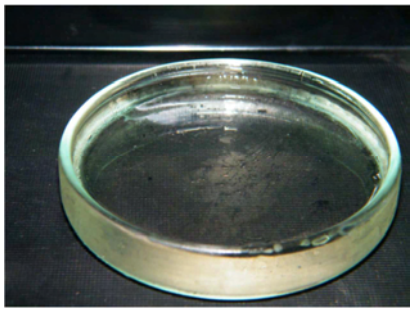

Figure 4.1: Optical image of standard R 90 P(NIPAAm-co-MBA) hydrogel produced by co- polymerisation of NIPAAm and MBA.

It has previously been reported that an increasing cross-linker content increases the degree of inhomogeneities in PNIPAAm hydrogels (Kara et al., 2002). The phase separation in the R 10 gel can be associated with the higher cross-linker content which enhances the reactivity of the reaction. The MBA cross-linker is tetrafunctional and displays a reactivity at least twice that of the NIPAAm due to the presence of two vinyl groups in its structure compared to only one for NIPAAm. The higher rate of reaction for the R 10 gels compared to the R 90-30 gels can result in two plausible effects. Firstly the higher MBA content can result in non-homogenous cross-linking thus resulting in a combination of lightly cross-linked and highly cross-linked domains which results in phase separation of the latter. Secondly the higher MBA content in the R 10 gel can induce a higher heat of polymerisation, resulting in the temperature exceeding the LCST of PNIPAAm during polymerisation, which thereby induces phase separation. This effect however still requires further investigation.Interestingly for both solvent systems the gels were not “transparent” as observed for the standard gel. The 30:70 acetone: water gel, 30:70 THF: water, and 50:50 THF: water gels appeared translucent while the 50:50 acetone: water gel was opaque (**Figure 4.2)**. A summary of the appearance of hydrogels 1-9 appear in **Table 4.3**.

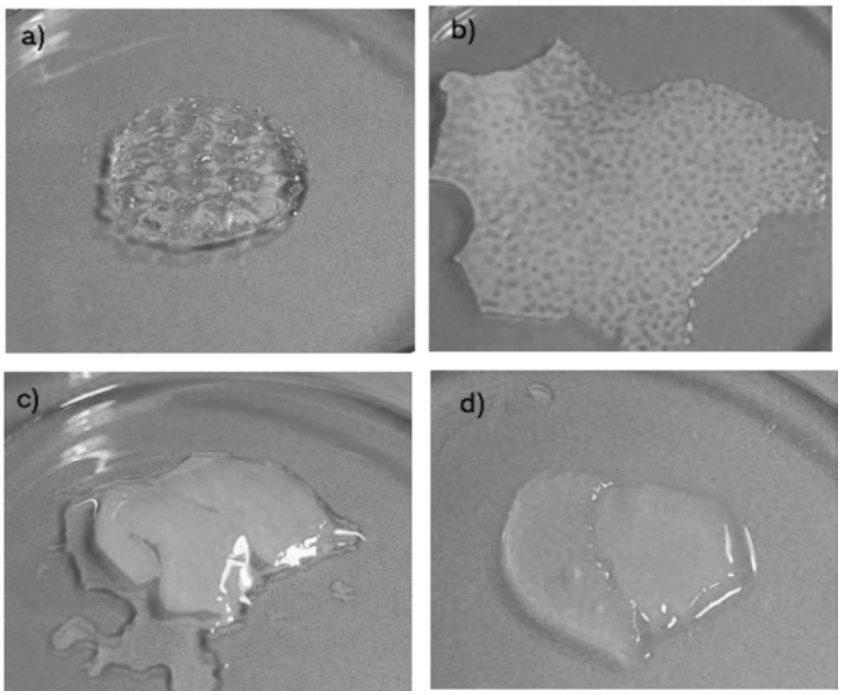

Figure 4.2: PNIPAAm gels prepared by free radical polymerisation using acetone: water and THF: water mixed solvent systems.

Table 4.3: Composition and appearance of gels 1-9 prepared by radical polymerisation.

Gel No.	R	Co-polymerisation medium	Solvent : water Vol%	MBA Mol %	Appearance
1	90	Water	100	1.1	Transparent
2	70	Water	100	1.4	Transparent
3	50	Water	100	2.0	Transparent
4	30	Water	100	3.2	Transparent
5	10	Water	100	9.1	Opaque
6	90	Acetone: water	30:70	1.1	Translucent
7	90	Acetone: water	50:50	1.1	Opaque
8	90	THF: water	30:70	1.1	Translucent
9	90	THF: water	50:50	1.1	Translucent

The phase separation of P(NIPAAm-*co*-MBA) hydrogels co-polymerized in mixed solvents is believed to be due to the co-non-solvency phenomena (Zhang et al., 2008). It is known that some polymers dissolve in pure solvents but are insoluble in their mixtures. PNIPAAm is soluble in water and pure organic solvents such as THF,

acetone, and phenol. However in solvent/water mixtures PNIPAAm solubility is drastically reduced, and the PNIPAAm chains collapse such that two phases form resulting in a heterogeneous structure (Zhang et al., 2008; Zhang et al., 2002b). Zhang *et al* suggested that in a two-phase reaction system, when the polymer chains collapse during polymerization, termination of chain ends are hindered resulting in a higher fraction of dangling chains in the hydrogel, and the effective cross-linking density in the gels are lowered due to the difficulty in cross-linking (Zhang et al., 2002b).

From physical handling, the solvent: water gels were substantially weaker compared to the water series gels. The THF gels showed poorer stability compared to the acetone gels, as they easily broke up even when gently handled. This will represent a significant challenge if for e.g. the hydrogels were to be used for cell culture. Due to the poorer stability of the mixed solvent gels, only DSC and swelling-deswelling studies were conducted using these gels and no other further work was done.

4.3.3 Determination of LCST by DSC

DSC was used to determine the LCST of the P(NIPAAm-*co*-MBA) hydrogels. During heating from 10-60 ℃, all of the hydrogels develop ed an endothermic peak (**Figure 4.3**), which indicates that the hydrogels underwent shrinking upon heating.

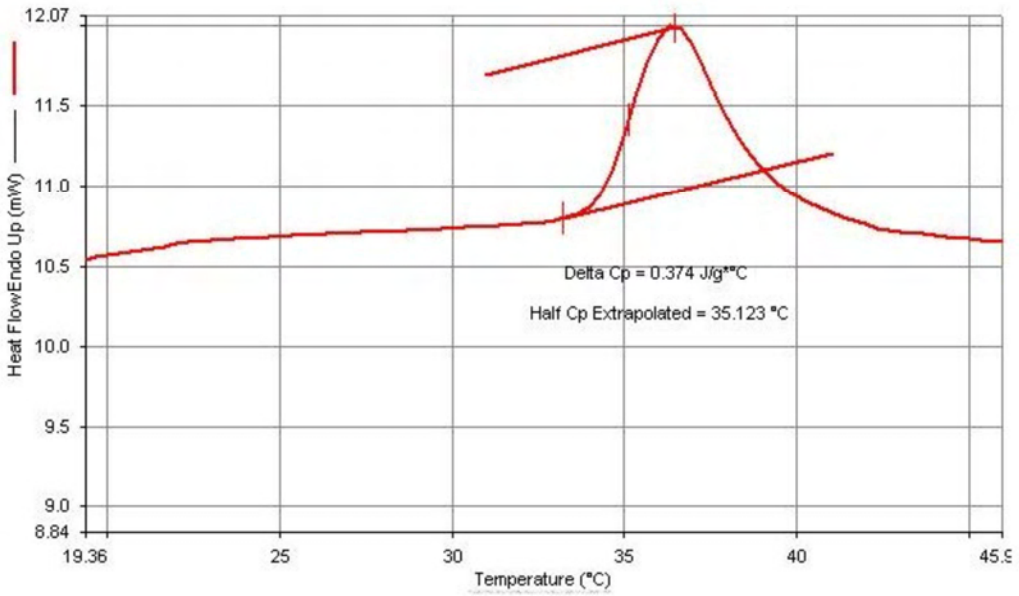

Figure 4.3: Typical DSC thermogram of P(NIPAAm-co-MBA) hydrogel with R 90 showing the LCST (endotherm is down).

The LCST was taken as the onset to the peak maximum and is the point at which the polymer network collapses and water is released. The average LCST's of the P(NIPAAm-*co*-MBA) hydrogels with varying cross-link densities are tabulated in **Table 4.4**. It was found that for all of the water series hydrogels (R 90-10), the LCST varied between 34-35 ℃ and was independent of the cross-linker range investigated (i.e. 1.1-9.1 Mol% MBA). Our findings has been corroborated with other studies reported in the literature (Zhang et al., 2003). It can be concluded that the overall hydrophilicity/hydrophobicity balance of the P(NIPAAm-*co*-MBA) gels was maintained in this MBA range. Even though MBA contains hydrophilic amide groups which would increase polymer-water interaction, in the cross-link range investigated, it can be assumed that the hydrophilic effect is counterbalanced by the additional methylene groups in MBA, which contribute to higher hydrophobic-hydrophobic interactions, thereby balancing the hydrophilic effect of the amide groups. The LCST of all the P(NIPAAm-*co*-MBA) hydrogels was higher than that of linear PNIPAAm (LCST = 32 ºC) indicating that the presence of MBA increased hydrogen bonding with water due to an increase in amide groups.

Table 4.4: Average LCST of P(NIPAAm-*co*-MBA) hydrogels determined by DSC with MBA cross-link density from R 90-10 (i.e. 1.1-9.1 Mol% MBA) (n=5).

R	MBA Mol %	LCST /°C	Copolymerisation medium
90	1.1	34 ± 1	Water
70	1.4	35 ± 1	Water
50	2.0	34 ± 0.4	Water
30	3.2	35 ± 0.9	Water
10	9.1	35 ± 0.4	Water
90	1.1	33.8 ± 0.5	30:70 Acetone: water
90	1.1	32.9 ± 0.3	50:50 Acetone: water
90	1.1	33.4 ± 0.4	30:70 THF:water
90	1.1	33.3 ± 0.3	50:50 THF:water

The LCST's of all the mixed solvent gels was lower than the pure water series gels, and on average ranged between 32-33 ℃. Similar results have also been reported previously for P(NIPAAm-co-MBA) gels with increasing THF:water content (Zhang et al., 2002b). According to Zhang *et a*l. the reduced LCST's for the mixed solvent gels, indicate that freed water diffuses out of the heterogeneous polymer networks more

easily than for the gels made in water (Zhang et al., 2002b). Hence it is expected that the de-swelling of the gels when prepared in the mixed solvents will be faster than for the homogenous standard gels.

For the PNIPAAm water-series hydrogels with R 90-30, the phase transition could be clearly observed visually by placing the hydrogels in an oven at 37 ℃. Upon heating to 37 ℃, the clear transparent hydrogels turned opaque and formed a white precipitate as shown in **Figure 4.4**. For the R 10 gel however which was already opaque at room temperature following polymerisation, and the change could not be visually detected by the naked eye upon heating at 37 ℃.

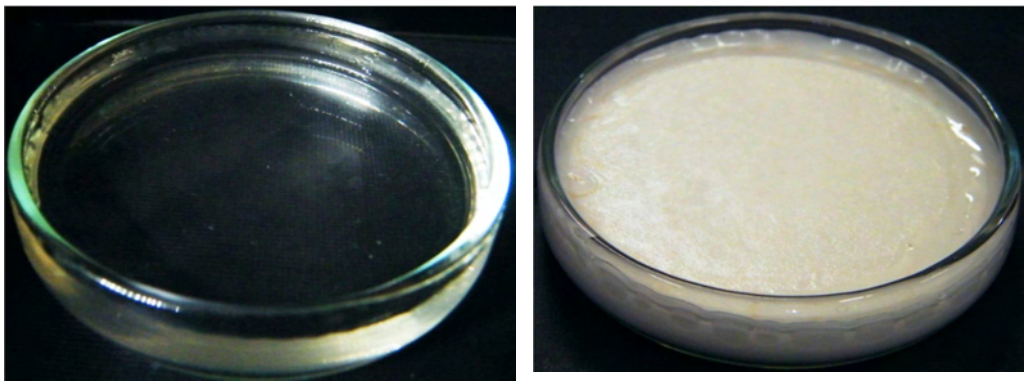

Figure 4.4: Phase transition of P(NIPAAm-*co*-MBA) hydrogel (R 90 gel) , showing the clear transparent hydrophilic state at 23 ℃ (left), and the hydrophobic state when heated to 37 ℃ (right).

4.3.4 Morphology

From literature, the morphology of PNIPAAm hydrogels is investigated using scanning electron microscopy (SEM), whereby the hydrogels are first immersed in liquid nitrogen followed by freeze drying (Caykara et al., 2006a; Zhang et al., 2003). However it is known that the cold treatment of the hydrogels can cause ice crystal artefacts which can increase the porosity of the hydrogels (Zhang et al., 2008). In Zhang *et al.* mention is made of “structural artefacts” due to the SEM preparation procedure, and therefore it was suggested that only structural differences between samples should be considered (Zhang et al., 2004). However this raises some scepticism regarding the “true” morphology of PNIPAAm hydrogels which have been previously reported. In this study the real morphology of the P(NIPAAm-*co*-MBA) hydrogels was investigated using ESEM. ESEM does not require any sample

treatment prior to imaging. The ESEM studies were performed at the Centre for Electron Microscopy at the University of Kwazulu Natal in Pietermaritzburg. The ESEM images of the PNIPAAm hydrogels prepared in water appear in **Figures 4.5-4.6**.

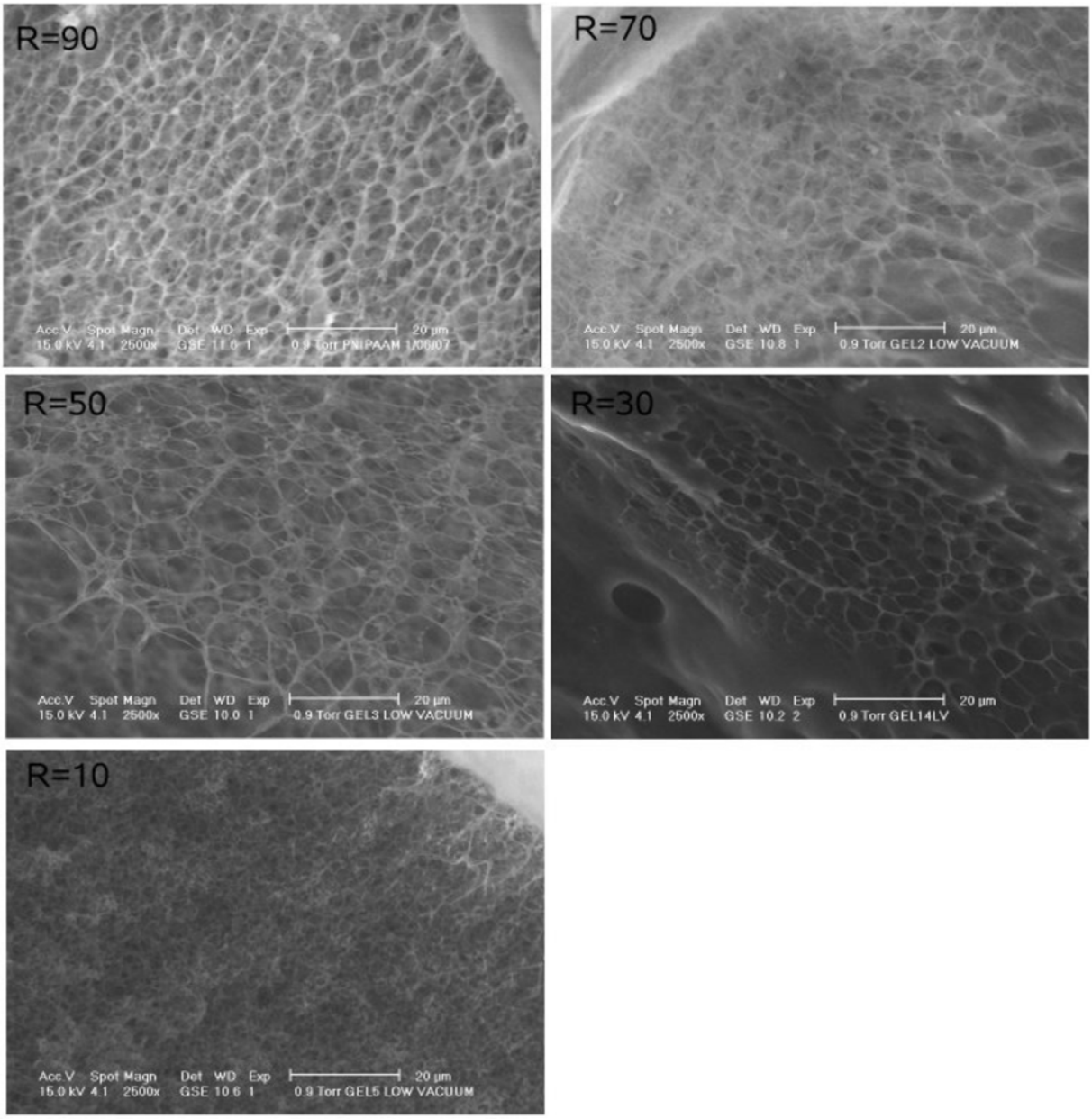

Figure 4.5: ESEM images of P(NIPAAm-*co*-MBA) hydrogels prepared in water with a cross-link density R ranging from 90 to 10 at 25 ℃.

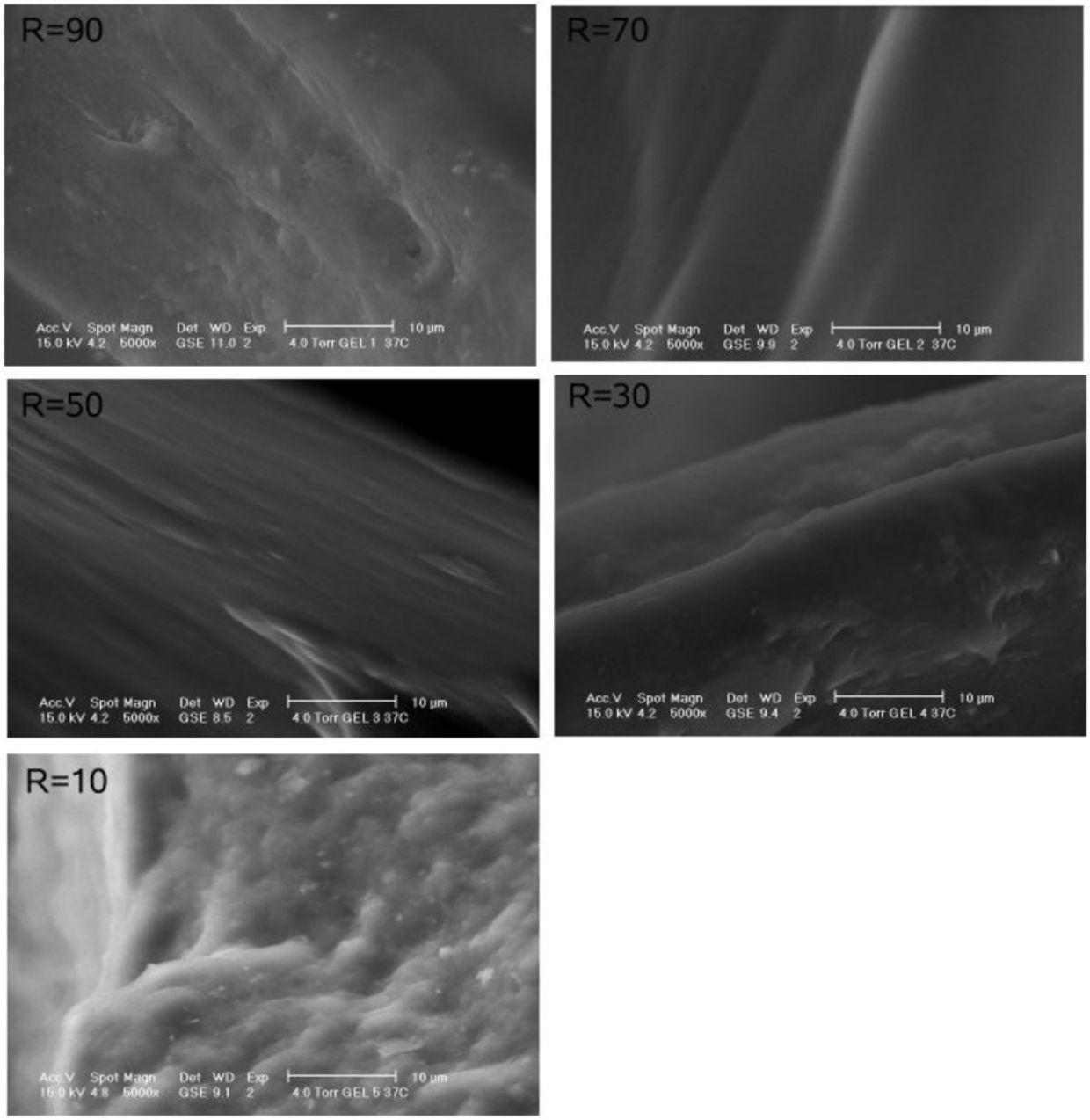

Figure 4.6: ESEM images of P(NIPAAm-*co*-MBA) hydrogels prepared in water with a cross-link density ranging from 90 to 10 at 37 ℃.

From the ESEM images, it could be seen that all of the hydrogels displayed porous structures at 25 ℃ (**Figure 4.5**), while when equilibrated at 37 ℃ all of the hydr ogels underwent a phase transition, and collapsed into dense structures with complete loss of porosity (**Figure 4.6**). The pore sizes in the R 90 gel (at 25 °C) was less than 10 µm and it can be seen that the pore sizes tended to decrease as the cross-link density was increased. The pores in gel R 10 appeared substantially smaller and more uniform compared to the gels with less cross-linker. For gel R 30 however it seems that part of the surface may have dried out during the imaging at 25 °C (**Figure 4.5**).

Zhang *et al.* studied the effect of cross-link density on the morphology of P(NIPAAm-*co*-MBA) hydrogels and they also reported that pore size decreased as the cross-link density was increased (Zhang et al., 2003). It is well known that for hydrogels with an increasing cross-link density, the molecular mass between cross-links are reduced, which results in an increase in pore density in the network structure (Caykara et al., 2006a).

The collapsed dense surface at 37 °C is indicative of the skin layer formation during de-swelling. It has been reported that PNIPAAm hydrogels display a dense skin layer which contributes to the slow de-swelling rate of the gels (Zhang et al, 2008). However it was observed that in the hydrophobic state, porosity is largely lost which implies that if cells were to be attached onto the hydrogels in the hydrophobic state during cell culture, they will be unable to grow in a structural 3D environment. It was reported previously (see Chapter 1) that highly porous scaffolds with interconnected pores in the size range of 100-300 µm are desirable for cell culture, since they enable optimal cell-cell interactions, while allowing for oxygen and nutrient supply to the cells. Additionally in the hydrophilic state, pore sizes are relatively small (<10 µm), and if cells penetrate into the hydrogel, cell release might be a challenge due to the path tortuosity in the hydrogels, whereby cells may become entrapped in the matrix. The use of mixed solvent systems during co-polymerisation may improve the porosity of the hydrogels; however this aspect was not investigated due to the relatively poor stability of the hydrogels. Zhang et al., 2002a prepared cross-linked PNIPAAm hydrogels in THF: water, and observed that in the shrunken state, some porosity was retained in the gel structure. However when dehydrated the pores were in the sub-micron range, which is undesirable for cell culture.

4.3.5 Swelling and de-swelling properties

1) Swelling Ratios

The maximum swelling ratios of the P(NIPAAm-*co*-MBA) hydrogels appear in **Table 4.5**. Firstly it was observed that when mixed solvents were used as the co-polymerisation medium (gels 6-9), the equilibrium swelling ratios were far superior compared to when water was used (gels 1-5). The 50:50 THF: water gels displayed the highest swelling ratio of ~48.3 ± 1.5 (i.e. ~ 4800% increase in weight). The equilibrium swelling ratios were found to decrease in the following order:

50:50 THF:water > 30:70 THF:water > 50:50 acetone:water > 30:70 acetone:water >100% water.

Table 4.5: The average equilibrium swelling ratios of PNIPAAm hydrogel prepared in water (R 90-10); acetone : water (R 90) and THF:water mixtures (R90). N=5.

Gel No.	R	Co-polymerisation medium	Swelling ratio
1	90	Water	16 ± 0.3
2	70	Water	16 ± 0.4
3	50	Water	12 ± 0.08
4	30	Water	11 ± 0.1
5	10	Water	11 ± 0.3
6	90	Acetone: water	21.7 ± 4.3
7	90	Acetone: water	33.6 ± 2.1
8	90	THF: water	45.3 ± 4.2
9	90	THF: water	48.3 ± 1.5

It was also observed that the maximum swelling ratios of the hydrogels was dependent on the cross-link density, such that with increasing MBA content, the equilibrium swelling ratio of the hydrogels decreased. It is believed that as the cross-link density increases, the expansion of the network structure and the free volume within the hydrogel network is reduced hence the swelling capacity of the hydrogels is also reduced (Caykara et al., 2006a; Zhang et al., 2003). For the water series gels, when R was 90 (i.e. the lowest cross-linker content), swelling ratio reached a maximum of ~16 ± 0.3 (n=5). This is in accordance with that observed by Zhang et al [2002] for PNIPAAm hydrogels. They have shown that the diffusion coefficient in PNIPAAm hydrogels decreases with an increase in MBA concentration. Additionally the reduced swelling of highly cross-linked networks has also been attributed to the glassy inner core of dried hydrogels (Caykara et al., 2006a; Zhang et al., 2003). Prior to swelling, in the dry hydrogel, there are strong intermolecular or polymer–polymer interactions, such as hydrogen bonds and hydrophobic interactions, which remain in a glassy state (Caykara et al., 2006a; Zhang et al., 2003). It has been suggested that in hydrogels with higher cross-linking, these interchain interactions are enhanced which leads to a significant reduction in water uptake (Caykara et al., 2006a).

The high swelling ratios of PNIPAAm gels polymerised in mixed solvents indicate highly porous and interconnected structures for the hydrogel networks. According to Zhang *et al*, polymer chains are widely expanded in the mixed solvents during polymerisation, and upon swelling in pure water, the solvent in the gel network is replaced by water, but the gel keeps its widely expanded state, which leads to large equilibrium swelling ratio of the gels (Zhang et al., 2002a). The mixed solvent gel series can be classified as “superabsorbent hydrogels” which are defined as hydrogels which absorb more than 20 times their own weight while maintaining their shape (Geever et al., 2007). Similar ratios have been reported previously for THF:water gels at 25 ℃ (Zhang et al., 2002b), howe ver for PNIPAAm gels prepared in 50:50 and 30:70 acetone:water mixtures previous studies report higher swelling ratios in the range of 45-55 (Zhang et al., 2002a). Although the formulations were similar to that reported in this study, discrepancies may be due to uncontrolled solvent evaporation in the present study.

2) Swelling kinetics

The swelling kinetics for the P(NIPAAm-*co*-MBA) hydrogels at 20 ℃ prepared in solvent : water mixtures are shown in **Figure 4.7**.

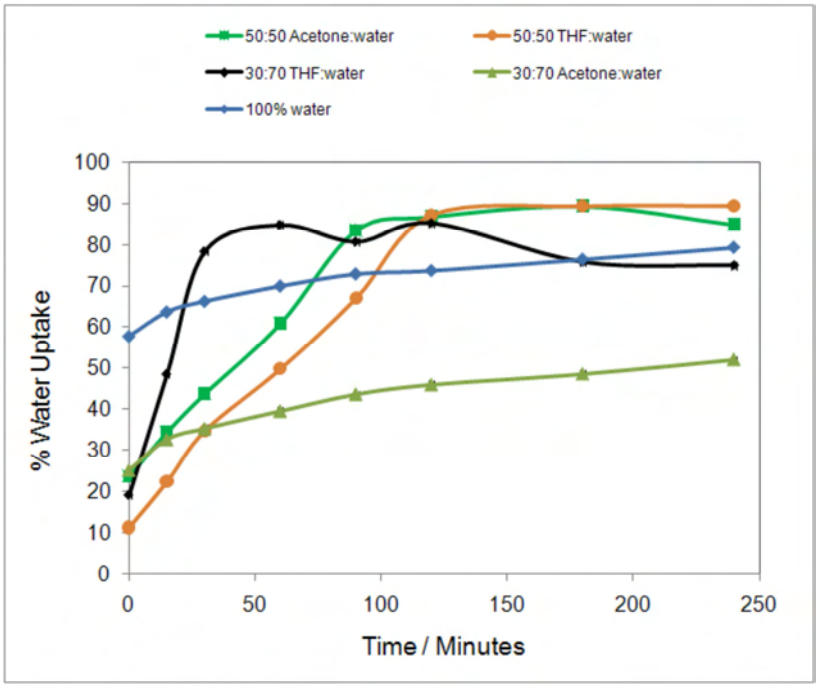

Figure 4.7: Swelling kinetics at 20 ℃ showing the percent wa ter uptake of partly swollen P(NIPAAm-*co*-MBA) hydrogels which were prepared in solvent : water mixtures with R 90, after air-drying for 24 hours. (Average taken of five samples.)

Prior to the kinetic studies, the polymerised gels were left open to air-dry for 24 hours. Since the gels were not completely dried it can be seen that at the start of the kinetics, gels were already partly swollen. Due to the higher solvent content in the solvent:water series gels these gels displayed higher solvent evaporation and hence lower initial swelling was observed at time zero compared to the 100% water gel. The 30:70 THF:water gel showed the fastest response rate and in just 15 minutes the percent water uptake increased from 19 ± 2% to 49 ± 10%. After an hour, the water uptake reached 85 ± 11%.Comparisons cannot be made to the standard PNIPAAm gels without solvent due to its higher initial water content. At 90 minutes both the 50:50 acetone:water and 50:50 THF:water reached ~80% water uptake. The 30:70 acetone:water gels however deviated from this trend and showed a very slow response whereby water uptake increased from 25 ± 9 at the start of the study to 52 ± 14 in 240 minutes. Large deviations were observed for the swelling ratios for all of the solvent series gels, which may be due to uncontrolled solvent evaporation during polymerisation.

It is known that swelling of hydrogel networks is a diffusion-controlled process which is thermodynamically driven. For the 30:70 THF:water; 50:50 THF:water and 50:50 acetone:water gels, swelling proceeded in two stages i.e. the initial stage was very rapid as water easily penetrated into the polymer network, and as the sample approached complete hydration in the second stage of swelling, the rate of water diffusion levelled off. This is believed to be due to the retractive force due to the cross-linking in the hydrogel structure which counterbalances the thermodynamically driven swelling process (Geever et al., 2007). The swelling kinetics of the R series gels prepared in water is given in **Figure 4.8**.

Since water was used as the co-polymerisation medium, all the gels were already highly swollen at the start of the swelling kinetics which has influenced the swelling rate reported here. Swelling kinetics was found to be dependent on the cross-link density. PNIPAAm hydrogels with the lowest cross-link densities i.e. R 90- 50 showed the fastest water uptake, while gels R 30 and 10 were the slowest. Since the gels of the present study were left to equilibrate for 24 hours prior to the kinetic studies, and already contained about 50% of its total water content, it can be assumed that the trend depicted in **Figure 4.8**, is probably for the second stage of swelling where rapid diffusion is no longer possible.

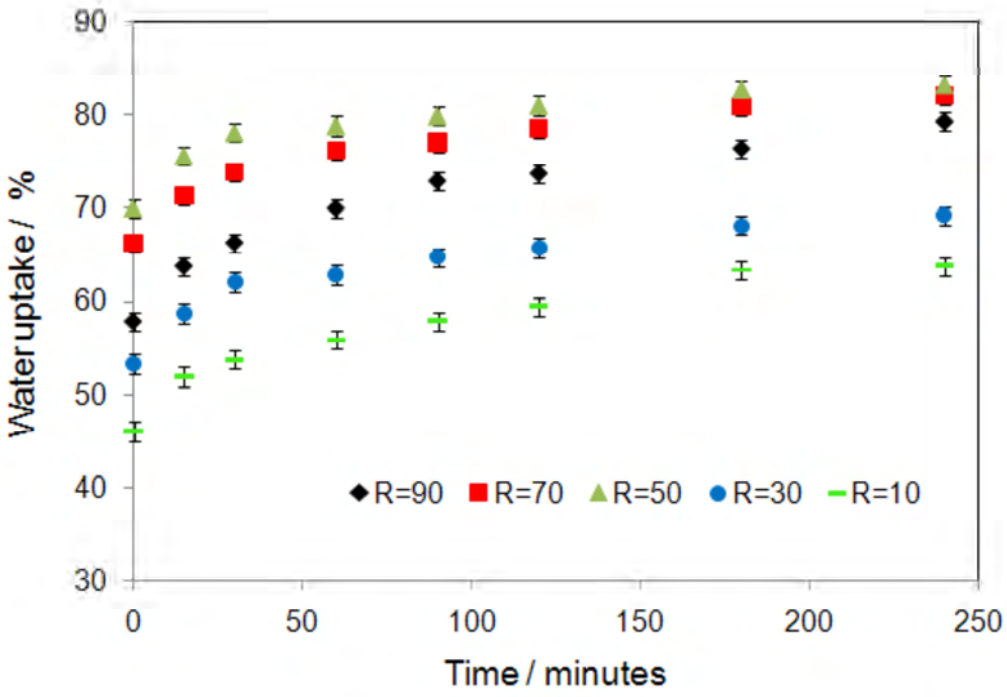

Figure 4.8: Swelling kinetics at 20 ℃ showing the percent water uptake of partly swollen P(NIPAAm-*co*-MBA) hydrogels which were prepared in water with varying cross-link densities, after air-drying for 24 hours.

Zhang *et al* prepared PNIPAAm hydrogels with a similar cross-link density to the present study (Zhang et al., 2003). They also showed an increase in swelling ratio of the PNIPAAm hydrogels with a decrease in cross-link content, however for water uptake, they reported the opposite trend, i.e. water uptake increased for gels with a higher cross-link density. Swelling of hydrogels is a complex process and is dependent on a number of network parameters as well as the pre-treatment prior to swelling. In the former study, hydrogels were completely dried either directly in a vacuum, or they were heated to 50 ℃ and then placed in a vacuum oven at 60 ℃. It is known that the pre-treatment of the hydrogels plays a major role in the swelling kinetics (Zhang et al., 2003).

3) De-swelling

De-swelling kinetics at 37 ℃ for the solvent:water PNIPAAm hydrogels appear in **Figure 4.9.** As can be seen the response rate for the mixed solvent gels was very rapid when compared to the standard gel which was prepared in pure water. Again the 50:50 THF:water gels showed the fastest response rate whereby in just 10 minutes the percent water retention decreased from 100% to 12 ± 1%, as compared

to 90 ± 0.6% for the standard gel at the same time period. The results indicate that the solvent : water PNIPAAm may be better suited for use in cell culture in terms of deswelling rates compared to the pure water gels.

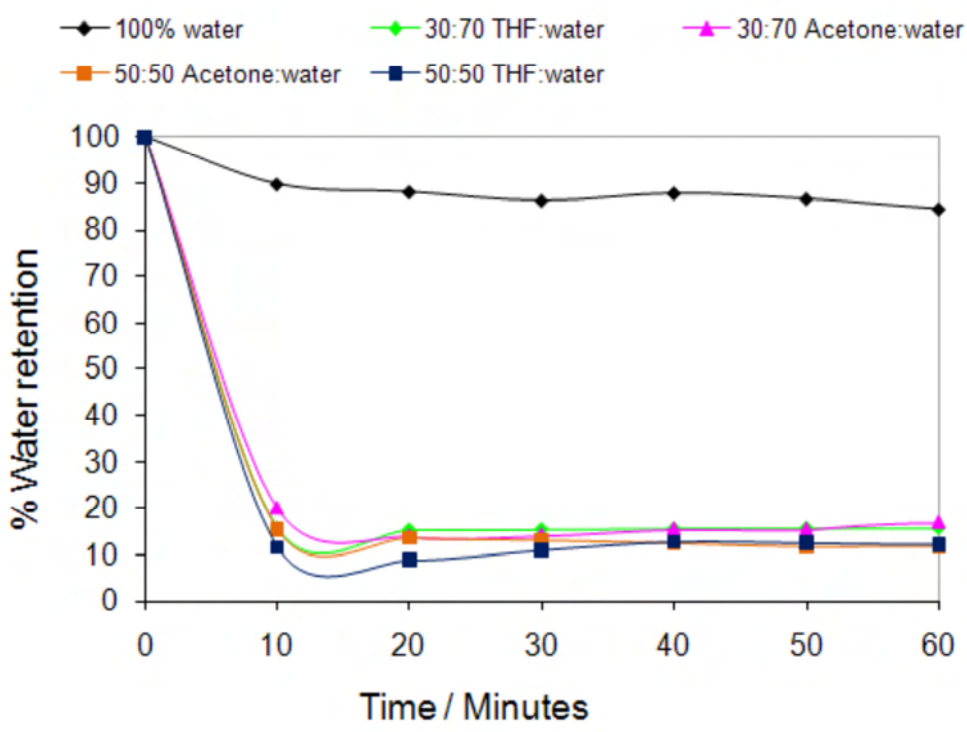

Figure 4.9: Percent water retention at 37 ℃ for P(NIPAAm-*co*-MBA) hydrogels synthesised in acetone:water and THF:water series. (Average taken of five samples.)

For most of the hydrogels, de-swelling proceeded in two steps, i.e. the initial phase was rapid and thereafter de-swelling slowed down. It is believed that the initial rapid phase is due to rapid diffusion of water out of the hydrogel network, while during the second phase the collapsed skin layer at the outermost surface of the hydrogels prevents the outward flow of water loss and de-swelling then is significantly reduced (Zhang et al., 2003).

It should be noted that de-swelling was performed at 37 ℃ which is very close to the LCST of the P(NIPAAm-*co*-MBA) hydrogels which in this case was found to be between 33-35 ℃ hence a very rapid de-swelling rat e was not seen. To enhance de-swelling, other groups have conducting de-swelling kinetics studies at much higher temperatures, e.g. 50 ℃ (Zhang et al., 2003).

The de-swelling kinetics in this study was performed at 37 ℃ (i.e. body temperature) since is the practical temperature for a number of applications, such as cell culture, drug delivery etc. Zhang *et al* suggests that the very rapid de-swelling of mixed solvent gels can be attributed to the existence of a non-equilibrated shrinking force in the heterogeneous networks, at different collapsed regions, whereby water rich and precipitated polymer rich phases exist in the hydrogel, and during shrinking the water release regions connect with each other forming interconnected water release channels resulting in quick water release from the heterogeneous hydrogel (Zhang et al., 2008). It has also been suggested that the interconnected porous structures of gels prepared in mixed solvents is responsible for the formation of a less dense surface skin layer during shrinking compared to the bulk PNIPAAm gels prepared in water (Zhang et al., 2002b). De-swelling kinetics for the water series gels for varying cross-link density appear in **Figure 4.10**.

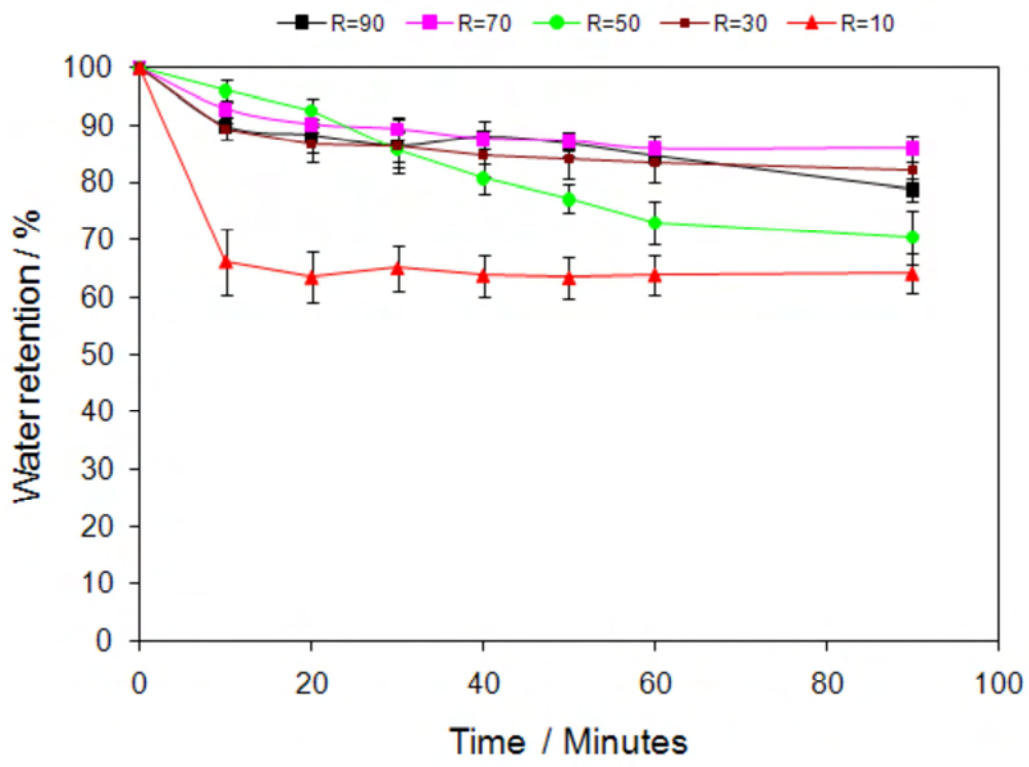

Figure 4.10: De-swelling kinetics at 37 ℃ for P(NIPAAm-*co*-MBA) hydrogels with varying cross-link density.(Average taken of five samples.)

The de-swelling rates for gels R 90-30 were similar (except for gel R 50 which showed anomalous behaviour). This may be attributed to a similar structure for gels R 90-30. Surprisingly gel R 10 showed the fastest de-swelling rate, and in 10 minutes

the water retention in the gels were reduced from 100% to 66% ± 6, whereas the water retention in the other gels were around 90% and higher for the same time period. This behaviour was unexpected and was initially thought to be anomalous. However according to Zhang *et al*, when the cross-link density of PNIPAAm hydrogels are increased, the skin layer formation is reduced thereby enabling faster de-swelling for hydrogels with higher cross-link density (Zhang et al., 2003). The higher de-swelling kinetics of the R 10 gels then can possibly be attributed to the formation of a more permeable skin layer and the higher pore density compared to the less cross-linked hydrogels, which creates interconnected water channel which enhance the water diffusion out of the gels. Further repeats are required to confirm the behaviour of the R 10 gel.

4.3.6 Viscoelastic properties

The viscoelastic behaviour of the P(NIPAAm-*co*-MBA) gels (prepared in water) was determined using dynamic shear rheology. The storage (elastic) G′ and loss (viscous) modulus G″ of the gels as a function of strain appear in **Figure 4.11.** The storage modulus refers to the elastic component of a hydrogel, and is an indication of the elastic strength or stiffness of the polymer network. The loss modulus refers to the viscous component of the complex modulus. For all the gels, the storage modulus remained constant with an increase in strain up until the linear viscoelastic (LVE) region, beyond which a sudden drop in storage modulus was observed for each gel. It can be assumed that beyond the LVE region, the gels become mechanically unstable which results in a decrease in the elastic strength of the gels. In contrast, the loss moduli continuously increased with increasing deformation. An increase in G″ suggests that as the strain increases, molecular interactions in the flexible networks of the hydrogels are increased (DeRossi et al, 1991).

Both storage and loss modulus was found to be dependent on the cross-link density. With an increase in cross-link density (i.e. decreasing R), storage and loss moduli, as well as tan δ increased (**Figure 4.12**). It was observed for all of the hydrogels, that G′ > G″ by more than an order of magnitude, which indicates a viscoelastic gel (Garbern et al., 2010). Additionally tan δ was <1 for the whole cross-link range confirming a gel structure (Garbern et al., 2010).

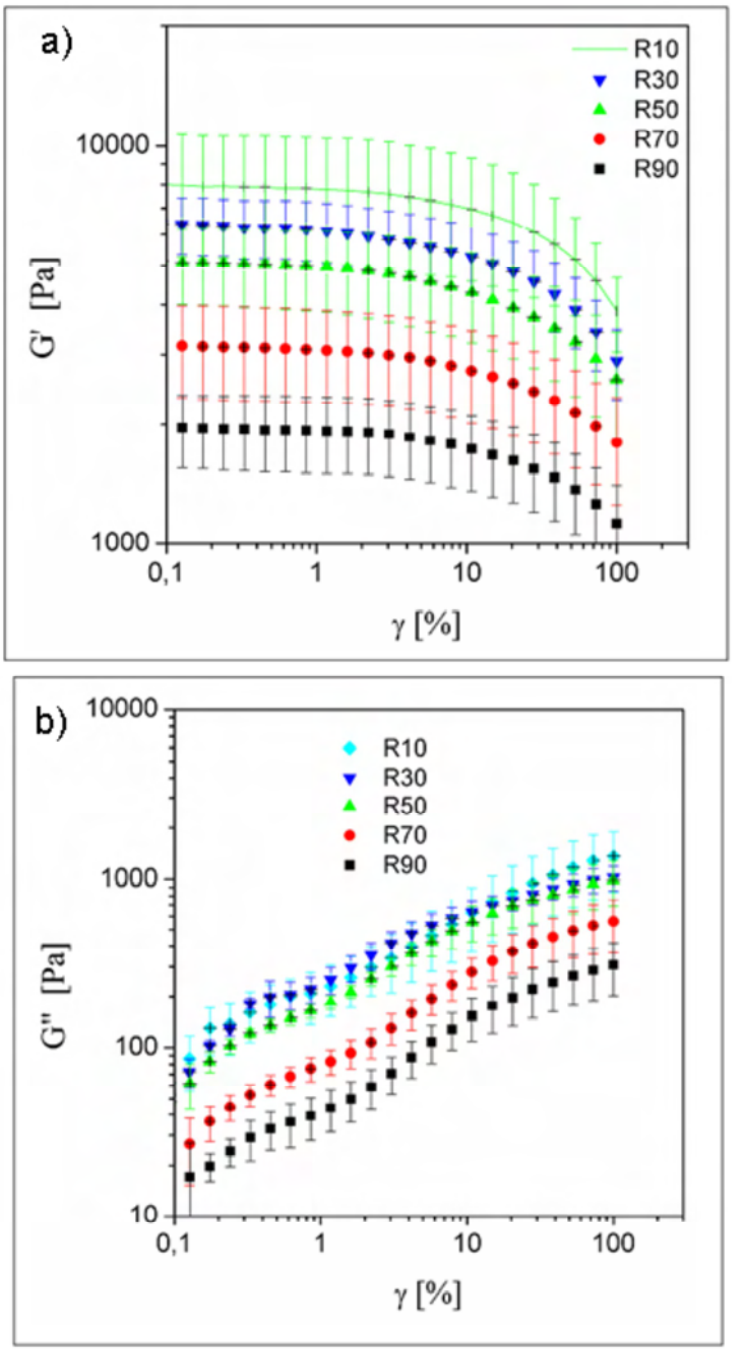

Figure 4.11: Storage modulus (G′) (a) and loss modulus (G″) (b) as a function of strain (γ) for P(NIPAAm-*co*-MBA) hydrogels with cross-link density R 90-10 at 25 ℃ (with ω =10 s^{-1}).

It appeared that tan δ displays a maximum at R 30. However on further analysis (from temperature and frequency sweeps), it was realised that gel R 10 behaved anomously due to gel heterogeniy. The threshold limit of linear viscoelasticity and the average storage modulus for the R 90-R 10 hydrogels appear in **Table 4.6**. The

strain at LVE and increased with an increasing cross-linker content. For gel R10 the storage modulus at the LVE region was 7143 ± 2467 Pa which was the highest for the gels investigated. This is due to greater elastic strength of the P(NIPAAm-*co*-MBA) gels as the cross-links are increased.

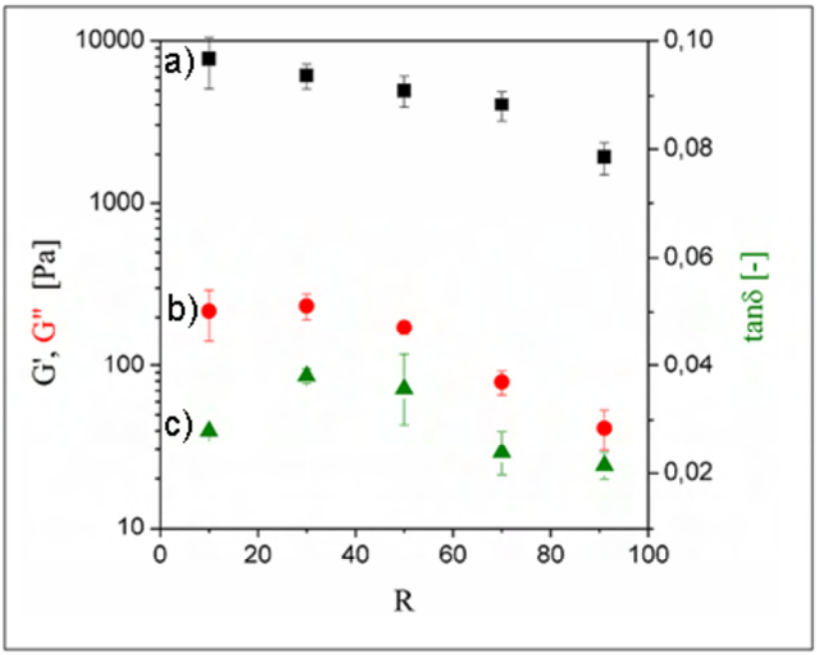

Figure 4.12: The change of a) storage modulus (G′), b) loss modulus (G″) and c) damping factor (tan δ) with decreasing cross-linker content (increasing R) at 25 ℃ with $\gamma = 1\%$; $\omega = 10\ s^{-1}$.

Table 4.6: Threshold limit of linear viscoelastic range of P(NIPAAm-*co*-MBA) hydrogels with different cross-link density (γ is the strain, and G′ is the storage modulus).

Gel /R	**γ at LVE /%**	G′ **/Pa**	**Std dev**
90	1.61	1917	417
70	1.89	3036	777
50	2.21	4863	1160
30	5.73	5570	1022
10	7.85	7143	2467

The temperature sweeps to investigate the thermal phase changes of the various hydrogels appear in **Figure 4.13**. Both storage and loss modulus (and hence tan δ) were highly dependent on temperature. As expected, below the temperature of volume phase transition the values of storage, and loss moduli are successively

higher for the gels with higher cross-linker content. Up to the temperature of volume phase transition the moduli decreases with increasing temperature for all the gels.

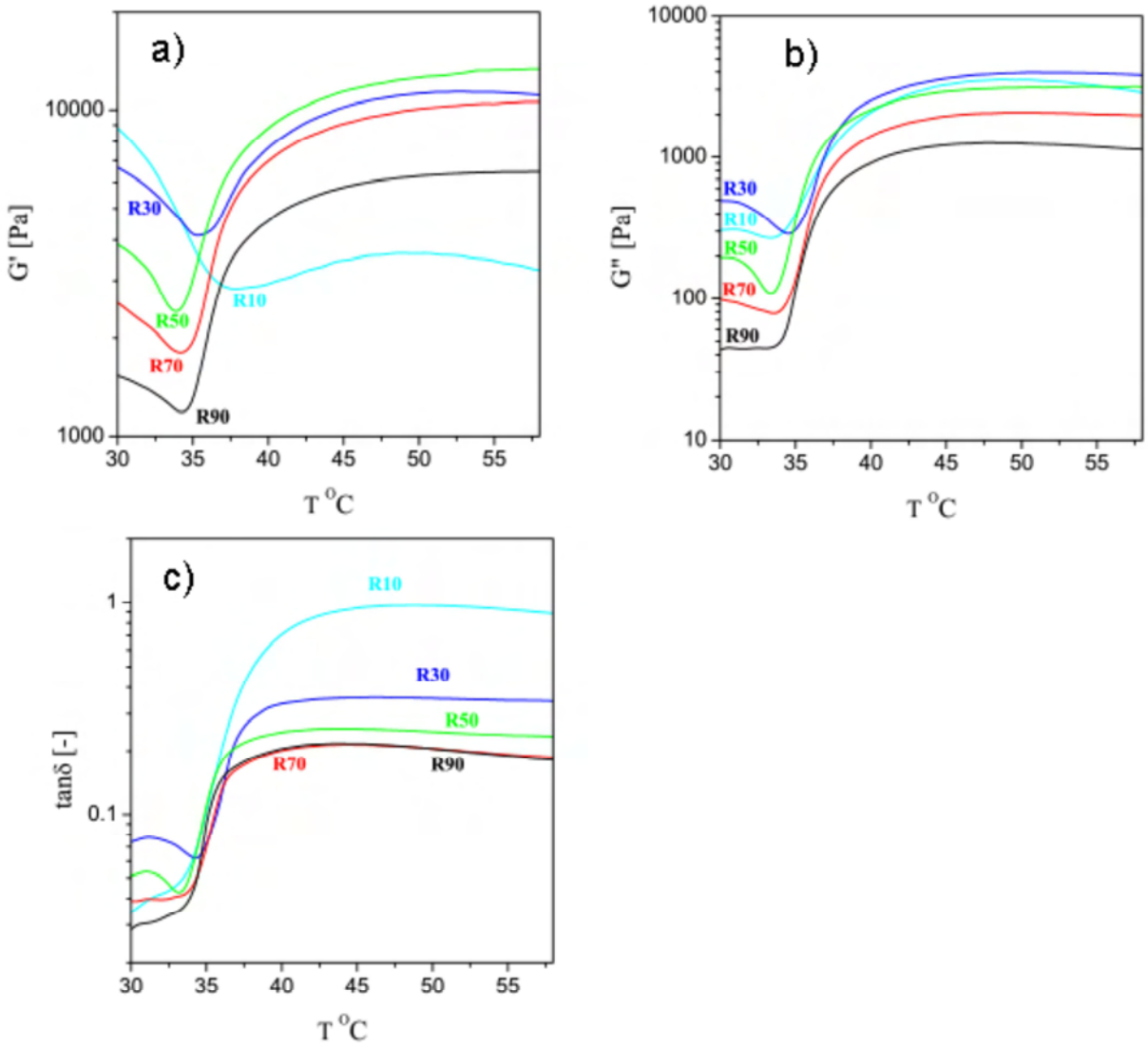

Figure 4.13: (a) Storage modulus (G′); (b) loss modulus (G″) and (c) tan δ as a function of temperature for P(NIPAAm-*co*-MBA) hydrogels R 10-90.

However at temperatures higher than the LCST dramatic increases in both storage and loss moduli were observed for all of the gels (except R 10) until equilibrium is reached. The initial decrease in moduli prior to the LCST was more prominent for G′ than G″. This may be related to a decrease in hydrogen bonding as the temperature approaches the LCST which has a larger impact on the storage modulus. Hydrogen bonds in the hydrogel structure start to break at temperatures close to the volumetric phase transition, as the molecules start to undergo a conformational change from hydrophilic to hydrophobic. At the LCST, both the storage and loss moduli are at a

minimum due to a maximum decrease in hydrogen bonding in the hydrogel structure. However when the temperature is increased beyond the LCST, the G′ and G″ increase which is related to the formation of molecular interaction in the gel at higher temperatures (DeRossi et al., 1991). At the LCST the polymer chains undergo coil to globule conformation which may result in enhanced aggregation resulting in an increase in loss modulus (Lessard et al., 2003). Additionally hydrophobic interactions between the polymer chains are favoured above the LCST which result in greater elastic strength (storage modulus) of the hydrogels. The behaviour of gel R 10 was found to be anomalous, and was attributed to heterogeneous cross-linking during polymerisation due to the higher cross-linker content.

The LCST of the P(NIPAAm-*co*-MBA) hydrogels was also determined from the storage modulus, loss modulus, and tan δ and the LCST values appear in **Table 4.7**. The LCST of all the hydrogels ranged between 32-34 °C which was slightly lower than that measured by DSC. Also the cross-link density in the investigated range of MBA concentration (1.1-9.1 Mol% MBA) did not affect the temperature of volume phase transition which corroborates with the DSC data. Although when 9.1 Mol% MBA was used, this resulted in a broader temperature range of transition of Gel R 10 which may be due to the heterogeneity of the polymer system (**Figure 4.13c**).

Table 4.7: Onset temperature of volumetric phase transition for hydrogels with different cross-link density from dynamic rheometry.

R	LCST from G′ /℃	LCST from G″/℃	LCST from Tan δ /℃
90	33.8 ± 0.5	33.3 ± 0.6	33.0 ± 0.1
70	33.8 ± 0.2	33.3 ± 0.2	33.2 ± 0.1
50	33.2 ± 0.3	33.0 ± 0.2	33.0 ± 0.1
30	34.4 ± 0.2	33.2 ± 0.2	33.3 ± 0.2
10	33.1 ± 0.7	32.3 ± 0.1	32.5 ± 0.5

To verify the stability of the P(NIPAAm-*co*-MBA) hydrogels below and above the phase transition temperature oscillatory measurements were carried out with increasing frequency (strain frequency sweep). The change of complex viscosity (η*), storage modulus and loss modulus with angular frequency (ω) below and above the volumetric phase transition for the different gels is given in **Figure 4.14**.

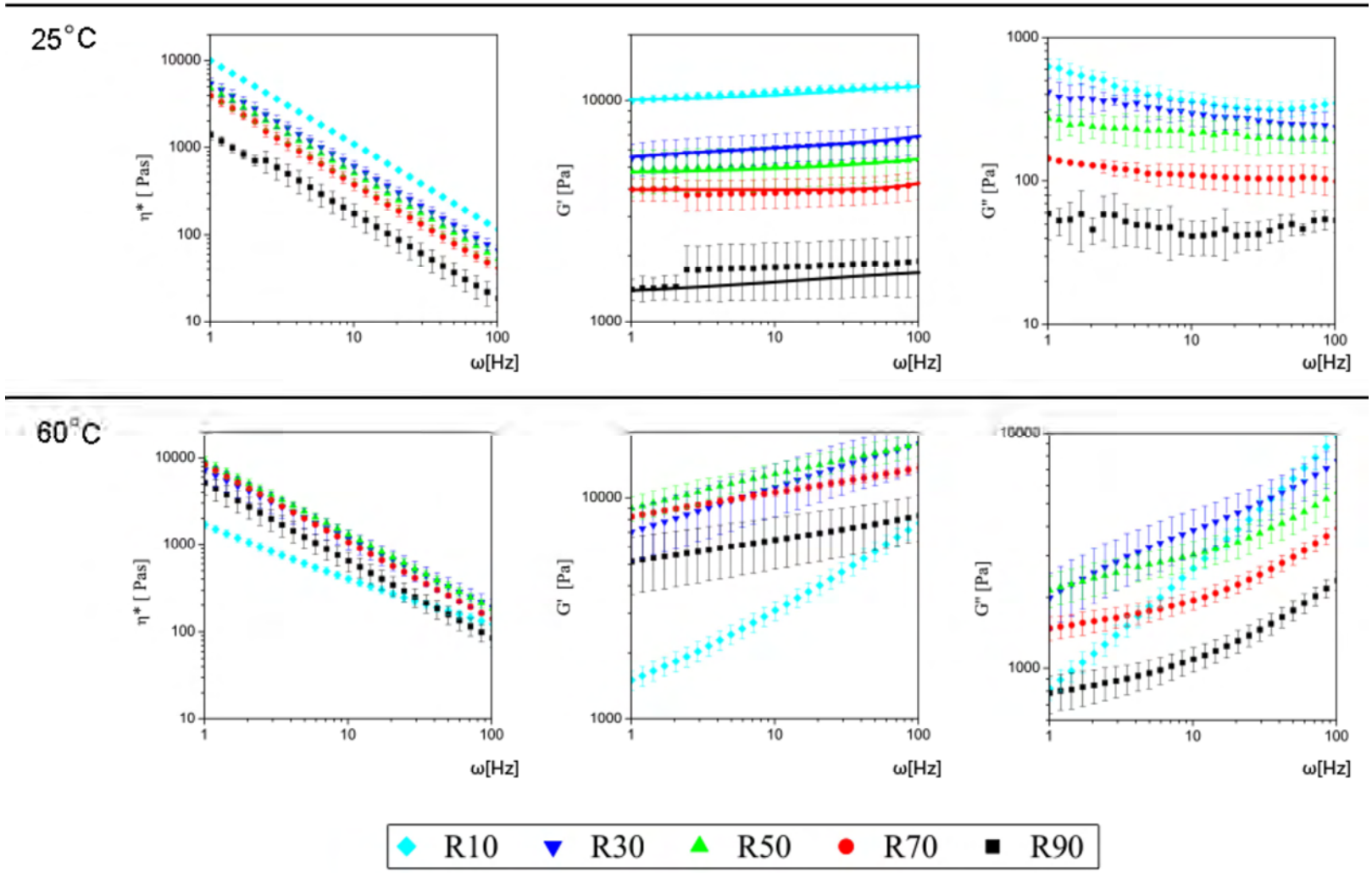

Figure 4.14: The change of complex viscosity (η*), storage modulus (G′) and loss modulus (G″) at 25 ℃ and 60 ℃ for the gels with different cross-linker content (γ=1%).

Firstly it was observed that G′ and G″ was independent of the frequency at 25 ℃ and the contribution of the storage (elastic) modulus was the greatest at all frequencies. This behaviour is typical of gel systems (Lessard et al., 2003). However the complex viscosity decreased with an increase in frequency which shows shear thinning which is typical of a polymer solution in water (Lessard et al., 2003). This may indicate that at higher frequencies, the shearing forces disrupt the molecular interaction between the polymer chains in the hydrogel resulting in a decrease in viscosity. This may indicate poor stability of the hydrogel structures. The complex viscosity, storage modulus and loss modulus increased with increasing cross-linker content. Above the phase transition temperature, gel R 10 (at 60 ℃) behaves anomalously just as in case of the temperature sweep. This may be attributed to the heterogeneous polymer structure due to the increased cross-linker. Above the phase transition temperature the hydrophobic gels behave like polymers, meaning that the modulus slightly increases with increasing frequency for each gel, except for gel R 10, where a steep increase in storage modulus was observed.

A comparison for the storage, loss modulus and tan δ as a function of cross-link density at a frequency of 10 s^{-1} is given in **Figure 4.15**. Below the volumetric phase transition (at 20 ℃) the G′ moduli are about two orders of magnitude higher than the G″ moduli, however above the phase transition (at 60 ℃) substantially highe r loss moduli were observed for the entire cross-link range. This implies that after the phase transition the loss modulus is impacted to a greater extent than the storage modulus. The increase in the loss modulus is indicative of the coil to globule transition at temperatures > LCST which results in precipitation causing increased molecular interaction in the flexible networks (DeRossi, et al. 1991, Lessard et al., 2003).

The viscoelastic properties of the P(NIPAAm-*co*-MBA) hydrogels prepared in mixed solvents were not assessed, since these hydrogels were substantially weaker compared to the R 90 - 10 water series gels. Further work can involve investigating the effect of increasing cross-link density on the mechanical properties of the mixed solvent gels.

4.3.7 Water contact angle

The static contact angle of P(NIPAAm-co-MBA) hydrogels with varying cross-link density at 40 ℃ and at 20 ℃ is given in **Table 4.8**. Contact angle measurements provide information about the outermost surface layer of the hydrogels. For all of the hydrogels, at 40 ℃ the contact angle values were relatively higher hence the surface was more hydrophobic

compared to 20 ℃ confirming the phase transition of the surface layers of the PNIPAAm hydrogels.

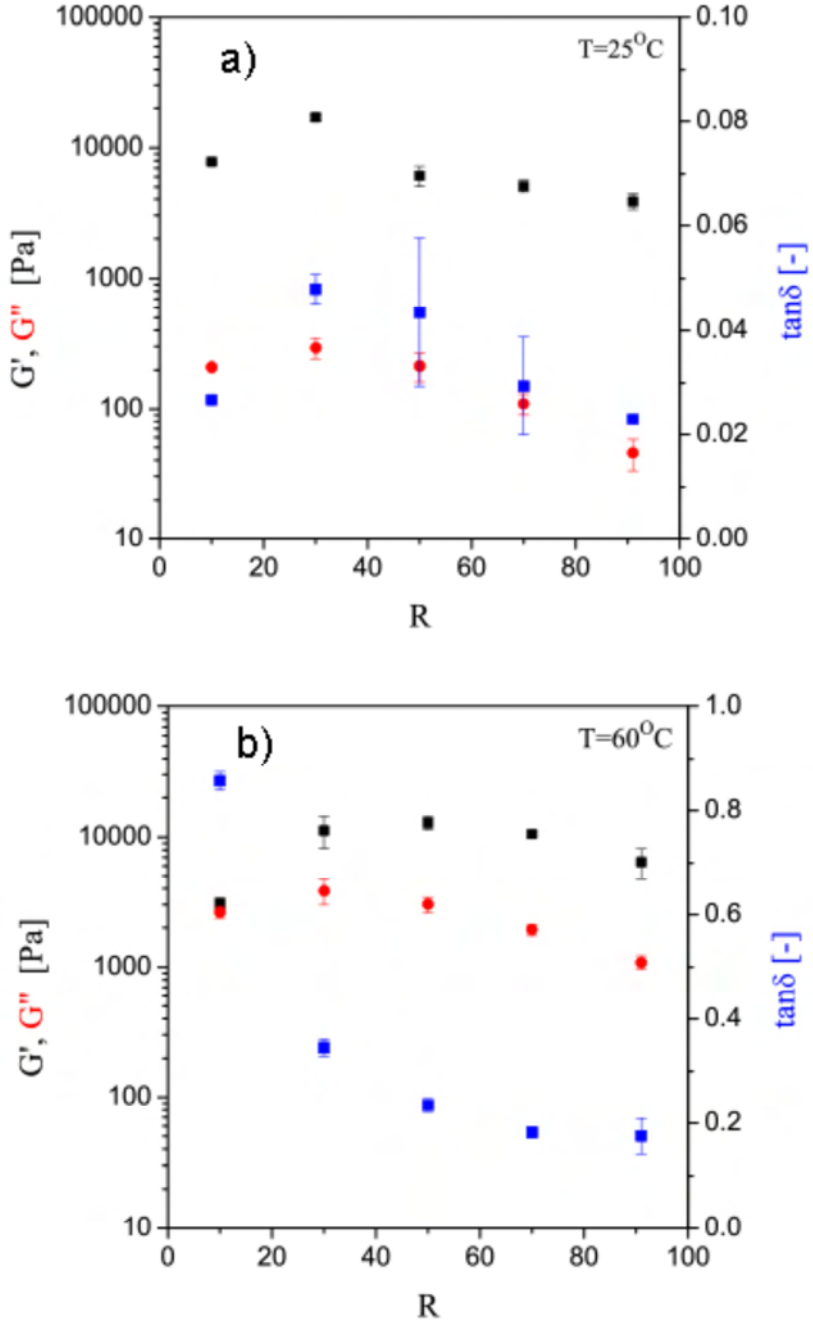

Figure 4.15: Change in storage modulus, loss modulus and damping factor (tan δ) with decreasing cross-linker content at (a) 25 ℃ and (b) 60 ℃ from frequency sweep measurements at 10 s^{-1} (γ = 1%).

Table 4.8: Static contact angle of P(NIPAAm-*co*-MBA) hydrogels (prepared in water) with varying cross-link density at 40 ℃ and 20 ℃ (n=5).

R	MBA wt%	Contact Angle	
		40 °C	20 °C
90	1.5	86 ± 5	62 ± 5
70	1.9	77 ± 4	57 ± 3
50	2.7	65 ± 4	48 ± 3
30	4.3	62 ± 1	48 ± 5
10	12.0	35 ± 6	23 ± 6

The contact angle was dependent on the cross-link density of the gels. As the cross-link density increased i.e. R decreased, the contact angle values decreased. Even though the surface of the P(NIPAAm-*co*-MBA) gels was relatively more hydrophobic at 40 °C compared to 20 °C, the contact angles were still low, and more so for the higher crosslink gels. This implies that the hydrogels are still hydrated in the hydrophobic state, which may be due to the dense skin layer formation, which retards water expulsion. Gels were equilibrated for 30 minutes prior to contact angle analysis, which is insufficient to dehydrate the gels. These results however do not correlate with the de-swelling studies for the water series gels (R 90 - 10) where we observed the R 10 hydrogel to demonstrate the fastest deswelling for the R series gels.

The change in contact angle with temperature and the effect of cross-link density on contact angle can both be explained by the concept of surface configuration change and surface-state equilibration which occurs on polymer surfaces (Yasuda and Okuno, 1994).

In general polymers, due to their long molecular chains, have the capability to reorient their functional groups at the surface by means of rotational and migrational rearrangement in order to minimise the interfacial tension at the polymer-air interface (Yasuda and Okano, 1994). A high degree of segmental mobility is possible in highly swollen hydrogels. For hydrogels with less cross-linker, greater chain mobility is possible at the gel-air interface compared to hydrogels with a higher cross-link density. In a highly swollen hydrogel with less cross-linker, since a large amount of water is in the bulk phase of the gel, in order to minimise the interfacial tension at the surface, hydrophilic groups re-orientate towards the interior of the gel rather than remain on the surface, while the hydrophobic groups reorient

towards the surface hence contact angles for the R 90 gels are higher than that for gels which contain more cross-linker. However hydrogels with larger MBA content display reduced chain mobility, and enhanced polymer-polymer interactions due to an increase in the hydrophobic effect, hence the hydrophobic groups orientate towards the inner core while more hydrophilic groups and water remain on the surface consequently the contact angles of the R 10 gels are lower compared to R 90. The thermoresponsive behaviour of the hydrogels with a change in contact angle then can also be explained by the same concept, in that at 40 ℃, the hydrophobic isopropyl groups re-orientate at the surface and the contact angle increases, while at 20 ℃, some of the amide groups and water is also present at the gel-air interface due to an increase in hydrogen bonding and the contact angle is reduced (Zhang et al., 1995).

It can also be observed that the difference in contact angle at 20 ℃ and 40 ℃ decreases as the cross-link density increases. This can be attributed to restricted chain mobility at the gel-air interface with an increase in cross-link density; hence the difference in surface reorientation at both temperatures is smaller than for the gels with larger chain mobility.

4.4 Conclusions and recommendations

P(NIPAAm-*co*-MBA) hydrogels were successfully synthesised using the free radical polymerisation method and we have studied the thermoresponsive and physical properties of PNIPAAm hydrogels. To improve the response rate of PNIPAAm hydrogels, the cross-link density (R 90 to 10) and the use of mixed solvents were investigated. It was found that the swelling capacity of the PNIPAAm hydrogels decreased when the cross-link density increased from 90 to 10, however the de-swelling rate and pore density in the hydrogels increased with cross-link density. At 25 ℃ P(NIPAA m-*co*-MBA) hydrogels displayed relatively small pores, while at 37 ℃ porosity was completely lost. The LCST of the hydrogels was determined from micro DSC, and by dynamic oscillation shear rheology. The LCST was unaffected by the cross-link density. However the storage and loss modulus of the hydrogels was highly dependent on temperature and on the cross-link density for the gels. When NIPAAm was polymerised in mixed solvents, the LCST of PNIPAAm was maintained and superabsorbent heterogeneous polymer networks were created with very rapid response rates.

With respect to use of the P(NIPAAm-co-MBA) hydrogels for non-invasive cell culture, the following assessment was made:

- The porosity of the P(NIPAAm-*co*-MBA) hydrogels was largely lost at 37 °C which implies that during cell culture, the hydrogel surface will be similar to a 2D surface, and will not provide 3D structural support for the cells
- The pore size of the hydrogels in the hydrophilic state was also too small to enable release of 3D cell clusters, since if cells did penetrate into the bulk hydrogel during culture, cell release may be problematic
- De-swelling of standard PNIPAAm hydrogels in water is too slow and such a material will not be suitable for use in a robust system where a quick response is required
- Use of mixed solvents significantly improved the response rates of PNIPAAm hydrogels, but these gels displayed very poor stability. Effect of increasing the crosslink density on mixed-solvent gels could be the subject of future work
- The mechanical properties of the P(NIPAAm-*co*-MBA) hydrogels may be insufficient for use in a bioreactor with a perfusion system with a relatively high flow rate. It was observed that the R series gels underwent shear thinning with increases in frequency
- Difficulty with use of the bulk PNIPAAm polymer in e.g. a bioreactor where the entire scaffold will shrink and thereby influence the reactor flow rates etc.
- Use of bulk PNIPAAm hydrogel as a cell culture scaffold will be relatively expensive

Based on the considerations above, it was concluded that PNIPAAm bulk hydrogels may not be the ideal scaffold for cell culture, and cell culture studies was not pursued with this material. Application of a PNIPAAm layer onto a 3D preformed scaffold might prove more effective and hence was the subject of further investigation (**Chapter 5**).

4.5 References

Anseth KS, Bowman CN, Brannon-Peppas, L. 1996. Review Mechanical properties of hydrogels and their experimental determination, Biomaterials 17: 1647-1657.

Caykara T, Kiper S, Demirel G. 2006a. Network parameters and volume phase transition behaviour of poly(*N*-isopropylacrylamide) hydrogels. Journal of Applied Polymer Science 101:1756-1762.

Caykara T, Kiper S, Demirel G. 2006b. Thermosensitive poly(*N*-isopropylacrylamide-*co*-acrylamide hydrogels: Synthesis, swelling and interaction with ionic surfactants. European Polymer Journal 42:348-355.

Chetty AS, Kovács J, Vargha V, Mészáros A, Fekete J, Domján A. 2012.' A versatile characterisation of poly(*N*-isopropylacrylamide-*co*-N,N'-methylene-bis-acrylamide) hydrogels for composition, mechanical strength, and rheology, EXPRESS Polymer Letters, EPL-0003831, accepted: 26 June 2012.

DeRosa ME, DeRosa RL, Noni LM, Hendrick ES. 2007. Phase separation of Poly(*N*-isopropylacrylamide) solutions and gels using a near infrared fiber laser. Journal of Applied Polymer Science 105:2083–2090.

DeRossi D, Kajiwara K, Osada Y, Yamauchi A.(eds) 1991. Polymer gels - fundamental and biomedical applications. Plenum Press, New York pg 265.

Garbern JC, Hoffman AS, Stayton PS. 2010. Injectable pH and temperature-responsive poly(*N*-isopropylacrylamide-*co*-propylacrylic acid) copolymers for delivery of angiogenic growth factors. Biomacromolecules 11(7): 1833–1839.

Geever LM, Mi´nguez CM, Devine DM, Nugent MJD, Kennedy JE, Lyons JG, Hanley A, Devery S, Tomkins PT, Higginbotham CL. 2007. The synthesis, swelling behaviour and rheological properties of chemically cross-linked thermosensitive copolymers based on *N*-isopropylacrylamide. Journal of Material Science 42:4136–4148

Kara S, Okay O, Pekcan O. 2002. Real-time temperature and photon transmission measurements for monitoring phase separation during the formation of poly(*N*-isopropylacrylamide) gels. Journal of Applied Polymer Science 86:3589–3595.

Liang L, Shi M, Viswanathan VV, Peurrung LM, Young JS. 2000. Temperature-sensitive polypropylene membranes prepared by plasma polymerization. Journal of Membrane Science 177:97–108.

Lessard DG, Ousalem M, Zhu XX, Eisenberg A, Carreau PJ. 2003. Study of the phase transition of poly(N,N-diethylacrylamide) in water by rheology and dynamic light scattering. Journal of Polymer Science: Part B: Polymer Physics 41: 1627–1637.

Muniz EC, Geuskens G. 2001. Compressive elastic modulus of polyacrylamide hydrogels and semi-IPNs with poly(*N*-isopropylacrylamide). Macromolecules 34:4480-4484.

Riggs IP, Rodriguez F. 1967. Persulfate-initiated polymerisation of acrylamide. Journal of Polymer Science, Part A-1: Polymer. Chem. 5:3151-3165.

Takigawa T, Yamawaki T, Takahashi K, Masuda T. 1997. Change in Young's modulus of poly(*N*-isopropylacrylamide) gels by volume phase transition. Polymer Gels and Networks 5:585-589.

Yasuda T, Okuno T. 1994. Contact angle of water on polymer surfaces. Langmuir 10:2435-2439

Zhang J, Pelton R, Deng Y. 1995. Temperature-dependent contact angles of water on poly(*N*-isopropylacrylamide) gels. Langmuir 11:2301-2302.

Zhang X, Wu D, Chu CC. 2004. Synthesis, characterisation and controlled drug release of thermosensitive IPN-PNIPAAm hydrogels. Biomaterials 25:3793-3805.

Zhang X, Zhuo R, Yang Y. 2002a. Using mixed solvent to synthesize temperature sensitive poly(N-isopropylacrylamide) gel with rapid dynamics properties. Biomaterials 23:1313-1318.

Zhang XZ, Wu DQ, Chu CC. 2003. Effect of the cross-linking level on the properties of temperature-sensitive poly(*N*-isopropylacrylamide) hydrogels. Journal of Polymer Science: Part B: Polymer Physics 41:582–593

Zhang XZ, Xu XD, Cheng SX, and Zhuo RX. 2008. Strategies to improve the response rate of thermosensitive PNIPAAm hydrogels. Soft Matter 4:385–391.

Zhang XZ, Yang YY, Chung TS. 2002b. Effect of mixed solvents on characteristics of Poly(*N*-isopropylacrylamide) gel. Langmuir 18:2538-2542.

CHAPTER 5

Development of PNIPAAm Grafted 3D NWF Scaffolds

-Published in 1) Journal of Thermal Analysis and Calorimetry; 2) Biotechnology and Bioengineering; and 3) Colloids and Surfaces A: Interfaces and Engineering aspects

5.1 Introduction

Although the conventional cell culture method based on the use of tissue-culture polystyrene (TCPS) trays is convenient for use in routine work, it is well-known that this method is highly tedious, prone to contamination, and sometimes inaccurate. Due to the constraints and limitations of conventional 2D cell culture (refer to **Section 1.2** for a detailed discussion), researchers, developers, and manufacturers alike, are now turning to 3D cultures for a more physiological representation of mammalian cells. When grown on 3D surfaces, cells maintain more of their native characteristics like phenotype, differentiated state, and other biological functions (Justice et al., 2009). Another major concern with the conventional cell culture method is that enzymes are routinely used to release confluent cells, which damages critical cell surface proteins, growth factor receptors, and cell-to-cell gap junction proteins (Yamato et al., 2007). There thus is a need for a 3D scaffold capable of non-destructive cell release.

The requirements for the ideal cell culture scaffold are as follows:

- It should display a porous structure with open pores to enable cell-cell interactions, oxygenation, nutrient supply to cells, and removal of waste products
- It should display a 3D structure to support cell growth in 3D as opposed to 2D monolayer cultures
- It should enable cells to be released spontaneously from its surface without requiring enzymes or other destructive cell release methods
- It should be low-cost
- It should be cytocompatible to cells without inducing any toxic effects
- It should enable high-density cell culture with ease

Poly(*N*-isopropylacrylamide) (PNIPAAm), a temperature responsive polymer, has revolutionised the cell culture fraternity by providing a non-invasive means of harvesting adherent cells, whereby confluent cells can be spontaneously released by simply cooling the cell culture medium and without requiring enzymes. PNIPAAm is a thermoresponsive polymer that switches its properties reversibly between hydrophobic (cell adhesive) and hydrophilic (non-cell adhesive) states at temperatures higher and lower than its lower critical solution temperature (LCST) (~32 °C) respectively (Schild, 1992). PNIPAAm provides a unique means of harvesting adherent cells, whereby confluent cells can be spontaneously released by simply cooling the cell culture medium (Okano et al., 1995). However majority of the studies which have been conducted to date has focussed on the use of 2D PNIPAAm surfaces, which lack 3D structural support to cells.

The Council for Scientific and Industrial Research (CSIR) is developing a thermoresponsive 3D (T3D) cell culture device consisting of a smart thermoresponsive 3D scaffold housed in a perfused bioreactor, whereby the manual cell culturing steps are automated, and cells are released non-invasively by changing the temperature of the cell culture media, and without requiring enzymes.

This chapter deals with development of the 3D PNIPAAm grafted scaffolds for use in the T3D bioreactor.

5.1.1 Choice of 3D scaffold

When cells are cultured *in vitro*, the scaffold plays a critical role in directing cellular behaviour and performance. The choice of scaffold and scaffold architecture is very important since it is known that a change in environment for cells translate into a change in function and capacity for growth and differentiation. The scaffold should therefore as far as possible resemble the *in vivo* 3D environment of native tissue. Some of the important characteristics of the scaffold include porosity, pore size, pore interconnectivity, surface chemistry, and mechanical properties amongst others (Chang et al., 2011). The porous structure would enable cell-cell interactions and allow diffusion of nutrients and oxygen to the cells. Additionally the 3D structure of the scaffolds would support cell growth in 3D which is known to be superior to 2D cell culture (see detailed discussion in Section 2.).

In this study, a number of different 3D scaffold architectures were considered including hydrogels, foams, porous films, beads, and fibres. PNIPAAm hydrogels based on PNIPAAm were studied in detail (see Chapter 4); however the hydrogels were found to be unsuitable for use in a robust system such as a bioreactor due to their slow response time, poor stability, unsuitable porous structure, dense surface layer at 37°C, and high cost. An initial study was conducted using polyurethane foams as the base scaffold onto which PNIPAAm was attached (unreported). However difficulties were experienced with respect to manufacture of open celled foams and the foams were relatively dense with low free volume. Foams typically display lower open volume compared to non-woven fibers, also reduced interconnectivity of pores. Microbeads are currently quite common for cell culture, however these were excluded in this study, since the surface of microbeads is typically 2D and does not provide cells with the 3D architecture of the ECM; additional they are difficult to handle especially during washing steps. However a fibre-based scaffold whereby the fibres are

bonded into a non-woven fabric (NWF) matrix was found to be the ideal scaffold for cell culture.

A NWF is a scaffold comprised of a sheet or web structure whereby fibers or filaments are bonded together by entangling which can be achieved by various methods such as mechanical, thermal or chemical treatment (Singha et al., 2012) (**Figure 5.1a**). To enable spontaneous cell release from the 3D NWF, (**Figure 5.1b)** the fiber surface was grafted with a layer of PNIPAAm.

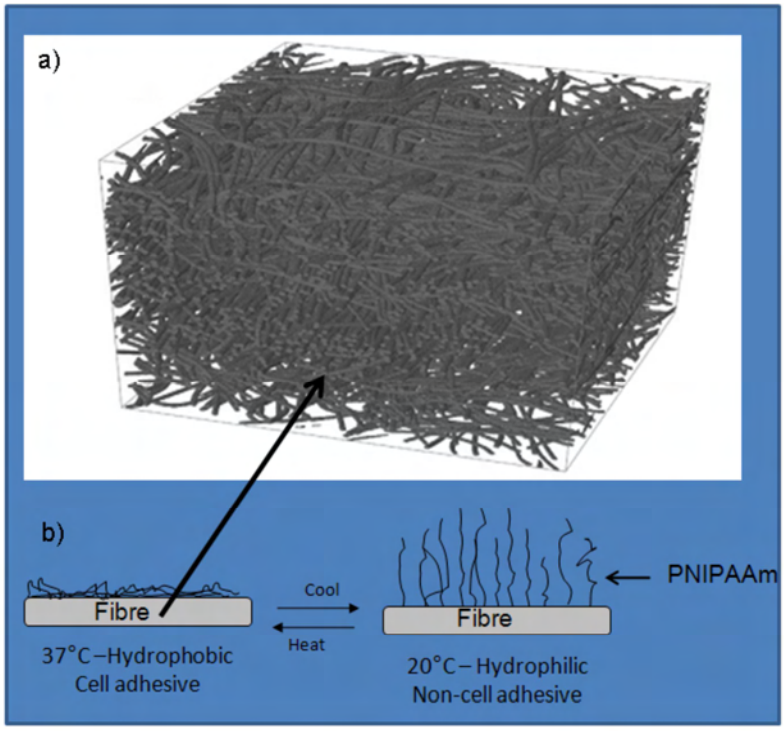

Figure 5.1: (a) 3D image showing morphology of a typical non-woven fabric (Jaganathan et al., 2009) and (b) schematic showing the thermoresponsive behaviour of a single fibre contained in the NWF when the surface is grafted with PNIPAAm.

NWF scaffolds display a number of advantages over other scaffold types, which includes:

- Porous 3D structure
- High porosity content
- High volume of open interconnected pores
- High surface area per volume ratio
- Ease of manipulation of scaffold structure and mechanical properties
- Non-woven manufacture is an industrial method
- Scaffolds can be cut into any size or shape and readily used as a cell culture insert

The NWF scaffolds were manufactured using polypropylene (PP), poly(ethylene)terephthalate) (PET) and nylon 6.6 (nylon) since they can be easily processed into fibres, they are cytocompatible to cells, and have been used for various biomedical applications (Mark, 1999). PP and PET which belong to the polyolefin and polyester polymer classes respectively, are known for low cost, good chemical resistance and mechanical properties (Mark, 1999). Nylon is a polyamide which contains polar groups; it is hydrophilic and displays a similar chemical structure to PNIPAAm which would be desirable for grafting in an aqueous medium.

5.1.2 Graft polymerisation method-OAGP

Techniques reported in literature to graft PNIPAAm onto polymer surfaces include electron-beam radiation, gamma radiation, plasma radiation; UV-irradiation; ozonation; corona-discharge; chemical treatment, and controlled radical polymerisation techniques (Bucio et al., 2005; Contreras-Garcıa et al., 2008; Wan et al., 2009). A major concern with the high energy radiation techniques is unwanted side reactions. Some of these include cross-linking, chain scission, post-irradiation degradation, discolouration, and limited long-term stability of the radiated products (Clough, 2001).

In this study, oxyfluorination-assisted graft polymerisation (OAGP) technique was used to synthesise the PNIPAAm grafted NWF scaffolds. This method is based on surface functionalisation of the NWF using oxyfluorination (or direct fluorination), followed by free-radical graft polymerisation in solution. Oxyfluorination is a polymer surface modification technique which involves treatment of a polymer surface with a F_2:O_2 gas mixture. For direct fluorination, typically a F_2:N_2 gas mixture is used. However it has been reported that oxyfluorination always accompanies direct fluorination due to the presence of oxygen in technical grade nitrogen gas (Kharitonov, 2008). In this study both oxyfluorination and direct fluorination were investigated to functionalise the NWF surfaces. (A detailed discussion on the fluorination process was presented in **Chapter 2**).

Oxyfluorination was preferred over the radiation techniques, since it is dry technology which is simple to perform and it is less invasive than some of the other radiation based surface modification methods. Additionally the main elementary stage of the process is highly exothermic and proceeds spontaneously at room temperature without requiring initiation or catalysts (Kharitonov and Kharitonova, 2009; Lee et al., 2003). The spontaneity of the oxyfluorination process is due to the high electronegativity of fluorine.

It has been reported that when oxygen groups are introduced onto a polymeric surface during oxyfluorination, the surface wettability and adhesion properties are increased. Oxyfluorination is known to form reactive polar groups on polymer surfaces, which can serve as active centres for grafting (Jeong et al., 2011). The main functional groups which have been reported previously include CF, CF_2, CF_3, C(=O)F, C(=O)OH, CO-O$^{\bullet}$ (peroxyradicals), CO-OH (peroxides) (Jeong et al., 2011; Kharitonov, 2008; Lee et al., 2003; Park et al., 2005 ; Woo et al., 2005). The formation of reactive peroxide groups (ROOH; ROOR) and long-lived trapped peroxyradicals (ROO$^{\bullet}$) on oxyfluorinated polymer surfaces have been shown to form active sites for graft polymerisation (Jeong et al., 2011). However, to our knowledge, the use of oxyfluorination as a pre-treatment for graft polymerisation has not been widely reported.

In this study, an oxyfluorination-assisted graft polymerisation (OAGP) method was employed to synthesise the PNIPAAm grafted 3D NWF scaffolds. Development of the 3D PNIPAAm grafted NWF scaffolds involved the following steps:

1) *NWF manufacture:*
   Highly porous NWF scaffolds based on PP, PET and nylon were manufactured using a needle-punching technology

2) *Functionalisation:*
   Oxyfluorination and direct fluorination were investigated as functionalisation techniques to modify the surface of the NWF scaffolds with reactive groups which could then serve as active sites for graft polymerisation.

3) *Graft polymerisation*:
   The NWF (either pre-functionalised or pure) were treated by graft polymerisation in an aqueous NIPAAm solution using ammonium persulphate (APS) as the initiator to produce the PNIPAAm grafted NWF scaffolds.

The NWF scaffolds have been characterised using capillary flow porometer, attenuated total reflectance Fourier transform infrared (ATR-FTIR), X-ray photo electron spectroscopy (XPS), scanning electron microscopy (SEM), static water contact angle, X-ray diffraction (XRD), differential scanning calorimetry (DSC), electron spin resonance (ESR), and UV-VIS spectroscopy.

5.2 Experimental

5.2.1 Materials

PP, PET, and nylon fibres were purchased from FiberVision (Denmark). PP and PET fibres of linear density of 6.7 dtex and fibre staple length of 60 mm were used, while the nylon fibres displayed a linear density of 3.3 dtex and 50 mm fibre staple length. *N*-isopropylacrylamide (NIPAAm) (97%), PNIPAAm (Mw 20 000 g/mol) and ammonium persulphate (APS) (> 98%, ACS reagent) were obtained from Sigma Aldrich and used without further purification. Ethanol, benzene (anhydrous 99.8%), and 2,2-Diphenyl-1-1-picrylhydrazyl were also obtained from Sigma Aldrich. High purity (99.99%) argon and nitrogen gas were obtained from Air Products.

5.2.2 Manufacture of NWF scaffolds

PP, PET, and nylon NWF were manufactured using the needle-punching technology. Manufacture of the NWF was conducted at CSIR Material Science and Manufacturing in Port Elizabeth by Boguslavsky *et al* (Boguslavsky, 2009; Boguslavsky and Anandjiwala, 2007; Boguslavsky et al., 2008). Briefly for the needle-punching process, fibres were either opened (by carding) or unopened and the resulting web was cross-lapped and then needle-punched on the Dilo needle-punching machine (Boguslavsky, 2010). Needle punching involved mechanical intertwining of fibres using needles. To improve the mechanical integrity of the NWF, some of the needle-punched scaffolds were post-treated by a thermo bonding process in an oven with varying conveyor speeds. Five trials were conducted whereby the following parameters were varied, i.e. needling arrangement; depth of needle penetration; speed of needling; and thermo bonding temperature to produce NWF scaffolds with varying morphologies (Boguslavsky, 2009; Boguslavsky and Anandjiwala, 2007; Boguslavsky et al., 2008).

5.2.3 Graft polymerisation of PNIPAAm onto the NWF

Graft polymerisation of PNIPAAm onto the NWF scaffolds was performed on the pre-functionalised NWF scaffolds with the use of APS as the chemical initiator. To verify if grafting could be initiated by the surface peroxy groups, graft polymerisation was also conducted without any chemical initiation. For the latter NWF scaffolds were heated to activate the free radicals. Grafting was also conducted on the pure non-functionalised NWF scaffolds which served as controls.

5.2.3.1 Step 1: Surface functionalisation of NWF

Prior to surface functionalisation, PP, PET and nylon NWF were washed in ethanol to remove impurities, followed by water and then the NWF scaffolds were dried in an oven. Washed NWF scaffolds were treated at Pelchem Pty. Ltd. (SA) by a proprietary method which involved either oxyfluorination or direct fluorination (Louw and Carstens, 2006). The NWF scaffolds were loaded into a reaction vessel and the treatment protocols were as follows:

- *Oxyfluorination*: The reaction vessel was purged with air and partially evacuated, and then a 20:80 (vol%) F_2:N_2 gas mixture at 5 kPa was introduced into the vessel at room temperature for 30 minutes to allow the oxyfluorination reaction to proceed. The gas mixture was then cycle purged from the vessel with air at 25 kPa to complete the oxyfluorination process. The oxygen present in the reactor during the oxyfluorination treatment was from air which was introduced during both the partial evacuation and the cycle purging steps in air.
- *Direct fluorination*: The reaction vessel was fully evacuated and a 5:95 (vol%) F_2:N_2 gas mixture was introduced into the vessel for a given time.

5.2.3.2 Step 2: Graft polymerisation

1) Use of chemical initiation

The experimental set-up which was used for graft polymerisation is shown in **Figure 5.2**. Briefly aqueous solutions of 10 wt% NIPAAm and 10 wt% APS were prepared in deionised water. Oxyfluorinated and direct fluorinated PP, PET, and nylon NWF (prepared as described above) were cut into disks (1.5 cm x 0.7 mm) and each disk was immersed in 10 ml of the APS solution in round bottom flasks and left to swell to saturation at 23 ºC for 16 hrs. Prior to grafting, the solutions were degassed for 30 mins by continuously flowing high purity argon gas into the flasks. The APS solution was decanted, and 10 ml of the NIPAAm (previously degassed) was added into each reaction vessel containing the swollen fluorinated NWF scaffolds. The reaction vessels were immediately capped and graft polymerisation was conducted by immersing the flasks in an oil bath at 70 $^{\circ}$C for 7 hrs. The grafted NWF disks were washed in copious amounts of cold deionised water for 72 hrs with regular water changes to remove PNIPAAm homopolymer or residual monomer. Control grafting experiments were performed using pure non-functionalised NWF scaffolds.

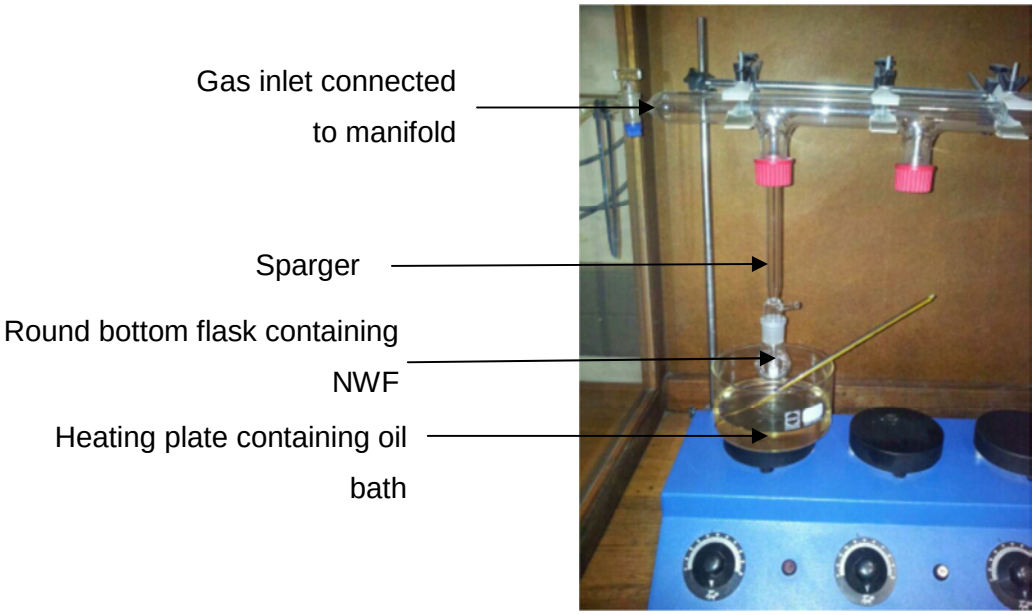

Figure 5.2: Photo showing experimental set-up used for graft polymerisation of PNIPAAm onto NWF scaffolds.

2) Without chemical initiator

Graft polymerisation was also conducted as described above, except the fluorinated samples were swollen directly in 10 wt% aqueous NIPAAm solution overnight and no APS was used. Samples were degassed as above, and then placed in an oil bath at 70 ^{o}C for 7 hrs to enable grafting. The grafted NWF scaffolds were then washed as described previously.

5.2.4 Characterisation of pure and functionalised NWF

5.2.4.1 Physical properties of pure NWF

The pure NWF scaffolds were characterised by Ms Lydia Boguslavsky at CSIR MSM in Pretoria for thickness, mean are weight, pore size distribution, water permeability, and tensile strength (Boguslavsky, 2009; Boguslavsky and Anandjiwala, 2007; Boguslavsky et al., 2008). A capillary flow porometer was employed to determine the pore size distribution and the mean flow pores (MFP) according to the 6212005-134 Test of the ASTM E 1294 Method.

5.2.4.2 Attenuated-total reflectance Fourier transform infrared spectroscopy

A Spectrum 100 FTIR spectrometer was used, with a diamond crystal for attenuated-total reflectance Fourier transform infrared (ATR-FTIR) analysis. For each measurement, 16 scans were taken, with a resolution of 4 cm^{-1} and an average of 8 spots were taken per sample to get representative data. To see the stability of the new functional groups following oxyfluorination, oxyfluorinated PP NWF scaffolds were incubated in water either at 25 °C for 3 hrs or at 70 ºC for 10 mins. Samples were thereafter dried and re-analysed by ATR-FTIR.

Determination of graft yield by ATR-FTIR

A stock solution of 0.8 g/L of PNIPAAm was prepared in ethanol. A serial dilution of the stock PNIPAAm solution was prepared such that the new solutions had the following concentrations: 0.4 g/L, 0.24 g/L, 0.12g/L, 0.04 g/L and 0.002 g/L. A commercially available polypropylene sheet (obtained from a hardware store) was cut into disks of 27 mm diameter and 0.7 mm thickness and weighed. The disks were soaked in 3 ml of PNIPAAm solution each in capped 25 ml beakers for 16 hrs. The ethanol was then evaporated in the oven at 50 ^{o}C. The dried disks were then weighed and characterised by ATR-FTIR. For the peak area ratio determination, the ratio of the carbonyl peak at 1644 cm^{-1} and the methyl group at 1455 cm^{-1} was measured. In the absorbance mode, peaks were first normalised before the peak areas were measured. Using Lamberts-Beer law a calibration graph was constructed by plotting the absorption ratios with the known PNIPAAm concentrations and a linear relationship was predicted between peak intensity and concentration as follows (Skoog et al., 1996):

$$A = \varepsilon c \ell \qquad \text{(Eq 5.1)}$$

whereby A is the absorbance; ε is the molar absorptivity (extinction coefficient) of the absorber, c is the concentration of absorbing species in the material and ℓ is the distance the light travels through the material (i.e. the path length). A trendline was added through the data points and an equation was determined relating peak area ratios to PNIPAAm mass which was used to calculate the graft yield on the scaffolds (µg/cm^2). Statistics was performed using the Anova Single Factor test with α=0.05.

5.2.4.3 X-ray photoelectron spectroscopy

X-ray photoelectron spectroscopy (XPS) was performed to determine the elemental composition of the surface of the NWF scaffolds. A Quantum 2000 (Physical Electronic) scanning XPS was used. The XPS was equipped with an Al K α (1486 eV) X-ray source (20 W), and a beam diameter of 100 µm. Both wide and high-resolution scans for the F1s, O1s, N1s, and the C1s binding energies were performed for all the NWF scaffolds.

5.2.4.4 Contact Angle

The water contact angle of the NWF scaffolds was determined using the Kruss DSA 100. 4 µl of pure deionised water was dispensed onto the surface of the NWF disks using a needle. The contact angle was measured every second with a total drop age of 10 seconds using either the circle or sessile-drop fitting. When measurements were taken at 40 ℃, a heated stage was used, and samples were equilibrated at 40 ℃ in an oven for 1 hr prior to analysis. Measurements were performed in triplicates for each time point.

5.2.4.5 Percent swelling

The pure and oxyfluorinated NWF scaffolds were cut into small pieces with masses ranging between 0.02-0.03 g. The dry mass was taken at time 0 by equilibrating the scaffolds in an oven at 50 ºC for 2 hrs. Scaffolds were placed in 5 ml of water in polytops, and the wet masses were taken after 2, 4, 6, and 24 hrs. Wet NWF scaffolds were gently dabbed between tissue paper. The percent swelling of the NWF scaffolds in water was calculated as follows:

$$\%\ \text{swelling} = \frac{\text{Ww}-\text{Wd}}{\text{Wd}} * 100 \qquad \text{(Eq. 5.2)}$$

where Ww is the weight of the wet NWF, while Wd is the initial weight of the dried NWF.

5.2.4.6 Scanning electron microscopy

Scanning electron microscopy (SEM) was performed to determine the surface morphology of the NWF scaffolds. A LEO 1525 field emission SEM with Oxford's INCA system was used. All samples were sputter coated with carbon prior to imaging.

5.2.4.7 X-ray diffraction

An X'PertPro wide angle X-ray diffraction (XRD) system was used to determine the crystal structure of the NWF scaffolds. A Ni filtered CuKα source was used with radiation of λ= 0.154 nm, with operating conditions of 40 mA, 45 kV, and exposure time of 12 minutes. For the WAXS measurements, 2 theta (2θ) was measured from 5°to 60°for all samples.

5.2.4.8 Differential scanning calorimetry

Differential scanning calorimetry (DSC) was used to measure the heat flux in the NWF scaffolds. A Tzero™ (DSC-Q2000) and a micro DSC (MicroDSCIII apparatus (SETARAM)) were used for determining the melting crystallisation peaks of the NWF scaffolds and the LCST of PNIPAAm on the grafted NWF scaffolds respectively. For the melting and crystallisation curves, NWF scaffolds of mass ranging between 2-5 mg were weighed and pressed in Tzero™ pans and Tzero™ Hermetic lids. Samples were heated from 50 ℃ to 220 ℃ at a heating rate of 20 ℃/min under nitroge n gas. This was followed by an isothermal step at 220 ℃ for 1 min; then a cooling cycle from 220 ℃ to 50 ℃ at 20 ℃ /min; and a final isothermal step at 50 ℃ for 1 minute. Quantitative analysis for melting was obtained from the second heating cycle. The degree of crystallisation was estimated from heat of fusion measurements from the melting thermogram according to:

$$\%\ \text{crystallisation} = \left(\frac{\Delta H_f^*}{\Delta H_f}\right) * 100 \qquad \text{(Eq. 5.3)}$$

where ΔH_f^* is the measured heat of fusion of the sample; and ΔH_f is the heat of fusion of 100% crystalline polymer, which was taken as 146.5 J/g in the case of PP (Huda et al., 1985). For the LCST determination of the PNIPAAm grafted PP NWF scaffolds, 20 mg of dry grafted sample was placed in contact with 500 µL of deionised water and kept at 10 ℃ for 2 hours to obtain equilibrium. The samples were heated from 0 ℃ to 80 ℃ at a heating rate of 0.5 ℃ / min (László et al., 2004).

5.2.4.9 Electron spin resonance

Electron spin resonance (ESR) of the oxyfluorinated PP NWF was conducted using a Bruker Elexsys 500 spectrometer operating at X-band frequencies of ~9–10 GHz, 100 kHz modulation frequency and 1G modulation amplitude. Spectra were recorded as first

derivatives of microwave absorption at ambient temperature, using 2 mW microwave power. Spectra were recorded both at room temperature and at 70 °C.

5.2.4.10 Determination of peroxides using DPPH method

It is well-known that 2,2-diphenyl-l-picrylhydrazyl (DPPH) is a stable free-radical which can be used as radical scavenger to determine peroxide content (Fargere et al., 1995; Ionita, 2005; Jeong et al., 2011). For the DPPH- radical scavenger method, firstly 20 ppm stock solution of DPPH was prepared in benzene, and serial dilutions of 10 ppm, 5 ppm, 2 ppm, and 1 ppm were prepared in volumetric flasks. A calibration graph of absorbance versus concentration was constructed by measuring the UV-VIS absorbance of each DPPH solution at 520 nm using a Lambda 35 UV-VIS spectrometer (Perkin Elmer). The amount of peroxides on the oxyfluorinated PP NWF scaffolds was determined by incubating 1.5 cm NWF disks in 10 ml of 20 ppm DPPH solution in a glass reaction vessel, at 70 ºC for 7 hrs. The control experiments consisted of pure PP NWF, and a blank control (DPPH solution treated as above but without any sample). The moles of peroxide present on the oxyfluorinated PP were determined as follows:

$$\frac{\text{Moles peroxide}}{\text{Surface area of NWF}}\ (\text{Mol.cm}^2) = \frac{(C_0 - C) * V}{2A} \qquad \text{(Eq 5.4)}$$

Where Co is the initial DPPH concentration which was determined from the absorbance of the blank control, C is the concentration of DPPH remaining in solution which was measured after reaction with the oxyfluorinated PP NWF, and V is the volume of the DPPH solution. It is assumed that the molar ratio of peroxide: DPPH is 1:2 (Fargere et al., 1995) .

5.3 Results and discussion

In this study NWF scaffolds based on PP, PET, and nylon were prepared using the needle-punching technology. Two surface functionalisation treatments were investigated to improve the reactivity of the NWF scaffolds towards graft polymerisation. This included direct fluorination and oxyfluorination treatments. Direct fluorination involved exposure of the NWF scaffolds with 5:95 F_2:N_2 gas mixture; while for oxyfluorination a 20:80 F_2:N_2 gas mixture was used, and air was introduced during the partial evacuation and cycle purging steps. The NWF scaffolds were graft polymerised with PNIPAAm in an aqueous medium for use in cell culture. This chapter deals with the synthesis and physicochemical properties of the synthesised NWF scaffolds.

5.3.1 Physical properties of pure NWF scaffolds

Using the needle-punching technique, PP, PET, and nylon NWF scaffolds were produced as shown in **Figure 5.3**. A number of different trials (T1-4) were conducted to manufacture the NWF scaffolds. The processing parameters and physical properties of the scaffolds which were selected for functionalisation appear in **Table 5.1**.

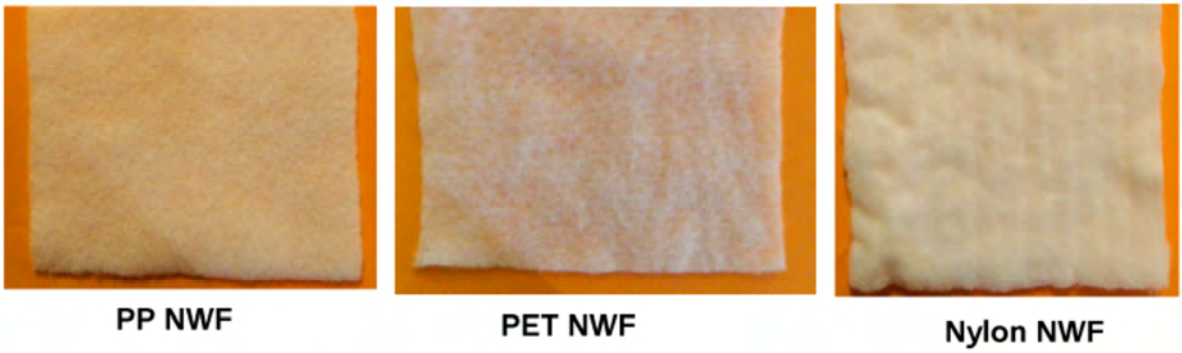

Figure 5.3: Images of PP T2-N6(1), PET T2-N7(1), and nylon T3-N8 developed by needle-punching.

The main criteria for selection of the NWF scaffolds were pore size, porosity, and mechanical integrity. In literature various optimal pore sizes have been reported to encourage cell migration and proliferation (Chang et al., 2011). These include sub-micron pores (1-10 µm) for sub-cellular interactions and for providing oxygenation and nutrient transport as well as larger micron sized pores (100-1000µm) for multiple cellular interactions (Chang et al., 2011). Since pore size also influences the structural stability of NWF scaffolds, in this study, we selected 100-300 µm as the optimal mean pore sizes for the scaffolds. Capillary flow porometry was used to measure the minimum, mean and maximum pore sizes of the NWF scaffolds. A wide range in pore sizes was reported for the manufactured NWF scaffolds (**Table 5.1**), with the MFP diameters for the PP and PET NWF ranging between 100-200 µm which was within the desired range. However for the nylon NWF, the MFP was ~60 µm, which was substantially lower. The smaller pore sizes in the nylon NWF scaffolds were attributed to the lower linear density of the fibres used (i.e. 3.3 dtex compared to 6.7 dtex for PP and PET fibres respectively). To improve the structural stability of the NWF scaffolds, the fibers were thermobonded but pore size was slightly reduced (Boguslavsky and Anandjiwala, 2007; Boguslavsky et al., 2008). The PP and PET NWF showed higher water permeability than the nylon NWF due to the higher pore size of the former (data not shown) (Boguslavsky and Anandjiwala, 2007; Boguslavsky et al., 2008). A higher depth of needle punching and needling from both sides resulted in more intense interlocking of fibres, resulting in more stable structures.

Table 5.1: Processing parameters and physical properties of NWF scaffolds produced by needle-punching technology.

NWF	Batch*	Fibre linear density / dtex	Machine processing parameters			Thermobonding temperature / ºC	Area weight / g.m^{-2}	Thickness / mm	Pore size / µm		
			Needling Arrangement	Feeding speed / m.min^{-1}	Depth of Needling / mm				Min	Mean MFP	Max
PP	T2- N6(1)	6.7	Opened	1.6	10	145	130	3.21	7.74	127.44	247.46
	T4-N11	6.7	Unopened single	0.55	10	-	202	5.1	7.69	101.37	195.6
	T4-N12	6.7	Unopened single	0.55	15	-	95	3.2	7.18	156.84	572.84
	T4-N13	6.7	Unopened double	0.55	6	-	98	3.3	7.68	199.38	411.09
PET	T2-N7(1)	6.7	Opened single	1.6	10	180	150	3.14	7.55	142.55	263.80
Nylon 6.6	T3-N7	3.3	Unopened single	0.25	10	190	195	2.84	6.97	59.37	123.87
	T3 - N8	3.3	Opened	0.25	10	-	103	1.86	7.47	78.82	152.24

(*T refers to the trial number, and N is the NWF number)

5.3.2 Analysis of NWF by ATR-FTIR

ATR-FTIR was used to determine the functional groups on the surface of pure and fluorinated NWF scaffolds (**Section 5.3.2.1**), and PNIPAAm grafted NWF scaffolds (**Section 5.3.2.2**).

5.3.2.1 Assessment of functional groups on NWF before and after fluorination

The functional groups on the NWF scaffolds were assessed before and after fluorination using ATR-FTIR to determine the efficiency of the fluorination process.

1) Pure and fluorinated PP NWF

The chemical structures for pure PP, PET, nylon, and PNIPAAm appear in **Figure 5.4**. Pure PP NWF was characterised by four distinctive absorption bands between 3000-2800 cm^{-1} which were due to the C-H asymmetric and C-H symmetric stretches of the methyl (2950 cm^{-1}; 2868 cm^{-1}) and methylene groups (2917 cm^{-1}; and 2838 cm^{-1}) respectively (**Figure 5.5a**), and two strongly absorbing bands at 1455 cm^{-1}, and 1375 cm^{-1}, which were assigned to the bending vibration of the methylene and isopropyl groups respectively.

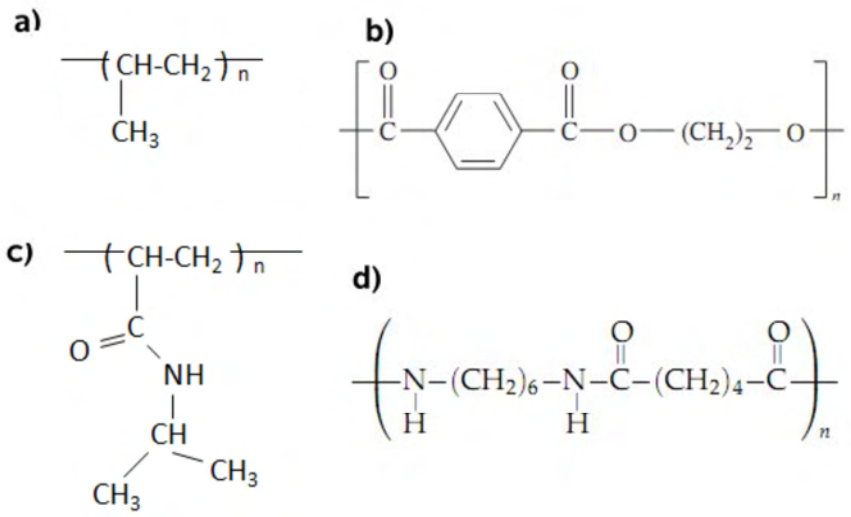

Figure 5.4: Chemical structures of (a) PP; (b) PET; (c) PNIPAAm and (d) nylon.

After the direct fluorination treatment (**Figure 5.5b**), slight changes were observed to the absorption bands of the fluorinated PP. A new broad band appeared at 3100-3550 cm^{-1} which was assigned to the O-H stretching vibration. Additionally at 900-1300 cm^{-1} a declining baseline was observed which could be indicative of a C-F stretching vibration. For the oxyfluorinated PP surface, the changes were more clearly discernible.

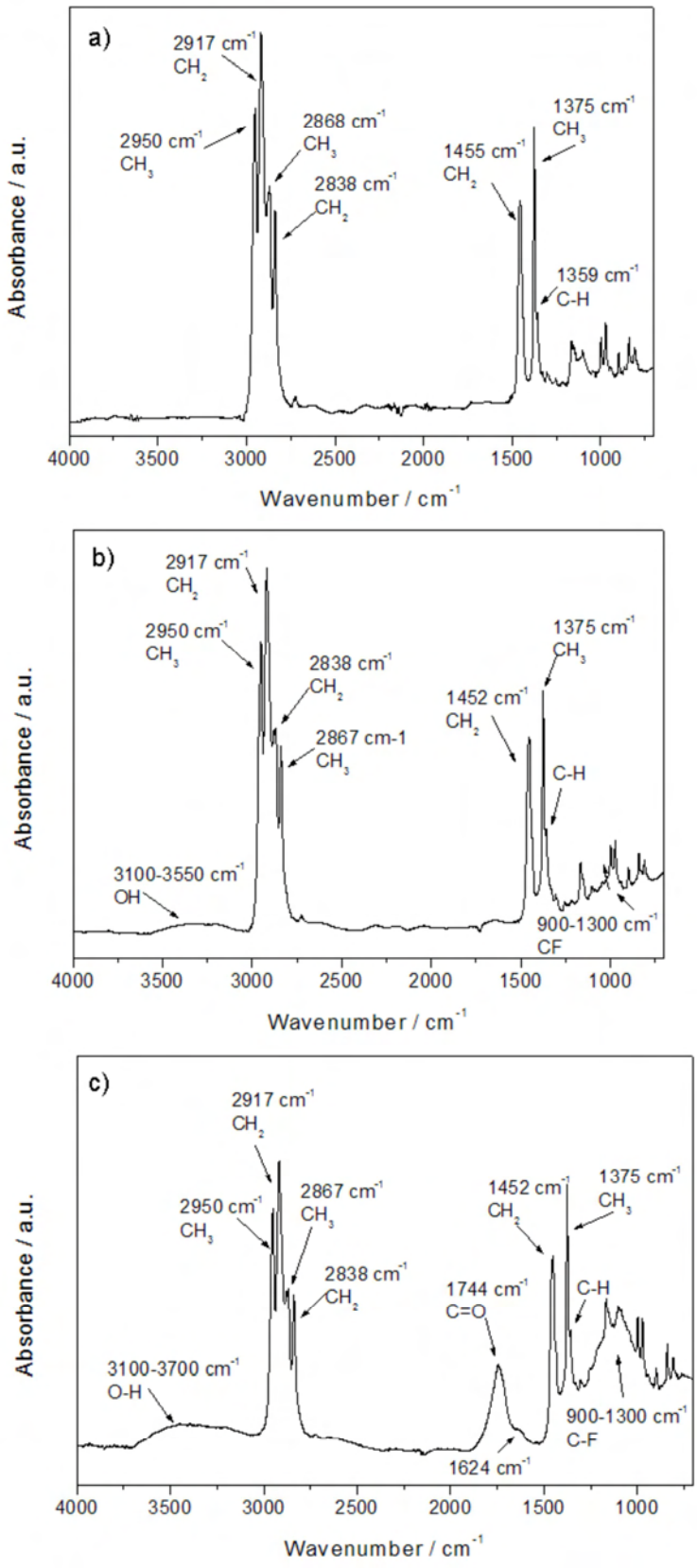

Figure 5.5: ATR-FTIR spectra of (a) pure PP NWF (control) prior to surface functionalisation, and PP NWF after (b) direct fluorination and c) oxyfluorination treatments.

A broad O-H stretching band and a distinctive C=O peak appeared at 3100-3700 cm^{-1} and 1744 cm^{-1} respectively. A small shoulder peak was also observed at 1624 cm^{-1}. Finally a broad diffuse band occurred at 900-1300 cm^{-1} which was attributed to the stretching vibration of the C-F group (Kharitonov and Kharitonova, 2009). It could also be seen that under the present processing conditions, oxyfluorination was more effective than direct fluorination in adding new functionality to the surface of PP NWF scaffolds.

It has been reported previously that direct fluorination of polymers results in replacement of H atoms with F (Kharitonov, 2008). It has also been reported that in the presence of oxygen, acid fluorides, carboxylic acids, peroxy radicals ($RO_2^{\bullet}$) and peroxide groups (ROOH, ROOR) also form on oxyfluorinated surfaces (Jeong et al., 2011; Kharitonov, 2008; Park et al., 2005). Many authors have also shown that the acid fluoride groups (-COF) which display an absorbance peak at 1850 cm^{-1} easily hydrolyse by moisture to the corresponding carboxylic acid which displays an absorbance peak at 1750 cm^{-1} (du Toit and Sanderson, 1999; Kharitonov et al., 2005; Lee et al., 2003). Only trace levels of COF was seen on the PP NWF scaffolds following oxyfluorination.

Due to the presence of the C=O and OH peaks on the oxyfluorinated PP NWF scaffolds, it can be assumed that the acid fluoride groups may have already hydrolysed to the corresponding carboxylic acid. The band at 1744 cm^{-1} could possibly indicate a carboxylic acid (CHF-(C=O)OH; α-fluoroester –CHF–(C=O)–O–; α-fluoroaldehyde –CHF–(C=O)H; or a α-fluoroketone $–CH_2–(C=O)–CHF–$ (Kharitonov and Kharitonova, 2009). A weak shoulder band at 1624 cm^{-1} has been reported previously following oxyfluorination of low-density polyethylene and it was attributed to both C=O vibration in the enol form of the β-diketones –(C=O)–CF=C(OH)– or the double bond C=C (e.g. –FC=CH–) stretching vibration (Kharitonov and Kharitonova, 2009). A summary of the main adsorption bands for pure PP appear in **Table 5.2**. For the C-F stretching vibration for the oxyfluorinated PP, peak maximum was observed at ~ 1160 cm^{-1} and 1150 cm^{-1} which was attributing to CF, CF_2 and CF_3 groups (Kharitonov and Kharitonova, 2009). After oxyfluorination, the CH_3, CH_2, and CH PP peaks were still present indicating that PP was only partially fluorinated. According to Kharitonov, the formation of a totally fluorinated polymer having a Teflon-like structure $(–CF_2–CF_2–)_n$ is not common by fluorination, since the latter needs a duration exceeding several weeks or even months at conditions exceeding industrially acceptable limits (Kharitonov and Kharitonova, 2009).

Hydrolysis post-treatment of the oxyfluorinated PP NWF revealed a decrease in peak intensities of the newly formed functional groups as shown in **Figure 5.6**.

Table 5.2: Assignment of FTIR peaks for pure PP NWF scaffolds (Mark, 1999; Socrates, 2001).

Functional group	Wavenumber / cm^{-1}	Peak assignment
Methyl (CH_3)	2950	CH_3 asymmetric stretch
	2868	CH_3 symmetric stretch
	1455	CH_3 asymmetric bend
	1375	Isopropyl
Methylene (CH_2)	2917	CH_2 asymmetric stretch
	2838	CH_2 symmetric stretch
	1455	CH_2 bend
Methyne (CH)	1359	C-H bend
	1300-700	C-C vibrations

Changes were observed to all of the newly formed functional groups, i.e. O-H, C=O and the C-F groups on the oxyfluorinated PP NWF when samples were treated in water at either room temperature or at elevated temperatures. It is likely that the lower ATR-FTIR peak intensities can be attributed to direct hydrolysis of the new functional groups. Studies have indicated that fluorinated esters are very unstable due to the high electronegativity of the fluorine group and can undergo rapid hydrolysis even under neutral conditions (Uchimaru et al., 2003). It can be postulated that oxyfluorination resulted in a fluorine substituted ester, which degrade due to hydrolysis.

Additionally the lower ATR-FTIR peak intensities can be attributed to a reduction in the Lewis basicity of the oxyfluorinated PP surface during hydrolysis due to conversion of the pure carbonyl group of the acid fluoride to carboxylic acid (Tu et al., [1997]). According to Tu et al., during hydrolysis, an inter-hydrogen bonded conjugated structure occurs in oxyfluorinated PP between two neighbouring COOH groups. This inter-hydrogen bonded structure could likely reduce the net dipole on the carbonyl peak and neighbouring C-F peaks, which would account for the reduced peak intensities of the newly formed oxyfluorinated groups after hydrolysis. Also after hydrolysis, the shoulder peak at ~1623 cm^{-1} grew in intensity. Absorption at 1620-1623 cm^{-1} was also reported by Kharitonov *et al* following hydrolysis of oxyfluorinated low density polyethylene which was attributed to C=O vibration in the enol form of the β-diketone or the double bond C=C stretching vibration (e.g. FC=CH) (Kharitonov, 2008). Further investigations are required to confirm the structural changes on oxyfluorinated PP upon hydrolysis.

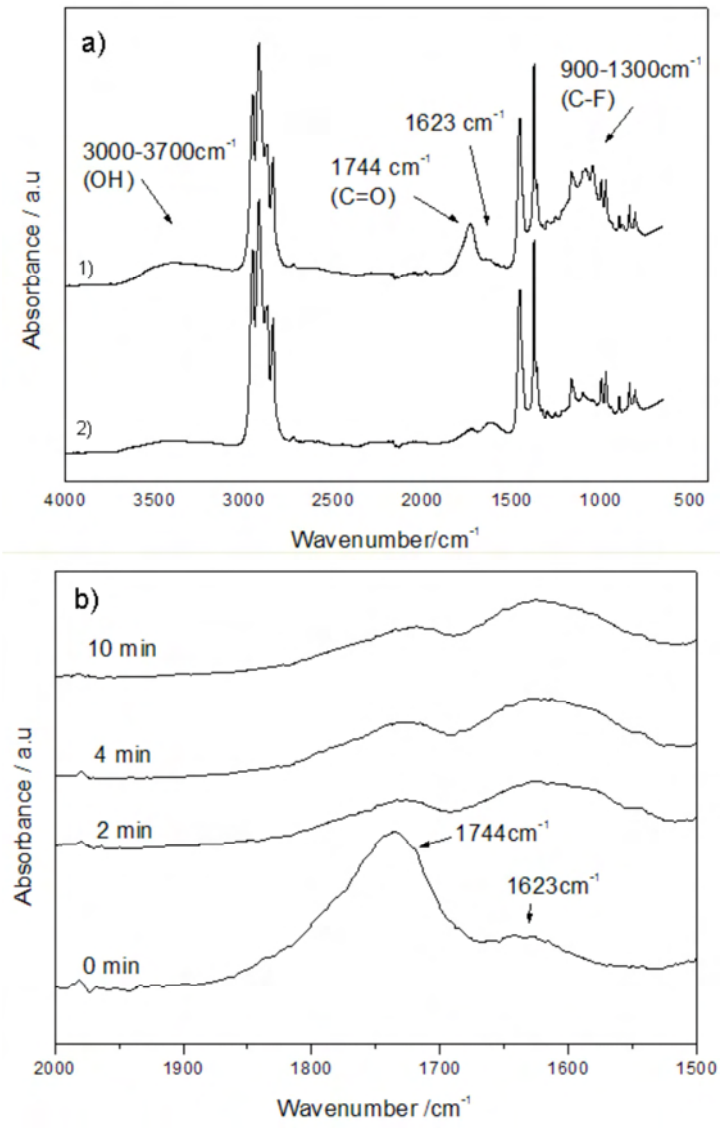

Figure 5.6: ATR-FTIR spectra of hydrolysis post-treatment of oxyfluorinated PP (a) at 25 °C (1) before hydrolysis and (2) after hydrolysis; and (b) treatment at 70 ºC for 0-10 minutes.

2) Pure and fluorinated nylon and PET NWF

The ATR-FTIR spectra for pure and functionalised nylon appear in **Figure 5.7** and a summary of the peaks is given in **Table 5.3**. For nylon 6.6 the main absorption bands were due to methylene and amide groups in the polymer backbone. For the amide group, the peak assignments were as follows: 3295 cm^{-1}; 1632 cm^{-1}; and 1532 cm^{-1} which were assigned to amide II N-H stretch, amide I C=O stretch, and the N-H bend/C-N stretch respectively (Mark, 1999).

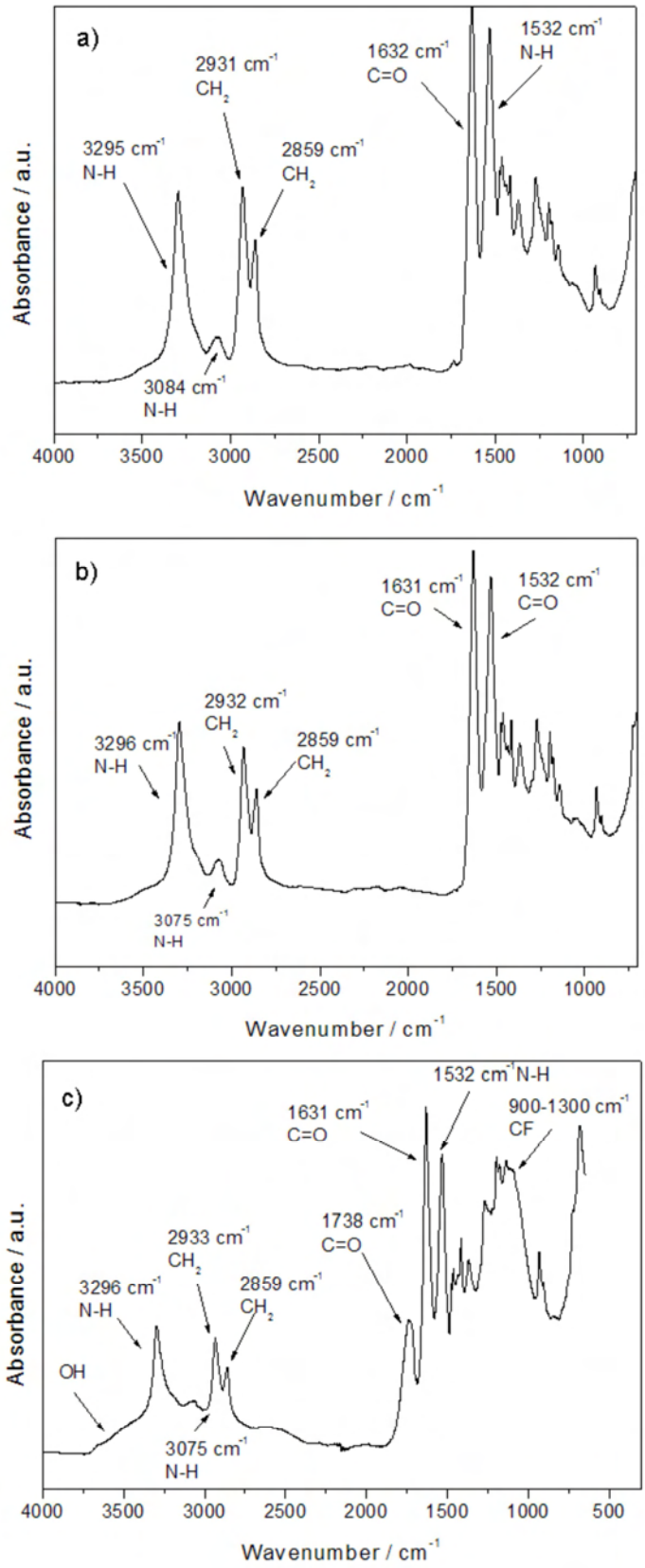

Figure 5.7: ATR-FTIR spectra of (a) pure nylon NWF (control) prior to surface functionalisation, and following (b) direct fluorination and (c) oxyfluorination treatments.

Table 5.3: Assignment of FTIR peaks for pure nylon 6.6. and PET NWF scaffolds (Mark, 1999; Socrates, 2001).

Functional group	Wavenumber / cm^{-1}	Peak assignment
Nylon		
Methylene	2931	CH_2 asymmetric stretch
	2859	CH_2 symmetric stretch
	1460	CH_2 symmetric scissors deformation
	1440	CH_2 symmetric scissors deformation – (CH_2 next to N)
	1420	CH_2 symmetric scissors deformation – (CH_2 next to C=O
	1370	CH_2 wag
	722	CH_2 rock
Amide	3295	Amide II N-H stretch
	3084	NH bend overtone
	1632	Amide I C=O stretch
	1532	N-H bend/C-N stretch
	1200	N-C=O skeletal vibration
	1170	N-C=O skeletal vibration
	700	N-H wag (broad)
PET		
Carbonyl	1712	C=O stretch
Aromatic ester	1242	Asymmetric stretching of C-O-C due to aromatic ester
	1095	Symmetric stretching of C-O-C due to aromatic ester
	722	Aromatic ring out of plane deformation

The CH_2 asymmetric and symmetric stretch appeared at 2931 cm^{-1} and 2859 cm^{-1} respectively, and between 1500-700 cm^{-1} numerous smaller peaks were present due to the amide I, II and CH_2 bond interactions. After direct fluorination, changes to the chemical structure of nylon could not be clearly distinguishable from that of pure nylon. However oxyfluorination was successful in introducing new surface groups on the nylon NWF. A new absorption peak was identified at 1738 cm^{-1} and a broad diffuse band appeared at 900-1300 cm^{-1} which corresponded to C=O and C-F stretching vibrations respectively. On careful examination, a broad O-H shoulder peak was also discernible at around 3500-3700 cm^{-1}.

For the PET NWF scaffolds (**Figure 5.8**), many adsorption bands were seen in the IR region.

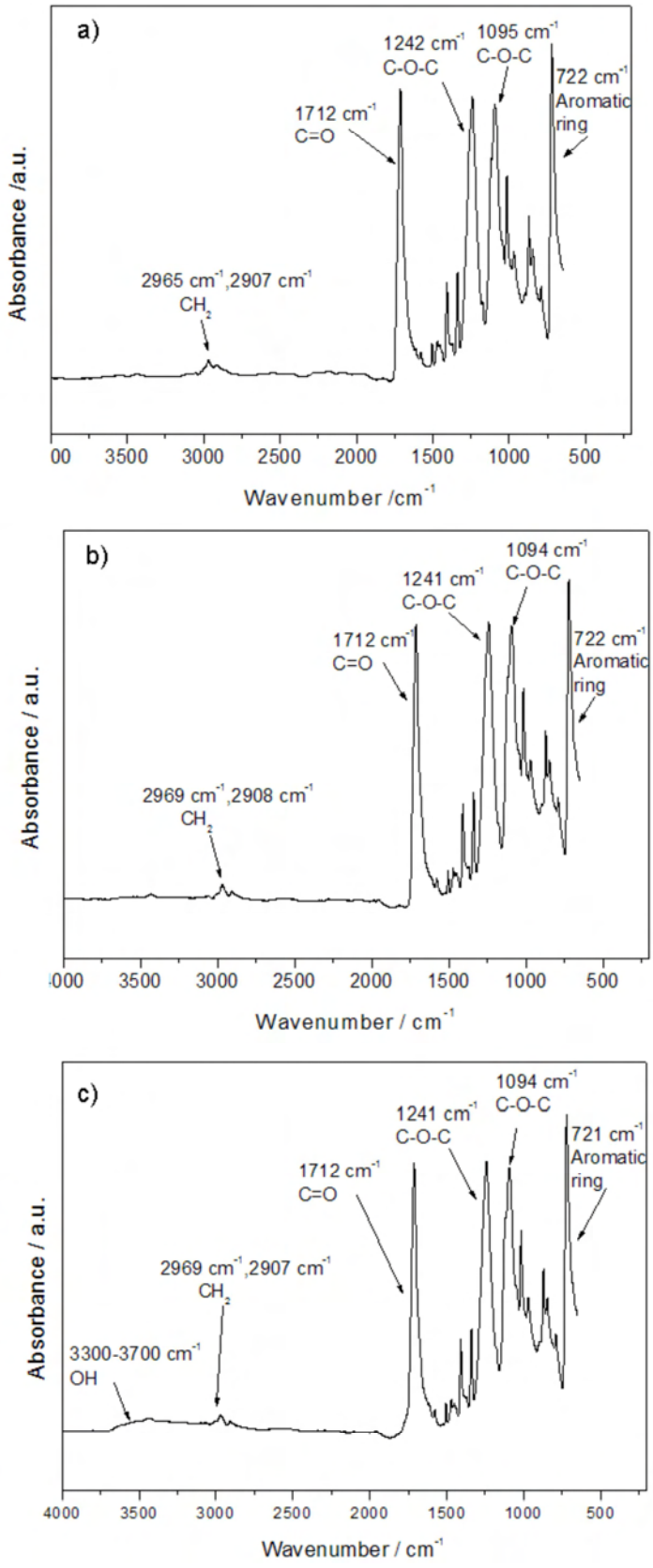

Figure 5.8: ATR-FTIR spectra of (a) pure PET NWF (control) prior to surface functionalisation, and following (b) direct fluorination and c) oxyfluorination treatments.

The most distinctive peaks for PET occurred at 1712 cm^{-1}; 1242 cm^{-1}; 1095 cm^{-1}; and 722 cm^{-1} which were due to the C=O of the ester group, the asymmetric and symmetric stretching respectively of the C-O-C group, and the out-of plan deformation of the benzene ring respectively (Socrates, 2001). After direct fluorination, no new functionality could be detected on the PET surface by ATR-FTIR while after oxyfluorination a slight OH peak could be seen at 3500-3700 cm^{-1}. Due to overlapping IR peaks occurring in the C=O and C-F region emanating from the PET backbone, it was unclear if any further modification occurred on the PET surface, due to the oxyfluorination treatment.

For all of the NWF scaffolds investigated, oxyfluorination was superior to direct fluorination for surface modification of the NWF scaffolds. The lack of functionality following the direct fluorination treatment may be due to the low F content (5:95 F_2:N_2) which was present during the direct fluorination as compared to the oxyfluorination treatment (20:80 F_2:N_2). The low fluorine content in the former may have been insufficient to replace a significant number of H atoms on the polymer backbones. Additionally studies have previously reported that F_2/O_2 gas mixtures achieve stronger fluorination compared to when F_2 is used alone (Lee et al., 2003). It is known that fluorine requires a Lewis acid such as O_2 due to its small orientational polarizability, such that when oxygen is present, it acidifies the surface and the fluorination reaction is kinetically more favourable whereby F_2 is reduced to the basic F^- anion (Lee et al., 2003). Hence the Lewis acidity of the oxyfluorination process and the higher F content used may have contributed to improving the efficiency of oxyfluorination of the NWF scaffolds.

A summary of the main absorption bands on the oxyfluorinated NWF scaffolds is given in **Table 5.4**. Of the polymers investigated in this study, PP displayed the highest modification after oxyfluorination, which was followed by nylon and then PET. PP was easily modified by fluorination, due to the tertiary C in its structure (**Figure 5.4**). It is well-known that tertiary C-H bonds are the weakest, and that tertiary H's are abstracted at the fastest rate compared to secondary or primary hydrogens (Pryor, 1966). Hence of the polymers investigated, PP was the most susceptible to forming free radicals. Nylon was also easily modified by oxyfluorination, however due to its smaller pore size, the nylon NWF scaffolds were not preferred for cell culture. PET, on the other hand was the least susceptible to formation of free radicals due to the resonance effect of the aromatic ring. PET displayed a relatively poor propensity to form free radicals on the polymer backbone (Bhattacharya et al., 2004).

Table 5.4: Summary of new functional groups present on the NWF scaffold which was detected by ATR-FTIR after oxyfluorination.

Sample	Wavenumber / cm^{-1}	Peak Assignment
Oxyfluorinated PP	3100 - 3700 1744 1624 900-1300	O-H C=O C=O or C=C C-F
Oxyfluorinated Nylon	3500-3700 1738 900-1300	O-H C=O C-F
Oxyfluorinated PET	3300-3700	O-H

5.3.2.2 Assessment of PNIPAAm grafted NWF scaffolds

To ensure all PNIPAAm homopolymer was removed from the grafted NWF scaffolds, grafted scaffolds were thoroughly washed in cold water for several days prior to analysis. PNIPAAm homopolymer is water soluble at temperatures < 32℃. Graft polymerisation was performed on the oxyfluorinated and pure NWF scaffolds (control) with and without APS as the initiator.

1) ATR-FTIR analysis of PNIPAAm

The ATR-FTIR spectrum for PNIPAAm is given in **Figure 5.9**. The most distinctive absorption bands for PNIPAAm was the broad associated amide (N-H) stretching (~3300 cm^{-1}), triplet peaks assigned to the asymmetric and symmetric stretches of the methyl groups (at 2971 cm^{-1} and 2880 cm^{-1} respectively) and the anti-symmetric stretch of the methylene group (at 2930 cm^{-1}). Additionally sharp amide I peaks (C=O and C-N stretching) and amide II (N-H deformation bands and C-N stretching) occurred at 1639 cm^{-1} and 1529 cm^{-1} respectively. A summary of the main absorption peaks for PNIPAAm homopolymer is tabulated in **Table 5.5**.

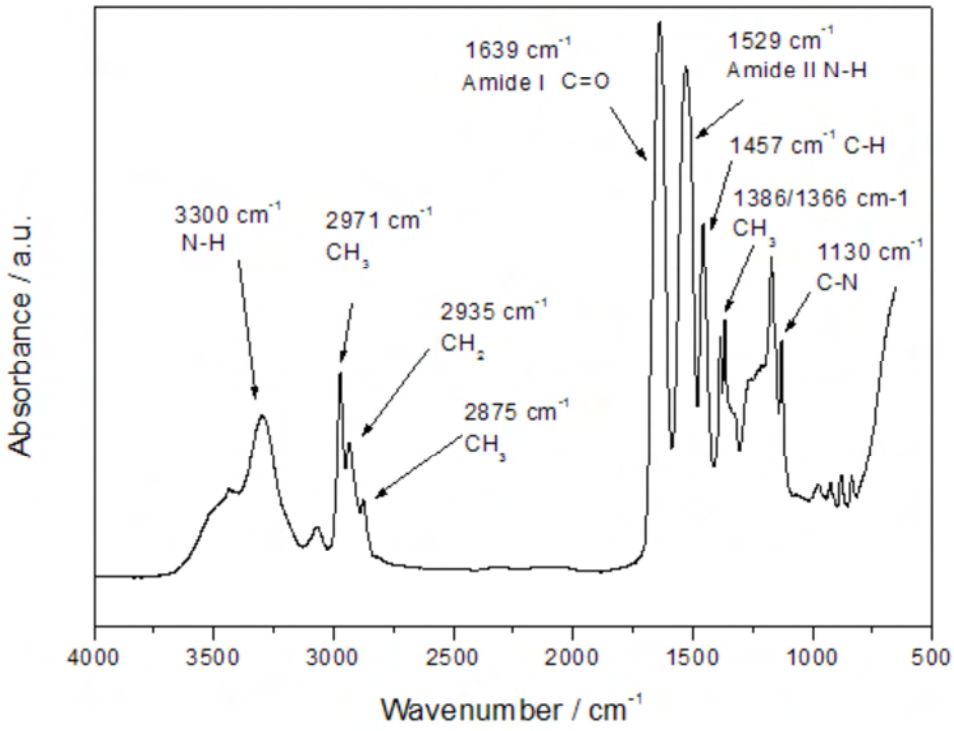

Figure 5.9: ATR-FTIR spectrum for pure PNIPAAm (Sigma).

Table 5.5: The FTIR absorption peak assignment for pure PNIPAAm homopolymer.

Functional group	Wavenumber / cm^{-1}	Assignment
Methyl CH_3	2971	C-H asymmetric stretch
	2875	C-H symmetric stretch
	1457	C-H asymmetric bend
	1386/1366	Isopropyl (doublet)
Methylene CH_2	2935	C-H asymmetric stretch
	2875	C-H symmetric stretch
	1457	C-H bend
Amide	3300-3100	Associated N-H stretch
	3065	Overtone of amide II N-H
	1639	Amide I C=O and C-N stretch
	1529	Amide II N-H in plane deformation (bend) and C-N stretch
	1130	Amide III C-N stretch and NH in plane deformation

2) ATR-FTIR spectra of PP-*g*-PNIPAAm

The ATR-FTIR spectra when graft polymerisation was performed on the functionalised PP NWF scaffolds appear in **Figure 5.10**. After graft polymerisation new peaks associated with PNIPAAm appeared on the grafted PP NWF following both the oxyfluorination and direct fluorination treatments. For the grafted PP NWF scaffolds, the new peaks occurred at 3290 cm^{-1} and 3301 cm^{-1}; 1643 cm^{-1} and 1644 cm^{-1}; and 1542 cm^{-1} respectively which were assigned to the amide (N-H) stretching vibration, amide I (C=O and C-N) stretching and amide II (N-H deformation and C-N stretching) bands respectively. The presence of PNIPAAm absorption bands in the grafted NWF scaffolds, confirmed the PNIPAAm layer on the PP-*g*-PNIPAAm NWF. The CH_3 and CH_2 peaks for pure PP were still present on both grafted samples indicating that the PP backbone was preserved during graft polymerisation. Additionally from **Figure 5.10** it was observed that the C=O peak which was present on the oxyfluorinated PP NWF prior to grafting, diminished after graft polymerisation. Also the broad C-F stretching vibration after oxyfluorination, could still be detected on the grafted NWF but it was reduced (**Figure 5.10b**). We identified the C=O peak on the oxyfluorinated NWF as a possible fluorinated ester which may have being hydrolysed during graft polymerisation.

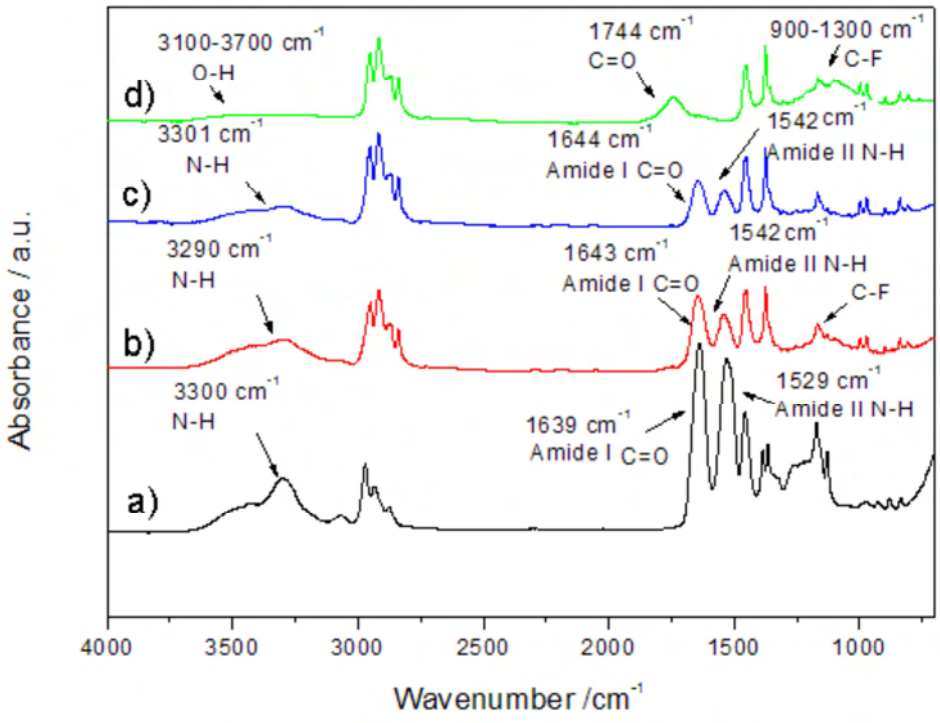

Figure 5.10: ATR-FTIR spectra of (a) PNIPAAm homopolymer control, (b) PP-*g*-PNIPAAm (grafting on oxyfluorinated PP), (c) PP-*g*-PNIPAAm (grafting on direct fluorinated PP); (d) oxyfluorinated PP control.

Interestingly shifts in the amide I and II peaks were observed for the grafted PP NWF (for both oxyfluorinated and direct fluorinated PP) compared to PNIPAAm homopolymer indicating a change in the molecular structure of the groups. For the PP-*g*-PNIPAAm NWF, the amide I and amide II bands shifted to higher wavenumbers (**Table 5.6**) after grafting which could be due to a change in H-bonding (Liu et al., 2005).

Table 5.6: FTIR absorption wavenumbers for PNIPAAm and PP-*g*-PNIPAAm on pre-oxyfluorinated surfaces.

NWF	C=0 / cm^{-1}	N-H / cm^{-1}
Pure PNIPAAm	1639	1529
PP-*g*-PNIPAAm	1643	1542

It is known that H bonding associated with the C=O group in a molecular structure can influence the position of absorption bands in the IR region. According to Lui *et al* the stronger the H bonding involving the C=O group, the lower the electron density surrounding the C=O group, hence the lower the absorption frequency and wavenumber. It is known that in PNIPAAm, intramolecular H bonding occurs between the C=O and N-H groups (**Figure 5.11**).

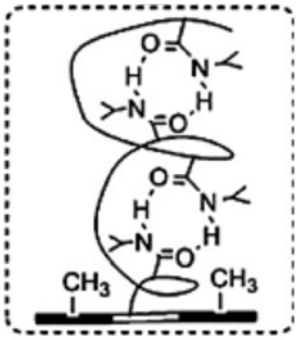

Figure 5.11: Schematic showing intramolecular H bonding between the C=O and N-H groups in PNIPAAm which can influence the absorption frequencies for the amide I and II groups (Gu et al., 2011).

It can be postulated that in the grafted structure, the placement of PNIPAAm moieties on the PP backbone is irregular therefore less H bonding is expected between the C=O and N-H groups compared to pure PNIPAAm, where the molecules are more densely packed than in the graft. Weaker H bonding would then result in a higher electron density available around the amide I and II groups which would result in higher absorption wavenumbers for both groups.

Graft polymerisation was also performed on pure non-functionalised PP as a control **(Figure 5.12)**. Results indicated that without functionalisation, PNIPAAm was still detected on the PP surface following graft polymerisation even though the PP surface was thoroughly washed following graft polymerisation. This was confirmed by the amide I and amide II peaks. It was postulated that the presence of PNIPAAm on the PP surface may be due to homopolymer adsorption rather than grafting. The PNIPAAm peak intensities on the pure grafted PP were substantially lower compared to when the scaffolds were fluorinated prior to grafting.

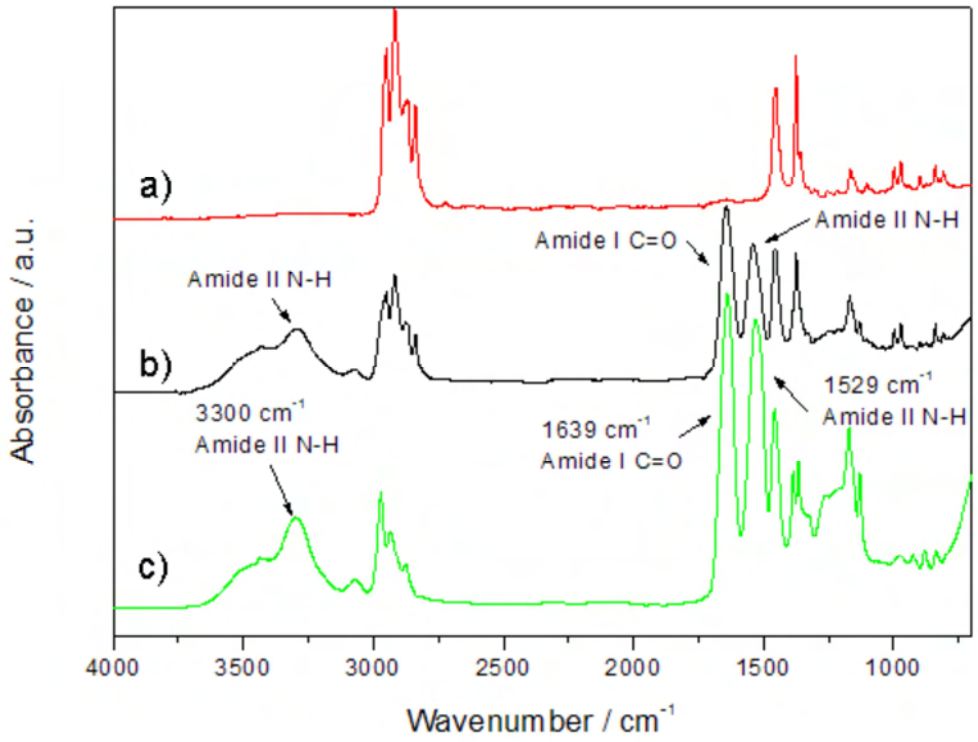

Figure 5.12: ATR-FTIR spectrum of (a) PNIPAAm homopolymer; (b) PP surface after graft polymerisation (without pre-functionalisation); and (c) pure PP.

3) ATR-FTIR spectra of PET-*g*-PNIPAAm NWF

The ATR-FTIR spectra for the grafted PET NWF scaffolds when oxyfluorinated and pure NWF scaffolds were used appear in **Figures 5.13 - 5.14**. For the grafted PET NWF scaffold, the presence of PNIPAAm peaks in the grafted scaffolds could not be clearly identified when either oxyfluorinated or direct fluorinated PET NWF scaffold was used. On closer examination, however a small amide peak was visible around 3300 cm^{-1}. This peak was more discernible when pure PET was used (**Figure 5.14**), which may be due to homopolymer formation on the pure PET surface. Additionally for both samples, the C=O peak at 1712 cm^{-1} displayed a shoulder peak which was assigned to the amide I C=O and C-

N peak of PNIPAAm. Furthermore a small peak at 1540 cm^{-1} associated with the amide II deformation peak of N-H and C-N stretch was also detected.

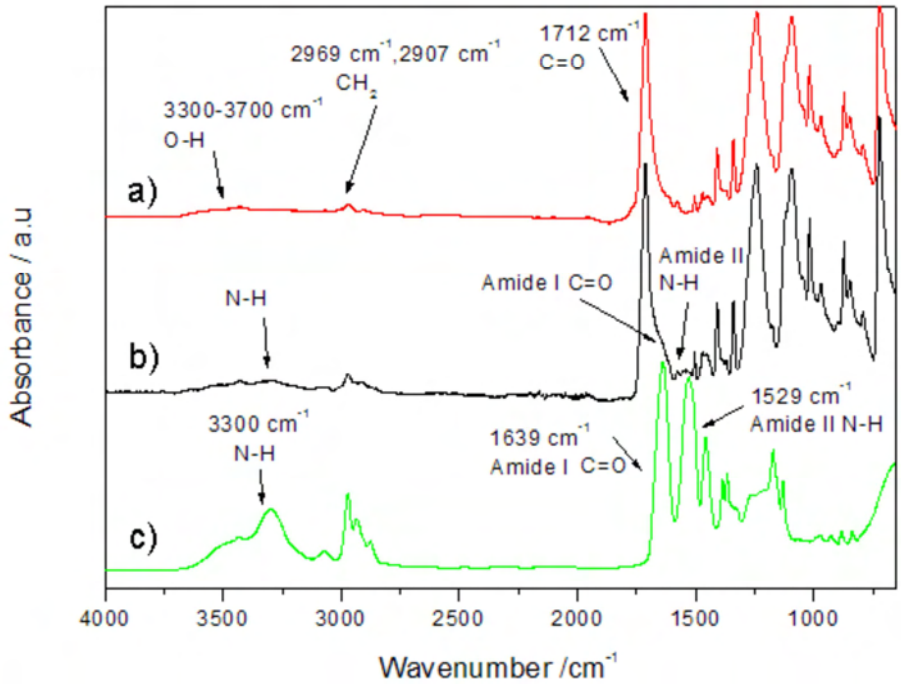

Figure 5.13: ATR-FTIR spectra of (a) pure PET NWF; (b) PET-*g*-PNIPAAm (pre-oxyfluorinated) (c) PNIPAAm control.

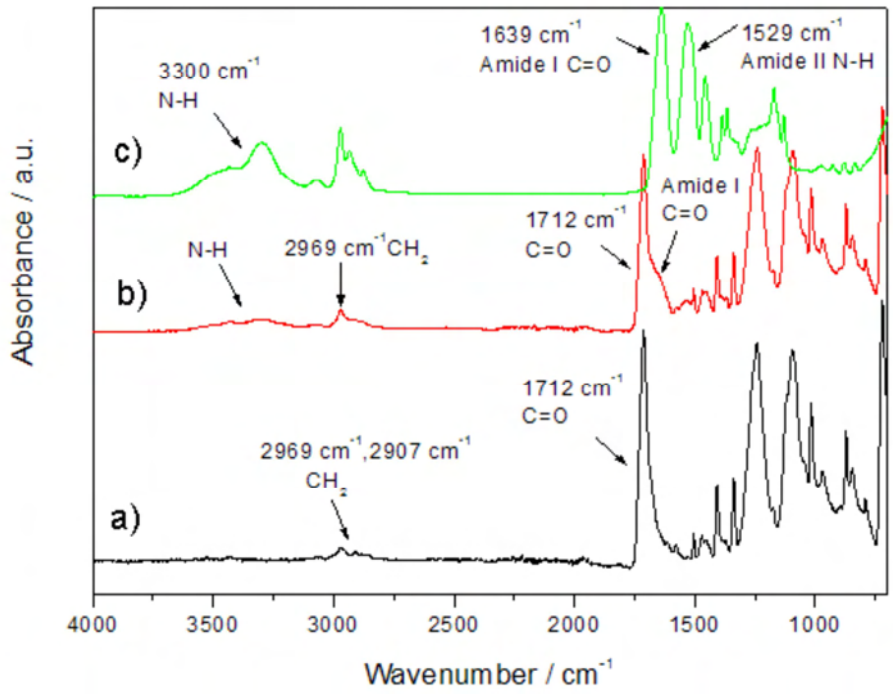

Figure 5.14: ATR-FTIR spectrum of (a) pure PET NWF; (b) PET-*g*-PNIPAAm (without pre-functionalisation); and (c) PNIPAAm.

4) ATR-FTIR spectra for nylon-*g*-PNIPAAm

The ATR-FTIR spectra for nylon-*g*-PNIPAAm when oxyfluorinated nylon was used appear in **Figure 5.15.** Detection of PNIPAAm in the nylon-*g*-PNIPAAm NWF scaffolds posed a challenge since both nylon and PNIPAAm are polyamides, and display similar functional groups and similar absorption bands are expected in the infrared region. Hence the amide I and II absorption regions could not be used for detecting PNIPAAm chains on the nylon surface. The difference in chemical composition between PNIPAAm and nylon, is that only the former contains a methyl group. Other authors have reported that the absorption band of 2970 cm^{-1} attributed to the CH_3 asymmetric stretching of PNIPAAm chains can be used to monitor the grafting of PNIPAAm onto nylon (Wang and McCord, 2007).

From **Figure 5.15**, the CH_3 stretching peak due to PNIPAAm could not be detected on the grafted nylon NWF, indicating that graft polymerisation may have been unsuccessful however due to the small intensity of the 2970 cm^{-1} peak in PNIPAAm, use of this peak was not reliable for confirming graft polymerisation on nylon.

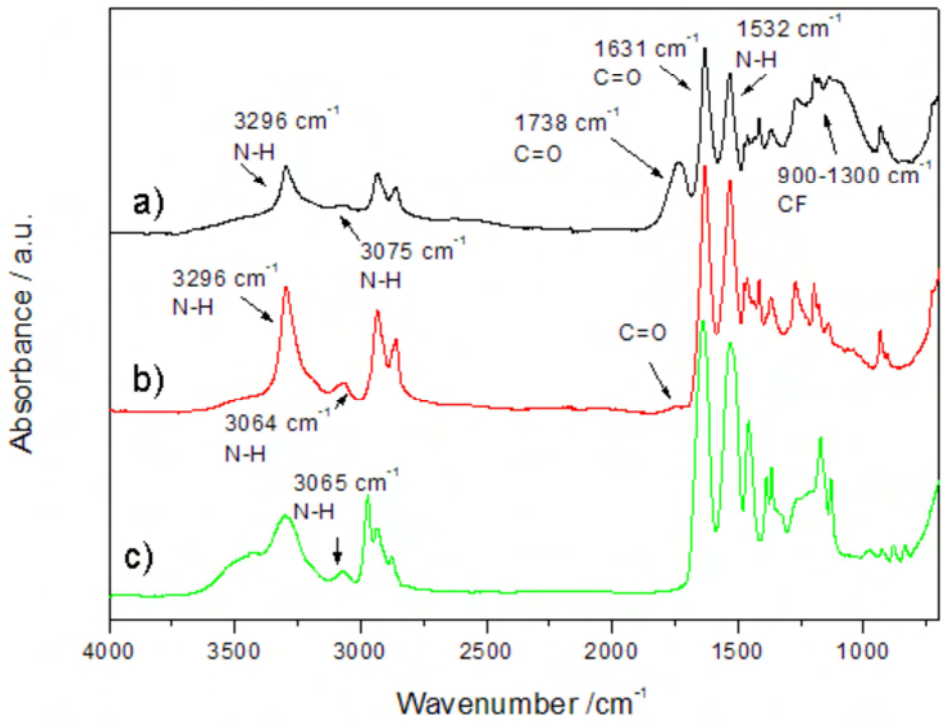

Figure 5.15: ATR-FTIR spectrum of (a) oxyfluorinated nylon NWF; (b) nylon-*g*-PNIPAAm (pre- oxyfluorinated), and (c) PNIPAAm homopolymer control.

However it was observed that the N-H overtone vibration band which appeared at 3075 cm^{-1} on the oxyfluorinated nylon shifted to 3064 cm^{-1} in the nylon-*g*-PNIPAAm spectrum, which corresponded to the N-H overtone band in pure PNIPAAm (i.e. 3065 cm^{-1}). Additionally it was also observed that the new functional groups i.e. C=O, C-F, and O-H (present after oxyfluorination) were reduced after graft polymerisation as was the case when graft polymerisation was on oxyfluorinated PP. Similar results were seen when graft polymerisation was conducted on pure nylon. However after analysis of various spots on the grafted nylon NWF, the CH_3 peak was detectable on some areas of the NWF confirming that the PNIPAAm layer was present; however the graft layer varied and was non-homogenous **(Figure 5.16).** Since no active groups were present on the pure nylon to induce grafting, it was postulated that homopolymerisation formed on pure nylon surface during graft polymerisation.

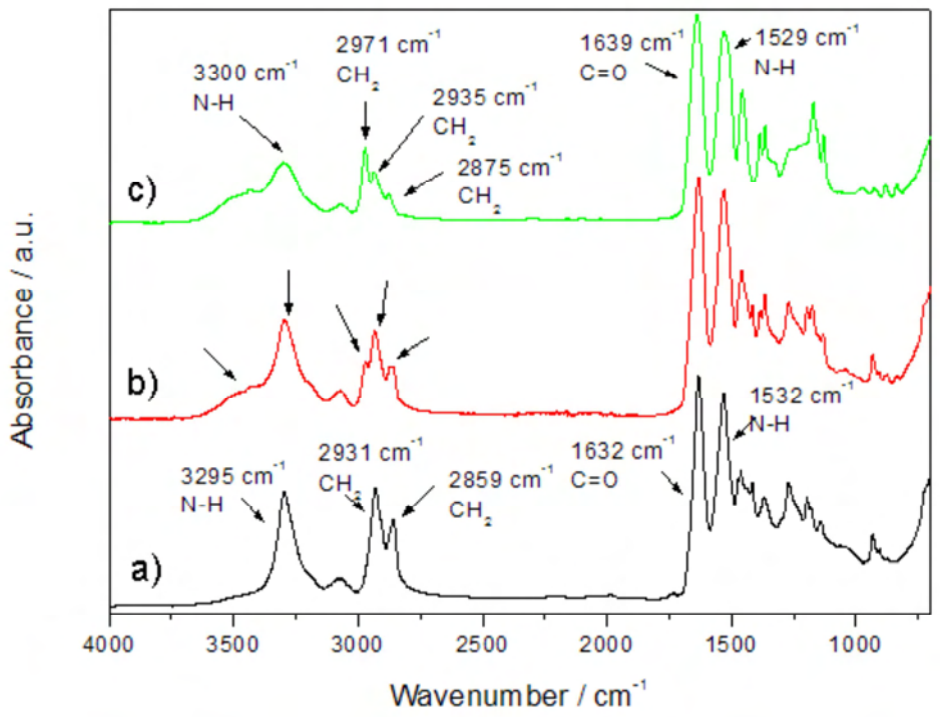

Figure 5.16: ATR-FTIR spectra of (a) pure nylon NWF; (b) nylon-*g*-PNIPAAm (without pre-functionalisation) and (c) PNIPAAm homopolymer control.

5) Graft polymerisation on the NWF in the absence of initiator

It has previously been reported that oxyfluorination produces peroxide and hydroperoxide groups on the surface of polymers which can then be used as active sites for graft polymerisation without any exogenous initiators (Jeong et al., 2011). To verify if graft

polymerisation was possible by heat activation only, grafting was attempted on oxyfluorinated and direct fluorinated NWF scaffolds without the use of a chemical initiator. Pure NWF scaffolds were used as the control.

Of all the NWF tested, the PNIPAAm graft layer was only confirmed when the oxyfluorinated PP NWF was used (**Figure 5.17**). Graft polymerisation was unsuccessful without an initiator on the direct fluorinated and pure NWF scaffolds (data not shown). This result indicates that either peroxides or trapped free radicals (peroxy, fluorine) are present on the oxyfluorinated PP NWF. Upon heating, the peroxide groups would undergo cleavage to form active peroxy radicals, or trapped radicals would diffuse out to the surface which can then induce initiation of the graft polymerisation reaction without requiring an exogenous initiator.

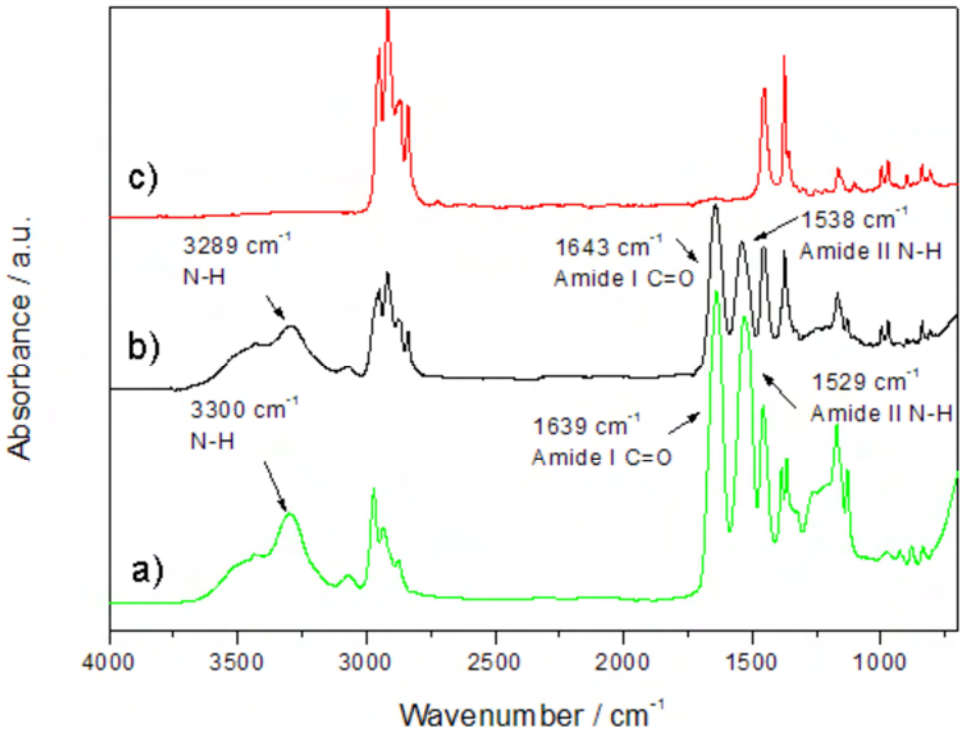

Figure 5.17: ATR-FTIR spectra of (a) PNIPAAm control; and PP-*g*-PNIPAAm NWF scaffolds when graft polymerisation was without initiator and grafting was performed on (b) oxyfluorinated PP NWF; and c) direct fluorinated PP NWF.

However using both oxyfluorinated PET and nylon NWF scaffolds, PNIPAAm could not be detected on the grafted surfaces by ATR-FTIR, using this method, which indicates that peroxy groups or trapped peroxy radicals were absent on these surfaces or were insufficient to induce a significant amount of graft chains on the polymer backbone. Also as we observed previously when graft polymerisation was performed on oxyfluorinated PP, the new functional groups following oxyfluorination (i.e. C=O, O-H, C-F) were reduced after graft

polymerisation. Seeing that grafting could not be confirmed on the nylon NWF scaffolds using ATR-FTIR, it can be assumed that C-F and C=O functional groups (which were also reduced for nylon) do not play a role in initiating graft polymerisation, and these bonds are not the active sites for grafting.

6) Graft yield determination from ATR-FTIR

To determine the graft yield of PNIPAAm onto PP NWF, a semi-quantitative calibration graph was constructed based on the peak area ratios of the C=O peak (at 1644 cm^{-1}) to the C-H peak on PP (at 1455 cm^{-1}). Flat disks were incubated in a series of PNIPAAm solutions of known concentrations in polytops. PNIPAAm of a known mass was precipitated on the PP disks, and the peak area ratios were measured. The difference in intensity of the peaks was attributed to the concentration or mass of the PNIPAAm layer. Anova single factor statistical test was conducted to determine the statistical significance of the results. Accurate results could not be obtained when the NWF scaffolds were used for determining the calibration graph due to the porous structure of the NWF scaffolds. The calibration graph is given in **Figure 5.18**.

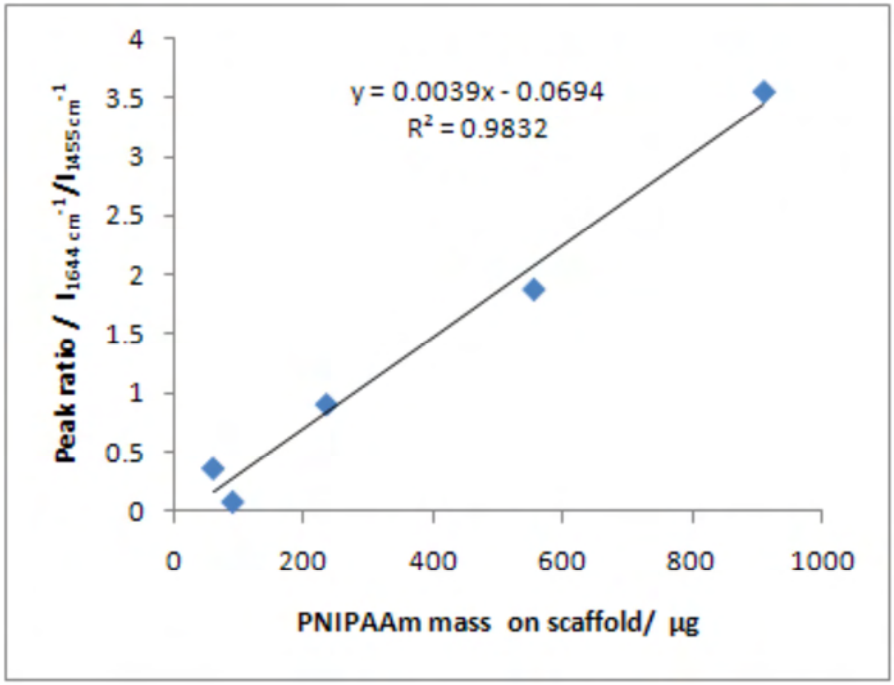

Figure 5.18: Calibration graph showing relationship between PNIPAAm mass on scaffolds and intensity of the peak area ratios of the C=O peak (at 1644 cm^{-1}) to the CH_3 peak in PP (at 1455 cm^{-1}).

From the equation of the graph, parameter x (i.e. PNIPAAm mass) was calculated as follows:

x=(y + 0.0694) / 0.0039 (Eq 5.5)

Where y is the peak area ratios and x is the PNIPAAm mass.

The graft yield was expressed as PNIPAAm mass/ total surface area of the NWF disks. The total surface area of the NWF disks (**Equation 5.13**) was derived for PP (T4-N13) using the NWF physical properties as follows:

- NWF disk area (A_{NWF}):

  $$A_{NWF} = \pi r^2$$ (Eq 5.6)

  Where r is the radius of the NWF disk (0.075 cm), and π = 3.14159.

- NWF weight (M_{NWF}):

  The mass of the NWF could be determined by weighting the sample or alternatively it could be calculated from the A_{NWF} (m^2) and the mean area weight M/A_{NWF} (g/m^2) as follows:

  $$M_{NWF} = A_{NWF} * M/A_{NWF}$$ (Eq 5.7)

- NWF volume (V_{NWF})

  The volume of the NWF (V_{NWF}) was calculated using the M_{NWF} (g) and the density of PP (ρ) (g/cm^3) as follows:

  $$V_{NWF} = \frac{M_{NWF}}{\rho_{NWF}}$$ (Eq 5.8)

  ρPP was taken as 0.903 g/cm^3

- Total surface area of NWF(A_{Total})

  The total surface area of the NWF can be determined using the volume of a fibre as follows:

  $$A_{total} = \pi dl$$ (Eq. 5.9)

  Where π = 3.14159, d is the diameter of a fibre, and l is the length of a fibre. The Volume of a fibre (V_{fibre}) is as follows:

  $$V_{fibre} = \frac{\pi}{4} d^2 l$$ (Eq 5.10)

  Where $l = \frac{4 * V_{fibre}}{\pi d^2}$ (Eq 5.11)

  $$A_{NWF} = \pi d * \frac{4 * V_{fibre}}{\pi d^2}$$ (Eq 5.12)

A_{total} (cm^2) was then derived as: $A_{NWF} = \frac{4V_{NWF}}{d_{fibre}}$ (Eq. 5.13)

By dividing by the mass of the NWF the total surface area per 1 g of NWF could be determined.

The total surface area of the PP NWF disks with mean flow pores of 200 µm (T3-N13) was determined to be ~25 cm^2 i.e. ~1400 cm^2/g. This compares relatively well to some of the 3D scaffolds on the market (**Table 5.7**). It should be noted that the total surface area available for cell culture in the bioreactor can be increased substantially by stacking a number of NWF disks onto each other.

Table 5.7: Relative surface areas of currently available 3D scaffolds versus NWF scaffold of present study (Fibra-Cel ® disks, 2012; GE Healthcare, 2012).

Competing 3D scaffolds	**Surface area (cm^2/g)**
Fibra-Cell disks	1200
Cytodex 1	4400
Cytodex3	2700
PP NWF scaffold of present study	~1440

Using the graft yield and a density of PNIPAAm of 1.1 $g.cm^3$, the graft thickness could also be calculated by **Equation 5.14** as follows:

$$\text{Graft thickness (nm)} = \frac{\text{Graft yeild (g/cm}^2\text{)}}{\rho_{\text{PNIPAAm}}\left(\frac{\text{g}}{\text{cm}^3}\right)} * 10^7 \quad \text{(Eq 5.14)}$$

The graft yield for PP-*g*-PNIPAAm NWF scaffolds when grafting was on oxyfluorinated and pure PP NWF appear in **Figure 5.19**. PNIPAAm graft yield on the PP NWF was ~24 ± 6 µg/cm^2 on grafted pre-oxyfluorinated NWF when APS was used; which was found to be significantly higher compared to when pre-oxyfluorinated NWF was used without initiator (9 ± 6 µg/cm^2, p= 1.7x10^{-7}); or when grafting was on pure PP with APS (2 ± 0.3 µg/cm^2, p = 8.4x10^{-12}). This corresponded to an average PNIPAAm layer thickness of ~220 ± 54 nm; 92 ± 60 nm; and 19 ± 3 nm respectively. For the pure PP NWF scaffolds, it is postulated that PNIPAAm homopolymer formed on the PP surface rather than grafting. When grafting was performed on the oxyfluorinated PP without initiator, large deviations were observed between samples, which may be attributed to the instability of the peroxide groups and/or the trapped radicals on the PP surface upon storage.

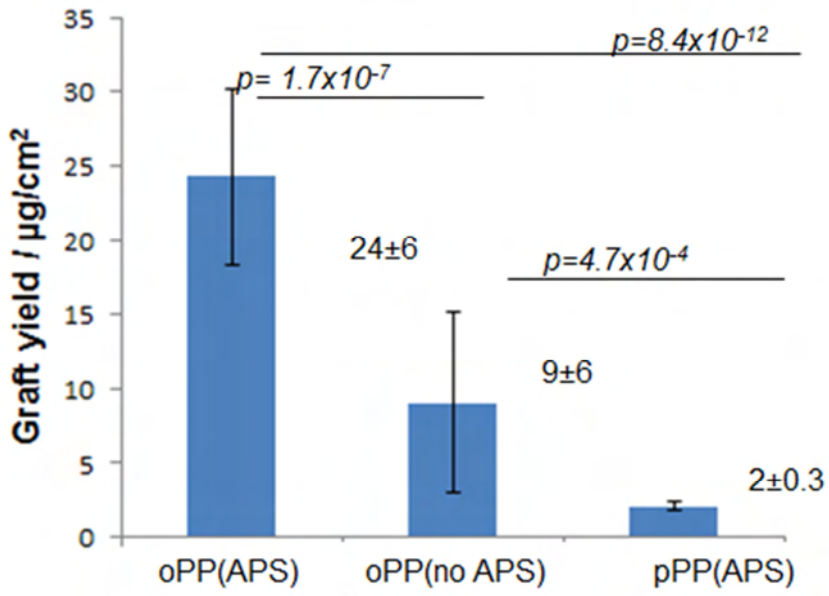

Figure 5.19: Graft yield determination for PP-*g*-PNIPAAm whereby grafting was performed on oxyfluorinated PP with APS treatment [oPP(APS)]; oxyfluorinated PP without APS treatment [oPP(no APS)], and pure PP with APS treatment [pPP(APS)].

PNIPAAm surfaces with various graft thickness have been developed previously for cell culture. Studies conducted by Akiyama *et al* have demonstrated that endothelial cells only attached onto PNIPAAm TCPS trays of graft thickness 15.5 nm ± 7.2 nm (1.4 ± 0.1 µg/cm^2), whereas no cells attached on surfaces when the graft layer was thicker (29.3 nm ± 8.4 nm, i.e. 2.9 ± 0.1 µg/cm^2) (Akiyama et al., 2004). An optimum PNIPAAm graft thickness of ~15-20 nm was reported for optimal cell attachment/release (Akiyama et al., 2004). In the present study, the graft thickness reported is relatively high. However as discussed in **Chapter 2**, discrepancy exists in the literature with regards to the optimum graft thickness (Kumashiro et al., 2010). Also it should be noted that the morphology of the NWF of the current study differs substantially to that of 2D TCPS on which most of the previous studies are based. Hence the dehydration/hydration of the PNIPAAm layer to enable cell attachment/release will also be different. Refer to **Chapter 6** for the cell culture studies using the PP-*g*-PNIPAAm NWF scaffolds.

5.3.3 XPS analysis

Since graft polymerisation on PP gave the most promising results, XPS analysis was only performed on the PP NWF scaffolds.

5.3.3.1 XPS analysis of functionalised NWF scaffolds

To investigate the changes to the chemical functionality of the NWF scaffold surfaces after fluorination, XPS studies were also conducted. The wide XPS spectra for pure PP NWF, direct fluorinated PP NWF, and oxyfluorinated PP NWF appear in **Figure 5.20**.

For the pure PP NWF, mainly C (and a small amount of oxygen) was detected, however for the direct fluorinated and oxyfluorinated PP, various functional groups including oxygen, fluorine, and nitrogen formed on the surface of PP. The new functional groups display high electronegativity and could be responsible for increasing the hydrophilicity of the direct fluorinated and oxyfluorinated PP (Woo et al., 2005).

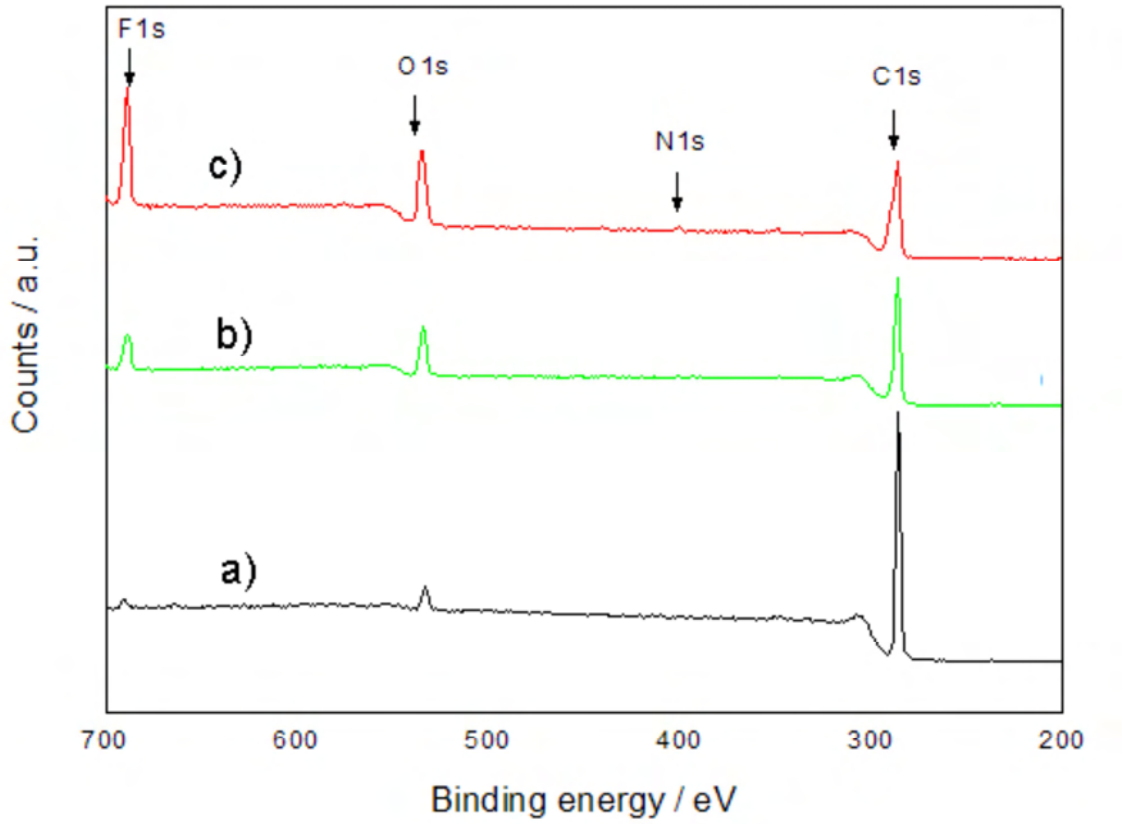

Figure 5.20: Wide XPS spectra of (a) pure PP NWF; (b) direct fluorinated PP NWF; and (c) oxyfluorinated PP NWF.

The high resolution C1s spectra for pure PP, fluorinated PP, and oxyfluorinated PP is given in **Figure 5.21**. From the C1s spectra, only one symmetric peak was measured for the pure PP NWF at 284.8 eV (with 100 % peak area), which represents the C-H of the PP backbone (Lee et al., 2003). For the direct fluorinated and oxyfluorinated PP, asymmetric C1s spectra

were observed which were fitted with multiple peaks due to new fluorine and oxygen functionality.

For the direct fluorinated PP the following peaks were identified: 284.8 eV (C-H); 286.5 eV (C-O), and 287.9 eV (CHF-CH_2, CHF-CHF); while for the oxfluorinated PP, peaks were assigned as follows: 284.7 eV (C-H); 286.4 eV (C-O); 287.8 eV (CHF-CH_2, CHF-CHF), and 288.9 eV (C=O) (Lee et al., 2003; Park et al., 2005).

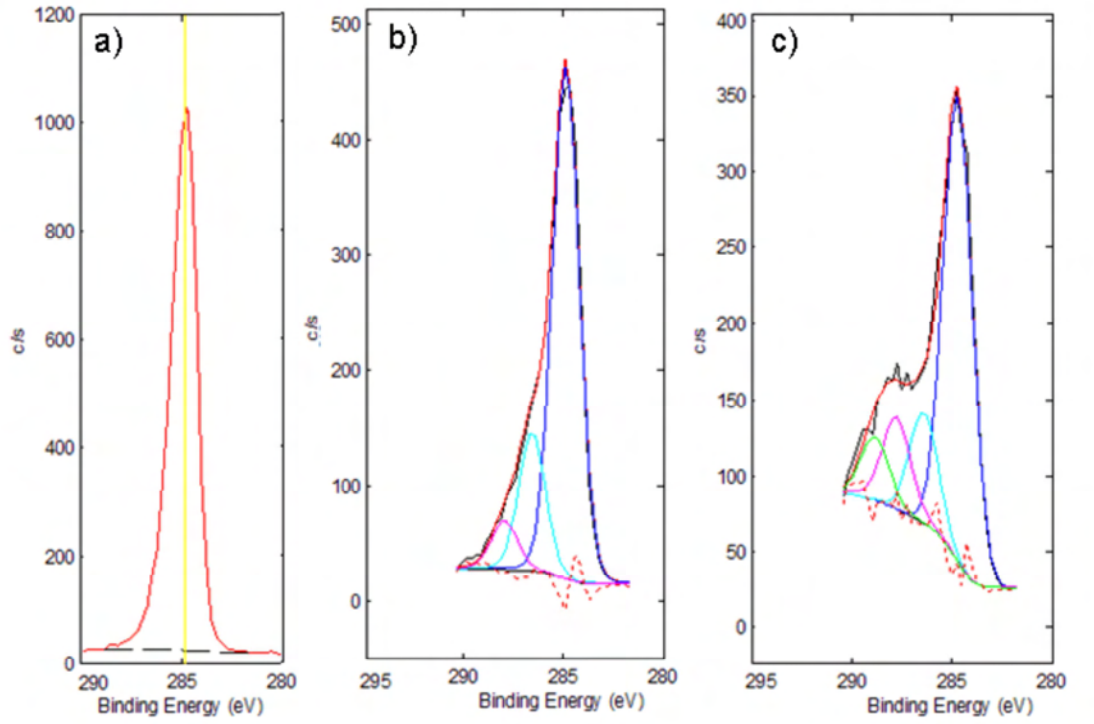

Figure 5.21: Narrow C1s for (a) pure PP NWF; (b) direct fluorinated PP NWF; and (c) oxyfluorinated PP NWF.

From the binding energies in **Table 5.8**, it can be seen that some of the hydrogen's of the C-H group of the PP backbone was substituted with either F or O atoms following the fluorination treatment. The relative amount of the C-H group at 284 eV decreased from 100% for pure PP to 72.69% and 63.12% for direct fluorinated and oxyfluorinated PP respectively. The O1s peak increased from 4.2 % (atomic) for pure PP NWF, to 14.8 % (atomic) and 18.2 % (atomic) for direct fluorinated and oxyfluorinated PP respectively, while F1s peak almost doubled from 9.1 % (atomic) for direct fluorinated PP to 17.9 % (atomic) for the oxyfluorinated sample. These results indicate that the extent of modification was the highest for the oxyfluorination process compared to direct fluorination, and corroborates with the ATR-FTIR data.

Table 5.8: Atomic percent of C, O, F, and N present on the surface of pure and functionalised PP NWF and probable peak assignments (Lee et al., 2003; Park et al., 2005 ; Woo et al., 2005).

Element	Atomic concentration / %	Binding energy / eV	Area %	Assignment
C1s				
Pure PP	94.8	284.8	100	CH
Direct fluorinated PP	76.1	284.8 286.5 287.9	72.69 20.00 7.31	CH C-O CHF-CH_2;CHF-CHF
Oxyfluorinated PP	62.5	284.7 286.4 287.8 288.9	63.12 14.95 13.45 8.49	CH C-O CHF-CH_2;CHF-CHF C=O
O1s				
Pure PP	4.2	532.2	100	C-O
Direct fluorinated PP	14.8	532.6	100	C-O
Oxyfluorinated PP	18.2	533.3	100	C-O-C
F1s				
Pure PP	-	-	-	-
Direct fluorinated PP	9.1	686.9	100	C-F
Oxyfluorinated PP	17.9	687.4	100	C-F
N1s				
Pure PP	-	-	-	-
Direct fluorinated PP	-	-	-	-
Oxyfluorinated PP	1.4	389.8	100	N-H

On pure PP, ~4.2 at% of elemental oxygen was detected from the O1s spectra at 532.2 eV. The presence of a small amount of oxygen on pure PP was reported previously and was attributed to the impurities incorporated in PP as a result of degradation occurring during processing in air (Kranz et al., 1994). Oxygen was also detected on the direct fluorinated PP by XPS, even though O was not directly introduced into the reactor during this process.

It is known that commercial fluorine contains trace amounts of oxygen, and other authors have indicated that fluorination always accompanies oxyfluorination (du Toit and Sanderson, 1999). According to Kranz *et al* even a small O_2 content of 1 vol% during fluorination can still result in significant changes to the oxygen functionality (C=O, COF) (Kranz et al., 1994). The oxygen present in the reactor during the oxyfluorination treatment was mainly from air which was introduced during both the partial evacuation and the cycle purging steps in air.

The high-resolution O1s and F1s spectra for the direct fluorinated and oxyfluorinated PP NWF scaffolds, showed single peaks at 532.2 eV & 533.3 eV and 686.9 eV & 687.4 eV which were assigned to the presence of C-O, and C-F respectively (Park et al., 2005). Formation of fluorinated groups such as -C-F, $-CF_2$, and/or $-CF_3$ are preferential due to the higher energy of the C-F bond compared to C-H (Kharitonov, 2008). Some nitrogen was also detected on oxyfluorinated PP, which may be due to the high N_2 content used during oxyfluorination.

The F/C, O/C, and F/O ratios were higher for the oxyfluorination process compared to direct fluorination (**Table 5.9**). Since the oxyfluorination treatment demonstrated superior performance, oxyfluorinated PP underwent further analysis.

Table 5.9: Atomic ratios for F, C, and O present on pure, direct fluorinated and oxyfluorinated PP surfaces.

Atomic ratios	**F /C**	**O / C**	**F /O**
Pure PP	-	0.04	-
Direct fluorinated PP	0.6	0.2	0.1
Oxyfluorinated PP	1.0	0.3	0.3

5.3.3.2 XPS analysis of PP-*g*-PNIPAAm NWF scaffolds

The C1s XPS spectra for the PP-*g*-PNIPAAm NWF scaffolds, when graft polymerisation was conducted on oxyfluorinated, direct fluorinated and pure NWF scaffolds appear in **Figure 5.22.** In each case, the C1s spectra were fitted with three peaks and peak assignments were as follows: C1s: 284.8-284.9 eV (CH_3, CH_2, CH); 286.5-286.6 eV (CH-NH); 287.9-288 eV (C=O: 10.47). The amide group on the grafted PP NWF was confirmed by the O1s and N1s spectra which displayed single peaks at 531.2 eV(C=O) and 399,6 eV (N-H) respectively (Akiyama et al., 2007).

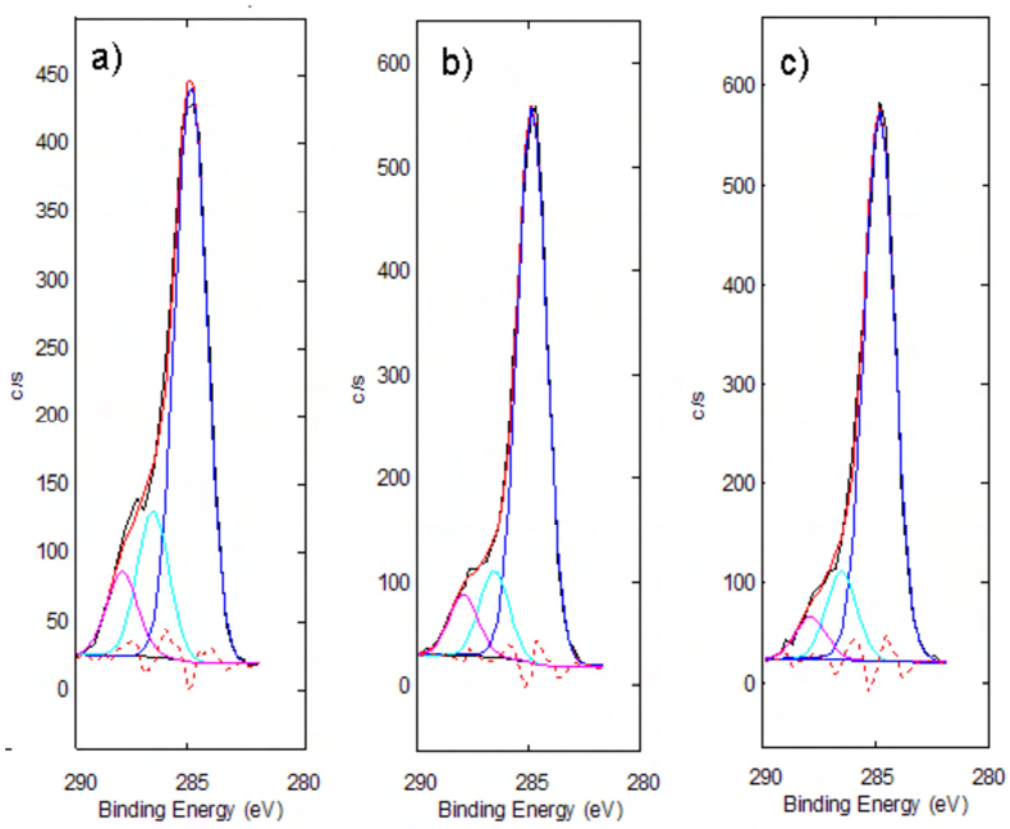

Figure 5.22: Narrow C1s for PP-*g*-PNIPAAm when graft polymerisation was conducted on (a) oxyfluorinated PP NWF; (b) direct fluorinated PP NWF; and (c) pure PP NWF.

The composition of the elements appear in **Table 5.10**. The degree of grafting was estimated from XPS and was based on the N atomic concentration present on the grafted surface as compared to the theoretical N atomic content in PNIPAAm (Akiyama et al., 2007).

Table 5.10: Atomic % of C, N, O, F present on the surface of the PP NWF scaffolds when graft polymerisation was conducted on oxyfluorinated (gNWF1-2), direct fluorinated (gNWF3) and pure NWF (gNWF4) scaffolds.

PP-*g*-PNIPAAm	Functionalisation	APS	Heat	C	N	O	F	Degree of grafting (%)
gNWF1	Oxyfluorination	+	+	74.9	10.4	13.1	1.6	84
gNWF2	Oxyfluorination	-	+	76.8	6.4	13.5	2.8	52
gNWF3	Direct fluorination	+	+	76.6	8.5	13.0	1,5	69
gNWF4	None	+	+	82.6	7.1	10.3	-	57
PNIPAAm calculated				75	12.5	12.5	-	-

The theoretical N content on pure PNIPAAm was calculated to be 12.5% (Akiyama et al., 2007). When graft polymerisation was performed on oxyfluorinated PP NWF surfaces (with APS and heat), the N content was ~10.4 (%) (atomic) which corresponded to a PNIPAAm graft yield was ~84%. This implies that ~84% of the surface was covered by PNIPAAm chains. However more measurements are required per sample, for statistical significance.

5.3.4 SEM analysis

5.3.4.1 Morphology of pure and oxyfluorinated NWF surfaces

SEM images of the pure and oxyfluorinated NWF scaffolds are given in **Figures 5.23-5.24** respectively. The NWF scaffolds were highly porous and displayed open and interconnected pores. All of the NWF displayed a smooth fibre surface. However some artefacts were observed on the surface of the control fibres for all of the NWF scaffolds which could be as a result of accumulation of dust or debris during the non-woven manufacturing process. Furthermore the fibres used in the NWF manufacture may have been treated with a spin finish for commercial applications. Hence the artefacts observed could be due to this treatment process. From **Figure 5.24**, significant surface changes were detectable on the oxyfluorinated PP NWF compared to pure PP. The oxyfluorinated PP surface displayed increased roughness compared to the control and the oxyfluorinated surface contained numerous vein-like cracks which appeared to run across the fibre length. Other authors have also reported an increase in surface roughness on PP and PE following fluorination (Kranz et al., 1994).

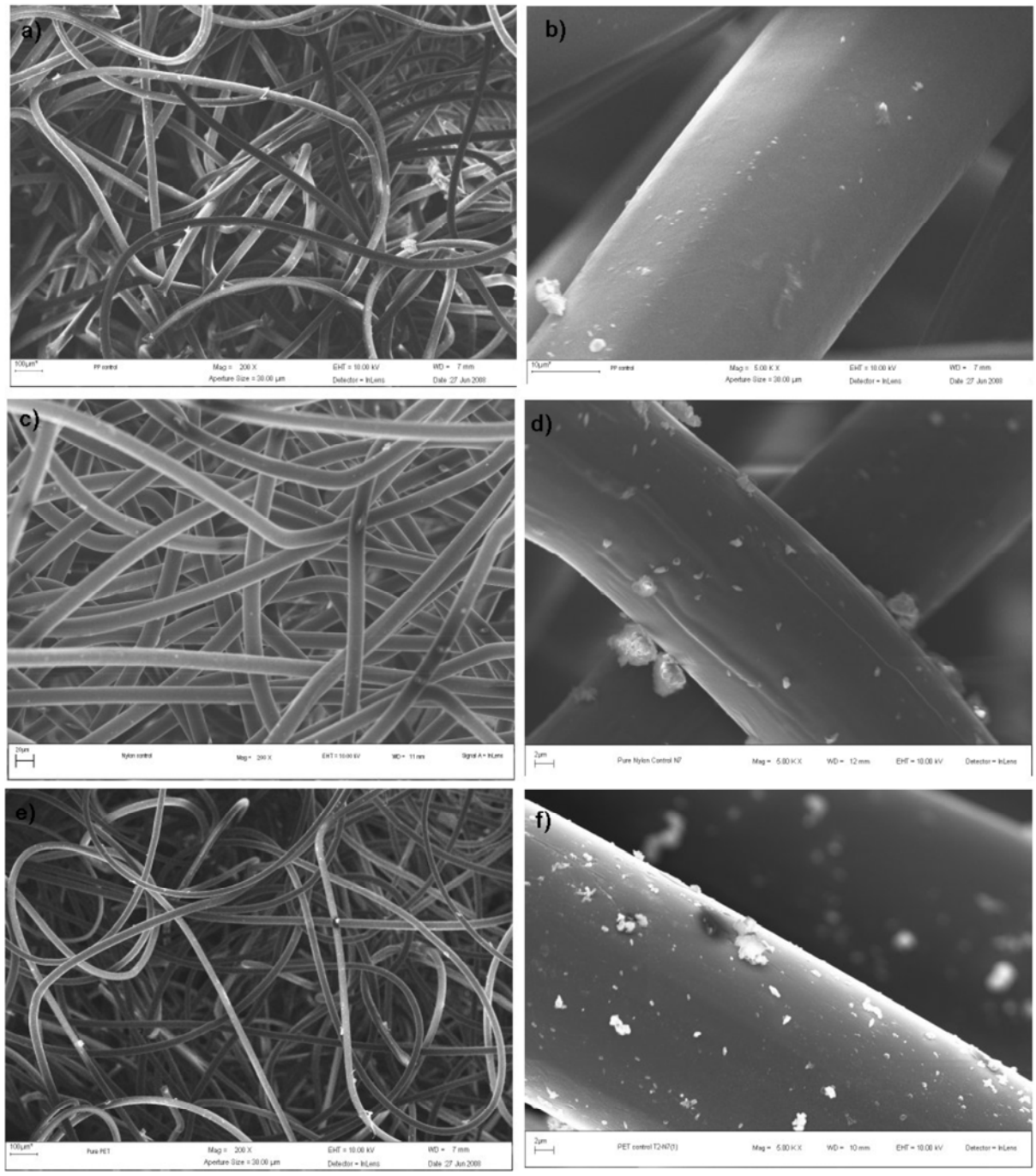

Figure 5.23: SEM images showing the highly porous structures of (a-b) PP NWF (T2-N6 (1)); (c-d) nylon (T3-N7 NWF) and (e-f) PET NWF (T2-N7).

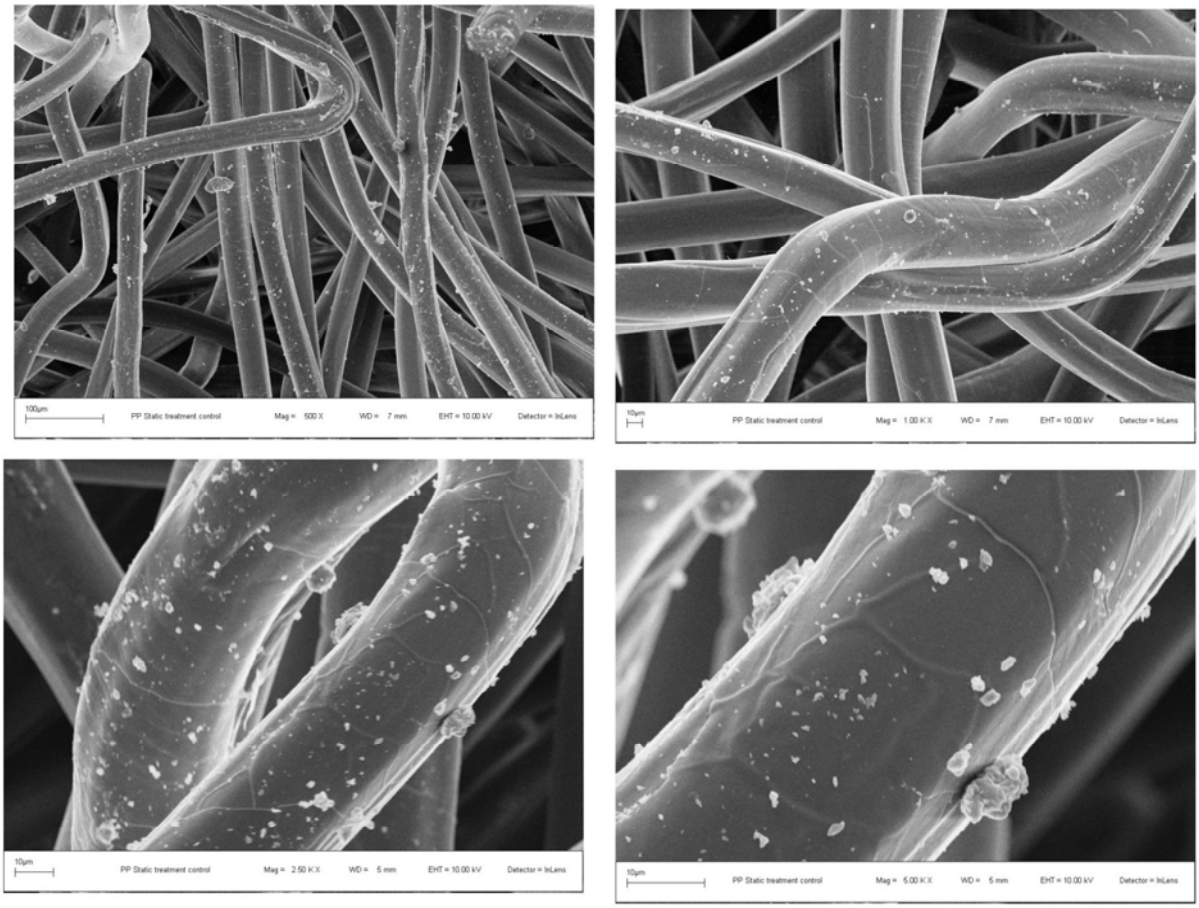

Figure 5.24: SEM images of PP NWF T2-N6 (1) after oxyfluorination.

Fluorination was performed at Pelchem Ltd. Pelchem operates an industrial fluorination plants and due to the large size of the reactor, our samples had to be processed together with other commercial samples during normal operation. All effort was made to ensure that similar processing conditions were maintained for all the samples during oxyfluorination; however we did observe some batch to batch variation amongst samples. The lack of surface functionality on the NWF following direct fluorination was corroborated by the SEM analysis where no significant changes were observed to the surfaces for any of the NWF scaffolds (images not shown).

5.3.4.2 Morphology of PNIPAAm grafted NWF

The SEM images of the PP surface when graft polymerisation was performed on the oxyfluorinated and pure PP NWF scaffolds appear in **Figures 5.25-5.26** respectively. From the SEM analysis, the PP-*g*-PNIPAAm NWF scaffolds prepared by the OAGP method displayed increased roughness and a surface layer was clearly discernible for both methods. The graft layer appeared as node-like structures on the PP surface for the pre-oxyfluorinated

NWF scaffolds (**Figure 5.25**), which was intimately attached on to the fibre surface. The node like structures on the grafted PP surface may have formed at active sites on the polymer backbone. Also the graft layer appeared to be homogenously distributed throughout the sample. This however was in direct contrast to when graft polymerisation was performed on the pure PP NWF scaffolds.

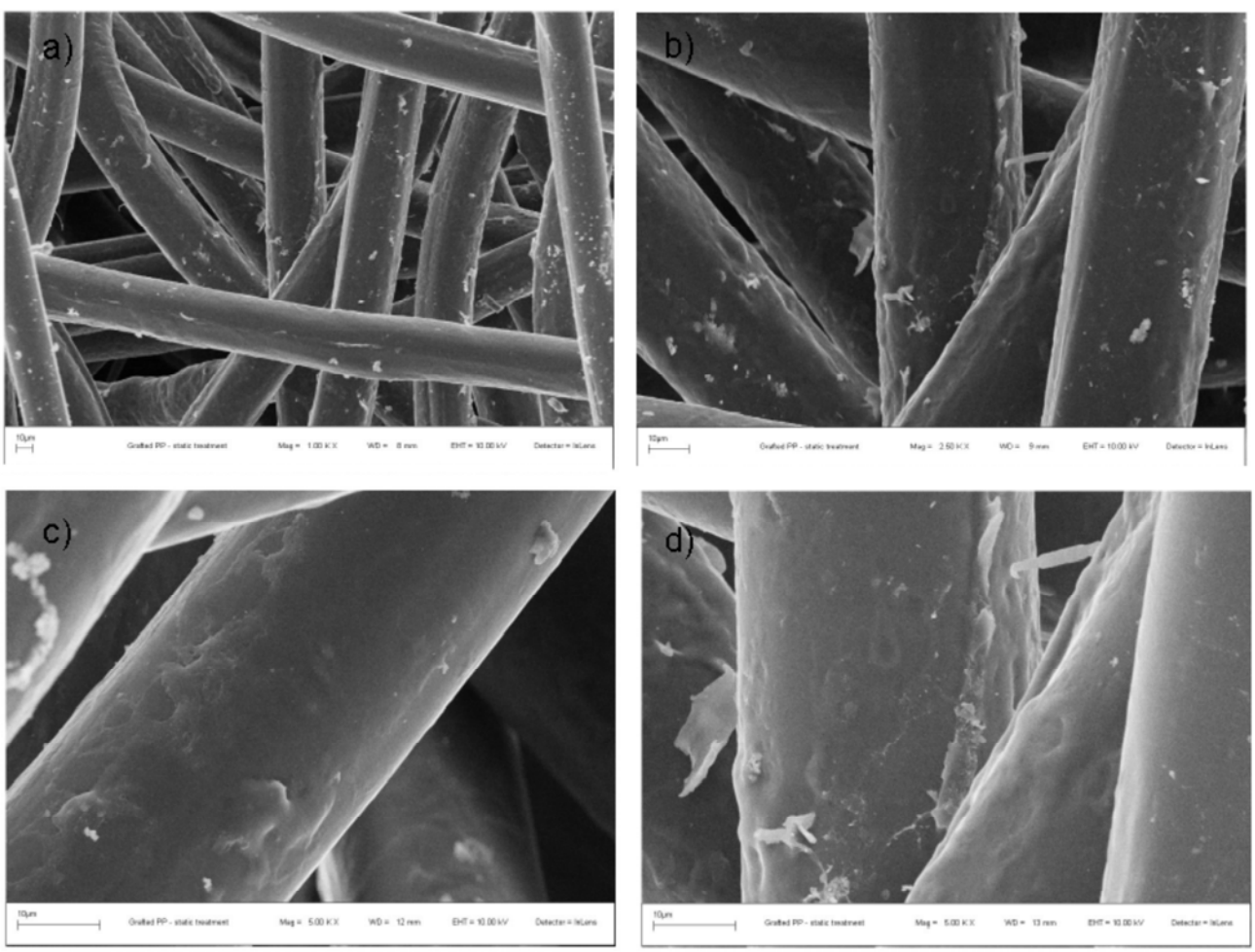

Figure 5.25: SEM images of PP-*g*-PNIPAAm NWF scaffolds at (a) 1000x; (b) 2500x and (c-d) 5000x magnification, where NWF were pre-treated by oxyfluorination and grafting was with an initiator.

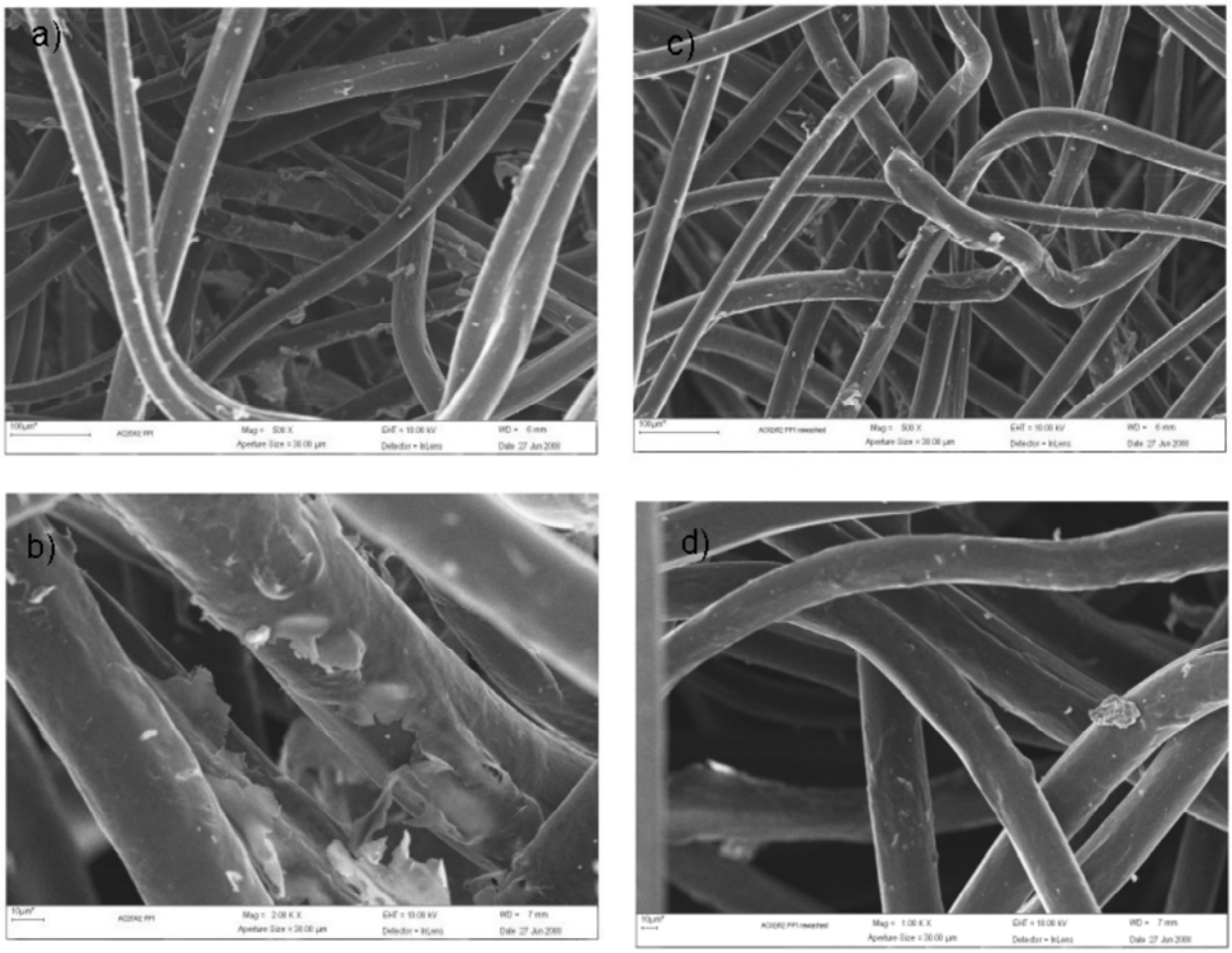

Figure 5.26: SEM images of PP-*g*-PNIPAAm NWF scaffolds when graft polymerisation was conducted on pure NWF, (a-b) shows the surface of the grafted NWF after three days of washing in water; (c-d) shows the same grafted NWF after a second washing cycle of three days.

From **Figure 5.26** it can be seen that when pure non-functionalised PP NWF were used, the PNIPAAm layer appeared to be loosely bound to the fibre surface, and appeared to be "peeling" off the surface. This was attributed to excessive PNIPAAm homopolymer which precipitated and adsorbed onto the pure PP surface during polymerisation. When graft polymerisation was conducted on the pure PP at 70 °C which is above the LCST of PNIPAAm, PNIPAAm is hydrophobic, and will preferentially precipitate onto the pure hydrophobic PP NWF matrix rather than remain in the aqueous solution which may have contributed to the high homopolymerisation seen on the surface of the pure grafted NWF scaffolds. Homopolymer could also be seen within the 3D structure of the NWF scaffolds. This was undesired since the original morphology of the NWF was compromised. To investigate if the layer was covalently attached, a second wash step was conducted on the

PP-*g*-PNIPAAm scaffolds (**Figure 5.26 c-d**). As can be seen after further washing of the PP-*g*-PNIPAAm, the PNIPAAm layer was significantly reduced indicating the presence of PNIPAAm homopolymer on the NWF surface. Due to the elevated temperature, it is possible that the homopolymer becomes entrapped in the PP polymer chains, which would then require prolonged periods of washing to be completely removed.

For the nylon-*g*–PNIPAAm NWF (**Figure 5.27-5.28**), the surface appeared rough, and the PNIPAAm graft layer was clearly visible. When the pre-oxyfluorinated PP NWF surface was used, the PNIPAAm layer was bound on to the fibre surface. Again for the pure nylon surface, homopolymerisation was clearly visible. However the extent of modification was reduced compared to the PP-*g*-PNIPAAm surface.

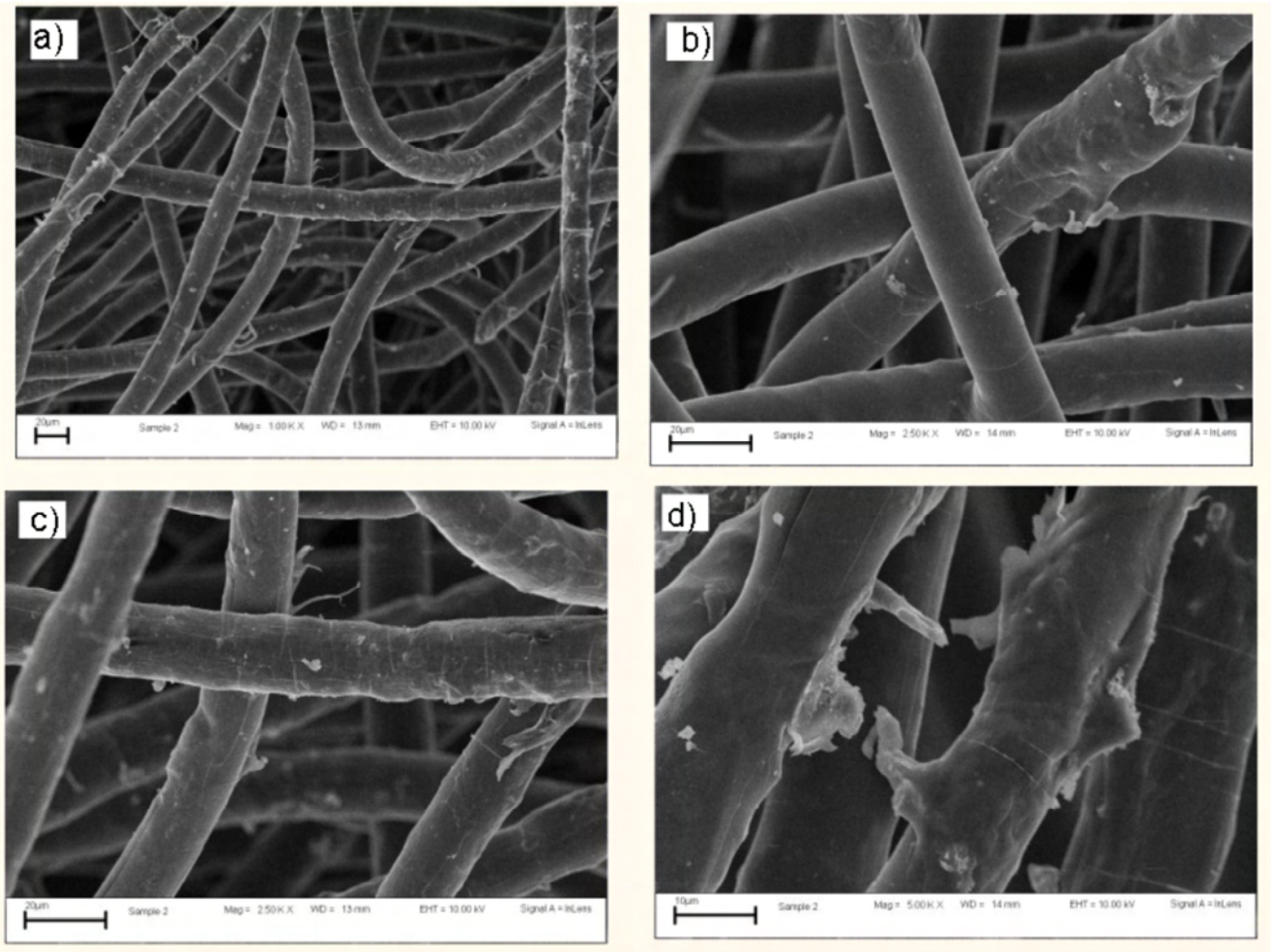

Figure 5.27: SEM images of nylon-*g*-PNIPAAm NWF scaffolds at (a) 1000x; (b-c) 2500x; and (d) 5000x magnification, when grafting was on the oxyfluorinated nylon NWF.

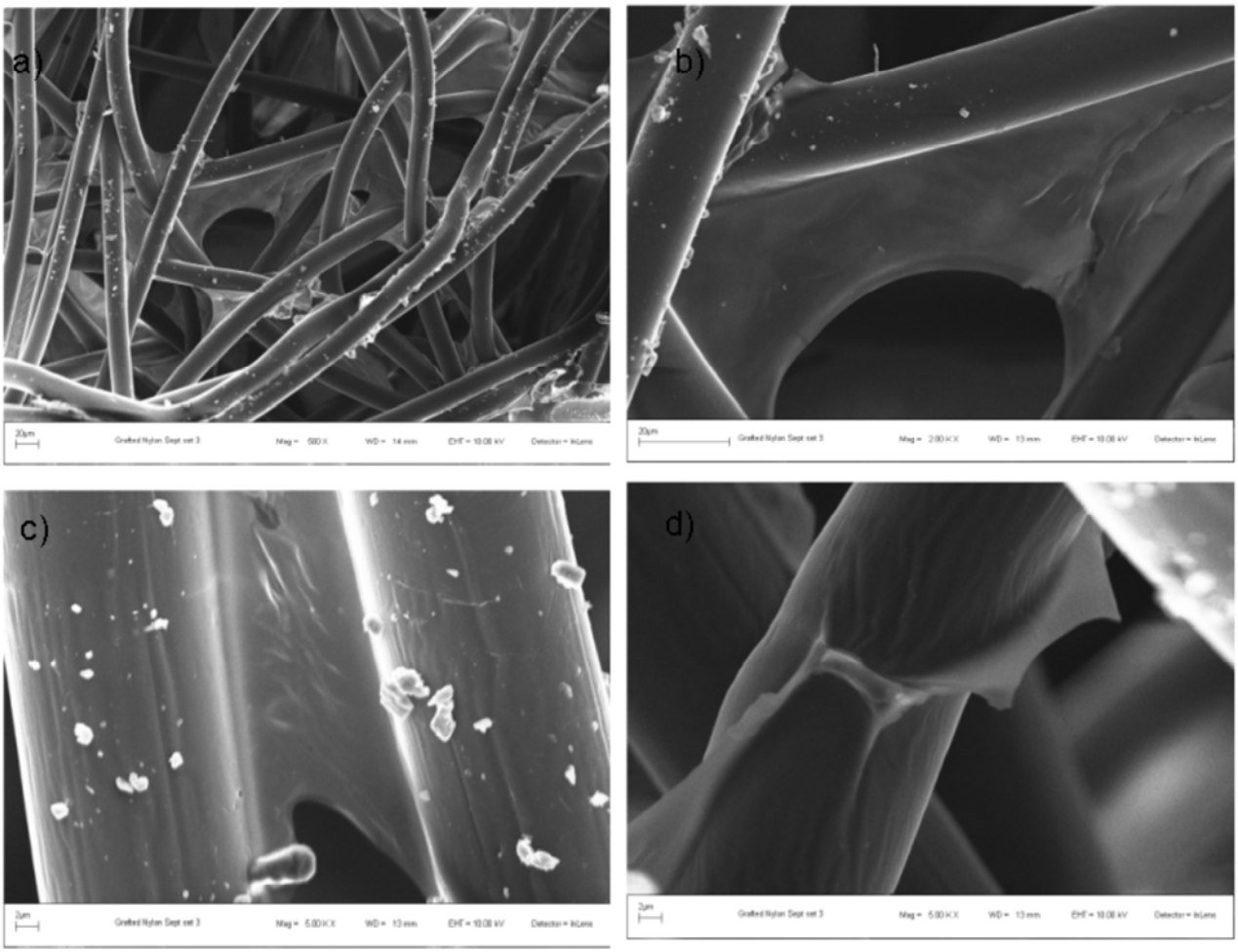

Figure 5.28: SEM images of nylon-*g*-PNIPAAm NWF scaffolds at (a) 500x; (b) 2000x; and (c-d) 5000x magnification when graft polymerisation was conducted on pure NWF.

A further observation made for the nylon-*g*-PNIPAAm surfaces, is that cracks appeared on the fibre surfaces which indicates fibre damage due to the heat treatment during graft polymerisation. For the PET-*g*-PNIPAAm scaffolds (**Figure 5.29-5.30**), ribbon-like structures were observed emanating from some of the fibre surfaces however the occurrence of these structures was very limited, indicating that graft polymerisation was very limited on the PET surface. From the morphological changes it appeared that graft polymerisation was largest for PP, followed by nylon, and then PET.

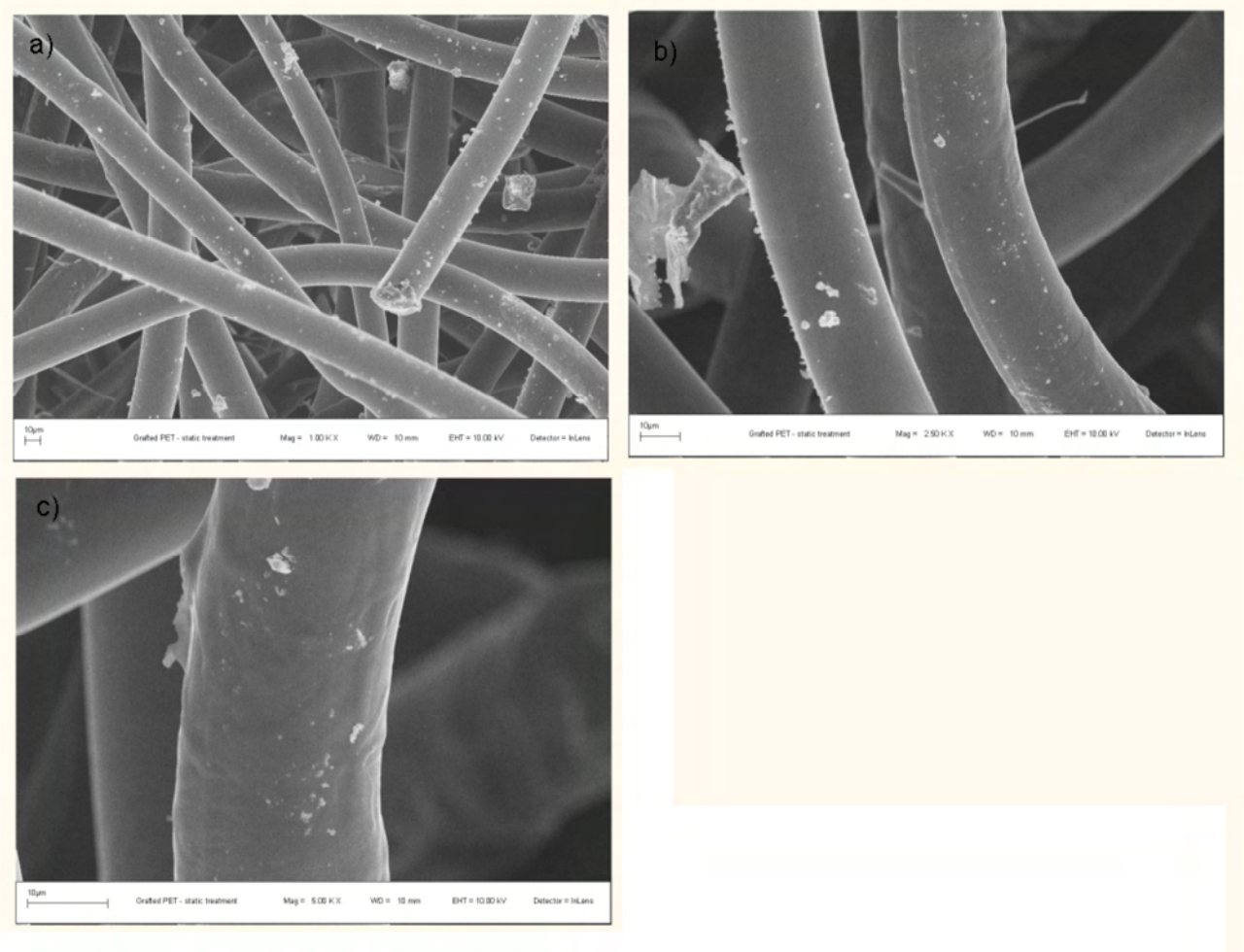

Figure 5.29: SEM images of PET-*g*-PNIPAAm NWF scaffolds at (a) 1000x; (b) 2500x and (c) 5000x magnification when grafting was on oxyfluorinated PET.

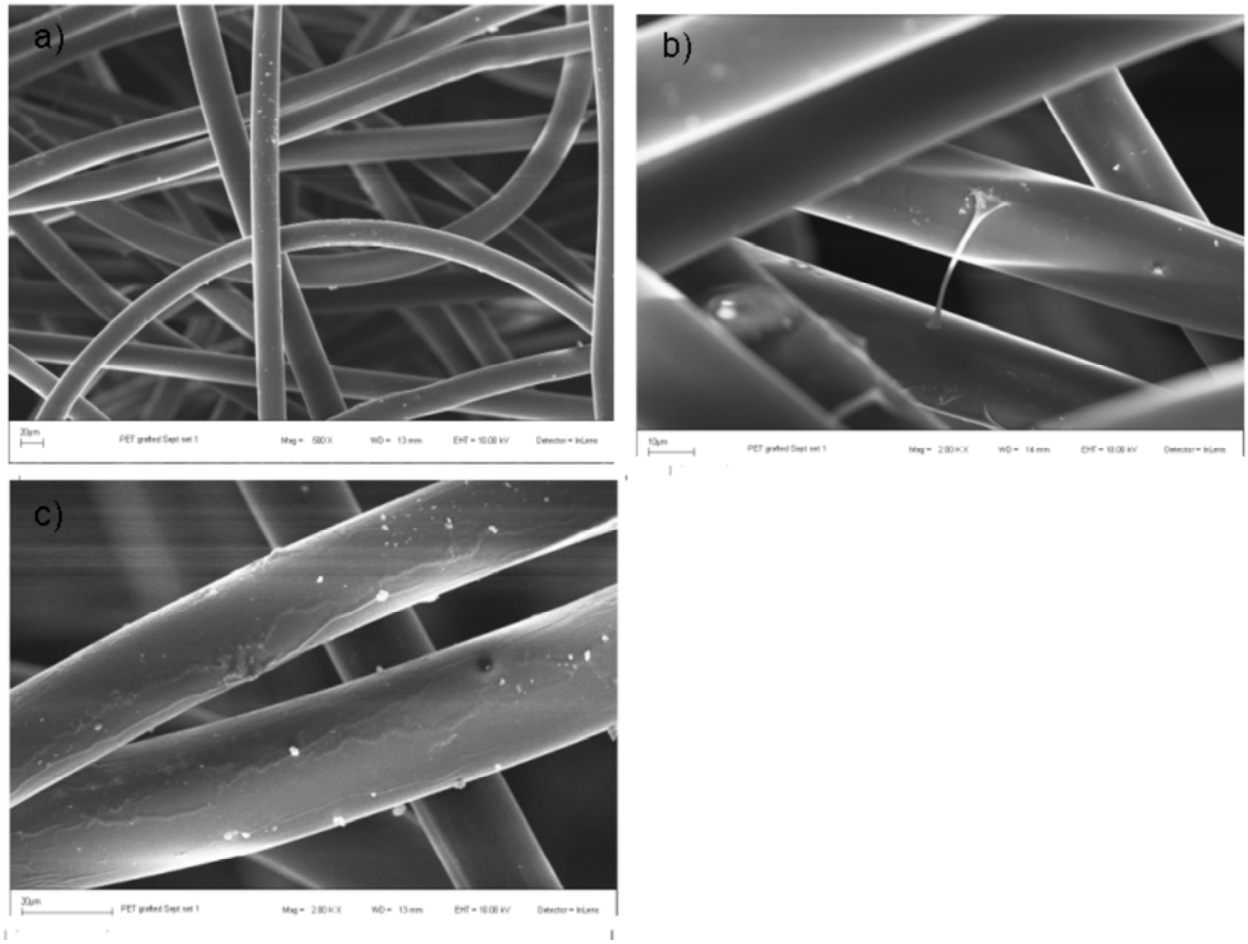

Figure 5.30: SEM images of PET-*g*-PNIPAAm NWF scaffolds at (a) 500x and b-c) 2000x magnification when graft polymerisation was conducted on pure NWF after 1st washing.

The SEM images of PP-*g*-PNIPAAm synthesised by the OAGP but without the chemical initiator appear in **Figures 5.31**. The PNIPAAm layer was reduced compared to when APS was used. Hence this indicates that peroxyradicals from the oxyfluorinated PP as well as the APS contributes to free radical sites on the polymer backbone and the monomer respectively, both of which are required for grafting.

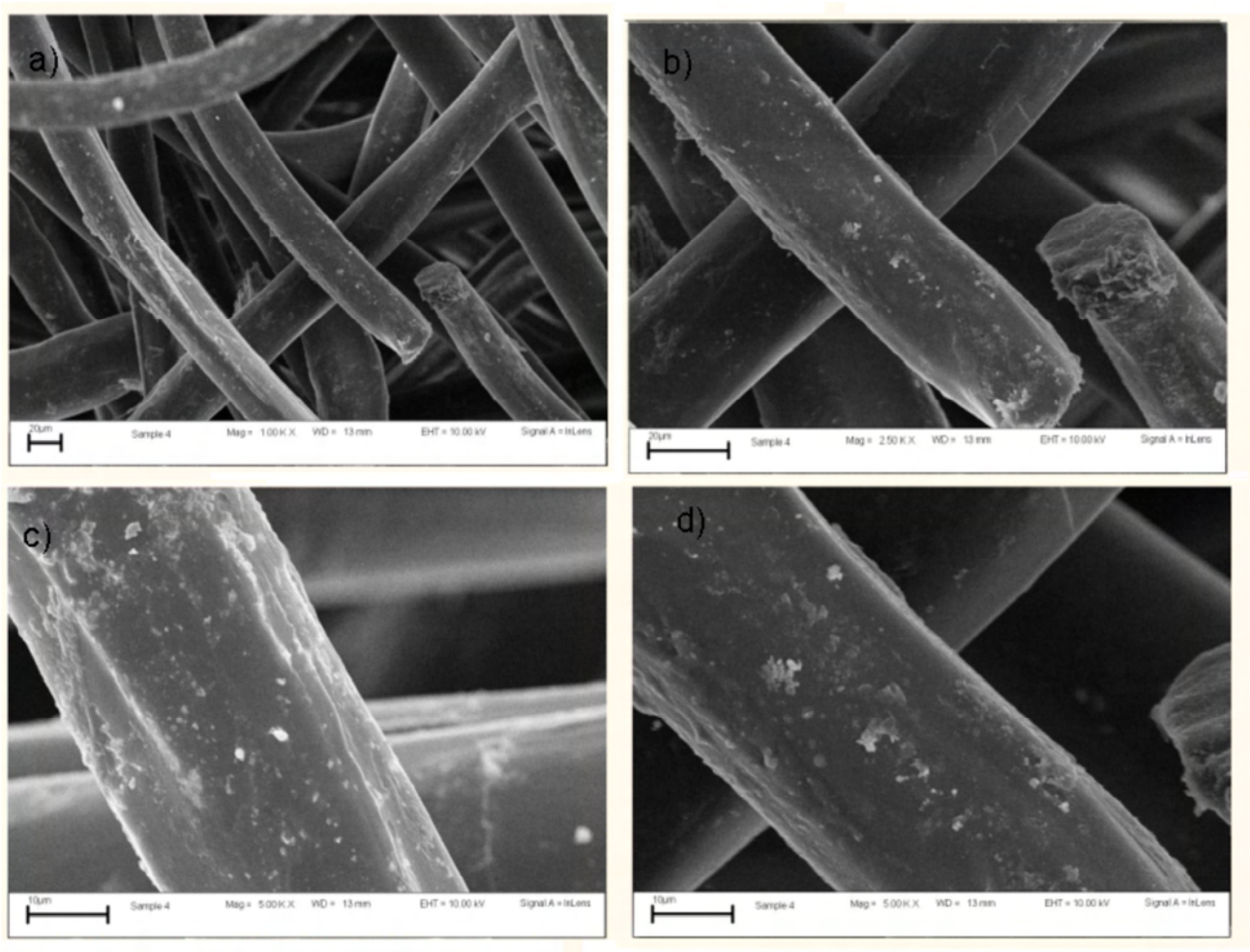

Figure 5.31: SEM images of PP-*g*-PNIPAAm NWF scaffolds at (a) 1000x; (b) 2500x; and (c-d) 5000x magnification when PP NWF scaffolds were pre-treated by oxyfluorination and graft polymerisation is by heat activation only without an initiator.

5.3.5 Water contact angle and swelling of NWF scaffolds in water

It is known that graft polymerisation is highly dependent on the monomer permeability into the polymer bulk, and monomer availability to the graft sites (Anjum et al., 2006). Good wetting would ensure that the monomer and the monomer radicals can easily access the backbone polymer to induce graft polymerisation. Since NIPAAm and PNIPAAm are water soluble, water was preferred as the graft medium over the use of toxic solvents. It has been reported previously that oxyfluorination increases the hydrophilicity, and surface energy of polymers thereby improving wetting (Kharitonov and Kharitonova, 2009). To assess the wettability of the NWF scaffolds in water, water contact angle and swelling studies were performed.

5.3.5.1 Water contact angle studies

Water contact angle studies were performed on pure PP, oxyfluorinated PP and PP-*g*-PNIPAAm NWF scaffolds (**Figure 5.32).** Improved wetting was observed particularly on the PP-*g*-PNIPAAm surfaces compared to the pure or oxyfluorinated PP surfaces. The water contact angles were quantified over an ageing period of 10 seconds (**Figure 5.33**).

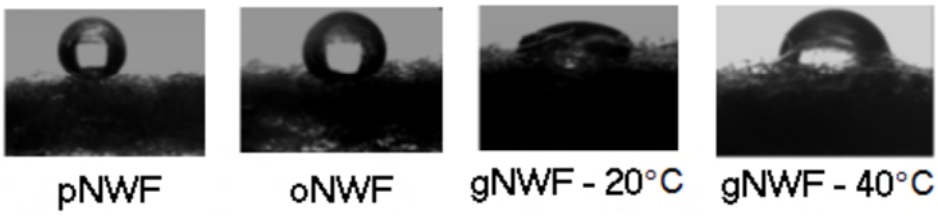

Figure 5.32: Images showing a representative water drop on the surface of pure PP NWF (pNWF), oxyfluorinated NWF (oNWF); PP-*g*-PNIPAAm NWF (gNWF) at 20°C, and gNWF at 40°C. For pNWF and oNWF similar images were obtained at both temperatures. Images were taken a few seconds after the drop contacted the surface.

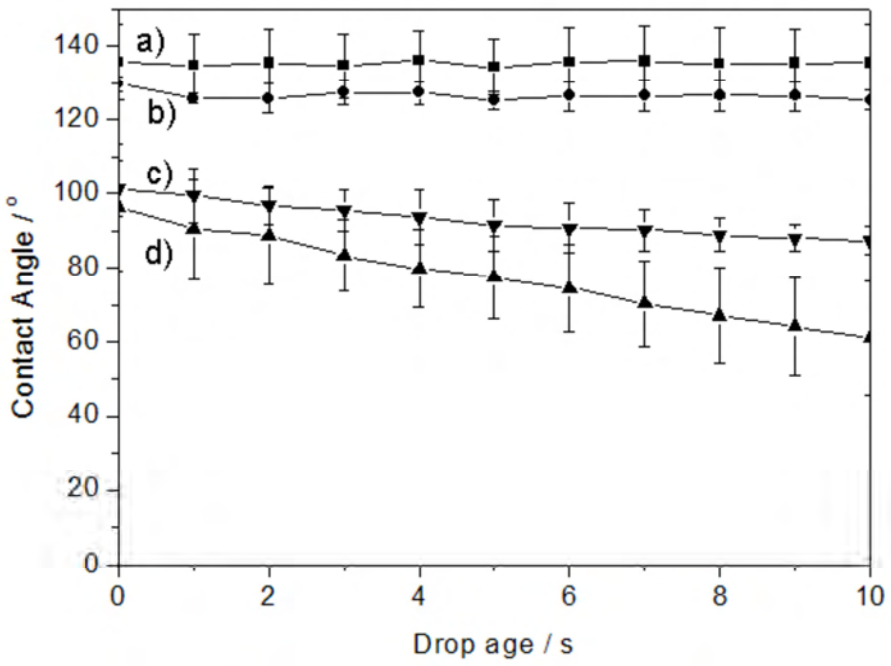

Figure 5.33: Static water contact angle on the surface of (a) pure PP NWF at 20 °C, (b) oxyfluorinated NWF at 20 °C, (c) PP-*g*-PNIPAAm at 40 ℃; and (d) PP- *g*-PNIPAAm at 20 ℃ as a function of the drop age. The average of three drops per time point was taken.

Pure PP NWF as expected displayed an intrinsically hydrophobic surface with a relatively stable water contact angle at ~135 ± 6° at 20℃, while for the oxyfluorinated PP NWF th e contact angle was reduced to ~127 ± 3° at 20 ℃, indicating improved wetting for the l atter. The contact angle for the PP-*g*-PNIPAAm NWF was found to be temperature-dependent showing a relatively hydrophobic surface at 40 ℃ w ith improved hydrophilicity at 20 ℃, confirming the presence of PNIPAAm in the graft layer. For the grafted NWF scaffolds, stable water drops could not be obtained at each time point within the 10 second ageing period (hence the large standard deviations reported here). This was attributed to rapid wetting due to intramolecular hydrogen bond formation between the C=O and N-H groups in the PNIPAAm chain and water molecules (Gu et al, 2012). The contact angles for both the pure and oxyfluorinated PP NWF however was independent of temperature and similar contact angle values were obtained at 20 ℃ and at 40 ℃ (data not shown).

Although the contact angle measurements for oxyfluorinated PP decreased compared to pure PP at 20 ℃, it was also observed that the dif ference in contact angle between the pure PP NWF and the oxyfluorinated PP NWF was relatively small, which was unexpected, and in contrast to other reported studies (Lee et al, 2003). Lee *et al* reports on the oxyfluorination of PP films, and in that study when the F_2: O_2 content varied from 9:1 to 1:9 the contact angle decreased from 103.3 for pure PP film, to 98.7 and 80.8 respectively for the oxyfluorinated PP surfaces at a reaction pressure of 5 kPa (Lee et al, 2003). Although in the present study the oxygen used for the oxyfluorination process was not directly introduced in the reactor as O_2 gas but was due to O_2 present in air, it can be argued that the O_2 content was insufficient to improve surface wetting. However this finding is contradictory to the ATR-FTIR and XPS data reported previously where we have shown a relatively high oxygen content on the surface of the NWF after oxyfluorination i.e. 4.2% (atomic) for pure PP compared to 18.2% (atomic) for oxyfluorinated PP.

It has been reported that morphology of surfaces can also influence contact angle. It has been reported that porous surfaces are non-ideal for contact angle measurements using the Young equation due to the heterogeneity, roughness, capillary forces within pores, contraction of the polymer in the dry state, and restructuring of the surfaces (Kou et al., 2003). While it is acknowledged that the NWF scaffolds used in the present study is non-ideal for contact angle measurements using the DSA due to the highly porous structures, and hence comparisons with other reported studies cannot be directly made, this method is still valuable in providing a quantitative tool for accessing the wetting and comparing data between the different NWF samples under investigation.

A possible explanation for the relatively high contact angle on the oxyfluorinated PP surface in comparison to pure PP may be due to a physical surface rearrangement process. Hruska *et al* have reported that the contact angle and surface energy of oxyfluorinated PP increases significantly with storage time due to re-orientation of the new polar functional groups away from the polymer surface into the polymer bulk in order to minimise the interfacial free energy at the surface (Hruska and Lepot, 2000). Since freshly oxyfluorinated NWF was unavailable during the contact angle studies, aged oxyfluorinated NWF which had been stored for several months were used, hence surface restructuring could have been possible. Also it should be noted that contact angle provides information about the outermost 5-10 Å of a solid surface whereas for ATR-FTIR for example the depth of analysis is substantially higher.

Thus, although the contact angle of the oxyfluorinated PP surface was only marginally lower than that of pure PP, the oxygen functionality was still present in the oxyfluorinated surface which we have already confirmed by ATR-FTIR and SXPS. To further confirm if the "relatively poor wetting" observed from the contact angle measurements was just a surface phenomenon, swelling studies were conducted in water.

5.3.5.2 Swelling studies

Swelling studies were performed in water for pure and oxyfluorinated PP and PET NWF scaffolds, and the mass of wet samples were recorded to determine the water uptake with time (**Figure 5.34**). It can be seen that pure PP and pure PET displayed very poor swelling in water, while substantial improvements to swelling were observed for the oxyfluorinated samples. Oxyfluorinated PP displayed the highest swelling response and after only 2 hours, more than 60% increase in its dry weight was observed. To further visualise swelling of the scaffolds, optical images were taken of the pure and oxyfluorinated PP NWF scaffolds immediately upon submersion in water (**Figure 5.35**). For the pure PP NWF almost no wetting could be detected, however when oxyfluorinated PP NWF was immersed in water, wetting was instantaneous (**Figure 5.35**). The improved swelling of the oxyfluorinated NWF can be attributed to the presence of new polar functional groups on the oxyfluorinated surfaces which we have previously confirmed.

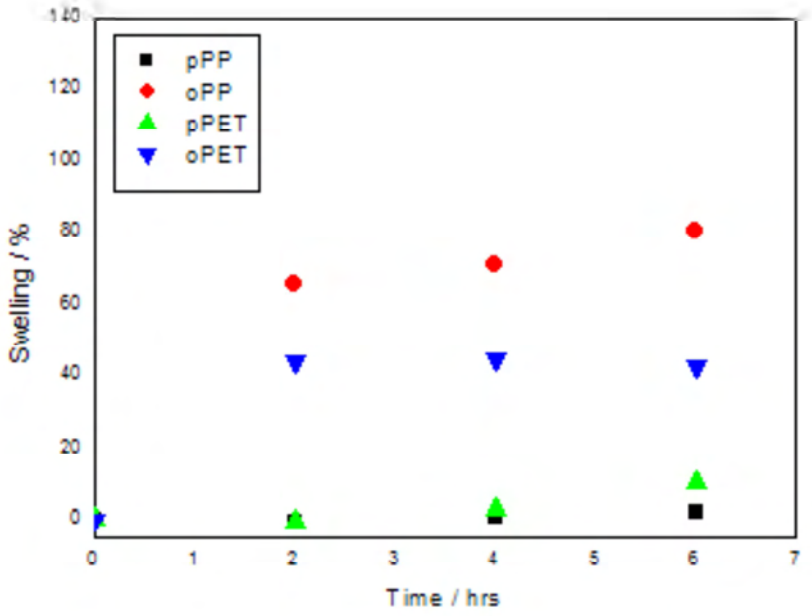

Figure 5.34: Percent swelling based on mass % for pure PP (pPP); oxyfluorinated PP (oPP), pure PET (pPET), and oxyfluorinated PET (oPET).

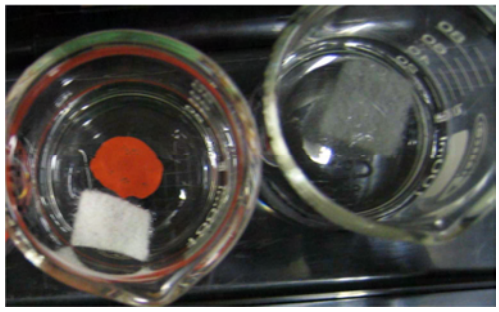

Figure 5.35: Visual observation of wettability of (a) pure PP NWF (indicated by red dot); and b) oxyfluorinated PP NWF in water (right). Images were taken immediately after immersion in water.

5.3.6 Determination of peroxides on NWF

In this study the DPPH – UV-VIS method and ESR was used to detect peroxy radicals on the oxyfluorinated PP NWF scaffolds.

5.3.6.1 DPPH radical-scavenger method

It is well-known that DPPH is a free-radical scavenger which can be used to react with other free radical species in solution (Fargere et al., 1995; Ionita, 2005; Jeong et al., 2011). DPPH exists as a stable free radical in solution because it delocalises its unpaired electron over the whole molecule. Three types of DPPH free radicals are possible as shown in **Figure 5.36**.

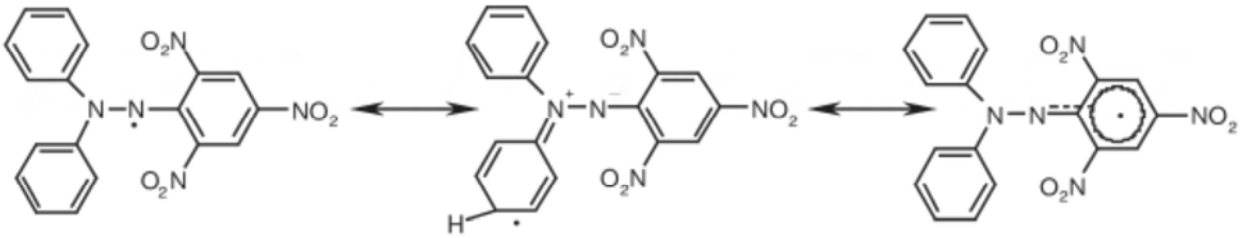

Figure 5.36: Scheme showing electron delocalisation in DPPH (Ionita, 2005).

DPPH is intensely violet in colour and it is known as a good hydrogen abstractor forming DPPH-H which has an orange-yellow colour (Ionita, 2005). The reduction of DPPH to DPPH-H can be easily monitored both visually and also by UV-VIS spectroscopy due to a high λ-shift in the visible spectra from 520 nm (for DPPH) to 330 nm (for DPPH-H) (Ionita, 2005). DPPH has been shown to react with a number of species including hydrogen peroxide, hydroxyl radical, and superoxide anion radical species. Reaction of DPPH with peroxides leads to chain scission as shown below (Fargere et al., 1994):

$$R - O - O - R + 2X \rightarrow 2R - OX \qquad \text{(Eq. 5.15)}$$

Where R-O-O-R and X refers to the peroxide and DPPH respectively.

According to Ionita *et al*, reaction of DPPH with oxygen species (such as hydrogen peroxide, tert-butyl peroxide, tert-butyl hydroperoxide, sodium peroxide, hydroxyl radical etc.) yield DPPH-H as the main product and not an oxy-derivative of DPPH. Jeong *et al* have reported the use of DPPH for detection of hydroperoxide species on oxyfluorinated LDPE films by monitoring the absorbance at 520 nm (Jeong et al., 2011).

In this study, both oxyfluorinated and pure PP were incubated in DPPH solution for 7 hrs at 70 ℃ and colour was detected visually (**Figure 5.36**) as well as using UV-VIS absorbance. However when compared to the oxyfluorinated PP NWF samples, a clear colour difference of the DPPH solution could be seen. The blank DPPH solution, and the sample containing

the pure NWF, displayed a violet colour as expected, however for the sample containing the oxyfluorinated PP the solution turned light pink as can be seen in **Figure 5.36**.

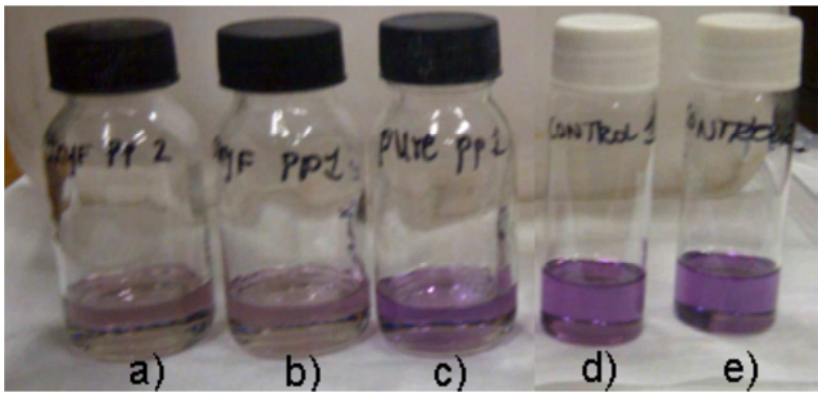

Figure 5.37: Colour observation after reaction with DPPH at 70 ℃ for 7 hours for (a-b) oxyfluorinated PP NWF; (c) pure PP NWF; and (d-e) DPPH blank.

The UV-VIS absorbance spectrum for each solution measured at 520 nm appears in **Figure 5.37**. For the oxyfluorinated NWF sample, a reduction in the 520 nm peak was observed, as compared to the blank and pure PP control.

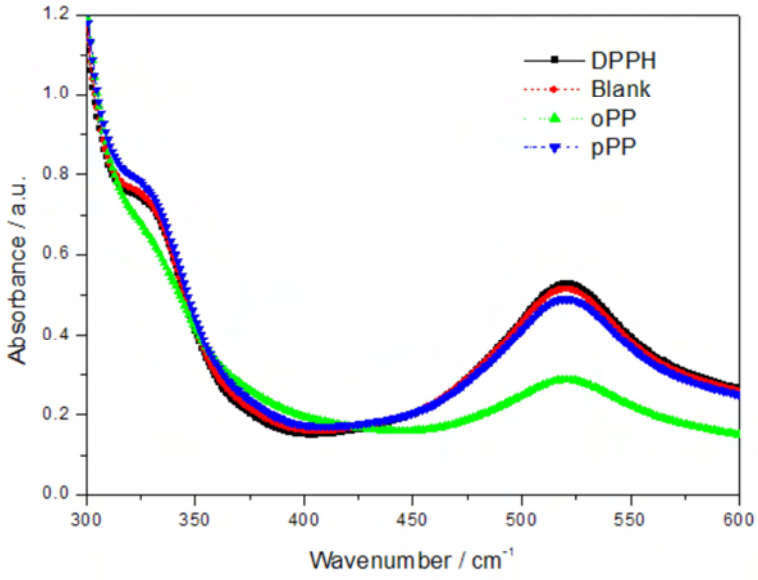

Figure 5.38: UV-VIS absorbance of DPPH solution at 520 nm prior to treatment (DPPH), and the DPPH blank (Blank), oxyfluorinated PP (oPP), and pure PP (pPP) which were all treated at 70℃ for 7 hours.

To determine the amount of hydroperoxides present on the scaffold surface, a calibration graph was determined using DPPH concentrations from 1-10 ppm (**Figure 5.39**).

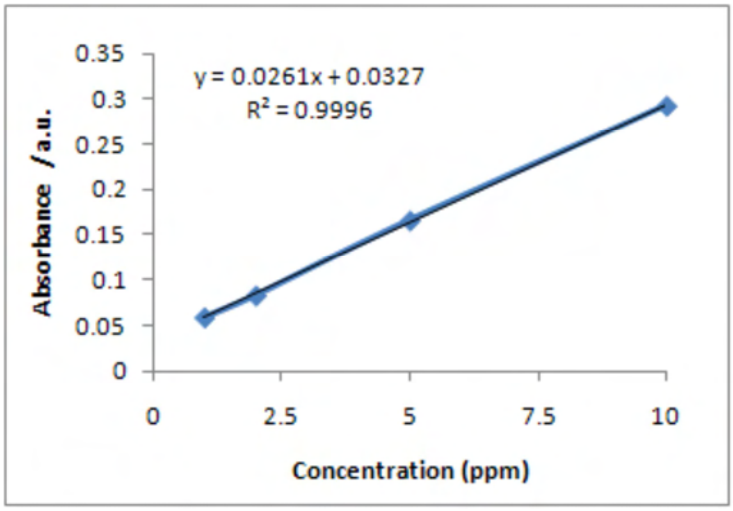

Figure 5.39: Calibration graph relating absorbance and DPPH concentration.

From **Figure 5.39**, the DPPH present in solution after reaction with the oxyfluorinated PP NWF was determined by: x = (y – 0.037) /0.0261, where x is the DPPH concentration (ppm), and y is the absorbance. The moles hydroperoxide per surface area of NWF was then calculated using **Equation 5.15** given previously and the results appear in **Table 5.11,** and are also shown graphically in **Figure 5.40.**

Table 5.11: Moles peroxides on oxyfluorinated NWF (oPP) using DPPH method. Controls included pure NWF (pPP), and a blank DPPH sample containing no NWF.

Sample	A_{520nm}	C_{DPPH} (solution)/ppm	$(Co\text{-}C)_{DPPH}$ (consumed) /ppm	Moles DPPH consumed/Mol	Moles peroxides/ Mol	Moles peroxides per surface area/ Mol/cm^2
oPP	0.286	9.7	8.72	2.21×10^{-7}	1.11×10^{-7}	4.34×10^{-9}
oPP	0.286	9.7	8.72	2.21×10^{-7}	1.11×10^{-7}	4.34×10^{-9}
pPP	0.490	17.5	0.90	2.28×10^{-8}	1.14×10^{-8}	4.49×10^{-10}
Blank	0.513	18.4	-	-	-	-
Blank	0.514	18.4	-	-	-	-

Interestingly for pure PP NWF a slight decrease in absorbance was observed compared to the blank. This perhaps may be due to some active oxygen species entrapped in the PP surface as a result of oxidation due to ageing of PP. From XPS, we also observed a small oxygen content on the pure PP. Alternatively the decrease in DPPH, could be due to

adsorption of some DPPH molecules onto the PP surface. However the moles of peroxide on the oxyfluorinated PP surface increased by a factor compared to the pure PP which can be attributed to the oxyfluorination treatment. The amount of hydroperoxides present on the oxyfluorinated PP is relatively low compared to other studies (Jeong et al., 2011). The yield of hydroperoxides can be improved by varying the O_2 content during oxyfluorination.

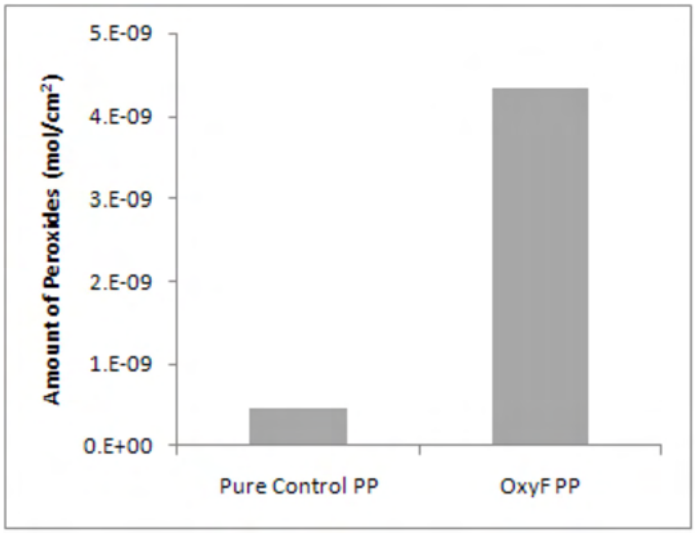

Figure 5.40: Comparison of peroxides or free radicals on pure PP and oxyfluorinated PP.

5.3.6.2 ESR

ESR was also used to detect peroxy radicals on the PP oxyfluorinated NWF. The ESR analysis was performed by Prof László Korecz at the Chemical Research Centre of the Hungarian Academy of Sciences in Hungary. ESR studies were conducted at room temperature and at 70°C. The ESR spectra for the oxyfluorinated PP NWF at room temperature appear in **Figure 5.41.** A weak asymmetric singlet absorption peak was detected for the oxyfluorinated NWF, indicating the presence of long-lived free radicals in the polymer structure. To interpret the ESR spectrum, the experimental results were compared to a simulated spectrum. Excellent agreement with the experimental data was obtained in case of g factor $g_{\perp}$=2.0022 and $g_{||}$=2.0054 where $g_{\perp}$ and $g_{||}$ refers to the electrons perpendicular and parallel to the magnetic field respectively. This indicates anisotropy, i.e. the g factor differs for all orientations of the free electron in the magnetic field. The g-factor refers to the intrinsic magnetic moment of the electron, and the g-factor for a free electron is

2.0023 (Bovet, 2009). The $g_{\perp}$ and $g_{||}$ values observed for the oxyfluorinated PP correspond to mid chain peroxyradicals (Schlick and Mcgarvey, 1983).

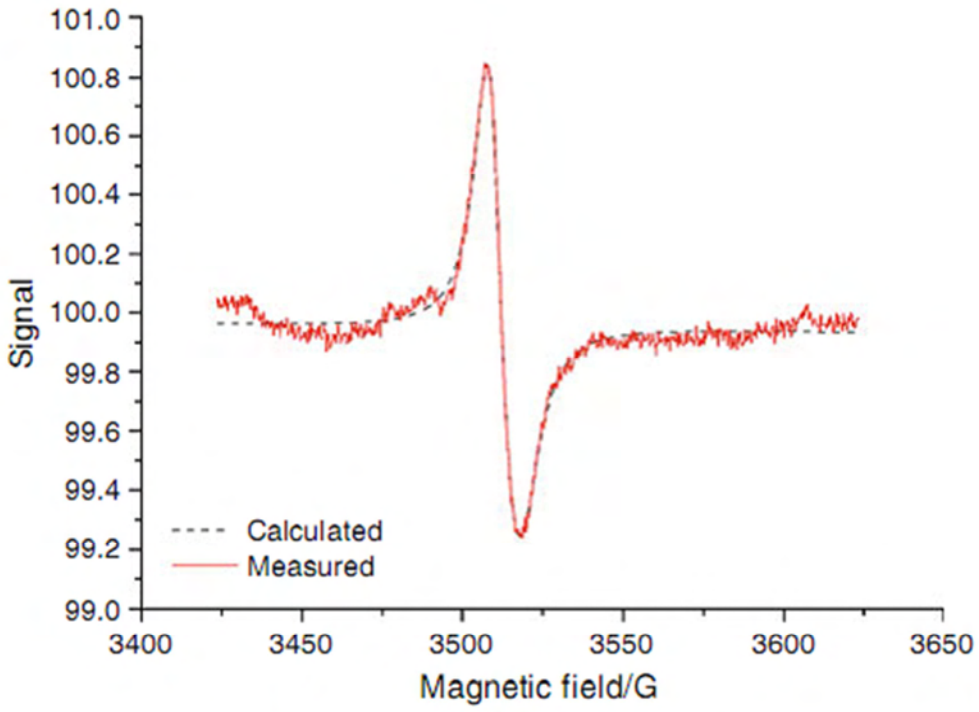

Figure 5.41: Experimental (measured) and simulated (calculated) ESR spectra of PP oxyfluorinated NWF at ambient temperature.

In polymers treated with fluorine–oxygen mixtures, a controlled amount of long-lived peroxyradicals are generated (Kharitonov et al., 2005). The radicals formed in fluorinated polymers are long-lived ones; their amount is decreased by a factor 2 in several hours at room temperature from 1 to 15 hrs depending on the polymer nature (Kharitonov et al., 2005). Although the oxyfluorinated NWF scaffolds were tested several weeks after the oxyfluorination process, long-lived radicals could still be detected on the surfaces of the NWF scaffolds as mid chain peroxyradicals. It has been reported previously that peroxy radicals are more stable in the crystalline phase of polymers (Kharitonov et al., 2005). This may indicate that the radicals were entrapped in the crystalline structure of the NWF scaffolds during the oxyfluorination process, and slowly diffuse to the surface with time. Long-lived peroxyradicals will be very useful for inducing graft polymerisation for attachment of PNIPAAm on to the NWF scaffolds.

Further measurements were carried out at 70°C, to follow the change in radical concentration with time at the temperature of grafting (**Figure 5.42**).

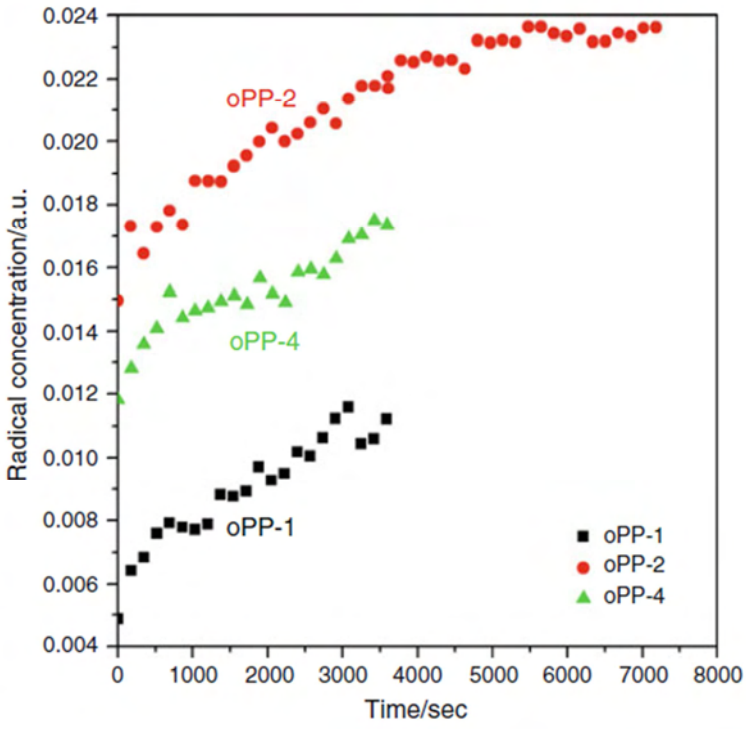

Figure 5.42: Typical change in radical concentration with time at 70°C for the oxyfluorinated PP NWF scaffolds.

Three oxyfluorinated PP NWF samples were analysed (i.e. oPP-2, oPP-3, and oPP-4). The concentration scale was not calibrated, although the samples were normalised to 1 mg, so that they could be compared. The absolute radical concentrations were found to be very small, and the background noise was rather high. However sample oPP-2 was the easiest to measure the time dependence of radical concentration at 70 °C. It can be seen that the radical concentration on the oxyfluorinated PP, at first increased, and after some time the concentration of the radicals remained constant. This result indicates that peroxide groups may be present on the oxyfluorinated PP surface, which upon heat activation at 70°C, leads to the formation of peroxy radicals, the concentration of which increases with time, until maximum peroxy radicals are formed.

5.3.7 Proposed mechanism for OAGP

In this study OAGP was used to graft PNIPAAm onto NWF scaffolds as shown in **Scheme 5.1**. It is known that graft polymerisation is highly dependent on the monomer permeability into the polymer bulk, and monomer availability to the graft sites (Anjum et al, 2005). This was enabled by ensuring that the fluorinated scaffolds were highly swollen prior to grafting to

ensure diffusion of the monomer molecules into the amorphous regions of the PP. NWF scaffolds were swollen in the APS initiator solution such that the initiator molecules were localised on the fibres to aid in graft polymerisation. An advantage of the OAGP method used here is that graft polymerisation was carried out in an aqueous medium under mild conditions.

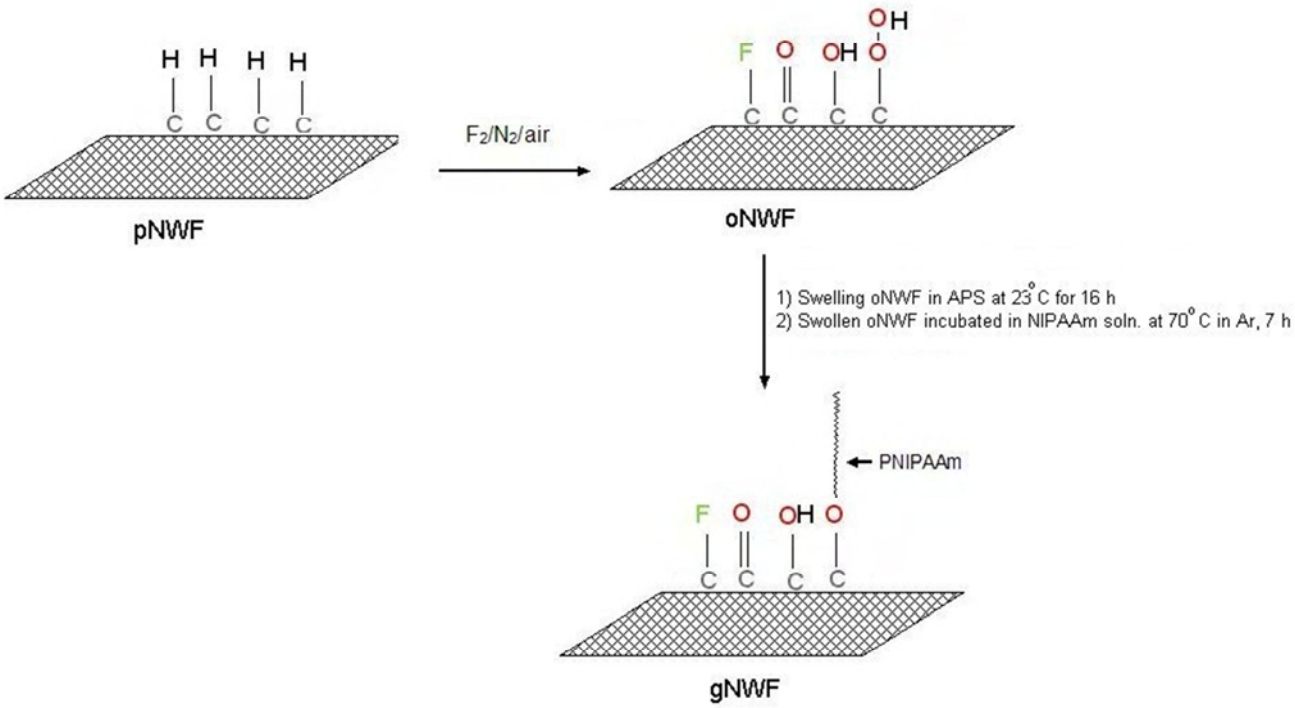

Scheme 5.1: Schematic representation showing OAGP of PNIPAAm on to NWF scaffolds.

The OAGP method of the present study proceeds via a free-radical mechanism which is diffusion driven (Woo et al., 2005). The reaction mechanism for the OAGP method is shown in **Scheme 5.2.**

$F_2 + RH \rightarrow R^{\cdot} + HF + F^{\cdot}$ ΔG=+4.1 kcal/mol

$R^{\cdot} + F^{\cdot} \rightarrow RF$ ΔG=-34 kcal/mol

$R^{\cdot} + F_2 \rightarrow RF + F^{\cdot}$ ΔG=-68 kcal/mol

$R^{\cdot} + O_2 \rightarrow R-O-O^{\cdot}$

$R-O-O^{\cdot} + H_2O \rightarrow R-O-OH$

$-C(=O)F + H_2O \rightarrow -COOH + HF$

Scheme 5.2: Reaction mechanism for fluorination of NWF scaffolds (Woo et al, 2005).

During fluorination, F_2 gas reacts exothermically with the surface of the polymer to form free radicals (du Toit and Sanderson, 1999). Fluorine, due to its high electronegativity, partially replaces the hydrogen on the polymer back bone to form alkyl free radicals ($R^{\bullet}$), fluorine free radicals ($F^{\bullet}$), as well as hydrogen fluoride (Woo et al., 2005). The formed alkyl and fluorine free radicals then react to form the fluorocarbon backbone (RF). Initiation via dissociation of molecular fluorine is not possible since homolysis of fluorine is too endothermic (ΔH=157.88 kJ/mol) to proceed at room or relatively low temperatures (Pryor, 1966). Since the bond energies of F_2 (157.88 kJ/mol) and C-H (410 kJ/mol) are relatively low compared with the bonding energy of C-F (456 kJ/mol) and H-F (569 kJ/mol), the formation of C-F and HF is preferred and the reaction is spontaneous (Woo et al., 2005). Also the Gibbs energy for the reactions indicates that the reactions proceed rapidly. Elemental oxygen and fluorine are introduced into the PP molecular chain to partially replace the H atoms. During oxyfluorination, molecular oxygen reacts spontaneously with the alkyl and fluorine radicals and oxygen functional groups are formed (Kharitonov, 2000). It has been reported that by reactions with R•, O_2, and F_2, peroxyradicals (RO_2•), acid fluorides (COF), and carboxylic acid (COOH) form on the oxyfluorinated surface (Jeong et al., 2011; Kharitonov, 2008; Park et al., 2005). According to Tu *et al*, oxidation of PP during oxyfluorination preferably occurs at the pendant methyl group (Tu et al., 1997). Many authors have reported that acid fluoride is hydrolysed to the highly polar carboxylic acid group (du Toit and Sanderson, 1999; Kharitonov et al., 2005; Lee et al., 2003).

The formation of reactive peroxide groups and long-lived trapped peroxy radicals on oxyfluorinated polymer surfaces is well-known (du Toit and Sanderson, 1999; Jeong et al., 2011; Kharitonov, 2000; Kharitonov et al., 2004). Kharitonov *et al* have reported middle (–$CH(OO^{\bullet})$– or –$CF(OO)^{\bullet}$-) and “end” peroxy groups (–$CH_2OO^{\bullet}$ or –$CHFOO^{\bullet}$ or –$CF_2OO^{\bullet}$) on oxyfluorinated LDPE (Kharitonov et al., 2005). It has been reported that the amount of peroxyradicals exceeds the amount of fluororadicals (Tressaud et al., 2007). Since the reactivity of peroxyradicals is much slower than alkyl radicals, peroxyradicals can exist as long-loved radicals (Woo et al., 2005). Using the DPPH UV-VIS method and electron-spin resonance we have detected peroxy radicals on the oxyfluorinated PP NWF. For graft polymerisation of PNIPAAm onto the oxyfluorinated NWF scaffolds, there exists two sources of initiators i.e. the peroxide groups on the oxyfluorinated NWF scaffolds as well as from the chemical initiator APS (**Scheme 5.3**).

Radical formation:

$$ROOH \xrightarrow{\Delta} RO^{\cdot} + OH^{\cdot}$$

$$S_2O_8^{2-} \xrightarrow{\Delta} 2SO_4^{-\cdot}$$

$$SO_4^{-\cdot} + H_2O \rightarrow HSO_4^{-} + OH^{\cdot}$$

Initiation of monomer:

$$SO_4^{-\cdot} + M \rightarrow M^{\cdot}$$

$$OH^{\cdot} + M \rightarrow M^{\cdot}$$

$$RO^{\cdot} + M \rightarrow R - OM^{\cdot}$$

Propagation:

$$M^{\cdot} \xrightarrow{nM} (M)_nM^{\cdot}$$

$$R - OM^{\cdot} \xrightarrow{nM} R - O(M)_nM^{\cdot}$$

Termination:

$(M)_nM^{\cdot} + M^{\cdot}(M)_n \rightarrow (M)_x$ (PNIPAAm homopolymer) [I]

$R - OM^{\cdot} + M^{\cdot}(M)_n \rightarrow R - O(M)_x$ (Grafted PNIPAAm) [II]

$R - O(M)_nM^{\cdot} + M^{\cdot}(M)_n OR \rightarrow R - O(M)_x - O - R$ (Grafted PNIPAAm) [III]

Scheme 5.3: Possible mechanism for graft polymerisation during synthesis of PNIPAAm grafted NWF scaffolds.

At elevated temperatures, the peroxide on the polymer backbone can be homolytically cleaved due to the low bond dissociation energy of the O-O bond to form alkoxy radicals ($RO^{\bullet}$) on the NWF surface which serve as active sites for grafting (Kildal et al, 2007). Conversely the APS initiator, which is also a peroxide, undergoes thermal decomposition to form sulphate radical ions ($SO_4^{\bullet-}$) and hydroxyl radicals ($OH^{\bullet}$), which are capable of initiating polymerisation by adding to the unsaturated double bond of the NIPAAm monomer (Riggs and Rodriguez, 1967). The alkoxy radicals ($RO^{\bullet}$) on the NWF is also capable of forming a free radical on the NIPAAm monomer. Propagation then pursues and a number of growing radicals are possible. Termination of the growing radicals involves formation of the PNIPAAm homopolymer as well as PNIPAAm graft chains which proceed via coupling of the growing NIPAAm chains [I] and the polymer radical and the propagating NIPAAm chains [II-III] respectively.

The method of graft polymerisation employed in the present study can be described as a combination “grafting from” the NWF surface as well as “grafting to” the NWF surface. For the former, oxyfluorination was used to form peroxide radicals on the NWF which then

enabled attachment of a propogating NIPAAm radical chain, leading to grafting and polymerisation of PNIPAAm from the PP surface (Grafted PNIPAAm [III]). However when APS was used as the initiator, PNIPAAm homopolymerisation occurred and it is possible that the growing PNIPAAm chain can terminate by reaction with the alkoxy radical on the PP surface, implying that “grafting to” the PP surface will also occur (Grafted PNIPAAm [II]). We have also shown that graft yeilds are significantly higher when APS is used, implying that a combination of both graft methods contribute to improving the graft efficiency.

5.3.8 XRD

The XRD patterns for pure PP NWF, oxyfluorinated PP NWF, and PP-*g*-PNIPAAm NWF appear in **Figure 5.43**. The diffractogram patterns for all the pure and modified PP NWF were similar displaying three relatively strong bands and three less-intense bands at 2θ between 13-28° indicating a semi-crystalline materi al, while PNIPAAm displayed 2 broad peaks indicating an amorphous material.

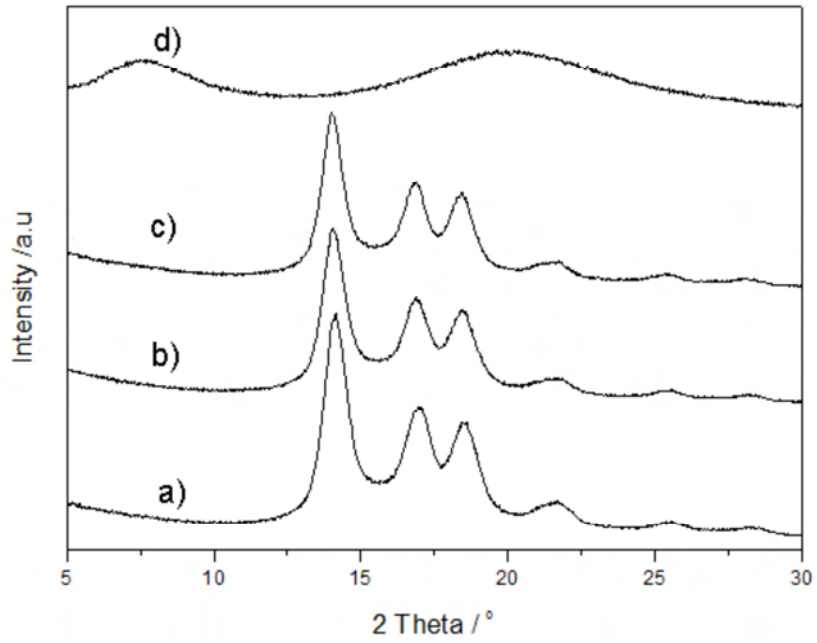

Figure 5.43: XRD diffractograms of (a) pure PP NWF; (b) oxyfluorinated PP NWF; (c) PP-*g*-PNIPAAm NWF; and (d) PNIPAAm (control).

To determine which isomer of PP was present, a matching was done using the X’Pert Prodatabase, and it was confirmed that the PP was isotactic. It is known in literature that isotactic PP can have three different polymorphs i.e. α, β, γ forms which corresponds to the monoclinic, trigonal, and orthorhombic crystal systems respectively, and can be identified by

characteristic reflections (Krache et al., 2007). The monoclinic α form is the most common and stable modification of isotactic PP. The trigonal β form is a metastable phase, the formation of which can be promoted by using specific nucleating agents while the orthorhombic γ form is favoured when there are stereo and / or region defects present in the structure interrupting the isotactic segments (Krache et al., 2007).

The XRD patterns for the pure PP NWF; oxyfluorinated PP NWF; and PP-*g*-PNIPAAm NWF in all cases matched to monoclinic α-form of polypropylene (a = 6.65Å; b = 20.8Å; c = 6.5Å) (a,b,c represents the lattice parameters). The results indicate that after OAGP treatment the crystal structure of PP was not affected, i.e. the arrangement of the atoms in the crystal lattice remained in the monoclinic form despite the introduction of randomly spaced functional groups.

5.3.9 DSC

The DSC thermograms for crystallisation and melting of the PP NWF appear in **Figures 5.44 - 5.45** respectively, and the results are summarised in **Table 5.12**. Two melting cycles were performed in this study, since 1st melting eliminates the material's thermal history, and 2nd melting after crystallisation is more accurate due to sample purity and thermal transitions are free from artefacts. During crystallisation, a sharp symmetric crystallisation peak was observed for the pure PP NWF at Tc_{max} of 111.6 ℃ indicating a relatively pure semi-crystalline material, however for the oxyfluorinated PP and PP-*g*-PNIPAAm, the crystallisation peaks appeared somewhat broader, and was shifted to a higher temperature (Tc_{max} 117.66 ℃ and 115.08 ℃ respectively). During melti ng, pure PP NWF displayed a single melting peak at 160.42 ℃ indicating one sta ble crystalline form in PP, while strikingly for the oxyfluorinated and grafted PP, twin melting peaks were observed at T_{m1}:147.24 ℃ & T_{m2}:161.66 ℃ and T_{m1}:148.63 ℃ & T_{m2}:165.22 ℃ respectively. Peak multiplication behaviour has been observed previously for isotactic PP (Horváth et al., 2010; Huda et al., 1985). Peak multiplication may be due to a number of different factors such as changes in the crystalline structure or crystal phases; crystal defects and irregularities; crystals of different sizes whereby the smaller and imperfect crystals will melt at lower temperatures compared to the perfect crystals; or re-crystallisation phenomena whereby during the slow melting process some of the melted crystals recrystallise (Horváth et al., 2010).

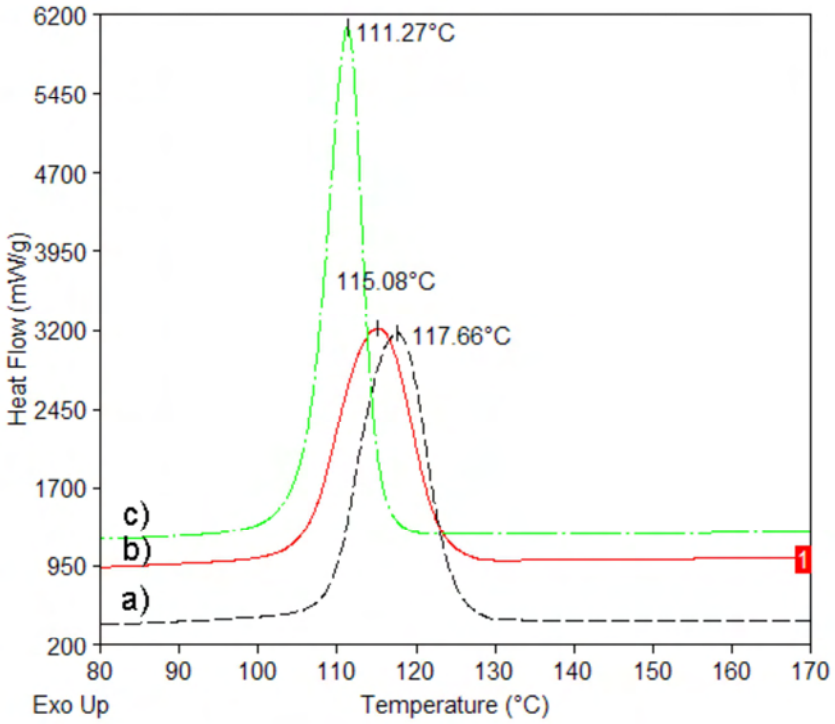

Figure 5.44: DSC thermograms showing 1st cooling for (a) oxfluorinated PP NWF; (b) PP-*g*-PNIPAAm NWF; and (c) pure PP NWF (Exothermic is up).

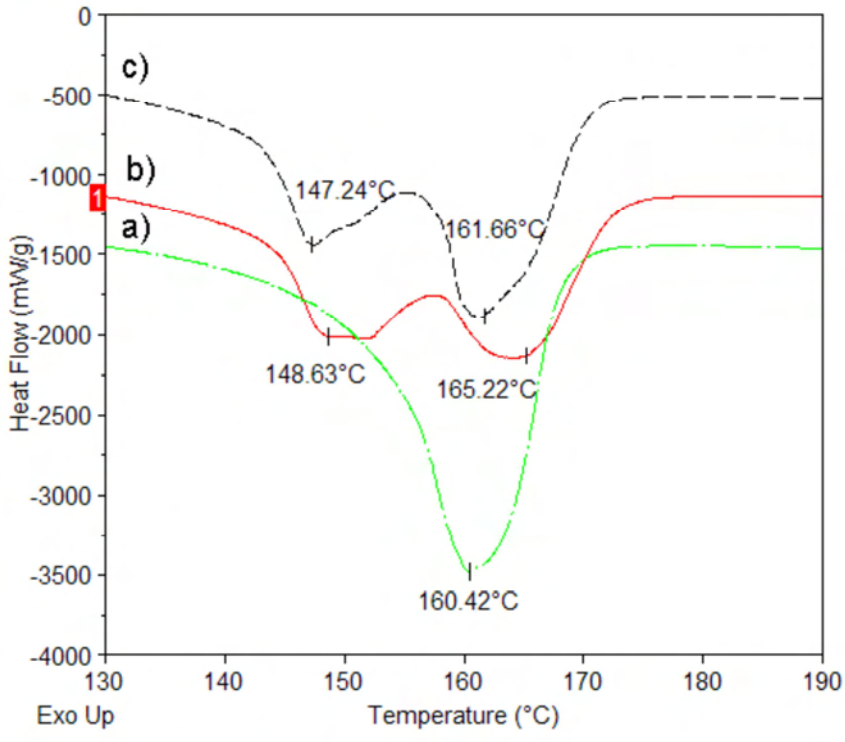

Figure 5.45: DSC thermograms showing 2nd heating for (a) pure PP NWF; (b) PP-*g*-PNIPAAm NWF and (c) oxyfluorinated PP NWF (Exothermic is up).

Table 5.12: Crystallisation and melting DSC data for pure and oxyfluorinated PP NWF scaffolds.

NWF	*Crystallisation*		*Melting*					ΔT
	T_{onset}/℃	T_c/℃	T_{onset}/℃	T_{m1}/℃	T_{m2}/℃	ΔH/J.g^{-1}	% crystall-isation	
Pure PP	106.51	111.27	142.38	-	160.42	74.26	50.69	49.15
Oxyfluorinated PP	109.54	117.66	152.71	147.24	161.66	72.92	49.78	44
PP-*g*-PNIPAAm	106.41	115.08	144.17	148.63	165.22	68.39	46.68	50.14

According to XRD (**see Section 5.3.8**) oxyfluorination and grafting did not affect the crystal structure of PP, i.e. even after the modification only the monoclinic α-form of isotactic polypropylene was present. It can be assumed that even though the crystal phases in oxyfluorinated and grafted PP are the same, it is possible that crystal defects may exist in the modified PP due to the presence of the new functional groups which lower the stereo regularity of the PP chains causing irregular packing and thereby creating defects in the crystal lattice structure. This would result in a combination of impure irregular crystals (due to the functional groups) which are less stable and which would melt first, and pure well-ordered crystals (due to the pure PP repeat units-which may have not been modified) which melt at a higher temperature. Additionally crystals of two sizes may be present due to the modification, which would melt at different rates.

The higher melting peak temperature (T_m) for the oxyfluorinated NWF and grafted NWF scaffolds compared to the pure NWF indicate improved structural stability for the modified NWF scaffolds (Horváth et al., 2010). This may be attributed to enhanced inter-/intramolecular forces in the modified polymers due to hydrogen bonding between adjacent positively charged hydrogen atoms and the electronegative atoms in the oxyfluorinated scaffolds (such as F and O), and between the N-H and C=O groups in the grafted NWF scaffolds. The improved inter-/intramolecular forces within the structure, may result in a more stable material with a higher T_m and T_c compared to pure untreated PP.

Crystallinity

The degree of crystallisation based on the heat of fusion was calculated from the enthalpy of melting as shown in **Table 5.13**. From the heat of fusion calculations it was determined that the degree of crystallinity of pure PP was 50.69% indicating a semi-crystalline material. After oxyfluorination and graft polymerisation, the crystallisation percent of the NWF decreased slightly to 49.78% and 46.68% respectively. Since the method used to determine crystallinity based on heat of fusion calculation from peak areas is only an approximate calculation, the difference observed here is negligible. It can be concluded that the degree of crystallinity of pure PP is unaffected by the OAGP method. This means that during oxyfluorination and grafting, new functional groups attack the amorphous domains in PP, with negligible modification to the crystalline regions.

Undercoolability

Another interesting observation which was made was that for all of the PP NWF scaffolds the Tc appeared at a lower temperature than T_m for both cycles. This may be due to the supercooling / undercooling effect, i.e. lowering of the liquid melt below the freezing point without the material solidifying. Undercooling is required to overcome the surface Gibbs energy barrier for the formation of the crystal phase (Horváth et al., 2010). The undercooling may be represented by ΔT, and it is the difference between the peak maximum for the melting and cooling.

According to Horváth et al., the lower the undercoolability the higher is the inclination for crystallisation. Oxyfluorinated PP NWF scaffolds displayed lower ΔT values compared to pure and grafted PP indicating a higher ability to crystallise for the functionalised polymers which could be due to the functional groups increasing the chain mobility (due to electrostatic attraction) which allows the molecules to more quickly rearrange into a crystalline structure compared to pure PP.

Determination of the LCST

To identify the LCST of PNIPAAm, DSC was also conducted on wet PP-*g*-PNIPAAm NWF scaffolds as shown in **Figure 5.46**. A LCST was detected at Tp of 33.4 ℃ which confir med the presence of PNIPAAm in the grafted PP NWF, and also indicated that the OAGP method did not modify the LCST of PNIPAAm.

\

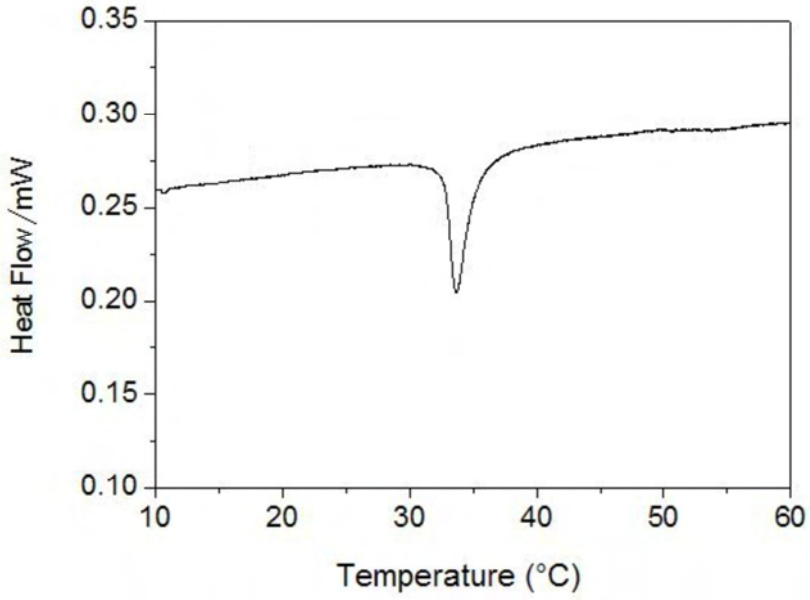

Figure 5.46: Heating DSC thermogram of PP-*g*-PNIPAAm NWF showing a LCST at ~33.4 ℃ using wet samples.

5.4 Conclusions

We have succeeded in grafting PNIPAAm onto PP, PET, and nylon NWF scaffolds using an OAGP two-step method which first involved fluorination, followed by free radical induced graft polymerisation. PP, PET, and nylon NWF scaffolds were manufactured using the needle-punching technology. PP and PET NWF scaffold displayed mean flow pores which was suitable for cell culturing while the MFP on the nylon NWF scaffold was below the required pore size range due to the lower linear density of the fibres used.

The PP, PET, and nylon were functionalised by direct fluorination and oxyfluorination. New functional groups formed on the surface of the NWF scaffolds included C-OH, C=O, CH_2-CHF and CHF-CHF. PP and nylon displaying the largest modification, while for PET very little changes were observed on the fibre surface. The high surface functionalisation on oxyfluorinated PP was attributed to the tertiary carbon in the polymer backbone. In the case of PET, the low surface modification was attributed to the resonance effect of the aromatic ring. Improved wetting and swelling in water was observed for the oxyfluorinated PP compared to pure PP, which is an important requirement for graft polymerisation in aqueous media. However the new functional groups on oxyfluorinated PP were significantly reduced after hydrolysis post-treatment. Water contact angle values showed reduced hydrophobicity

of the oxyfluorinated PP surface in comparison to pure PP, however the small reduction in contact angle value was attributed to a surface rearrangement process.

PNIPAAm on the grafted NWF surface was confirmed using a variety of techniques including ATR-FTIR, XPS, contact angle, and SEM. Additionally the LCST of PNIPAAm was preserved in PP-*g*-PNIPAAm NWF scaffolds. Oxyfluorinated PP NWF showed the highest graft yield when grafting was with the chemical initiator APS. Using the DPPH UV-VIS method and ESR, we have identified peroxide groups and trapped long-lived peroxy radicals on the surface of the oxyfluorinated PP NWF, which are believed to be involved in graft initiation. On the pure NWF scaffolds, excessive homopolymerisation was observed due to adsorption of the PNIPAAm homopolymer onto the NWF surfaces. The OAGP method did not affect the crystalline phase of bulk PP; however, twin-melting thermal peaks were detected for the oxyfluorinated and grafted PP NWF indicating crystal defects.

A free radical mechanism was proposed for the OAGP method with initiation via $SO_4^{\bullet -}$, $OH^{\bullet}$ and $RO^{\bullet}$ radicals. An advantage of this method is that no organic solvents, or toxic chemcials are used, and graft polymerisation is carried out in an aqueous medium under mild conditions. This method presents an attractive alternative to other more expensive graft polymerisation technologies such as gamma radiation, plasma-radiation etc.

5.5 References

Akiyama Y, Kushida A, Yamato M, Kikuchi A, Okano T. 2007. Surface characteristics of poly(*N*-isopropylacrylamide) grafted tissue culture polystyrene by electron-beam irradiation using atomic force microscopy and X-ray photoelectron spectroscopy. Journal of Nanoscience and Nanotechnology 7:796-802.

Anjum N, Moreau O, Riquet AM. 2006. Surface designing of polypropylene by critical monitoring of the grafting conditions. Journal of Applied Polymer Science 100:546–553.

Boguslavsky L. 2008. Needle-punched nonwovens from PP fibres for Scaffolds Application (Trial 4). unpublished report. 9 p.

Boguslavsky L. High efficiency particulate air (HEPA) filters from polyester and polypropylene-nonwovens. FILTREX; 2010; Cologne, Germany.1-15.

Boguslavsky L, Anandjiwala R. 2007. Needle-punched non-woven for scaffolds applications - 2nd trial. unpublished report. 1-12.

Boguslavsky L, Tsheloane C, Whitebooi H, Anandjiwala R. 2008. Needle-punched non-wovens for scaffold applications from nylon 6.6 (3rd Trial). unpublished. 1-9.

Bovet C, Barron AR. 2009. EPR Spectroscopy: An overview, http://cnx.org/content/m22370/latest/, Date accessed: 16 August 2012.

Bucio E, Burillo GA, E. , Coqueret X. 2005. Temperature sensitive behaviour of Poly(*N*-isopropylacrylamide) grafted onto electron beam-irradiated poly(propylene). Macromolecular Materials Engineering 290: 745-752.

Chang H, Wang Y. 2011. Cell Responses to Surface and Architecture of Tissue Engineering Scaffolds, Regenerative Medicine and Tissue Engineering - Cells and Biomaterials, Prof. Daniel Eberli (Ed.),ISBN: 978-953-307-663-8, InTech, 27: 570-588.

Clough RL. 2001. High-energy radiation and polymers: A review of commercial processes and emerging applications. Nuclear Instruments and Methods in Physics Research B 185: 8-33.

Contreras-Garcıa A, Burillo G, Aliev R, Bucio E. 2008. Radiation grafting of N,N-dimethylacrylamide and N-isopropylacrylamide onto polypropylene films by two-step method. Radiation Physics and Chemistry 77 936–940.

du Toit FJ, Sanderson RD. 1999. Surface fluorination of polypropylene 1. Characterisation of surface properties. Journal of Fluorine Chemistry 98:107-114.

Fargere T, Abdennadher M, Delmas M, Boutevin B. 1995. Determination of peroxides and hydroperoxides with 2,2-diphenyl-1-picrylhydrazyl (DPPH). Application to ozonized ethylene vinyl acetate copolymers (EVA) European Polymer Journal 31(5):489-497.

Geuskens G, Nedelkos G. 1993. The post-irradiation oxidation of poly(propylene), Radical decay and oxygen absorption. Makromolekulare Chemie 194:3349-3355.

Gu SY, Wang ZM, Li JB, Ren J. 2010. Swichability wettability of thermo-responsive biocompatible nanofibrous films created by electrospinning. Macromolecular Materials and Engineering 295: 32-36.

Horváth Z, Sajó IE, Stoll K, Menyhárd A, Varga J. 2010. The effect of molecular mass on the polymorphism and crystalline structure of isotactic polypropylene. Express Polymer Letters 4(2):101–114.

Hruska Z, Lepot X. 2000. Ageing of the oxyfluorinated polypropylene surface: evolution of the acid-base surface characteristics with time. Journal of Fluorine Chemistry 105:87-93.

Huda MN, Dragaun H, Bauer S, Muschik H, Skalicky P. 1985. A study of the crystallinity index of polypropylene fibres. Colloidal Polymer Science 263(9):730-737.

Ionita P. 2005. Is DPPH stable free radical a good scavenger for oxygen active species? Chemical Papers 59(1):11—16

Jaganathan S, Tafreshi HV, Shim E, Pourdeyhimi B. 2009. A study on compression-induced morphological changes of nonwoven fibrous materials. Colloids and Surfaces A: Physicochemical and Engineering Aspects 337:173-179.

Jeong E, Bae TS, Yun SM, Woo SW, Lee YS. 2011. Surface characteristics of low-density polyethylene films modified by oxyfluorination-assisted graft polymerization. Colloids and Surfaces A: Physicochemical and Engineering Aspects 373:36-41.

Justice BA, Badr NA, Felder RA. 2009. 3D cell culture opens new dimensions in cell-based assays. Drug Discovery Today 14(1/2):102-107.

Kharitonov AP. 2000. Practical applications of the direct fluorination of polymers. Journal of Fluorine Chemistry 103:123-127.

Kharitonov AP. 2008. Direct fluorination of polymers – From fundamental research to industrial application. Progress in Organic Coatings 61:192-204.

Kharitonov AP, Kharitonova LN. 2009. Surface modification of polymers by direct fluorination: A convenient approach to improve commercial properties of polymeric articles. Pure and Applied Chemistry 81(3):451-471.

Kharitonov AP, Moskvin YL, Syrtsova DA, Starov VM, Teplyakov VV. 2004. Direct fluorination of the polyimide matrimid® 5218: The formation kinetics and physicochemical properties of the fluorinated layers. Journal of Applied Polymer Science 92:6–17.

Kharitonov AP, Taege R, Ferrier G, Teplyakov VV, Syrtsova DA, Koops GH. 2005. Direct fluorination—Useful tool to enhance commercial properties of polymer articles. Journal of Fluorine Chemistry, 126:251–263.

Kildal K., Olafsen K, Stori A. 1992. Peroxide-initiated grafting of acrylamide onto polyethylene surfaces. Journal of Applied Polymer Science 44:1893-1898.

Kou RQ, Xu ZK, Deng HT, Liu ZM, Seta P, Xu Y. 2003. Surface modification of microporous polypropylene membranes by plasma-induced graft polymerization of a-Allyl glucoside. Langmuir 19:6869-6875.

Krache R, Benavente R, López-Majada JM, Pereña JM, Cerrada ML, Pèrez E. 2007. Competition between α, β, γ polymorphs in a – β nucleated metallocenic isotactic polypropylene. Macromolecules 40:6871-6878.

Kranz G, Luschen R, Gesang T, Schlett V, Hennemann OD, Stohrer WD. 1994. The effect of fluorination on the surface characteristics and adhesive properties of polyethylene and polypropylene. International Journal of Adhesion and Adhesives 14(4):243-253.

Kumashiro Y, Yamato M, Okano T. 2010. Cell attachment–detachment control on temperature-responsive thin surfaces for novel tissue engineering. Annals of Biomedical Engineering 38(6):1977–1988.

László K, Kosik K, Geissler E. 2004. High-sensitivity isothermal and scanning microcalorimetry in PNIPA hydrogels around the volume phase transition. Macromolecules 37:10067-10072.

Lee BK, Lee YS, Chong YB, Choi JB, Rho JR. 2003. Hydrophilic modification of polypropylene film by oxyfluorination. Journal of Industrial and Engineering Chemistry 9(4):426-432.

Liu M, Fengling B, Fenling S. 2005. FTIR study on molecular structure of poly(*N*-isopropylacrylamide) in mixed solvent of methanol and water. European Polymer Journal 41:283–291.

Louw IdV, Carstens PAB. 2006. Oxyfluorination. US patent PCT/IB03/04701.

Mark JE. 1999. Polymer data handbook: Oxford University Press. pg 1012.

Okano T, Yamada N, Okuhara M, Sakai H, Sakurai Y. 1995. Mechanism of cell detachment from temperature-modulated, hydrophilic-hydrophobic polymer surfaces. Biomaterials 16:297-303.

Park SJ, Song SY, Shin JS, J.M. R. 2005 Effect of surface oxyfluorination on the dyeability of polyethylene film. Journal of Colloid Interface Science 283:190–195.

Pryor WA. 1966. Introduction to free radical chemistry. Prentice-hall foundations of modern organic chemistry series. London: Prentice-Hall Inc. p 61.

Riggs IP, Rodriguez F. 1967. Persulfate-initiated polymerisation of acrylamide. Journal of Polymer Science Part A-1: Polymer Chemistry 5:3151-3165.

Schild H. 1992. Poly(*N*-isopropylacrylamide): Experiment, theory, and application. Progress in Polymer Science 17:163-249.

Schlick S, Mcgarvey BR. 1983. Motion of midchain peroxy-radicals in poly(tetrafluoroethylene). Journal of Physical Chemistry 87(2):352-352.

Singha K, Maity S, Singha M, Paul P, Gon DP. 2012. Effects of fiber diameter distribution of non-woven fabrics on its properties. International Journal of Textile Science 1(1): 7-14.

Skoog DA, West DM, Holler FJ. 1996. Fundamentals of analytical chemistry: Saunders College Publishing.

Socrates G. 2001. Infrared and raman characteristic group frequencies: tables and charts: John Wiley & Sons Ltd. 347 p.

Tressaud A, Durand E, Labruge`re C, Kharitonov AP, and Kharitonova LN. 2007. Modification of surface properties of carbon-based and polymeric materials through fluorination routes: From fundamental research to industrial applications. Journal of Fluorine Chemistry 128:378–391.

Tu L, Kruger D, Wagener JB, Carstens PAB. 1997. Wettability of surface oxyfluorinated polypropylene fibres and its effect on interfacial bonding with cementitious matrix. Journal of Adhesion 62:187-211.

Uchimaru A, Kutsuna S, Chandra AK, Sugie M, Sekiya A. 2003. Effect of fluorine substitution on the rate for ester hydrolysis: estimation of the hydrolysis rate of perfluoroalkyl esters. Journal of Molecular Structure (Theochem) 635:83–89.

Wan L-S, Yang Y-F, Tian J, Hu M-X, Xu Z-K. 2009. Construction of comb-like poly(*N*-isopropylacrylamide) layers on microporous polypropylene membrane by surface-initiated atom transfer radical polymerization. Journal of Membrane Science 327:174–181.

Wang X, McCord MG. 2007. Grafting of poly(N-isopropylacrylamide) onto nylon and polystyrene surfaces by atmospheric plasma treatment followed with free radical graft copolymerization. Journal of Applied Polymer Science 104:3614-3621.

Woo SW, Song MY, Rho JS, Lee YS. 2005. The effect of oxyfluorination on the surface characteristics of low-density polyethylene films. Journal of Industrial and Engineering Chemistry 11(1):55-61.

Yamato M, Akiyama Y, Kobayashi J, Yang J, Kikuchi A, Okano T. 2007. Temperature-responsive cell culture surfaces for regenerative medicine with cell sheet engineering. Progress in Polymer Science 32:1123–1133

CHAPTER 6

Temperature-induced Cell Culture

Published in Biotechnology and Bioengineering

Part of work has been published in Colloids and Surfaces A: Interfaces and Engineering aspects

6.1 Introduction

It is well-known that cells grown onto 3D surfaces show closer similarities to their *in vivo* counterparts in terms of cell morphologies, behaviour, and function than 2D surfaces (Justice et al., 2009; Pampaloni et al., 2007). Nowadays 3D scaffolds are routinely used to culture cells, however cell release from 3D scaffolds remains challenging. Often enzymatic digestion of the extracellular matrix (ECM), mechanical scraping of the cells, or chemical degradation of the matrix is required in order to release adherent cells. Such release mechanisms cause irreversible damage to cells leading to disruptions in essential receptor-ligand interactions on the cell surface (Canavan et al., 2005). Damage to the ECM is known to adversely influence cell signalling pathways which affects important cellular processes for downstream applications (Guillame-Gentil et al., 2010). Furthermore, concerns exist with regards to the animal origin of some of the 3D ECM scaffolds and the associated production variability (Justice et al., 2009). This, combined with the additional wash steps and extra handling requirements, results in high costs, well-to-well variations, and culture inconsistencies.

Poly(*N*-isopropylacrylamide) (PNIPAAm), a temperature responsive polymer, has revolutionised the cell culture fraternity by providing a non-invasive means of harvesting adherent cells, whereby confluent cells can be spontaneously released by simply cooling the cell culture medium and without requiring enzymes. The pioneering work by Okano *et al* showed that cells could be released as intact monolayer cell sheets from the surface of PNIPAAm coated tissue culture polystyrene trays with their deposited ECM and preserved cell-cell and cell-ECM interactions (Okano et al., 1995). PNIPAAm switches its properties reversibly between hydrophobic (cell adhesive) and hydrophilic (non-cell adhesive) states at temperatures higher and lower than its lower critical solution temperature (LCST) (~32 °C) respectively (Schild, 1992). In recent years, advances were made in the area of regenerative medicine where stacking of homotypic or heterotypic cell sheets onto patterned surfaces has shown the formation of functional 3D tissues and organ-like constructs (Yamato et al., 2007)

PNIPAAm monolayer cell culturing is a promising tool for engineering tissue but the current technology is essentially based on the use of flat 2D substrates. The method of culture lacks structural and organisational cues for cells since the 2D environment does not replicate the complexity of physiological tissue (Isenberg et al., 2008). Where layered or patterned co-culture cell sheets are used, the process requires multiple steps and does not address the need for a structural matrix to enable cell growth in three dimensions. In recent years, some

3D PNIPAAm scaffolds have been developed based on hydrogels, grafted porous 3D membranes and micro-textured PNIPAAm surfaces (Isenberg et al., 2008; Kwon and Matsuda, 2006; Ohya et al., 2005). Additionally a PP-*g*-PNIPAAm non-woven membrane with adsorbed antibodies has recently been reported in the literature for selective cell separation and enrichment of target cells (Okamura et al., 2008). However, to date little work has been done regarding applying the PNIPAAm technology to highly porous 3D scaffolds for the purpose of 3D cell propagation and non-invasive recovery of 3D cell constructs. Additionally many of these studies still focus on the formation of 2D cell monolayers for the purpose of tissue engineering and regenerative medicine (**See Table 6.1**).

We have developed a new 3D scaffold based on PNIPAAm for use in 3D non-invasive cell culture. The scaffolds were developed to firstly support cell attachment, enhanced proliferation, and the growth of 3D cellular aggregates or constructs as opposed to cell monolayers. Furthermore the scaffolds were modified such that 3D cellular structures could be released non-invasively from its surface with surface proteins and extracellular matrix proteins remaining largely intact. We are also developing a novel cell culturing device (T3D) (**Section 6.1.1**) which will contain a bioreactor containing the 3D scaffolds for improving the efficiency of the cell culture process. The device is novel since such a device does not exist for cell culture anywhere in the world. The combination of a perfused bioreactor capable of culturing cells on a 3D scaffold capable of high-density cell culture and non-invasive cell release has not been reported / demonstrated previously in literature.

In this study three different scaffolds were developed i.e. PP-*g*-PNIPAAm, PET-*g*-PNIPAAm, and nylon-*g*-PNIPAAm non-woven fabric (NWF) scaffolds, using an oxyfluorination-assisted graft polymerisation method as detailed in Chapter 5 which included functionalisation of the NWF scaffolds using fluorination followed by graft polymerisation in an aqueous NIPAAm solution. This chapter focuses on proof of concept or validation for the use of the developed scaffolds in non-invasive 3D culture of hepatocytes. Cell culture studies in the T3D bioreactor are also discussed.

6.1.1 CSIR's cell culturing device T3D

The Council for Scientific and Industrial Research (CSIR) in South Africa is developing a thermoresponsive 3D (T3D) cell culturing device for culturing of adherent (or anchorage-dependent) cells. The device consists of a 3D thermoresponsive NWF scaffold which is contained in a sterile perfused bioreactor allowing for non-destructive and high-density cell

culture in a continuous manner (Moolman et al., 2009). The T3D bioreactor was designed and constructed by Mr Kobus van Wyk from BlueLine Designs (Pretoria, South Africa).

The specific attributes of the T3D device is as follows:

- **A bioreactor**: Cells are cultured in a closed, sterile, perfused bioreactor more closely simulating the physiological conditions, with sufficient media circulation, oxygen and nutrient supply, and waste removal.
- **A 3D scaffold**: Cells are cultured on a highly porous 3D scaffold based on a NWF to enhance cell-to-cell and cell-to-media interactions, with a high surface area to more closely resemble the physiological microenvironment compared to 2D culture trays. The NWF contains an open porous highly permeable polypropylene non-woven scaffold that enables cells to be cultured in a 3D environment allowing for cell-to-cell and cell-media interactions as well as direct perfusion of media containing nutrients and oxygen.
- **Non-destructive cell harvesting**: The device allows for the proliferation and non-destructive harvest of cells by containing a PNIPAAm graft layer on the 3D NWF. Cell release is then possible by changing the temperature of the cell culture media/or gas without requiring harsh detachment methods (such as using enzymes). The cell membrane of cultured cells is preserved whereby critical cell surface proteins remain intact after cell release.
- **Bench-top system**: The device is a small, cost-effective bench-top system which is very easy to operate.
- **Automation**: It is envisaged that the T3D device will be automated whereby cell culturing will be possible with minimal human intervention since the manual cell culturing steps are automated (such as cell seeding, cell proliferation and cell release) with automatic regulation and real time monitoring of system parameters such as temperature, pH, flow rates, oxygen consumption, etc.

A schematic of the final T3D prototype device is given in **Figure 6.1**. The device works by circulating cell culture medium maintained at 37 °C between the medium reservoir and the bioreactor with axial flow using a peristaltic pump; whereby the bioreactor will contain the NWF disks; cells are then seeded into the bioreactor via the sampling port and allowed to settle via gravity onto the NWF disks in the bioreactor; sufficient time is given for the bioreactor to be populated with cells; and then cold media is perfused through the bioreactor to detach cells from the scaffold. The media would then be recovered and centrifuged separately for cell recovery, or a continuous centrifuge would be incorporated into the

system for automatic separation of cells. The cells can then be stored in the cell reservoir until required.

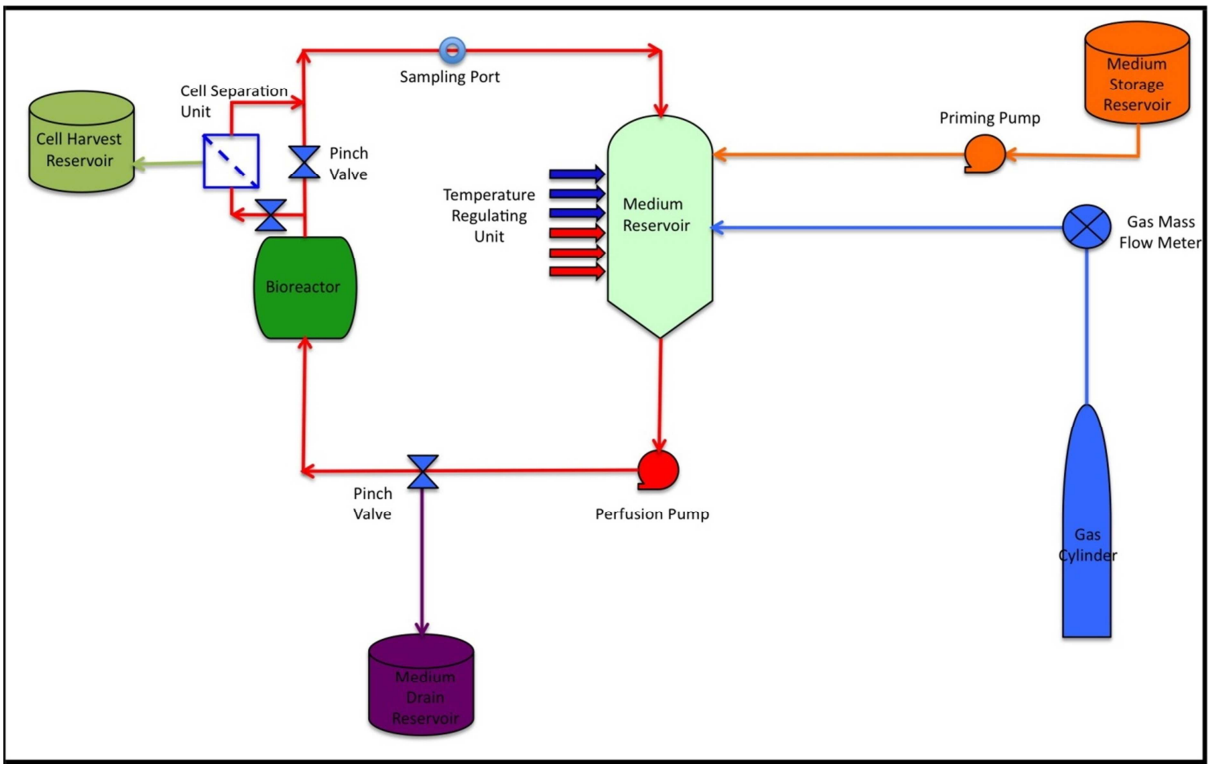

Figure 6.1: Schematic of the CSIR's T3D cell culture device showing the process-flow diagram for the bioreactor containing the 3D thermoresponsive non-woven scaffold.

The completed bioreactor system, including the bioreactor housing, the cell scaffold, the piping, the reservoir etc., would be off–the-shelf components, which would be easily sterilisable or pre-sterilised. All the system hardware (pumps, heating /cooling equipment, valves, etc.), instrumentation, electronic control and user interface and consumable location unit, are once-off acquisition that will be re-used for consecutive cell culturing experiments. The consumable set contains the "wetted" perfusion components (incl. the perfusion tubing, media reservoir, etc. and the bioreactor itself) and will be for a once-off single-use.

6.2 Experimental

To show proof-of-concept for the PNIPAAm grafted NWF as a new 3D scaffold for non-invasive culture of adherent cells, cells were cultured onto the scaffolds by Claire Rossouw at CSIR Biosciences and several assays were performed to determine cell viability,

metabolic activity, and thermal release potential. Assays which were conducted include AlamarBlue® cell viability assay, DNA cell quantification using Hoechst 33258, fluorescent staining of viable cells using fluorescein diacetate, metabolic activity using albumin blue, cytochrome P450 mRNA expression, and enzymatic and thermal-induced cell release (Rossouw et al., 2012). Comparisons were also made to a commercially available 3D scaffolds i.e. Algimatrix ™. This chapter focuses on validation of the scaffolds for 3D cell culture and temperature-triggered cell release.

6.2.1 Materials

HC04 (MRA-156, MR4) and HepG2 (ATCC HB-8065TM) hepatocyte cell lines were used in this study and obtained from ATCC ®, Manassas, VA, U.S.A. Dulbecco's Modified Eagle Medium (DMEM) was obtained from Lonza (Walkersville, Inc. Maryland, USA). All other chemicals (glutamine, foetal calf serum (FCS), penicillin, streptomycin) were obtained from Sigma-Aldrich Chemie, GmbH. The NWF scaffolds tested included: PP NWF scaffold (T2-N6(1): Mean –flow pores (MFP) ~ 127 µm; and T4-N13 : MFP ~200µm); PET NWF (T2-N7(1) : MWF ~142 µm, and nylon NWF (T3-N8(1)) : MFP ~79 µm.

6.2.2 Cell –scaffold interaction

To assess if the PNIPAAm grafted scaffolds could be used as a potential new scaffold for cell attachment, and enhanced proliferation, hepatocyte cells were cultured in static on PP-*g*-PNIPAAm which were pre-oxyfluorinated. The grafted NWF was cut into 5 x 5 x 3 mm pieces and were ethanol sterilised. 2 x 10^5 HepG2 and HCO4 hepatocytes were seeded separately into the scaffolds which were maintained in 2 mL DMEM with 2 $mM.L^{-1}$ glutamine and supplemented with 10% (v/v) FCS, 100 $g.mL^{-1}$ penicillin and 10 $\mu g.mL^{-1}$ streptomycin in a 12 well tissue culture plate for 21 days under standard conditions. Media changes were performed every 48 hours. The HC04 and HepG2 cells growing on the scaffolds were visualised with fluorescent microscopy using fluorescein diacetate (FDA, Sigma-Aldrich Chemie) to monitor cell attachment and morphology on 3, 7, 11, 15 and 21 days post inoculation. After a specified time period, cells on the scaffolds were incubated with a FDA solution (enough to cover the scaffold) for 5 min, after which the cells were gently rinsed in PBS to remove any residual dye (Rossouw et al., 2012). The non-specific esterase activity in the cytoplasm of viable cells converts non-fluorescent FDA to fluorescein, a green fluorescent dye. Both the top and bottom of the scaffolds were viewed for cell attachment at the days mentioned above at 40x magnification using a standard fluorescence microscope

(Olympus BX41, Olympus Microscopy, Essex, UK) equipped with a 490 nm bandpass filter with a 510 nm cut-off filter for fluorescence emission.

6.2.3 Temperature-induced cell release from PNIPAAm grafted NWF scaffolds in static culture

After it was ascertained that the grafted NWF scaffolds was suitable for cell culture, PP-*g*-PNIPAAm; PET-*g*-PNIPAAm; and nylon-*g*-PNIPAAm NWF scaffolds were all assessed for their potential to enable temperature-triggered cell release. Cells were cultured on the scaffolds as described above, however on day 10, the scaffolds were gently rinsed in warm, sterile phosphate buffered saline (PBS) solution to remove loose or dead cells and were placed (3 / well) into a six-well plate containing 2 mL of cooled (20 ℃) culture media. Nine scaffolds were used for testing: three scaffolds remained in the incubator at 37 ℃, three at 20 ℃ for 1 hr, and three at 20 ℃ for 2 hrs to est ablish the length of time necessary for temperature-mediated cell detachment. The cell culture plates containing the scaffolds were periodically agitated by gentle swirling during the incubations, where after the scaffolds were removed and the released cells on the bottom of the wells were photographed at 40x magnification using a standard microscope (Olympus BX41).

6.2.4 Cell release from PP-*g*-PNIPAAm NWF in T3D bioreactor

Based on the device functional requirements, a preliminary prototype T3D device was initially developed as shown in **Figures 6.2**. PP-*g*-PNIPAAm NWF scaffolds (mean flow pore size: 200 µm) were cut into disks (15 mm in diameter) which were ethanol sterilised. Three disks were stacked horizontally in the preliminary prototype T3D bioreactor. 4.5 x 10^6 HepG2 hepatocytes were seeded into the bioreactor via the sampling port. The cells were then allowed to settle and attach to the grafted NWF disks for 3 hrs. DMEM Medium with 2 mM L^{-1} glutamine and supplemented with 10% (v/v) FCS, 100 $g.mL^{-1}$ penicillin and 10 $\mu g.mL^{-1}$ streptomycin was perfused into the bioreactor at 2 mL min^{-1} for a period of 10 days. A bioreactor running in parallel containing the pure PP NWF was used as the control. To ascertain thermal release potential of the grafted NWF, the bioreactor was perfused with cold media at 20 ℃ for 2 hrs. The media containing the released cells was then drained from the bioreactor, and the cells on the grafted NWF (before and after thermal release) were stained with FDA and visualised at 40x magnification using a standard fluorescence microscope (Olympus BX41) equipped with a 490 nm bandpass filter with a 510 nm cut-off filter for fluorescence emission.

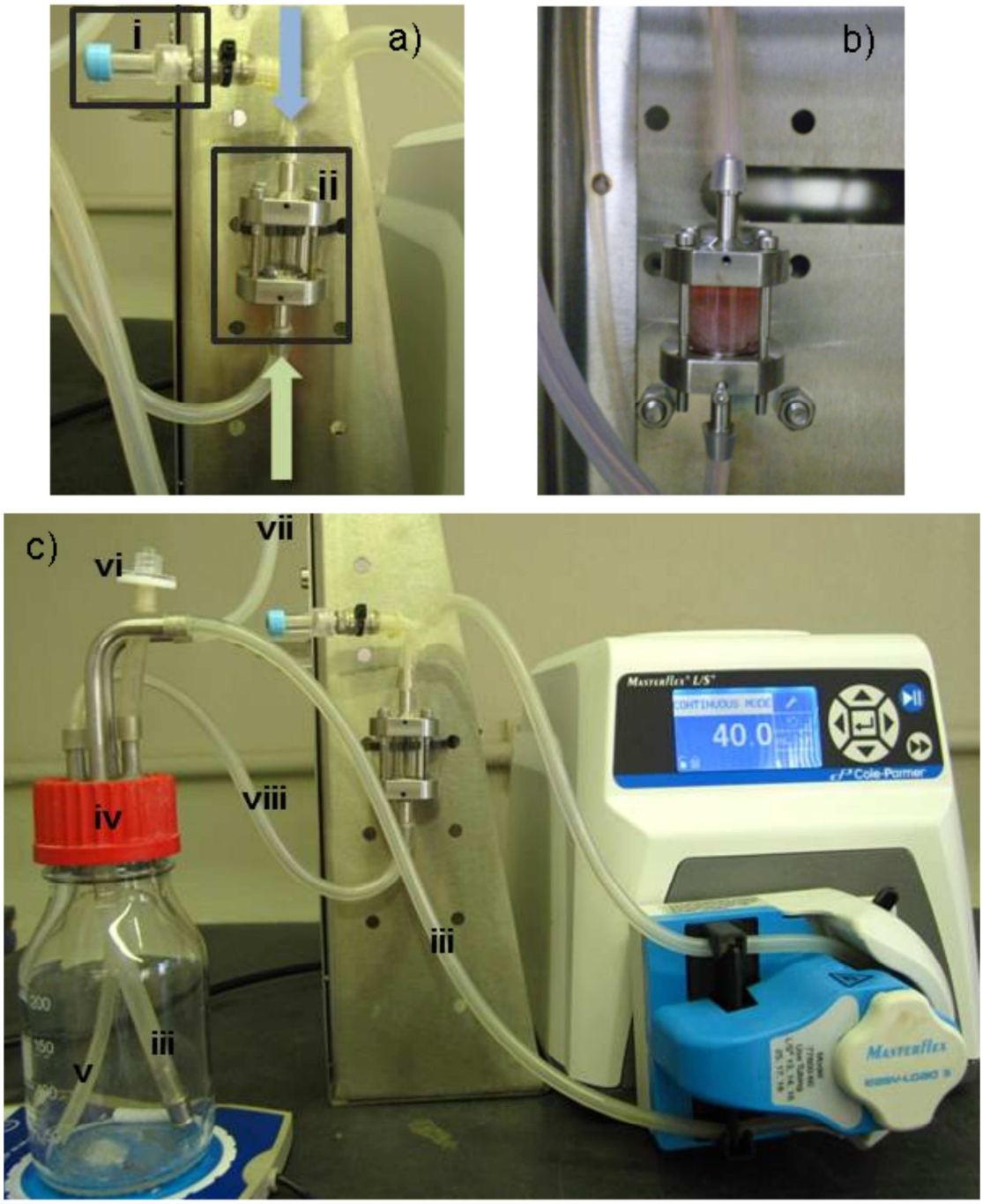

Figure 6.2: Preliminary prototype of the CSIR's T3D showing (a) i) sampling port through which cells are injected into the bioreactor; and ii) small volume bioreactor (without scaffolds); (b) close-up view of bioreactor containing stacked NWF disks (1.5mm diameter) with cells and media; and (c) full view of the preliminary prototype system showing the peristaltic pump used for pumping iii) media from (iv) media reservoir to the bioreactor; v) gas inlet (into the media); vi) gas vent; vii) gas line from tank; and viii) media return line (from the bioreactor).

To ascertain if high-density cell culture was possible on the 3D NWF in the bioreactor, a preliminary trial was performed and cells were cultured for 14 days in the bioreactor as indicated above but at day 14 the media was drained and the NWF disks containing the proliferated cells were gently removed from the bioreactor, and the disks were trypsinated and the cells were harvested and counted using tryphan blue dye exclusion on a haemocytometer.

6.3 Results and discussion

6.3.1 Cell morphology and proliferation

To determine if the scaffolds were able to support cell attachment and growth, HC04 and HepG2 hepatocyte cell lines were used. HCO4 cells are a hepatocyte line immortalised from normal human liver tissue to support the *in vitro* development of human malaria parasite (Sattabongkot et al., 2006). HepG2 cells are a cell line from a human hepatic carcinoma and it is routinely used as a tool for drug toxicity screening.

To visualise the cells on the NWF scaffolds, and as an indicator of cell viability, fluorescence microscopy was used whereby only viable cells stain green with FDA. Representative cell morphology and proliferation of the HC04 and HepG2 hepatocytes on the PP-*g*-PNIPAAm scaffold over 21 days is shown in **Figure 6.3**.

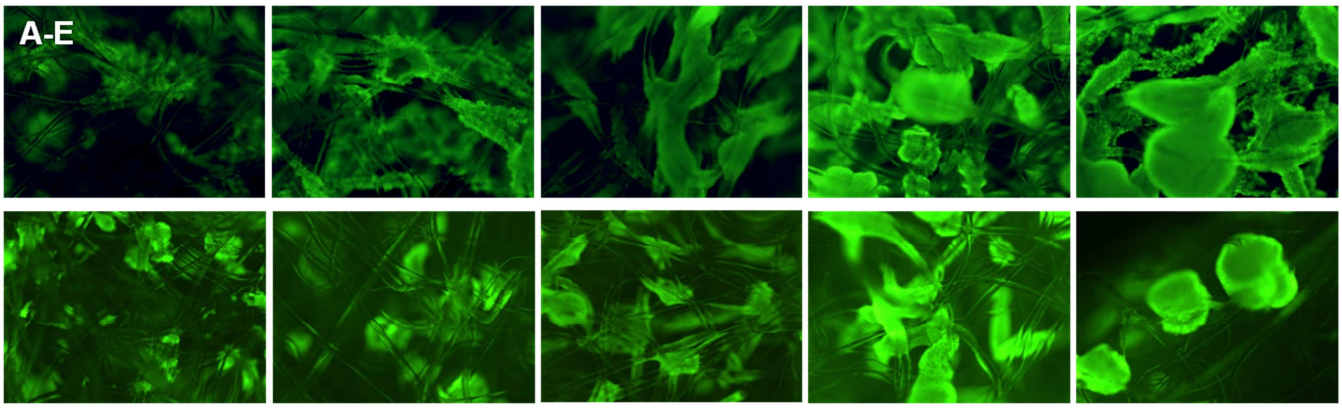

Figure 6.3: Fluorescence micrographs of HC04 (top panel) and HepG2 (bottom panel) hepatocytes growing on the PP-*g*-PNIPAAm (pre-oxyfluorinated) after 3, 7, 11, 14 and 21 day post-inoculation (A-E) (Rossouw, et al., 2012).

Cells remained viable during the duration of the 21 day culture period due to the large surface area of the NWF, and scaffolds become densely populated with the cells.

Interestingly it was observed that the HC04 hepatocytes (**Figure 6.3 , top row**) initially grew along the fibres in the NWF scaffold, and at later time points formed larger cellular clusters or constructs whereas the HepG2 hepatocytes (**Figure 6.3 , bottom row**) formed spheroids soon after seeding. It is known that hepatocytes rapidly de-differentiate in monolayer cultures while hepatospecific functions are maintained for longer periods in 3D cultures (Pampaloni et al., 2007). Additionally it has been reported previously that 3D hepatocyte colonies with cell-to-cell contact, display an up-regulation of genes approaching that of native tissue (Pampaloni et al., 2007). We have recently reported significantly improved and superior gene expression and albumin production from the PP-*g*-PNIPAAm NWF scaffolds compared to cells cultured under the same conditions on 2D tissue culture polystyrene (Rossouw et al., 2012)

6.3.2 Temperature-induced cell culturing from PNIPAAm grafted NWF

An initial trial was conducted to see which of the grafted NWF scaffolds enabled optimal cell release from the scaffolds at 20 ℃ and to investig ate the time required for cell release (**Figure 6.4**). PNIPAAm grafted PP, PET, and nylon NWF scaffolds were investigated when graft polymerisation was performed on direct fluorinated (gPP1, gPET1, and gnylon1), oxyfluorinated (gPP2, gPET2, and gnylon2) and the pure scaffolds (gPP3 and gPET3).

From **Figure 6.4**, it can be seen that cell release was most significant at 20 ℃ (as compared to 37 ℃) after 2 hours of incubation. Cell release was also most significant from gPP1, and gPP2 (when grafting was performed on the direct fluorinated and oxyfluorinated PP NWF scaffolds respectively), compared to the other scaffolds. Very few cells released at 20°C from the grafted PP surface when pure PP was used for grafting (**Figure 6.4, gPP3**). This can be attributed to the relatively poorer graft layer when grafting was performed on the pure PP scaffolds as compared to when the oxyfluorinated or direct fluorinated PP scaffolds were used and this result corroborates with the findings in Chapter 5. With respect to the PET-*g*-PNIPAAm and nylon-*g*-NIPAAm NWF scaffolds; some of the scaffolds appeared to have released cells however it was observed that these scaffolds also dropped a large number of fibres into the media indicating that thermal release alone was not responsible for the released cells. The release of fibres in the media may be due to poor stability of the NWF scaffolds such that upon handling and post- treatment, fibres were lost. It was observed that some cells did drop loose from almost all of the scaffolds at 37 ℃ which was attributed to agitation of the scaffolds during the cell release protocol.

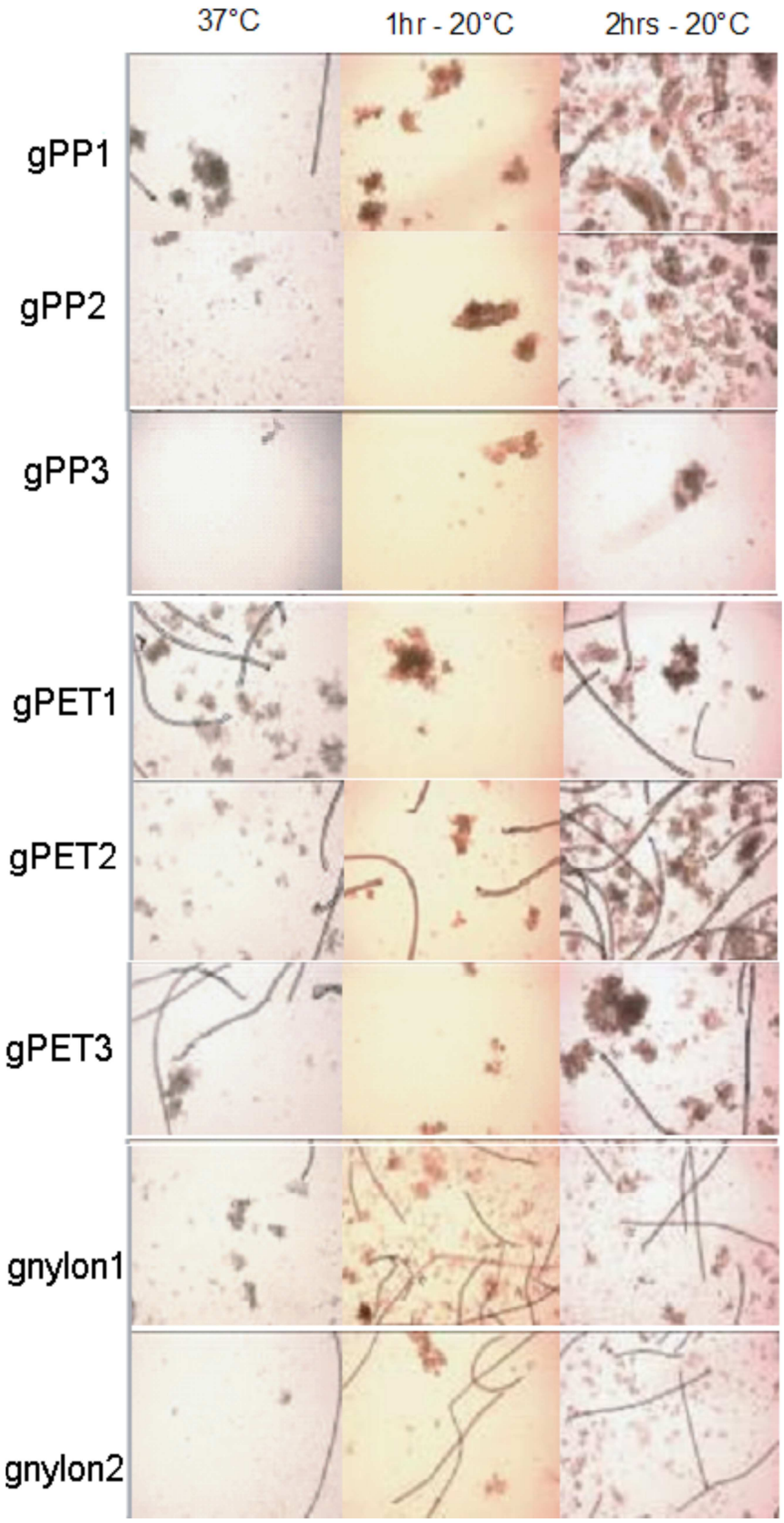

Figure 6.4: Thermal release of HCO4 hepatocytes after 10 days post-inoculation at 37 ℃ (control), and at 20 ℃ after either one or two hou rs of agitation. Scaffolds investigated were gPP1; gPP2; gPP3 (PP-*g*-PNIPAAm) where grafting was on direct fluorinated,

oxyfluorinated, and pure PP respectively); gPET1; gPET2; gPET3 (PET-*g*-PNIPAAm where grafting was on direct fluorinated, oxyfluorinated, and pure PET respectively); gnylon1; and gnylon2 (nylon-*g*-PNIPAAm where grafting was on direct fluorinated, and oxyfluorinated nylon respectively).

The results indicate that of the developed scaffolds PP-*g*-PNIPAAm (pre-fluorinated) NWF was the most feasible for use in non-invasive cell culture. This may be attributed to the superior graft layer on the PP NWF compared to PET and nylon. Another factor that may influence thermal cell release is the pore size distribution of the NWF scaffolds. Further optimisation is required for the PET-*g*-PNIPAAm and nylon-*g*-PNIPAAm NWF scaffolds and to improve the PNIPAAm graft yield before these scaffolds can be considered for temperature-induced cell culture.

To confirm the above results, temperature-induced cell release was repeated for the PP-*g*-PNIPAAm scaffolds (mean flow pores of 200 µm) using HCO4 and HepG2 cells when graft polymerisation was conducted on either direct fluorinated or oxyfluorinated PP NWF scaffolds (**Figure 6.5 gPP1 and gPP2 respectively**). As can been seen in **Figure 6.5**, a significant amount of cells were again released from both PP-*g*-PNIPAAm NWF scaffolds at 20 °C compared to 37 °C indicating that cell release is temperature-triggered due to the thermoresponsive nature of the PNIPAAm graft layer contained in the NWF scaffolds. Although both PP grafted scaffolds released a similar amount of cells, cell proliferation and growth was assessed to be better on the grafted pre-oxyfluorinated PP compared to the grafted direct fluorinated PP NWF scaffolds (Rossouw et al., [2012]). For both grafted scaffolds, cells were released as 3D cellular structures; and for the HepG2 cells, cell spheroids were observed. The 3D cell clusters and spheroids observed in this work, are a desirable morphology for certain cell culture applications (such as drug screening) as spheroids are highly metabolically active and a more relevant physiologically cell model.

Some contradictions exist in the literature with respect to the influence of graft thickness on cell attachment and release. Akiyama et al demonstrated that thickness of the PNIPAAm grafted onto tissue culture trays plays a key role in regulating cell adhesion of endothelial cells, whereby cells did not adhere to PNIPAAm grafted layers > 20 nm due to restricted molecular motion of the thicker grafted polymer chains resulting in insufficient dehydration of the outermost gel surface (Akiyama et al., 2007). In this study, we show that a PNIPAAm graft layer of ~200 nm (see Chapter 5) was still effective for both cell attachment and release. However it was observed that 2 hrs before a sufficient amount of cells could be

released. Further investigations are required to shorten the cell release time; which may involve reducing the thickness of the PNIPAAm graft layer such that attached cells can be released more efficiently.

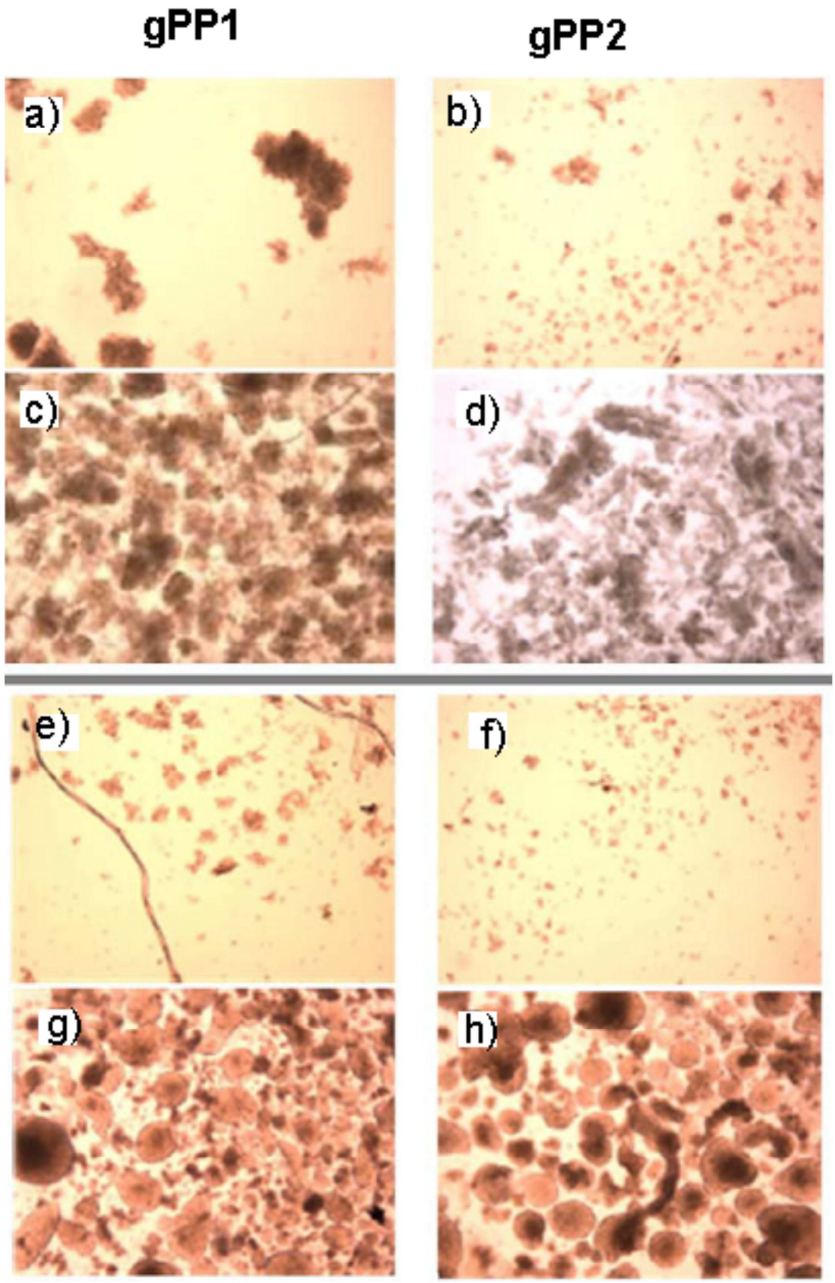

Figure 6.5: Temperature-induced cell release of HCO4 cells (a-d) and HepG2 cells (e-h) from PP-*g*-PNIPAAm NWF scaffolds; gPP1 (grafting on direct fluorinated PP NWF); gPP2 (grafting on oxyfluorinated PP NWF), where (a, b, e, f) and (c, d, g, h) shows cell release after 2 hours at 37 ℃ (control) and 20 ℃ respecti vely (Rossouw et al., 2012).

6.3.3 Temperature-induced cell release from PP-g-PNIPAAm NWF in the T3D device

We also investigated temperature-triggered cell release when cells were cultured on PP-*g*-PNIPAAm NWF disks in the preliminary prototype T3D bioreactor (**Figure 6.1**). Hepatocytes were seeded on three PP-*g*-PNIPAAm NWF disks and cultured for 10 days in the bioreactor to determine non-destructive cell release at 20 ℃. **Figure 6.6a** shows hepatocyte cells on the PP-*g*-PNIPAAm NWF disk at 37 ℃ at day 10 in culture while **Figure 6.6b** show cells remaining on the grafted PP NWF disk after temperature-induced cell release at 20 ℃. Cells remained viable on the NWF scaffold during in culture in the bioreactor. A significant amount of cells were released from the PP-*g*-PNIPAAm NWF at 20 ℃, confirming the thermoresponsive behaviour of the grafted NWF. Only minimal cell release was seen from the pure PP NWF disk at 20 ℃ due to loose cells falling off the scaffold (data not shown). As was observed previously, the hepatocyte cells grown on the PP-*g*-PNIPAAm NWF also arranged themselves as 3D multicellular aggregates (**Figure 6.6a**).

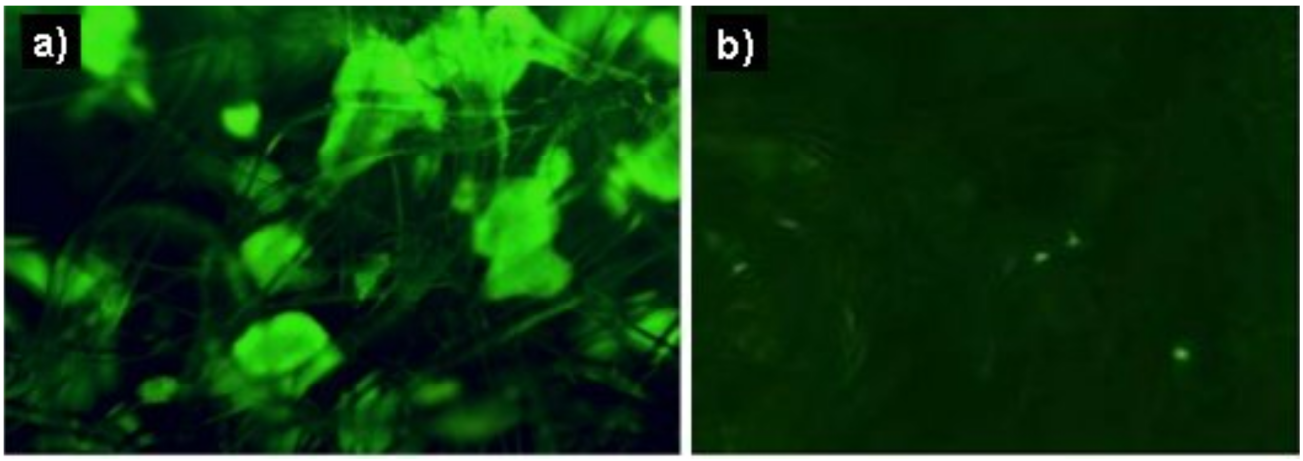

Figure 6.6: Fluorescence micrographs showing HepG2 cells on the PP-*g*-PNIPAAm NWF disks in the T3D device (preliminary prototype) (a) at 37 ℃ after 10 days of culture and (b) after thermal cell release at 20 ℃ for 2 hrs showing cells remaining on the NWF.

Fluorescent microscopy however did reveal that not all cells were released from the scaffold by a temperature change. Similar results were also observed for the thermal–release studies which were conducted in static culture. There are a number of factors which could contribute to cells still remaining on the NWF scaffolds after temperature-triggered cell release. This may possibly be attributed to inhomogeneity in the PNIPAAm layer on the NWF surface, whereby some of the fibre surface is not sufficiently grafted hence not all the attached cells

release using a temperature change. Another plausible explanation may be that due to the 3D cellular structural configuration of the cells in the NWF, not all cells may be easily able to navigate out of the matrix upon cell release.

An estimation of cell recovery from the PP-*g*-PNIPAAm scaffolds after 10 days of culture was conducted for thermal cell release versus trypsin treatment (Rossouw et al., 2012). This study indicated that in most cases approximately similar cell numbers were obtained when either trypsin or thermal cell release protocol was used, and in each case fewer cells were released compared to the estimated total number of cells growing on the scaffolds. This finding can be attributed to the 3D nature of the cell clusters. The results are promising in that it shows that the temperature release mechanism of the grafted scaffolds under the present culture conditions is comparable to the number of cells released when trypsin is used, however temperature triggered cell release, displays the added advantage in that it is less destructive to the cultured cells, and cells are released with intact surface proteins and membrane constituents. However further optimisation of the scaffold and the cell culture process is needed to improve cell recovery.

A preliminary trial was also conducted to ascertain if high-density cell culture was possible in the preliminary T3D bioreactor. A total of 4.5 $x10^6$ cells were initially seeded into the bioreactor containing three stacked pure PP NWF disks (15 mm diameter), and 39.7 x 10^6 and 49.9 x 10^6 hepatocytes were harvested from the bioreactor in two independent experiments at day 14, representing a 10 fold increase in cell numbers. Although these results are promising, further optimisation of the system is required to enable cell densities which are significantly higher that which can be obtained in conventional culture flasks.

Based on the results for the preliminary T3D device, the design of the T3D device was optimised and the final bench-top T3D system has now been constructed (**Figure 6.7)**. Further studies are now on going to verify high-density cell culture in the T3D final prototype system.

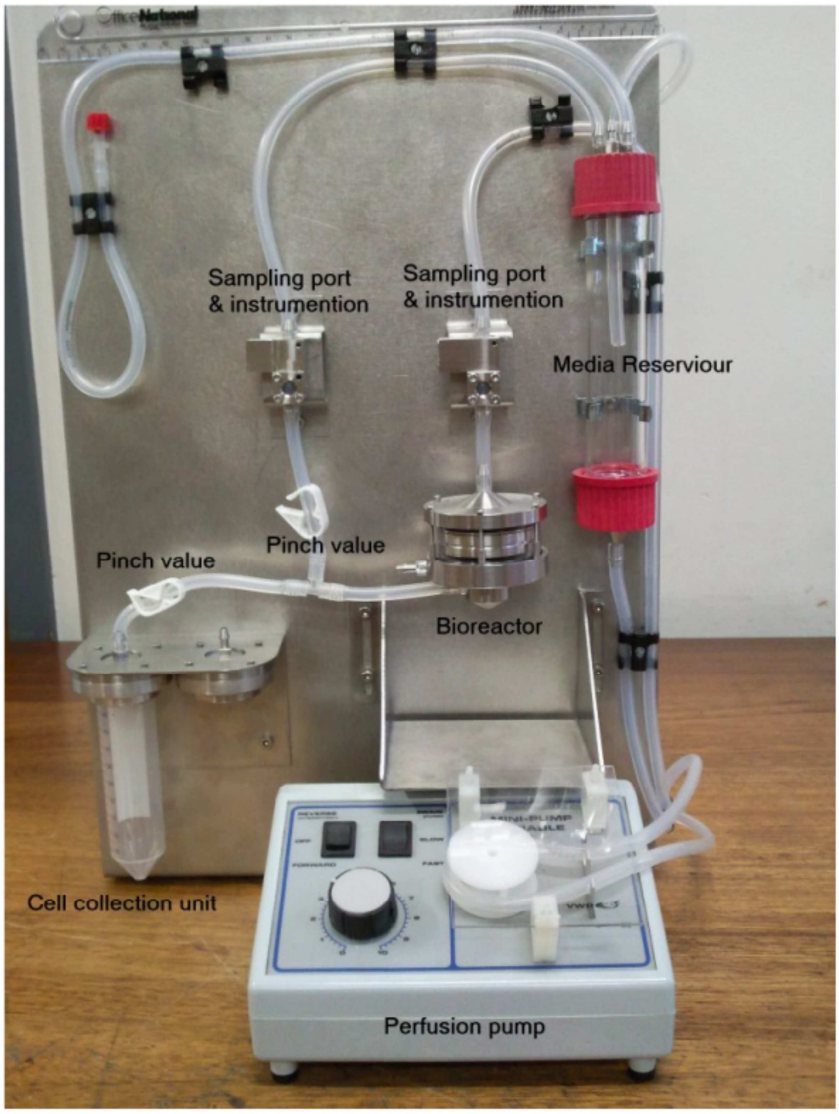

Figure 6.7: Final prototype bench-top system of CSIR's T3D device with a larger bioreactor (125 ml volume) containing media and gas outlets to remove trapped air-bubbles, and a tapered media reservoir. Several NWF disks (5cm diameter) can be stacked in the bioreactor to ensure high-density cell culture.

6.4 Conclusions

In this study we have demonstrated proof-of-concept for temperature-induced cell release from PNIPAAm grafted NWF scaffolds. Hepatocyte cells attached on the scaffolds at 37 °C and remained viable for 21 days post inoculation. Cell release was most significant at 20 ℃ after 2 hrs of incubation from the PP-*g*-PNIPAAm NWF scaffolds compared to the grafted PET and nylon NWF scaffolds. Cells release was possible without using trypsin or other

destructive means. Additionally the cells were harvested as functional 3D multi-cellular spheroidal aggregates. The CSIR has also developed a novel T3D device containing a bioreactor for housing the PNIPAAm grafted scaffolds for use in 3D non-invasive cell culture. We have also demonstrated that cell release was possible from the PP-*g*-PNIPAAm NWF scaffolds in the T3D bioreactor. Due to the large surface area of the 3D scaffold NWF scaffold, we have also shown in a preliminary trial, that large increase in cell numbers is possible from the T3D bioreactor, however further optimisation of the scaffolds and device are required for improved performance.

6.5 References

Akiyama Y, Kikuchi A, Yamato M, Okano T. 2004. Ultrathin poly(*N*-isopropylacrylamide) grafted layer on polystyrene surfaces for cell adhesion / detachment control. Langmuir 20:5506-5511.

Canavan HE, Cheng X, Graham DJ, Ratner BD, Castner DG. 2005. Cell sheet detachment affects the extracellular matrix: A surface science study comparing thermal liftoff, enzymatic, and mechanical methods. Journal of Biomedical Materials Research -A. 75(1):1-13.

Guillame-Gentil O, Semenov O, Roca AS, Groth T, Zahn R, Vörös J, Zenobi-Wong M. 2010. Engineering the extracellular environment: strategies for building 2D and 3D cellular structures. Advanced Materials 22:5443–5462.

Isenberg BC, Tsuda Y, Williams C, Shimizu T, Yamato M, Okano T, Wong JY. 2008. A thermoresponsive, microtextured substrate for cell sheet engineering with defined structural organization. Biomaterials 29:2565–2572.

Justice BA, Badr NA, Felder RA. 2009. 3D cell culture opens new dimensions in cell-based assays. Drug Discovery Today 14(1/2):102-107.

Kwon IK, Matsuda T. 2006. Photo-iniferter-based thermoresponsive block copolymers compose of poly(ethylene glycol) and poly(*N*-isopropylacrylamide) and chondrocyte immobilization. Biomaterials 27: 986–995.

Moolman FS, Naidoo K, Van Wyk AJ; 2009. Non-invasive automated cell proliferation apparatus patent WO 2009/031127 A2.

Ohya S, Kidoaki S, Matsuda T. 2005 Poly(*N*-isopropylacrylamide) (PNIPAM)-grafted gelatin hydrogel surfaces: interrelationship between microscopic structure and mechanical property of surface regions and cell adhesiveness. Biomaterials 26:3105–3111.

Okamura A, Hagiwara T, Yamagami S, Yamaguchi M, Shinbo T, Kanamori T, Kondo S, Miwa K, Itagaki I. 2008. Effective cell separation utilizing poly(N-

Isopropylacrylamide)-grafted polypropylene membrane containing adsorbed antibody. Journal of Bioscience and Bioengineering 105 (3):221–225.

Okano T, Yamada N, Okuhara M, Sakai H, Sakurai Y. 1995. Mechanism of cell detachment from temperature-modulated, hydrophilic-hydrophobic polymer surfaces. Biomaterials 16:297-303.

Pampaloni F, Reynaud EG, Stelzer EHK. 2007. The third dimension bridges the gap between cell culture and live tissue. Nature Reviews Molecular Cell Biology 8:839-845.

Prestwich GD. 2008. Evaluating drug efficacy and toxicology in three dimensions: Using synthetic extracellular matrices in drug discovery. Accounts of Chemical Research 41(1):139-148.

Rossouw CL, Chetty AS, Moolman FS, Birkholtz L-M, Hoppe H, Mancama DT. 2012. Thermo-responsive non-Woven scaffolds for ‘‘smart’’ 3D cell culture. Biotechnology and Bioengineering 109(8):2147-2158.

Sattabongkot J, Yimamnuaychoke N, Leelaudomlipi S, Rasameesoraj M, Jenwithisuk R, Coleman RE, Udomsangpetch R, Cui L, Brewer TG. 2006. Establishment of a human hepatocyte line that supports in vitro development of the exo-erythrocytic stages of the malaria parasites *Plasmodium falciparum* and *P.vivax*. American Journal of Tropical Medicine and Hygiene 74(5): 708–715.

Schild H. 1992. Poly(*N*-isopropylacrylamide): Experiment, theory, and application. Progress in Polymer Science 17:163-249.

Yamato M, Akiyama Y, Kobayashi J, Yang J, Kikuchi A, Okano T. 2007. Temperature-responsive cell culture surfaces for regenerative medicine with cell sheet engineering. Progress in Polymer Science 32:1123–1133

CHAPTER 7

Conclusions and Prospects

7.1 Conclusions of study

Although the conventional 2D monolayer cell culture method is currently the gold standard used to culture adherent cells, this method is highly tedious, prone to contamination, and is known to be an inaccurate representation of the manner in which cells exist in their physiological state. Nowadays there are numerous solutions being proposed to culture cells, however there is still a need for a bench-top type cell culturing system; capable of culturing cells in 3D with efficiency, minimal human intervention, and where cell release is non-invasive and achieved without damaging the harvested cells. The aim of this study was to develop a unique 3D highly porous scaffold containing poly(*N*-isopropylacrylamide) for use in non-invasive cell culture.

A summary of the main findings from phases 1-3 of this work is given below:

- **Phase 1: Development of P(NIPAAm-*co*-MBA) hydrogels**

We initially developed P(NIPAAm-*co*-MBA) hydrogels with the aim of investigating the effect of crosslink-density and the use of mixed solvents on the physical properties of PNIPAAm hydrogels. Cross-linking maintained the LCST of the hydrogels, and increasing the cross-link density, improved the viscoelastic properties of the hydrogels. However when water was used as the co-polymerisation medium the swelling-deswelling response rate of the gels was very poor. The swelling-deswelling response was significantly improved using mixed solvents as the co-polymerisation medium; however these gels displayed very poor stability and handling and were deemed unsuitable for use in a robust bioreactor. Additionally at 25 °C the PNIPAAm-co-MBA hydrogels displayed relatively small pores (<10 µm) which may present a challenge for cell release, whereas at 37 °C (temperature used for cell seeding and proliferation), porosity was completely lost due to the dense skin layer, implying that the hydrogels may be unsuitable with respect to providing 3D support for cells during culture.

- **Phase 2: Development of PNIPAAm grafted 3D NWF scaffolds**

We successfully synthesised highly porous 3D PNIPAAm grafted NWF scaffolds based on PP, PET and nylon using needle-punching and a facile oxyfluorination-assisted graft polymerisation (OAGP) method. The NWF scaffolds displayed highly porous 3D structures, with high porosity content. The mean flow pores for the PP, and PET NWF ranged between 100-200 µm which was the desired range for culturing cells, whereas the nylon NWF

scaffolds displayed substantially smaller pores. We showed that OAGP could be successfully used to covalently attach PNIPAAm onto the surface of the 3D NWF scaffolds, while preserving the open porous structure in the grafted scaffolds. The OAGP method resulted in new functional polar groups forming on the surface of the NWF scaffolds. No changes were seen to the crystalline phase of bulk PP after OAGP; however, twin-melting thermal peaks were detected, indicating crystal defects. The LCST of PNIPAAm was maintained in the grafted scaffolds. Graft yields was highest for the PP-*g*-PNIPAAm NWF which was pre-oxyfluorinated. A free radical mechanism was proposed for the OAGP method with initiation via $SO_4^{\bullet-}$; $OH^{\bullet}$ and $RO^{\bullet}$ radicals. This OAGP method used in this study, proved to be an attractive alternative to other polymerisation technologies (such as gamma radiation, plasma-radiation etc.) since it is simple to perform, does not require the use of expensive equipment or toxic solvents, and it is relatively less invasive compared to other radiation methods.

- **Phase 3: Proof-of-concept for temperature-induced cell culture**

Finally in phase 3 of this work, we showed temperature-triggered cell release from the PNIPAAm grafted NWF scaffolds whereby confluent cells were released spontaneously and non-destructively from the surface of the grafted NWF by cooling the cell culture medium from 37 ℃ to 20 ℃, and without requiring destruct ive enzymes. We demonstrated that hepatocyte cells attached onto the surface of the PP-*g*-PNIPAAm NWF scaffolds, and remained viable during 21 days of culture. PP-*g*-PNIPAAm NWF scaffolds which were pre-oxyfluorinated, demonstrated superior thermal cell release capability compared to the other scaffolds. During cell growth, cells arranged themselves as 3D multi-cellular constructs or spheroids and were released as cell aggregates. Temperature-induced cell release was also demonstrated in the T3D bioreactor with the potential for high-density cell culture.

7.2 Significance of study

With technological innovations in regenerative medicine, gene-therapy and stem-cell research, the demand for large quantities of mammalian cells closely resembling physiological state and new and improved cell culture systems for manufacturing such cells are projected to accelerate in the future. The CSIR has developed a simple-to-use, cost-effective bench-top type device (T3D) which contains a PNIPAAm grafted 3D NWF scaffold in a perfused bioreactor to improve the efficiency of the cell culture process. The T3D device

of the present study represents a substantial improvement to the way in which cells are cultured, compared to static 2D monolayer cell culture method, as well as other PNIPAAm scaffolds which have been developed. The combination of a perfused bioreactor capable of culturing cells on a 3D scaffold capable of high-density cell culture and non-invasive cell release has not been reported / demonstrated previously in literature. Currently most of the bioreactors capable of 3D cell culture rely on either enzymes or chemicals to release cells, which are destructive to the cell membrane. Additionally most of the literature pertaining to "3D PNIPAAm scaffolds" focus on scaffolds with relatively small pores (sub-micron) only for the purpose of facilitating oxygen supply, and nutrient to cells, as well as hydration from the basal cell layer. Also the focus of many of these studies is still on the release of cell monolayers for cell sheet engineering, and not on cell expansion, propagation and release of 3D cell cultures. No other study reported the growth, propagation and release of 3D multicellular structures in large volumes non-invasively using PNIPAAm 3D scaffolds.

Currently cell culturing is a substantial bottleneck hampering advancements in a number of fields including tissue engineering, drug-screening, stem cell research and gene therapy amongst others. Successful implementation of the cell culture device will have far reaching implications not just for research but for the larger biotechnology industry.

The potential impact of the T3D device proposed in this project:

- Cells are cultured on a 3D surface in a contained sterile dynamic bioreactor environment to more closely resemble the cell physiological state (as compared to static 2D cell culture) thereby improving the quality of the outputs of *in vitro* cell culture research.
- Proliferation & harvesting of 3D cell clusters or spheroids are achieved which are more metabolically active and representative of the native state of cells.
- Confluent cells are released spontaneously and non-destructively from the surface of the scaffolds by cooling the cell culture medium from 37 ℃ to 20 ℃, and without requiring destructive enzymes, thereby preserving the ECM and surface proteins, which are important for downstream applications.
- Cell recovery time during passaging cycles is also reduced since cells have a preserved cell membrane composition, and are able to recover much faster.
- Cell culture is simplified since no enzymes are required thereby lowering costs since less washing and purification steps are needed.
- When the bench-top system is fully automated, minimal human intervention will be required hence the labour-intensive process required for manual cell culturing is

mitigated, thereby leading to reduced contamination, improved repeatability, and lower costs.

- The scaffold is supplied pre-fabricated, sterile and ready to use without requiring any preparation steps prior to use, hence simplifying the cell culture process.
- The scaffolds are highly permeable, allowing cells to easily pass through, and can be used directly for cell lysis (e.g. in a QiaShredder) without requiring any additional digestion steps, thereby saving time for the researcher, and improving the efficiency of the cell culture process. We have demonstrated this in our labs.
- Potential to improve quality of human life by contributing towards advancements in tissue engineering, stem cell research, *in vitro* drug screening and drug development research amongst others.

The PNIPAAm grafted 3D NWF scaffold and the T3D device could either be commercialised as one entity or separately; whereby typically any other similar scaffold could be used in the device, and the scaffolds itself could be used as 3D cell-culture inserts for culture trays as well as other suitable cell culture system. Both the scaffold and device has a relatively short route to market, with no preclinical or clinical trials required. Potential end-users include universities, research institutes, pharmaceutical companies, hospitals, etc., where large cell numbers are required and would include applications such as biomaterial and drug testing; drug screening of new actives, tissue engineering, and genetic engineering. The cell culture device of the present study aims to provide a reliable tool to culture cells with an *in vitro* cell proliferation system that minimises human intervention and potential error in a cost-effective, easy-to-use package that would enable widespread uptake.

7.3 Recommendations

The PP-*g*-PNIPAAm NWF scaffold developed in this study is suitable as a new 3D scaffold for non-invasive cell culture. However further investigations into the following aspects is suggested for this technology:

- Further improvements are required with respect to the homogeneity of the graft layer on the PP NWF surface. This will likely contribute to further improving the efficiency of cell release from the PP-*g*-PNIPAAm NWF.
- Improvements are required with respect to the structural stability of the NWF. Fibers dropped in the media from the NWF scaffolds during culture more so for the PET and

nylon fibres. Optimisation of the needle-punching technology is required which may involve improving the thermo-bonding process.

- We have shown that 2 hrs at 20 °C is required to release a significant amount of cells from the PP-*g*-PNIPAAm scaffolds. This cell release period however is relatively long. Currently the commercially available thermo-responsive 2D plates (UPCell™, Cell Seed Inc, Tokyo, Japan) require 30 min for release of a monolayer of cells. UPCell™ however is based on PNIPAAm grafted 2D surface. The grafted scaffold and the cell release protocol of the present study should be optimised such that maximum cell release is possible in a minimal amount of time. This may involve reducing the thickness of the PNIPAAm graft layer on the NWF scaffolds.
- In preliminary studies we have shown that high-density cell culture is possible in the T3D device, however cell numbers still are not significantly higher than 2D culture. Further optimisation is required to improve cell density in the system.
- At this stage we only showed proof of concept for hepatocyte cell lines. The present technology needs to be validated for a variety of different cell types (including primary cells and cell lines) before it can be adopted as a universal tool for cell culture.
- To improve the efficiency and reproducibility of cell culture, the system still needs to be automated such that human intervention is minimal. This will involve incorporating a programmable logic control system to automate the manual cell culture steps.